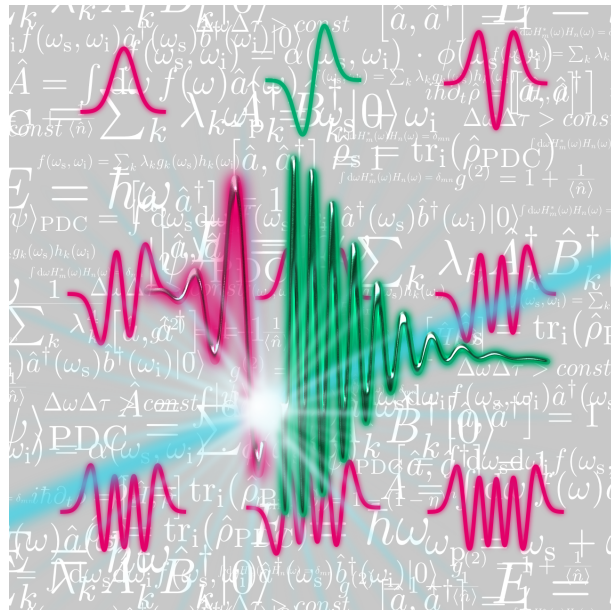


# Engineering ultrafast quantum frequency conversion



Der Naturwissenschaftlichen Fakultät  
der Universität Paderborn  
zur  
Erlangung des Doktorgrades Dr. rer. nat.  
vorgelegt von  
BENJAMIN BRECHT  
aus Nürnberg



*To Olga  
for Love and Support*



---

# Contents

---

1	Summary	1
2	Zusammenfassung	3
3	A brief history of ultrafast quantum optics	5
3.1	1900 – 1950 . . . . .	5
3.2	1950 – 2000 . . . . .	6
3.3	2000 – today . . . . .	8
4	Fundamental theory	11
4.1	Waveguides . . . . .	11
4.1.1	Waveguide modelling . . . . .	12
4.1.2	Spatial mode considerations . . . . .	14
4.2	Light-matter interaction . . . . .	16
4.2.1	Nonlinear polarisation . . . . .	16
4.2.2	Three-wave mixing . . . . .	17
4.2.3	More on phasematching . . . . .	18
4.3	Ultrafast pulses . . . . .	21
4.3.1	Time-bandwidth product . . . . .	22
4.3.2	Chronocyclic Wigner function . . . . .	22
4.3.3	Pulse shaping . . . . .	25
5	From classical to quantum optics	27
5.1	Speaking quantum . . . . .	27

5.1.1	Field quantisation in waveguides . . . . .	28
5.1.2	Quantum three-wave mixing . . . . .	30
5.1.3	Time-frequency representation . . . . .	32
5.1.3.1	Joint spectral amplitude functions . . . . .	32
5.1.3.2	Schmidt decomposition . . . . .	35
5.2	Understanding quantum . . . . .	36
5.2.1	Parametric down-conversion . . . . .	37
5.2.2	Time-frequency correlations . . . . .	39
5.2.2.1	The Schmidt number $K$ . . . . .	39
5.2.2.2	Impact of TF correlations . . . . .	40
5.2.3	Frequency conversion . . . . .	41
5.3	Engineering quantum . . . . .	44
5.3.1	Phasematching . . . . .	44
5.3.2	Pump . . . . .	49
5.4	Time-ordering . . . . .	54
6	Ultrafast parametric down-conversion . . . . .	59
6.1	Continuous variable description . . . . .	60
6.2	Chronocyclic representation of PDC states . . . . .	63
6.3	On the correlation time of ultrafast biphotons . . . . .	70
6.4	Theory put to test . . . . .	75
7	Quantum pulse gate and quantum pulse shaper . . . . .	81
7.1	Quantum pulse gate . . . . .	83
7.1.1	The QPG unitary operation . . . . .	83
7.1.2	Adding an input state . . . . .	85
7.1.3	Revealing the QPG TF structure . . . . .	86
7.1.4	Optimising the QPG TF modes . . . . .	89
7.1.5	Experimental limitations . . . . .	90
7.2	Quantitative Hamiltonian . . . . .	92
7.3	Experiment . . . . .	94
7.3.1	Pulse shaping with the Dazzler . . . . .	95
7.3.2	Overview over the setup . . . . .	95

7.3.3	Spatial mode adaption . . . . .	99
7.3.4	Mapping of the QPG time-frequency modes . . . . .	101
7.3.5	Adapting the QPG TF modes to an unknown input . . . . .	103
7.3.6	Performance benchmarks . . . . .	105
7.4	Next steps: Quantum pulse shaper . . . . .	107
8	Conclusion and outlook	111
8.1	Conclusion . . . . .	111
8.2	Outlook . . . . .	112
9	Acknowledgements	115
A	Appendix	117
A.1	Derivation of the vectorial wave equations in waveguides . . . . .	117
A.2	Calculation of the electric field strength . . . . .	119
A.3	The dielectric tensor . . . . .	120
A.3.1	Kleinman symmetry . . . . .	120
A.3.2	Nonlinear tensor and contracted notation . . . . .	120
A.3.3	Lithium niobate and potassium titanyl phosphate . . . . .	121
A.4	Three-wave mixing Hamiltonian . . . . .	122
A.5	4-f-spectrometer with tilted slit . . . . .	124
B	References	125



---

# Summary

---

Ultrafast quantum optics is a young research field. Its focus lies at the study of quantum phenomena at extreme timescales of a few hundreds of femtoseconds.

In this thesis, we investigate the intricate time-frequency (TF) structure of ultrafast quantum states of light. This structure is of particular interest, because it is the natural basis of energy-time entanglement, a resource for high-dimensional quantum information applications.

We study the process of parametric down-conversion (PDC) and introduce a novel measure for energy-time entanglement which is applicable to many current PDC sources. Moreover, we experimentally investigate the correlation time of the photon pair, a measure of the simultaneity of the photons, and find that is independent of the spectral-temporal properties of the PDC pump.

The main work is dedicated to two novel devices for high-dimensional TF quantum networks, the quantum pulse gate and quantum pulse shaper. Both are based on dispersion engineered frequency conversion in nonlinear waveguides and facilitate a mode-selective operation on TF modes of ultrafast quantum states.

We develop a theoretical framework, similar to the existing PDC description, to describe the TF structure of our devices and identify ideal operation parameters. These are used to realise a quantum pulse gate in the laboratory and verify its mode-selective operation.



---

# Zusammenfassung

---

Die Ultrakurzpuls-Quantenoptik ist ein junges Forschungsfeld. Sie beschäftigt sich vorwiegend mit Quantenphänomenen auf ultrakurzen Zeitskalen im Bereich einiger hundert Femtosekunden.

In dieser Dissertation untersuchen wir die komplexe Zeit-Frequenz (ZF) Struktur von ultrakurzen Quantenpulsen, welche die natürliche Basis zur Beschreibung von Energie-Zeit Verschränkung, einer Ressource für hochdimensionale Quanteninformations Anwendungen, ist.

Unsere Untersuchung von parametrischer Fluoreszenz (PF) führt zur Einführung eines neuen Energie-Zeit Verschränkungsmaßes, das sich auf viele PF Quellen anwenden lässt. Darüber hinaus bestimmen wir experimentell die Korrelationszeit von Photonenpaaren, die ein Maß für die Gleichzeitigkeit der Photonen ist. Sie hängt nicht von den Kohärenzeigenschaften des PF Pumplichts ab.

Der Hauptteil unserer Arbeit beschäftigt sich mit zwei neuen Bauelementen für hochdimensionale ZF Quantennetzwerke, dem Quantenpulsgatter und dem Quantenpulsformer. Beide basieren auf Frequenzkonversion in nichtlinearen Wellenleitern mit angepasster Dispersion und ermöglichen eine modenselektive Manipulation der ZF Moden ultrakurzer Quantenpulse.

Aus der bekannten PF Beschreibung entwickeln wir eine Theorie um die ZF Struktur unserer Bauelemente zu beschreiben und identifizieren ideale Parameter, welche wir verwenden um ein Quantenpulsgatter experimentell zu realisieren und zu verifizieren.



Geschrieben steht: "Im Anfang war das Wort!"  
 Hier stock ich schon! Wer hilft mir weiter fort?  
 Ich kann das Wort so hoch unmöglich schätzen,  
 Ich muß es anders übersetzen,  
 Wenn ich vom Geiste recht erleuchtet bin.  
 Geschrieben steht: Im Anfang war der Sinn.  
 Bedenke wohl die erste Zeile,  
 Daß deine Feder sich nicht übereile!  
 Ist es der Sinn, der alles wirkt und schafft?  
 Es sollte stehn: Im Anfang war die Kraft!  
 Doch, auch indem ich dieses niederschreibe,  
 Schon warnt mich was, daß ich dabei nicht bleibe.  
 Mir hilft der Geist! Auf einmal seh ich Rat  
 Und schreibe getrost: Im Anfang war die Tat!

*Faust - Johann Wolfgang von Goethe*

# 3

---

## A brief history of ultrafast quantum optics

---

### Contents

3.1 1900 – 1950 . . . . .	5
3.2 1950 – 2000 . . . . .	6
3.3 2000 – today. . . . .	8

The 20<sup>th</sup> century has been the cradle of modern physics. Discoveries like the theory of relativity and quantum mechanics have reformed our view of the world. At the beginning of the century, matter consisted of solid, undividable atoms and Maxwell's and Newton's equations could

precisely predict the evolution of any physical system, leaving no space for probabilistic behaviour. In addition, the physicist was considered a mere observer who did not exert any influence on the system under investigation. Today however, our views are radically different. Here, we present a brief timeline with selected developments, which led to our current perception of the world and to the rise of the research field of ultrafast quantum optics, in the context of which this thesis is embedded. Our results have contributed to promoting this young field and lay foundations for future advances along the lines of high-dimensional, ultrafast quantum information processing.

### 3.1 1900 – 1950: the origin of quantum mechanics

Some say that quantum mechanics started in 1900, when Max Planck presented his work '*Über irreversible Strahlungsvorgänge*' [1]. He explained the spectrum of black body radiation by postulating that radiation was only absorbed and emitted in discrete quanta, an idea which was

revisited by Albert Einstein to explain the photoelectric effect [2]. Works by Dirac, Bohr, Born, Heisenberg and others followed and led to the establishment of quantum mechanics as a young and fascinating theory.

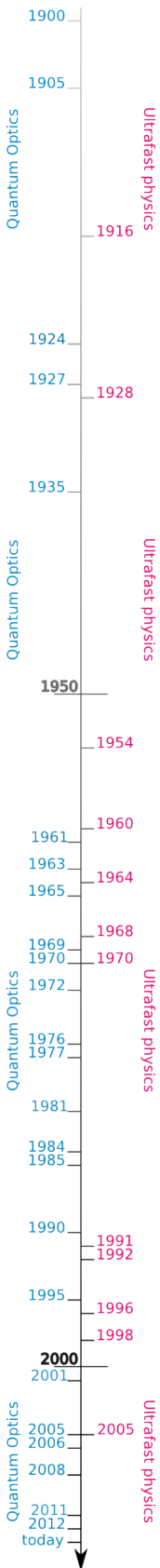
The quantum mechanical framework was first put to test, when Louis de Broglie suggested that matter particles should exhibit wavelike behaviour at small length scales [3]. At that point, this notion was not part of the theory, and the need for a formal construct which consistently explained all phenomena became obvious. Starting from 1925, Erwin Schrödinger and Werner Heisenberg followed two complementary approaches towards this aim. Schrödinger introduced the so-called wave mechanics, where a quantum state was described by a wave function which evolved with time [4]. In contrast, Heisenberg favoured the matrix mechanics approach, where the state itself was stationary, but the matrices describing the system were dynamic [5, 6]. This duality posed a severe problem. If the wave function was a physical entity, as Schrödinger claimed, then Heisenberg's approach had to be wrong. If, however, the contrary was true, what physical meaning could be attributed to the wave function?

In 1927, a solution to this was proposed in the Copenhagen interpretation of quantum mechanics [7]. Its essential statement is that quantum mechanics was and is inherently probabilistic in nature. The wave function is not an actual element of reality, but rather a means for predicting the probability of a measurement outcome. Although having been refined over the years, the Copenhagen interpretation is still the most prominent interpretation of quantum mechanics to date.

We might note at this point that Einstein's famous quote '*Der Alte würfelt nicht.*' nicely reflects the fact that not all physicists were happy with the new view of the world. Oddly enough, by trying to prove quantum mechanics wrong, Einstein, Podolsky and Rosen (EPR) involuntarily helped to strengthen it. In their famous paper from 1935 they argued that quantum mechanics had to be an incomplete theory, which relied on so-called hidden variables to regain determinism [8]. Otherwise, so they claimed, it would be possible to measure the momentum and position of a particle with arbitrary precision, which would be in disagreement with Heisenberg's uncertainty principle [9]. Today we know the outcome of the following discussion. Entanglement, a strictly non-classical resource, can provide the necessary means to seemingly overcome the uncertainty relation and is today an accepted reality. After this work it grew comparably quiet and we will skip the next 20 years. Then, however, a groundbreaking invention was to shed new light on quantum mechanics.

## 3.2 1950 – 2000: illuminating quantum optics

In 1955, Charles Townes invented the maser [10]. This device was capable of generating coherent microwave radiation by exploiting the process of stimulated emission [11–14] and allowed experimental access to novel quantum states of radiation. Now things began to move fast. Shortly after, in 1960, Ted Maiman implemented the first laser, which generated light pulses from a silver coated slab of ruby pumped by a high power flash lamp [15]. In contrast to the maser, the laser generated coherent *optical* radiation. During the 60s, a quantum theory of light started to evolve around the new experimental means. Consequently, quantum optics was established as an independent field of research. Tony Siegman et al formulated a quantum



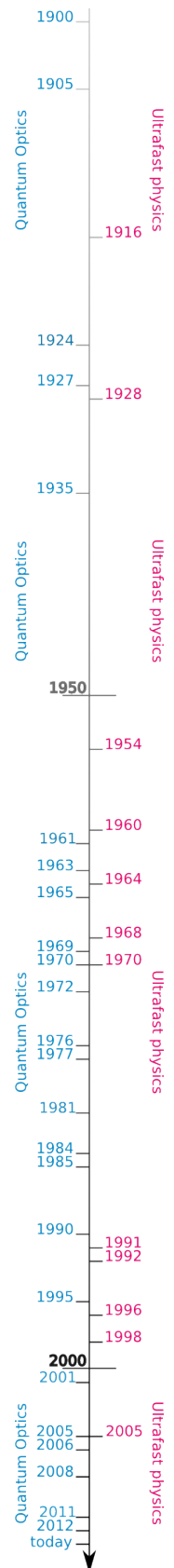
mechanical description of parametric processes [16], Roy Glauber published his seminal work on *'The quantum theory of optical coherence'* for which he was awarded the Nobel Prize in 2005 [17], and John Bell formulated his famous inequalities [18]. They were shortly thereafter refined by Clauser, Horne, Shimony and Holt [19] and provided, for the first time, a test for quantum mechanics which could be performed in the laboratory.

In parallel, new developments in laser technology – for instance mode locking [20] or the invention of the titanium sapphire (Ti:Sapph) laser [21] – brought into reach more exotic quantum states of light. For example, in 1970 Burnham and Weinberg realised a proposal by Zel'dovich and Klyshko [22] for the generation of photon-pair states and demonstrated the process of parametric luminescence [23], which today is better known as parametric down-conversion.

Besides that, however, the 70s were the high time of photonic quantum states emitted from atoms. In 1972, Freedman and Clauser demonstrated a clear and indisputable violation of Bell's inequality [24]. This experiment proved for the first time that quantum mechanics did not rely on hidden variables, as suspected by EPR. Further experiments followed, and in 1981 Alain Aspect and co-workers were able to perform novel types of Bell-tests with unprecedented low statistical errors [25]. Complementing these developments, Kimble et al demonstrated for the first time the anti-bunching behaviour of photons emitted from resonantly excited sodium atoms [26].

With the capability of generating exotic quantum states of light in the laboratories, people started to think seriously about applications for quantum optics during the 80s. In 1984, Charles Bennett and Gilles Brassard suggested exploiting photons for secure communication and introduced the famous BB84 protocol for quantum encryption [27]. One year later, Slusher and co-workers demonstrated the first squeezed quantum state [28]. These states were ideally adapted to high-precision interferometry applications, because they featured even smaller phase fluctuations than coherent states. Finally, the demonstration of the interference of single photons at a beam splitter by Hong, Ou and Mandel in 1988 [29] paved an avenue towards more complex quantum networks and quantum computation applications [30].

In parallel to these developments, the field of ultrafast laser physics had been developing. Since the first generation of a short, coherent pulse in 1964 [31], further techniques to generate ever shorter pulses have emerged. The driving force behind these advances were the potential applications in diverse fields such as physics, biology, chemistry, medical research and material processing. In these areas, short pulses, high peak powers and especially stability and reproducibility have been the major demands, which could not be fulfilled to full satisfaction until 1991. Then, the first experimental implementation of the Kerr-lens mode-locking technique in a Ti:sapphire laser enabled the direct generation of pulses with a duration of 60 femtoseconds and an unprecedented stability [32]. This development fostered research on the formal description [33] and experimental characterisation [34, 35] of these pulses, a task which was, and is not, trivial due to the limited temporal resolution of real-world detectors. These extreme pulses were the enabling technology for an intriguing field of physics: frequency metrology. It had already been known that trains of laser pulses from a modelocked laser formed frequency combs, which could serve as a precise ruler in the frequency domain. This unique property and the development of the photonic crystal fiber in 1996 [36], which facilitated the generation of so-called supercontinua [37–39], gave fresh impetus to optical frequency metrology. Exploiting ultrafast frequency combs with spectral widths of more than one octave allowed for the measurement



of frequencies with a precision of a few parts in  $10^{18}$ . This impressive development culminated in the Nobel Prize for Theodor Hänsch in 2005 for '*contributions to the development of laser-based precision spectroscopy, including the optical frequency comb technique*'.

On the quantum optics side, parametric down-conversion became an established tool for the generation of photon pairs (see, for instance [40–43]) and even optical EPR states [44]. Moreover, people began to investigate the prospects of harnessing other parametric processes for quantum applications. In 1990, Prem Kumar proposed using sum-frequency generation to exchange the quantum properties of two light beams at different frequencies [45]. His vision was a frequency-tuneable source of squeezed light states for spectroscopy applications: The special properties of these non-classical light states could improve the resolution of interferometers, but they were only available at very specific wavelengths. Frequency conversion suggested itself as an apt solution to this problem, and was confirmed as such in 1992 [46].

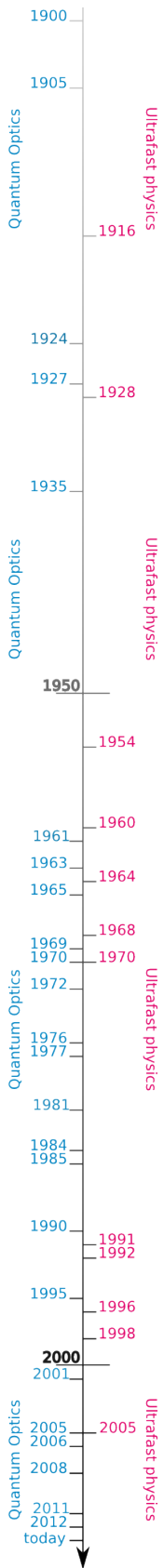
### 3.3 2000 – today: ultrafast quantum optics

At the beginning of this century, Tanzilli et al demonstrated for the first time a parametric down-conversion source based on integrated nonlinear waveguide technology [47]. This source design forced the generation of photons into discrete waveguide modes and thus decoupled the spectral and spatial degrees of freedom. In addition, the confinement of the light inside the waveguide led to an increased interaction length for the nonlinear process. In combination, these advances facilitated the implementation of a photon pair source with unprecedented brightness and spatial mode characteristics, which permitted an easy integration into fiber networks.

At the same time, considerable efforts towards merging the fields of quantum optics and ultrafast physics were made. Novel studies on the temporal-spectral structure of parametric down-conversion states highlighted their intrinsic ultrafast characteristics [48]. A follow-up in-depth study revealed that three ingredients were required to gain active control over this structure: firstly, the choice of the nonlinear material with its associated dispersion; secondly, ways to control the spatial mode structure of the generated light; thirdly, means to control the spectral-temporal characteristics of the photon pairs [49].

The choice of the nonlinear material was the most straightforward step. When focussing on second order nonlinear processes, nature provides us with a range of materials with fixed dispersion properties, and we get to choose the material which best meets our requirements. In addition, a certain degree of control over this dispersion is provided by the quasi-phaseshifting technique (see, for instance, [50]), which allows for an overall shift of the dispersion towards the desired working point. Active control over the spatial structure of the generated light had already been demonstrated in the waveguided parametric down-conversion source. This left mainly the control over the spectral-temporal degree of freedom, which can be conveniently achieved by using a spectrally broadband – or pulsed – pump.

One particularly appealing prospect of engineering parametric down-conversion was the generation of decorrelated photon pairs, which could be directly fed into quantum networks without applying any filtering. The first realisation of this kind of source was reported by Mosley et al in 2008. They succeeded in implementing a decorrelated parametric down-conversion in a bulk crystal, which was pumped by ultrafast pump pulses [51]. Three years later, Thomas Gerrits and



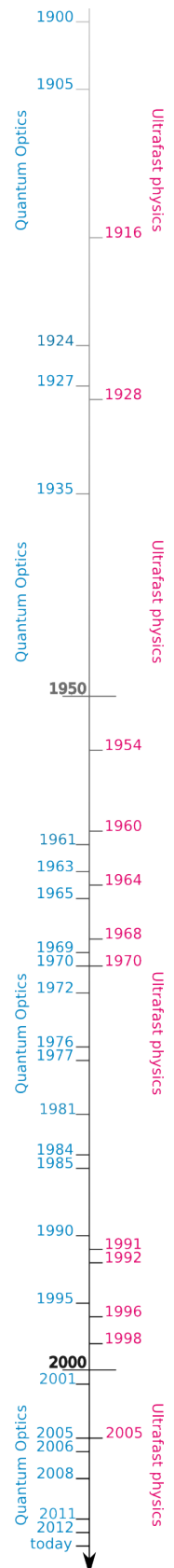
co-workers realised a similar source, which generated photons in the telecommunication wavelength regime [52]. In the same year, our group demonstrated the first decorrelated photon pair source in a nonlinear waveguide [53]. In parallel to this thesis, this source was further optimised and now features an exceptional brightness of up to 80 generated photon pairs per pump pulse and high coupling efficiencies to conventional fibres [54]. To date, our source is amongst the most promising photon pair sources for integrated quantum networks and collaborating groups are currently rebuilding it in their own laboratories.

In an alternative approach, engineering was applied to photon pair sources based on four-wave mixing in optical fibres. For these purpose, photonic crystal fibres turned out to be particularly appealing, because they allow for a precise tailoring of their dispersion properties. Along these lines, our group has investigated a highly non-degenerate photonic crystal fibre source of decorrelated photon pairs [55] as well as a source based upon commercial polarisation maintaining fibre [56]. The latter holds the promise of convenient integration into networks, whereas the former lends itself to the efficient heralding of single photons in the telecommunication wavelength regime.

In parallel, the groups of Nicholas Treps and Claude Fabre in Paris followed a different approach towards ultrafast quantum optics. They investigated the prospects of generating quantum frequency combs with a synchronously pumped optical parametric oscillator (SPOPO) [57, 58]. Similar to their classical counterparts, quantum frequency combs can be used for high precision measurements. However, the ultimate limit for the precision is now given by quantum mechanics, hence they are expected to outperform classical frequency combs. Moreover, quantum frequency combs carry a tremendous amount of entanglement, which makes them promising candidates for cluster state quantum computation in the time-frequency space. For these applications, engineering of the process facilitates the generation of cluster states with a structure that can be precisely adapted to the problem under investigation. By now, these groups have demonstrated the simultaneous generation and characterisation of eight quantum frequency combs in different time-frequency shapes [59].

Finally, we focus on recent results obtained on engineered sum- and difference-frequency generation. As a result of this thesis, we succeeded in transferring the knowledge on ultrafast parametric down-conversion and four-wave mixing present in our group to ultrafast quantum frequency conversion processes. In 2011, we published a proposal to implement two novel devices, the quantum pulse gate (QPG) and quantum pulse shaper (QPS), which facilitate a flexible single-mode operation on the basis of ultrafast time-frequency pulse shapes [60, 61]. Thus, they constitute de facto add/drop filters for novel high-dimensional (quantum) networks, where information is encoded onto ultrafast pulses. Our devices naturally lend themselves to the intrinsic ultrafast characteristics of ultrafast parametric down-conversion, which smoothly integrates the results from this thesis into the research on ultrafast quantum optics in our group. In this context the works of Michael Raymer and co-workers should be highlighted, who have studied the engineering of frequency translation in great detail, although from a different perspective [62–69].

As concluding remark we want to emphasise that ultrafast quantum optics is an emerging field of research. The work we have carried out during the course of this thesis has given us the exciting opportunity to contribute to the progress of this area. To reflect the different facets of our projects, we have structured the thesis as follows.



In Chap. 4, *"Fundamental theory"*, we introduce basic theoretical concepts from the fields of classical nonlinear, integrated and ultrafast optics, which form a solid basis for the understanding of the more advanced theory developed in later chapters. Then, in Chap. 5, *"From classical to quantum optics"*, we transfer this knowledge to the quantum domain. First, we focus on the quantisation of optical fields in nonlinear waveguides. Then, we introduce a general quantum description of three-wave mixing processes and continue with a detailed investigation of their characteristic functions. We comment on the prospects of engineering these functions and unveil the intrinsic time-frequency characteristics of the processes. We conclude this chapter with a few chosen remarks on the impact of time-ordering – a genuine quantum effect – on these processes. Chap. 6, *"Ultrafast parametric down-conversion"* is concerned with particular features of parametric down-conversion. To begin with, we briefly review the EPR formulation of parametric down-conversion states. Then, we build a bridge between this description and the time-frequency picture, by showing up surprising similarities. We share our thoughts about the correlation time of engineered photon pairs and finally put our theory to an experimental test. The main experimental work of this thesis is presented in Chap. 7, *"Quantum pulse gate and quantum pulse shaper"*. We revisit the theoretical concept behind the quantum pulse gate in detail and present first numerical estimates of the performance of this device. Then, we report on the experiments, which were required to actually implement a quantum pulse gate in the lab and present its remarkable performance benchmarks. We conclude this chapter by introducing the concept of our second device, the quantum pulse shaper. Finally, in Chap. 8, *"Conclusion and outlook"*, we conclude this thesis and highlight possible future avenues for and extensions of our work.



---

# Fundamental theory

---

## Contents

4.1 Waveguides . . . . .	11
4.2 Light-matter interaction . . . . .	16
4.3 Ultrafast pulses . . . . .	21

Ultrafast quantum optics unifies concepts from the fields of classical *integrated, non-linear* and *ultrafast* optics. Understanding these concepts is key to advancing the research in this novel area. In this chapter we briefly revisit the ideas crucial to our work and provide a common basis of un-

derstanding for the elaborate theoretical concepts which we developed during this work, while at the same time acquainting the reader with our notation and conventions. First, we introduce waveguiding structures and their effect on the electromagnetic field. Then, we concentrate on the nonlinear interaction between light and matter inside waveguides. Finally, we extend the basic description of the electromagnetic field to incorporate broad spectra, which consequently leads us to the field of ultrafast optics.

## 4.1 Waveguides

Optical waveguides are part of our daily life. The most prominent example are optical fibres, which form the backbone of today's communication networks. Optical waveguides are convenient structures: they confine light into a small cross-section, facilitating the miniaturisation of circuits and devices; they dictate a propagation direction, which allows us to send light along twisted paths; and, more fundamentally, they provide us with a high degree of control over the spatial structure of light fields, which enables the tailoring of devices for specific applications such as the heralded generation of pure single photons without spectral filtering [51, 53, 54]. In our group, there is long-lasting experience in the fabrication of optical waveguides in lithium niobate ( $\text{LiNbO}_3$ , LN). Moreover, we have recently begun to investigate potassium titanyl phosphate ( $\text{KTiOPO}_4$ , KTP) as an alternative material system. During this work we have deployed LN as well as KTP waveguides to realise different devices.

The precise modelling of the behaviour of our devices is a prerequisite step before any device fabrication. To assess the impact of the waveguide on the light field, we start from Maxwell's equations for a lossless dielectric medium with a space dependent relative permittivity  $\epsilon(\mathbf{r})$ . After some calculation (for more information see the appendix A.1), we retrieve two vectorial wave

equations which need to be solved in order to retrieve the electric field inside the waveguide:

$$\Delta \mathbf{E}(\mathbf{r}) + \frac{\omega^2}{c^2} \varepsilon(\mathbf{r}) \mathbf{E}(\mathbf{r}) + \nabla \left( \mathbf{E}(\mathbf{r}) \frac{\nabla \varepsilon(\mathbf{r})}{\varepsilon(\mathbf{r})} \right) = 0, \quad (4.1)$$

$$\Delta \mathbf{B}(\mathbf{r}) + \frac{\omega^2}{c^2} \varepsilon(\mathbf{r}) \mathbf{B}(\mathbf{r}) + \left[ \frac{\nabla \varepsilon(\mathbf{r})}{\varepsilon(\mathbf{r})} \times (\nabla \times \mathbf{B}(\mathbf{r})) \right] = 0. \quad (4.2)$$

The constant  $c$  labels the vacuum speed of light. In general, these equations cannot be solved analytically. However, we can make several assumptions which allow for a significant simplification of the vectorial wave equations. In the following, we will introduce these simplifications and briefly discuss the waveguide models, which have been used during this work.

### 4.1.1 Waveguide modelling

Our first approximation is that we model our waveguides as lossless media. This is justified, because the quality of our homemade devices facilitates transmission losses below  $0.1 \frac{\text{dB}}{\text{cm}}$  and we use samples with a maximum length of two centimetres. In that case we can substitute the refractive index for the relative permittivity as  $\varepsilon(\mathbf{r}) = n^2(\mathbf{r})$ . We then consider only waveguides with a low and gradual space dependence of the refractive index such that  $\nabla \varepsilon(\mathbf{r}) \approx 0$ . Finally, we define the  $z$ -axis of our coordinate system as the waveguide axis and hence propagation direction. This allows us to write the electric and magnetic field as  $\mathbf{E}(\mathbf{r}) = \mathbf{E}(x, y)e^{-i\beta z}$  and  $\mathbf{B}(\mathbf{r}) = \mathbf{B}(x, y)e^{-i\beta z}$ , respectively, where  $\beta$  is the so-called propagation constant of the field. Putting things together we find

$$\left( \Delta_t + \frac{\omega^2}{c^2} n^2(x, y) - \beta^2 \right) \mathbf{E}(x, y) = 0, \quad (4.3)$$

$$\left( \Delta_t + \frac{\omega^2}{c^2} n^2(x, y) - \beta^2 \right) \mathbf{B}(x, y) = 0. \quad (4.4)$$

Here  $\Delta_t = (\partial_x^2, \partial_y^2, 0)$  is the transverse Laplace operator.

Generally, there are two kinds of solutions to this equation. First, there are modes which have the highest amplitude near the waveguide axis and decay with distance. These are called *guided modes* and are distinguished by discrete propagation constants and discrete mode profiles  $\mathbf{E}(x, y)$  and  $\mathbf{B}(x, y)$ . Second, there are modes that do not decay with distance from the waveguide axis. These are called *radiation modes*, which are characterised by a continuous distribution of propagation constants. For the remainder of this work, we only consider guided modes, since radiation modes are equivalent to losses for our applications.

In the vectorial equations, there are in fact only two components that are linearly independent. This leads to the classification of modes into two categories. On the one hand, there are modes for which the  $E_y$  component is predominant. These are called quasi-transverse electric (QTE) modes. On the other hand, modes with a prevalent  $B_y$  component are referred to as quasi-transverse magnetic (QTM). This insight allows us to further reduce the wave equations and



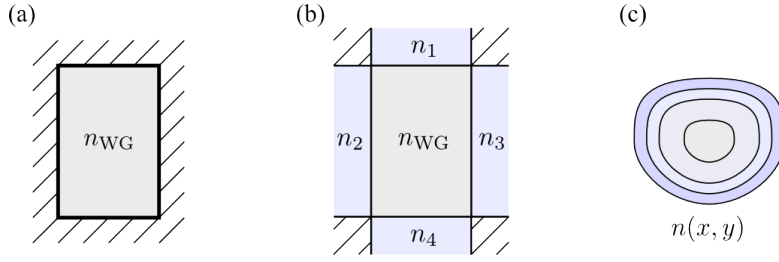


**Figure 4.1** – Schematics for the different waveguide models. (a) In the metallic waveguide model, the guiding structure has a uniform refractive index and perfectly conducting edges. (b) Marcatili’s method expands the simple model by allowing for a finite refractive index outside the guiding area. (c) For nonuniform refractive index distributions, involved numerical models are required.

write scalar versions as

$$\left( \Delta_t + \frac{\omega^2}{c^2} n^2(x, y) - \beta^2 \right) E_y(x, y) = 0, \quad (4.5)$$

$$\left( \Delta_t + \frac{\omega^2}{c^2} n^2(x, y) - \beta^2 \right) B_y(x, y) = 0. \quad (4.6)$$

The most simplistic model for a waveguide that can be exploited to solve the scalar equations is a rectangular or circular structure with perfectly conducting index and a uniform refractive index distribution (see Fig. 4.1(a)). This model is referred to as the *metallic waveguide model* and is formally similar to an infinitely deep potential well, the Eigenfunctions of which can be calculated analytically. This model is helpful for a quick parameter scan, for instance waveguide dimensions or refractive index, because the computation is exceptionally fast. We have commonly used it to qualitatively deduce the impact of different experimental situations on the measurement results.

Going one step further, we can make use of a semi-analytical approach as presented in [70]. In this model, the refractive index distribution inside the waveguide is still considered uniform, but the surrounding material now also has a finite refractive index (see Fig.4.1(b)). This situation corresponds to a finite potential well. Although slightly more complex than the metallic waveguide model, *Marcatili’s method* is still manageable and was used to cross-check the results from the metallic waveguide model at random.

For the quantitative modelling of our device performance, we deployed a full numerical model based on the *finite element method (FEM)*. Although computationally involved, this method was indispensable for tailoring of the device behaviour, since the refractive index distribution  $n(x, y)$  is not uniform in our waveguides (see Fig. 4.1(c)).



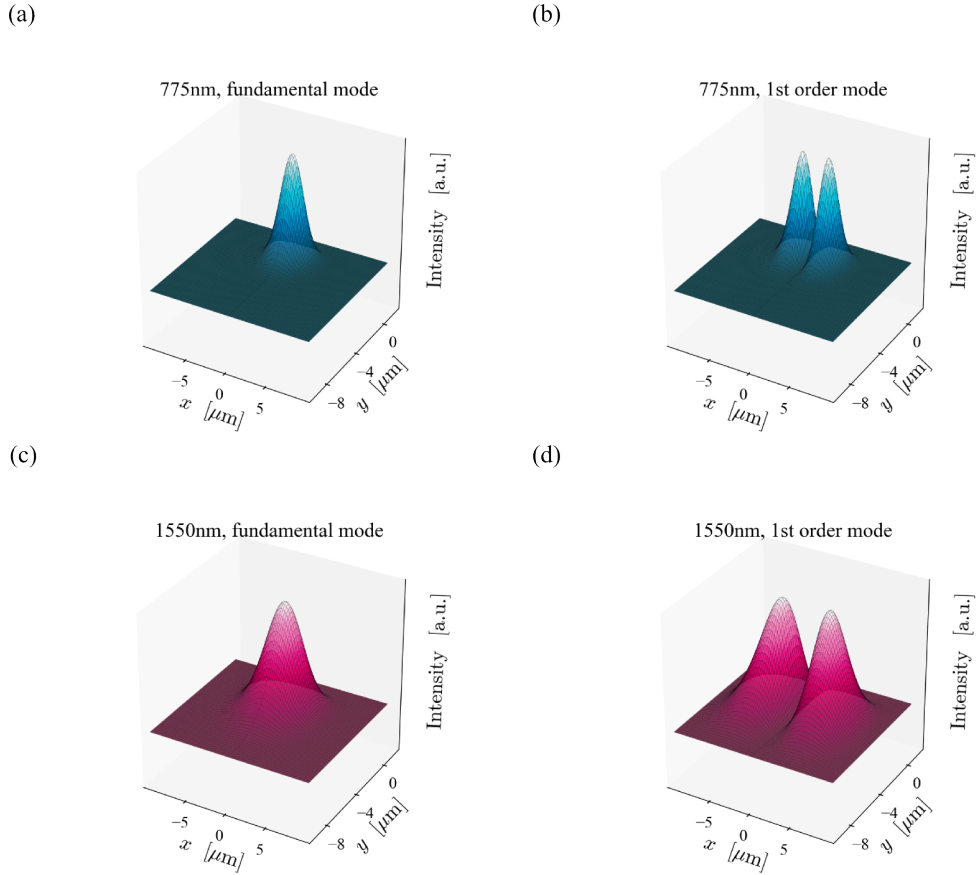


**Figure 4.2** – Spatial intensity distributions in our standard waveguide. (a), (b) Fundamental and first higher order mode for 775 nm radiation. (c), (d) The same for light at 1550 nm.

### 4.1.2 Spatial mode considerations

In general, waveguides support several guided modes with distinct propagation constants and spatial field distributions  $E_y(x, y)$  and  $B_y(x, y)$ . In this section, we will use a practical example to illustrate the influence of the spatial modes on the propagation and interaction of light in waveguiding structures. To keep our notation concise, we will now drop the distinction between QTE and QTM modes and label any spatial field mode with  $\zeta(x, y)$ . Note that we will specify the polarisation direction where needed. For the calculations we used the finite element method and assumed one of our *standard* LN waveguides with a waveguide width of  $6 \mu\text{m}$ .

As testbed, we chose a simple second harmonic generation (SHG) process (compare also Sec. 4.2), in which fundamental radiation at 1550 nm generates an SH field at 775 nm, corresponding to a doubling of the fundamental frequency, and we assume both fields to be in QTM modes. In Fig. 4.2, we display the spatial intensity distributions  $|\zeta(x, y)|^2$  of the fundamental and first



	Mode	$n_{\text{eff}}$	$n_{\text{bulk}}$	$b$
775 nm	fundamental	2.19469	2.17872	0.57481
	1 <sup>st</sup> order	2.19255		0.39007
1550 nm	fundamental	2.14810	2.13788	0.21947
	1 <sup>st</sup> order	2.14522		-0.05194

**Table 4.1** – Numeric values of the effective refractive index  $n_{\text{eff}}$ , the bulk refractive index  $n_{\text{bulk}}$  and the normalised propagation constant  $b$  for our SHG example. For more information see the text.

higher order modes for 775 nm (a), (b) and 1550 nm (c), (d), respectively. Note how the spatial modes of the fundamental field are larger than the modes of the second harmonic radiation. This can be reasoned with the help of the propagation constants  $\beta$  which we obtain from the scalar wave equation. In principle, we can define an effective wavevector  $\beta$ , which points along the waveguide axis and has a magnitude  $\beta$  given by

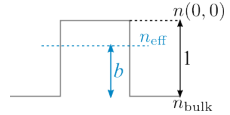
$$\beta = n_{\text{eff}} \frac{\omega}{c}, \quad (4.7)$$

where  $\omega$  is the light frequency and  $n_{\text{eff}}$  is the *effective refractive index* that is "seen" by the field mode. Using  $n_{\text{eff}}$ , we can calculate the so-called normalised propagation constant  $b$ , which is defined as

$$b = \frac{n_{\text{eff}}^2 - n_{\text{bulk}}^2}{n(0,0)^2 - n_{\text{bulk}}^2}, \quad (4.8)$$

where  $n(0,0)$  is the highest refractive index in the waveguide. If we describe the waveguide as a potential well with a normalised depth of one, the  $b$  parameter measures, how deep the mode sits inside the potential well<sup>1</sup>. A value of  $b = 1$  describes a perfectly guided mode, whereas  $b = 0$  corresponds to a radiation mode, which is not guided anymore. A negative value of  $b$ , which might result from FEM, hints at a non-physical solution, which has to be discarded. As a rule of thumb, modes exhibiting  $b \leq 0.4$  are considered to be well-guided [71].

We have collected the numeric values of the aforementioned constants in Tab. 4.1. First, we see that the  $b$  parameter for the SH radiation is higher than for the fundamental light. This illustrates the fact that lower wavelength light is confined more strongly in the waveguide (see Fig. 4.2), since the refractive index difference between  $n_{\text{eff}}$  and  $n_{\text{bulk}}$  is larger for shorter wavelengths. Second, the purely mathematical FEM calculation yields a negative  $b$  parameter for the 1<sup>st</sup> order mode at 1550 nm, meaning that this particular outcome is not a physical solution and must be discarded. This behaviour originates in the careful design of our waveguides, which we fabricate to be single-mode at telecommunication wavelengths.



<sup>1</sup>Note that for refractive indices, the waveguide corresponds to a potential hill and  $b$  measures *how high* the mode climbs on that hill, as sketched in the margins.

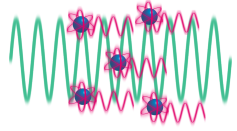


## Summary

We have illustrated how the complicated vectorial wave equations for electromagnetic fields are reduced to scalar versions which are computationally manageable. Then we briefly introduced three different waveguide models, ranging from purely analytical solutions for large parameter scans to full numerical computations for quantitative predictions of device performance. Finally, we have highlighted the influence of different spatial field distributions inside the waveguide. In this context we have introduced the effective refractive index and the  $b$ -parameter, which is a measure of how strongly a mode is supported by the waveguide.

## 4.2 Light-matter interaction

When a light wave propagates through a dielectric medium, its electric field polarises the atoms of the medium and thus induces oscillating dipole moments. These accelerated polarisation charges in turn emit electromagnetic radiation, which interferes with the original light wave. As long as the interaction between the light wave and the medium is weak and/or the intensity of the light wave is low, the medium responds with harmonic oscillations and we recover the linear effects of dispersion and absorption. However, due to the strong confinement of the light inside our waveguides, the high light intensities regularly drive the dipole oscillations into the anharmonic regime, where nonlinear effects emerge.



### 4.2.1 Nonlinear polarisation

We can relate the dipole moment per unit volume or the polarisation  $\mathbf{P}$  of a dielectric to the inducing electromagnetic field  $\mathbf{E}$ :

$$\mathbf{P} = \varepsilon_0 \chi \mathbf{E}. \quad (4.9)$$

The constant  $\varepsilon_0$  is the vacuum permittivity and the factor  $\chi$  is the electric susceptibility of the medium. To reveal the anharmonic contributions to the polarisation, it is advisable to expand the polarisation into a power series of the electric field, such that

$$\mathbf{P} = \varepsilon_0 \left( \underbrace{\chi^{(1)} \cdot \mathbf{E}}_{\mathbf{P}_L} + \underbrace{\chi^{(2)} : \mathbf{E} \mathbf{E} + \chi^{(3)} : \mathbf{E} \mathbf{E} \mathbf{E} + \dots}_{\mathbf{P}_{NL}} \right). \quad (4.10)$$

The  $\chi^{(j)}$  are susceptibility tensors of rank  $j + 1$  and the vectors  $\mathbf{P}_L$  and  $\mathbf{P}_{NL}$  label the *linear* and *nonlinear* contributions to the polarisation, respectively. From equation (4.10) we can deduce the units of the susceptibility tensors, when keeping in mind that the units of polarisation and electric field are  $[\text{C}/\text{m}^2]$  and  $[\text{V}/\text{m}]$ :

$$\chi^{(1)} \text{ is dimensionless, } [\chi^{(2)}] = \frac{\text{m}}{\text{V}}, \quad [\chi^{(3)}] = \frac{\text{m}^2}{\text{V}^2}. \quad (4.11)$$

For common dielectric materials,  $\chi^{(1)}$  is of the order of unity<sup>2</sup>. As a rough estimate, we find

<sup>2</sup>The refractive index of any material is given by  $n(\omega) = \sqrt{\varepsilon_r \mu_r}$ . For most materials,  $\mu_r \approx 1$  and we find  $n(\omega) \approx \sqrt{\chi^{(1)} + 1}$ .



for lithium niobate [72, 73]

$$\chi^{(2)} \approx 10^{-11} \frac{\text{m}}{\text{V}}, \quad (4.12)$$

$$\chi^{(3)} \approx 10^{-21} \frac{\text{m}^2}{\text{V}^2}. \quad (4.13)$$

For an estimate of the order at which we can truncate the Taylor expansion of the polarisation, we have to know the electric field strength. In this work, a typical value of the average field amplitude is  $|E| \approx 2.6 \cdot 10^5 \text{ V/m}$  (for more information see the appendix A.2). Already the term associated with  $\chi^{(3)}$  is five orders of magnitude smaller than the second-order term, hence we write

$$\mathbf{P} \approx \varepsilon_0 \chi^{(1)} \mathbf{E} + \varepsilon_0 \chi^{(2)} \mathbf{E} \mathbf{E} =: \mathbf{P}_L + \mathbf{P}_{\text{NL}}. \quad (4.14)$$

Note that here, the nonlinear polarisation depends quadratically on the original electric field. Since the medial response leads to the generation of radiation, which interferes with the original field, the nonlinear polarisation induces the coupling between three-electric fields. Thus, these processes are referred to as *three-wave mixing* processes, which we cover in more detail in the next section.

## 4.2.2 Three-wave mixing

In the following, we briefly sketch the results of different three-wave mixing processes inside nonlinear optical waveguides. In the simplest case, the original electric field is a monochromatic plain wave with frequency  $\omega_0$  and amplitude  $E_0$ , given by

$$\mathbf{E}(t, z) = E_0 e^{i\omega_0 t - i\beta(\omega_0)z} + \text{c.c.}, \quad (4.15)$$

where  $\beta(\omega_0)$  is the propagation constant of the lightwave inside the waveguide. Note that we drop the explicit  $x$ - and  $y$ -dependence of the spatial field modes, to keep the notation clean. Using this electric field, we calculate the nonlinear polarisation:

$$\mathbf{P}_{\text{NL}}(t, z) = \varepsilon_0 \chi^{(2)} \left( E_0^2 e^{i(2\omega_0 t - 2\beta(\omega_0)z)} + \text{c.c.} \right) + \varepsilon_0 \chi^{(2)} |E_0|^2. \quad (4.16)$$

The nonlinear polarisation comprises a term, which oscillates at two-times the original frequency and is referred to as the *second harmonic*<sup>3</sup> of the original field. The generated second harmonic radiation is emitted with a space dependent phase given by  $2\beta(\omega_0)z$ , whereas it acquires a phase  $\beta(2\omega_0)z$  during propagation. Generally this leads to a self-cancellation of the generated radiation. Only if the phases of generated and propagating radiation match at every point in the medium, that is if  $2\beta(\omega_0) = \beta(2\omega_0)$ , a coherent buildup of the generated radiation is possible. Consequently, this condition is called the *phasematching* condition. The constant term in equation (4.16) describes the process of optical rectification, which we do not consider in this work.

<sup>3</sup>The associated process is called second harmonic generation (SHG).



Let us now consider the more general case of two monochromatic plain waves with respective frequencies  $\omega_1$  and  $\omega_2$  and amplitudes  $E_1$  and  $E_2$ , which interact in a dielectric medium. Repeating the calculation of the nonlinear polarisation, we now find:

$$\begin{aligned} \mathbf{P}_{\text{NL}}(t, z) = \varepsilon_0 \chi^{(2)} & \left[ \underbrace{\left( E_1^2 e^{i(2\omega_1 t - 2\beta_1 z)} + \text{c.c.} \right)}_{=: \mathbf{E}_{\text{SH},1}(t, z)} + \underbrace{\left( E_2^2 e^{i(2\omega_2 t - 2\beta_2 z)} + \text{c.c.} \right)}_{=: \mathbf{E}_{\text{SH},2}(t, z)} \right. \\ & \left. + 2 \underbrace{\left( E_1 E_2 e^{i(\omega_1 + \omega_2)t - i(\beta_1 + \beta_2)z} + \text{c.c.} \right)}_{=: \mathbf{E}_{\text{SFG}}(t, z)} + 2 \underbrace{\left( E_1 E_2^* e^{i(\omega_1 - \omega_2)t - i(\beta_1 - \beta_2)z} + \text{c.c.} \right)}_{=: \mathbf{E}_{\text{DFG}}(t, z)} \right], \end{aligned} \quad (4.17)$$

where we already have neglected the contributions from optical rectification. Besides the two second harmonic fields  $\mathbf{E}_{\text{SH},1}(t, z)$  and  $\mathbf{E}_{\text{SH},2}(t, z)$ , we obtain two additional contributions oscillating at  $\omega_1 + \omega_2$  and  $\omega_1 - \omega_2$ . The processes associated with these terms are – with a characteristic lack of creativity – called *sum-* and *difference-frequency generation* (SFG and DFG), and we have labeled the corresponding electric fields  $\mathbf{E}_{\text{SFG}}(t, z)$  and  $\mathbf{E}_{\text{DFG}}(t, z)$ , respectively. Similar to the case of SHG, phasematching conditions have to be fulfilled in order for SFG and DFG to result in a coherent field buildup. These read  $\beta_{\text{SFG/DFG}} = \beta_1 \pm \beta_2$ .

Let us point out an important subtlety in the calculation of the nonlinear polarisation. One might have already noticed the additional factors of two in front of the SFG- and DFG-fields in equation (4.17). These are the so-called degeneracy factors. In our Gedankenexperiment, we have only considered the situation that field one is at frequency  $\omega_1$  and field two at  $\omega_2$ , respectively. However, the opposite might be true as well, which is the origin of that factor of two.

### 4.2.3 More on phasematching

In principle, the choice of the nonlinear material dictates phasematched frequency tuples for the different processes through the dispersion relation  $\beta = \frac{n_{\text{eff}}(\omega)\omega}{c}$ . There are however several ways to tackle this issue. One possible approach with our material systems is to exploit their intrinsic birefringence, a technique called *birefringence phasematching*. In this case, the original and generated fields are not necessarily polarised along the same crystal axis.

Let us review our example of the SHG from Sec. 4.1.2, where fundamental radiation at 1550 nm generated SH radiation at 775 nm inside our standard LN waveguides. We define a *phase mismatch* as

$$\Delta\beta = \beta_{\text{TM,TE}}(2\omega) - \beta_{\text{TM,TE}}(\omega) - \beta_{\text{TM,TE}}(\omega), \quad (4.18)$$

where the index labels the polarisation direction of the field. A value of the phase mismatch of  $\Delta\beta = 0$  is tantamount to perfect phasematching. Note that, depending on the nonlinear material, not all polarisation combinations are allowed (for more information see the appendix A.3).



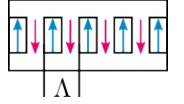
Fund. 1	Fund. 2	SH field	$\Delta\beta$ [1/m]
TM	TM	TM	$3.78 \cdot 10^5$
TE	TE	TM	$-1.48 \cdot 10^5$
TE	TM	TE	$6.74 \cdot 10^5$
TE	TE	TE	$4.12 \cdot 10^5$

**Table 4.2** – Numeric values of the phase mismatch  $\Delta\beta$  for different polarisation combinations of fundamental and SH fields.

In Tab. 4.2 we have collected the respective phase mismatches for the supported polarisation combinations in one of our standard lithium niobate waveguides. In columns one to three, we indicate the polarisations of the involved field, whereas in the last column we present the calculated phase mismatch. Although the latter changes for different polarisation combinations, none of these processes could be phasematched by exploiting the waveguide birefringence.

A second technique to achieve phasematching at arbitrary frequency tuples is called *quasi-phasematching* (QPM). This peculiar denotation originates from the modification of the phase-matching equations. For QPM, the sign of the  $\chi^{(2)}$ -nonlinearity of the waveguide is periodically inverted. This modulation can be achieved by applying a high voltage to those regions of the waveguide where the nonlinearity should be flipped [74]. Currently, our group is capable of fabricating poling periods as small as  $4 \mu\text{m}$  in LN, which required for achieving QPM for visible wavelengths in our devices. In essence, periodic inversion transforms the uniform  $\chi^{(2)}$ -nonlinearity into a Fourier series

$$\chi^{(2)} \rightarrow \chi^{(2)} \sum_{m=-\infty}^{\infty} G_m e^{im\beta_{\text{QPM}}z}. \quad (4.19)$$



Here,  $\beta_{\text{QPM}} = \frac{2\pi}{\Lambda}$  is the so-called *grating vector*, the magnitude of which is inversely proportional to the period  $\Lambda$  of the  $\chi^{(2)}$  modulation, and  $m$  is the so-called *quasi-phasematching* order. The Fourier coefficients  $G_m$  are retrieved from the actual shape of the  $\chi^{(2)}$ -modulation and describe the strength of the respective phasematching order. Typically, they are largest for first-order QPM.

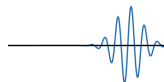
Consequently, we add an additional term to the phasematching equations, which then read

$$\beta_{\text{SH}} = 2\beta_{\text{fund}} \pm \beta_{\text{QPM}}, \quad (4.20)$$

$$\beta_{\text{SFG/DFG}} = \beta_1 \pm \beta_2 \pm \beta_{\text{QPM}} \quad (4.21)$$

for SHG and SFG/DFG, respectively. The sign in front of the grating vector depends on the actual experimental settings and corresponds to the  $+1^{\text{st}}$  and  $-1^{\text{st}}$  phasematching order, respectively. Applying the QPM technique to our SHG example, we find that a modulation with a period of  $\Lambda = 16.63 \mu\text{m}$  is required to achieve quasi-phasematching, if all fields are TM polarised.

Finally, we want to mention a possibility of fine-tuning the phase mismatch. Generally, the refractive index of our nonlinear materials is temperature dependent. Thus, we can change



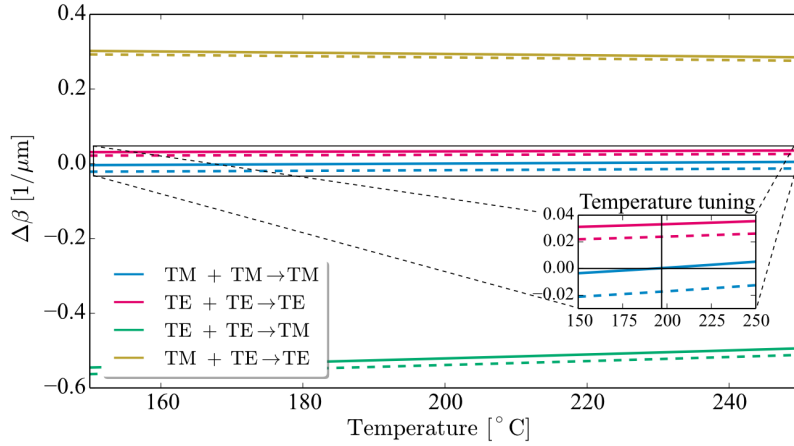


**Figure 4.3** – Phase mismatch  $\Delta\beta$  versus waveguide temperature. The colour coding corresponds to different polarisation combinations of the involved fields, dashed lines reflect cases in which one field resides in a higher order spatial mode. For more information see the text.

the phase mismatch by changing the temperature of our waveguide. This is illustrated in Fig. 4.3, where we bring together our previous findings. We consider again the example SHG from before. The colour coding reflects the polarisation combinations from Tab. 4.2 and we have assumed a QPM period of  $\Lambda = 16.63 \mu\text{m}$  to achieve phasematching for the completely TM polarised process. The solid lines correspond to the case that both fundamental and SH field reside in the fundamental spatial mode. In contrast, the dashed lines correspond to the SH field being in the first higher order spatial mode as discussed in Sec. 4.1.2. The inset shows a zoom into the perfectly phasematched region, where we have indicated  $\Delta\beta = 0$  at a temperature of  $197^\circ\text{C}$ . Several insights can be gained from this figure: firstly, different processes exhibit different  $\Delta\beta$  and only one process at a time can be quasi-phasematched ( $\Delta\beta = 0$ ) when deploying a uniform  $\chi^{(2)}$ -modulation, which provides only a single first-order grating vector  $\beta_{\text{QPM}}$ ; secondly, the impact of different spatial modes is not as severe as the impact of changing polarisations; finally, the impact of the temperature is weak compared to spatial modes or polarisation.

As a concluding remark we highlight that the devices used in this work rely on QPM and were designed to support processes where all fields reside in the fundamental spatial mode. Still, the insights from this section will become important for the analysis of the measurement results later in this thesis.



## Summary

We have motivated that an electric field induces a polarisation response in a dielectric medium, by introducing the image of oscillating atomic dipole moments. Inside our waveguides, these oscillations become anharmonic and nonlinear effects occur. We have discussed the processes of second harmonic generation as well as sum- and difference-frequency generation. The efficiency of these processes is governed by phasematching conditions, which can be adapted to different experimental situations via quasi-phasematching. Finally we compared the impact of different spatial modes, polarisations and waveguide temperatures on the phase mismatch. The temperature has the least impact on the phase mismatch and was identified as means for fine-tuning the phasematching.

## 4.3 Ultrafast pulses

Up to now, we have only considered monochromatic electric fields. This was a convenient assumption, which enabled us to deploy a concise and clean notation. However, the topic of this work is *ultrafast* quantum frequency conversion, which directly implies light pulses with broad spectra and forces us to extend our description of the light field.

In general, light pulses are electromagnetic wave packets with a finite duration. As a rule of thumb, pulses with durations shorter than one picosecond are called *ultrafast* or *ultrashort*. They are completely described by their complex time- and space-dependent electric field. During this thesis we exclusively deployed pulses for which the so-called slowly varying envelope approximation (SVEA) holds true. In this case, the spectral width of the pulse is much smaller than its central frequency ( $\sigma \ll \omega_0$ ) and the electric field can be separated into an envelope function and a monochromatic carrier wave. Consequently, we express the pulse as

$$E^+(t, z) = \frac{1}{2} \mathcal{E}(t, z) e^{i\omega_0 t - i\beta z}, \quad (4.22)$$

where  $E^+(t, z)$  is the positive frequency part of the electric field.  $\mathcal{E}(t, z)$  is the complex envelope function of the pulse and  $\beta$  is the propagation constant as defined before. The corresponding frequency representation of the electric field can be obtained from equation (4.22) via a Fourier transform, which evaluates to

$$E^+(\omega, z) = \int_{-\infty}^{\infty} dt E^+(t, z) e^{-i\omega t}. \quad (4.23)$$

Note that in an experiment, we generally measure the real-valued electric field  $E(t, z)$ , which is constructed by adding its positive and negative frequency parts such that

$$E(t, z) = E^+(t, z) + E^-(t, z), \quad (4.24)$$

where  $E^-(t, z) = (E^+(t, z))^*$ .

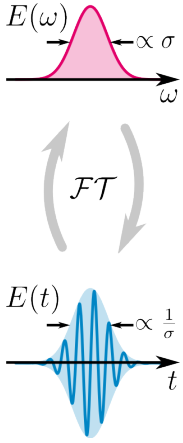


### 4.3.1 Time-bandwidth product

The time-bandwidth product (TBP) of an electromagnetic pulse describes the relation between its spectral width  $\sigma$  and its duration  $\tau$ . We have already emphasised that time and frequency are a pair of Fourier variables. This dictates that  $\sigma$  and  $\tau$  cannot be arbitrarily narrow simultaneously. Let us illustrate this with an example. We assume a pulse with a field envelope function, which exhibits a Gaussian shape and is centred around zero<sup>4</sup> and – for reasons of simplicity – neglect any spatial dependencies. This allows us to write

$$\mathcal{E}(\omega) = \mathcal{E}_0 e^{-\frac{\omega^2}{\sigma^2}}, \quad (4.25)$$

$$\mathcal{E}(t) = \frac{\mathcal{E}_0}{\sqrt{2\sigma}} e^{-\frac{t^2}{\tau^2}}. \quad (4.26)$$



Here,  $\sigma$  is the  $\frac{1}{e}$ -width of the spectral field envelope,  $\mathcal{E}_0$  is its amplitude and  $\tau = \frac{2}{\sigma}$  is the duration of the pulse, which is inversely proportional to the spectral width. Already at this stage we can discern that a narrow spectrum implies a long duration and vice versa.

However, we can put this statement onto formal footing by defining the TBP, which comprises the FWHMs of the spectral and temporal field intensities<sup>5</sup> and is given by  $\Delta\nu\Delta\tau$ . Performing the calculation for our Gaussian pulse, we find

$$\Delta\omega\Delta\tau = 2\pi\Delta\nu\Delta\tau \approx 2\pi \cdot 0.441 \quad (4.27)$$

We identify this situation with an *ideal* Gaussian pulse, that is a Gaussian pulse with a flat phase distribution. The result exemplifies our statement from above that the spectral and temporal distributions cannot both be arbitrarily narrow at the same time. Generally, the TBP is written as  $\Delta\nu\Delta\tau \geq c_{\text{TBP}}$ , where the numerical value of the constant depends on the shape of the spectral and temporal field envelopes and the equality is only fulfilled for the case of *ideal* pulses and violated otherwise.

### 4.3.2 Chronocyclic Wigner function

As we have already pointed out, full information on the pulse is contained in the complex electric field given in equation (4.22). However, for an intuitive visualisation of the time-frequency structure of an ultrafast pulse, this description is not ideal. To highlight this, we exemplarily consider a chirped pulse. A *chirped* pulse exhibits a time-dependent instantaneous frequency  $\omega(t)$  and is referred to as up-chirped (down-chirped) if  $\omega(t)$  increases (decreases) over the pulse duration. It is a non-ideal pulse with a TBP that is larger than the Fourier limit.

In the spectral envelope function, a chirp is associated with an additional phase factor. Chromatic dispersion for instance generates a phase, which varies quadratically with frequency, hence

$$\mathcal{E}(\omega) = \mathcal{E}_0 e^{-\frac{\omega^2}{\sigma^2} - i\xi\omega^2}, \quad (4.28)$$

where the factor  $\xi$  describes the sign and strength of the chirp. It is difficult to visualise this envelope, since amplitude and phase have to be plotted simultaneously. Adding higher order

<sup>4</sup>This can always be realised by applying a frequency shift to a pulse centred around a frequency  $\omega_0$ .

<sup>5</sup>Intensity FWHM and field  $\frac{1}{e}$ -width are related via  $\Delta\omega = \sqrt{2\ln 2}\sigma$  and  $\Delta\tau = \sqrt{2\ln 2}\tau$ , respectively.



chirps (for instance  $\propto \omega^3$ ) complicates the matter because they become hard to perceive in a graphic.

A solution to this problem was presented in 1994 by John Paye [33]. He borrowed from a concept known in quantum mechanics, namely the Wigner function, which is deployed to display the interplay of conjugate variables. This description can be readily translated to time and frequency, which constitute a pair of *Fourier conjugate* variables. Paye called it the *chronocyclic* Wigner function, to reflect the dependency on time<sup>6</sup> and frequency<sup>7</sup>. It is calculated by a Wigner transformation of the complex field envelope:

$$\mathcal{W}(t, \omega) = \frac{1}{2\pi} \int_{-\infty}^{\infty} ds \mathcal{E}\left(\omega + \frac{s}{2}\right) \mathcal{E}^*\left(\omega - \frac{s}{2}\right) e^{its}. \quad (4.29)$$

Note that by definition the chronocyclic Wigner function is a real-valued function and as such in principle accessible by measurement. Another particularly useful feature is that the marginals of  $\mathcal{W}(t, \omega)$  are the temporal and spectral intensities

$$I(t) = |\mathcal{E}(t)|^2 = \frac{1}{2\pi} \int_{-\infty}^{\infty} d\omega \mathcal{W}(t, \omega), \quad (4.30)$$

$$I(\omega) = |\mathcal{E}(\omega)|^2 = \int_{-\infty}^{\infty} dt \mathcal{W}(t, \omega). \quad (4.31)$$

From these equations it is obvious that the Wigner function also contains the energy of the pulse, since

$$S_{\text{pulse}} = \int_{-\infty}^{\infty} dt |\mathcal{E}(t)|^2 = \frac{1}{2\pi} \int_{-\infty}^{\infty} dt d\omega \mathcal{W}(t, \omega), \quad (4.32)$$

where  $S_{\text{pulse}}$  labels said energy.

In figure 4.4, we compare the complex spectral field envelope and the chronocyclic Wigner function of ultrafast pulses. Subplots (a) to (c) show the amplitude (solid lines) and phase (dashed lines) of the complex electric field envelope  $\mathcal{E}(\omega)$  plotted against  $\omega$ , whereas subplots (d) to (f) contain  $\mathcal{W}(t, \omega)$  plotted against frequency and time.

As a reference, we have chosen an ideal pulse (1<sup>st</sup> column). The complex electric field exhibits a Gaussian amplitude and a flat phase distribution. The corresponding chronocyclic Wigner function is a two-dimensional Gaussian centred around the origin. The next step is an additional linear phase term in the complex electric field, corresponding to a shift in the temporal domain. (2<sup>nd</sup> column). This is because of the Fourier relationship between frequency and time: a linear phase term in one of the variables is tantamount to a linear shift in the other, and vice versa. The phase term does not influence the amplitude of the complex electric field. However, as expected, we find that  $\mathcal{W}(t, \omega)$  gets shifted along the  $t$ -axis, while maintaining its overall shape.

<sup>6</sup>*Chronos* is Greek for *time*.

<sup>7</sup>*Cyclic* is reminiscent of the periodic oscillation of the electric field.



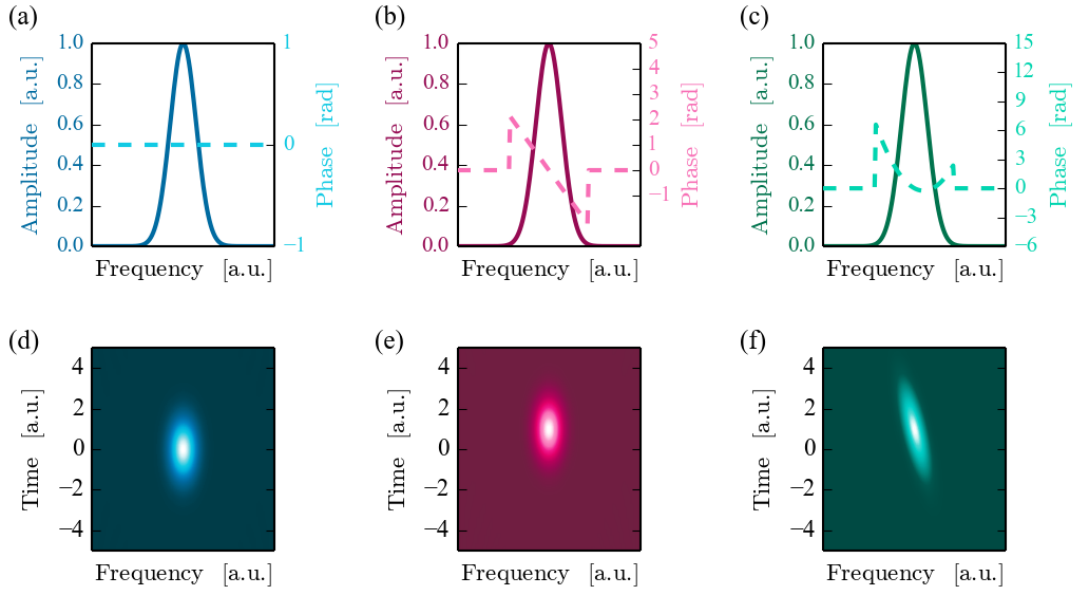


**Figure 4.4** – Visualisation of ultrafast laser pulses. (a)-(c): Amplitude (solid lines) and phase (dashed lines) of the complex spectral envelope for an unchirped pulse, a pulse with linear phase modulation and a pulse with linear and quadratic phase term, respectively. Note that the phase was manually set to zero outside the  $\frac{1}{e^2}$ -width of the pulses. (d)-(f): The chronocyclic Wigner function for the same pulses as in (a)-(c), where bright colours correspond to large values. For more information see the text.

Finally, we focus on an additional quadratic phase term, which is the signature of a linear frequency chirp (3<sup>rd</sup> column). Already for this small number of phase terms, it becomes visibly difficult to aptly read the phase of the complex electric field. In contrast, the phase terms are well separated in the chronocyclic representation. The linear term induces a shift along the  $t$ -axis and the quadratic term yields a tilt in the Wigner function, which reflects the temporal-spectral correlations introduced by a frequency chirp.

The chronocyclic Wigner function has become the standard description of ultrafast laser pulses to date, because of the intuitive access to different phenomena. From a numerical point of view however, working with either the spectral or temporal complex envelope function is preferable, because there is only one functional variable instead of two. Throughout this work we will use both methods, depending on their respective applicability.



### 4.3.3 Pulse shaping

In this section, we focus on the control over the time-frequency shape of ultrafast pulses. To date, there are many different ways to implement pulse shaping, which are nicely presented in [75]. Shaped pulses are predominantly used in the field of coherent control, which is covering applications to monitor and control system dynamics at ultrashort timescales. To highlight the limitations of classical pulse shaping schemes, we stick to the complex field envelope description of ultrafast pulses, which we rewrite

$$\mathcal{E}(\omega) = |\mathcal{E}(\omega)|e^{i\phi(\omega)}. \quad (4.33)$$

Here,  $\phi(\omega)$  denotes the phase including all higher order terms. Full control over the pulse shape is possible, if both amplitude and phase of the electric field can be controlled independently. This can be achieved by applying transfer functions  $f_{\text{amp}}(\omega)$  and  $f_{\phi}(\omega)$ , such that

$$|\mathcal{E}(\omega)| \rightarrow f_{\text{amp}}(\omega)|\mathcal{E}(\omega)|, \quad (4.34)$$

$$\phi(\omega) \rightarrow f_{\phi}(\omega)\phi(\omega). \quad (4.35)$$

With current experimental means,  $f_{\phi}(\omega)$  can take almost arbitrary values<sup>8</sup>. However, things are different for  $f_{\text{amp}}(\omega)$ . Commercial pulse shapers are passive linear devices, which do not feed additional energy to the pulse. In practice this means that  $f_{\text{amp}}(\omega)$  only takes on values between 0 and 1, meaning full suppression or transmission of the respective frequency. This statement enforces two main consequences: first, the input amplitude must have a sufficient spectral width, since no new spectral components can be generated; second, pulse shaping is inherently lossy. The latter is in fact deleterious for any quantum application, since losses inevitably introduce decoherence to the quantum state. Thus, quantum pulses cannot be reshaped with conventional pulse shaping techniques. Note however, that this does not hinder the shaping of bright, classical pulses.

#### Summary

We have introduced the complex field of ultrafast pulses and defined the associated time-bandwidth product. In our case of Gaussian shaped pulses, the time-bandwidth product must fulfil the inequality  $\Delta\omega\Delta\tau \geq 2\pi \cdot 0.441$ . Moreover, we have presented the chronocyclic Wigner function  $\mathcal{W}(t, \omega)$  of ultrafast pulses as an intuitive method to illustrate their time-frequency structure. Finally, we have motivated that pulse shaping, being a destructive operation, typically introduces losses, which are detrimental for quantum states.

<sup>8</sup>Particularly when taking into account the periodic nature of the phase.





So you can't sell brushes because nobody understands a word you say?

Yes.

Don't worry Donald. Don't give up! I have faith in you. Go out and try again.

Whoopee!

*Daisy and Donald Duck*

# 5

---

## From classical to quantum optics

---

### Contents

5.1 Speaking quantum . . . . .	27
5.2 Understanding quantum . . . . .	36
5.3 Engineering quantum . . . . .	44
5.4 Time-ordering . . . . .	54

In the previous chapter, we have introduced concepts from classical optics which form the fundament for our quantum description of frequency conversion processes. In this chapter, we take three steps to translate these results into the formal language of quantum optics: first, we derive expressions for the quantised fields

in nonlinear optical waveguides; second, we introduce a general quantum description of three-wave mixing processes comprising one strong, classical light field and two quantum fields; finally, we investigate two kinds of three-wave mixing processes, namely parametric down-conversion (PDC) and sum- and difference-frequency generation (SFG/DFG) in more detail, since they are the backbone of our experimental work. To this end, we reveal the intricate time-frequency (TF) structure of these processes and highlight means to exert complete control over it. We conclude this chapter with a brief detour on the genuine quantum effect of time-ordering and assess its impact on our experiments.

### 5.1 Speaking quantum

It is well-known from many quantum mechanics textbooks that in order to obtain a quantum description of a process one first has to find the Hamiltonian  $\hat{H}(t)$  of the process. Then, since we are interested in the revealing the physical implications of the Hamiltonians, we have to solve the time-evolution equations generated by the Hamiltonian. Depending on the specific physical situation and the personal taste, one can either deploy the Schrödinger picture to write

down the time-evolution of a quantum state

$$|\psi(T)\rangle = \hat{\mathcal{T}} \exp \left[ -\frac{i}{\hbar} \int_0^T dt \hat{H}(t) \right] |\psi(0)\rangle \quad (5.1)$$

or Heisenberg's equation of motion to express the time-evolution of the associated operators

$$\partial_t \hat{a}(t) = \frac{i}{\hbar} \left[ \hat{H}(t), \hat{a}(t) \right]. \quad (5.2)$$

Here,  $\hbar = \frac{h}{2\pi}$  is the reduced Planck's constant and  $\hat{\mathcal{T}}$  is the so-called *time-ordering operator*, which we ignore for the time being, in agreement with recent results [76]. Note that we will discuss time-ordering at the end of this chapter. The angular brackets in the second equation label the commutator between the Hamiltonian and the operator under consideration.

For our particular case of three-wave mixing processes, the Hamiltonian is given by the interaction of the initial electric field with the induced nonlinear polarisation inside the nonlinear medium and hence reads [77]

$$\hat{H}_{\text{TWM}}(t) = \int_V d\mathbf{r} \hat{\mathbf{P}}_{\text{NL}}(\mathbf{r}, t) \hat{\mathbf{E}}(\mathbf{r}, t), \quad (5.3)$$

where the operators  $\hat{\mathbf{P}}_{\text{NL}}(\mathbf{r}, t)$  and  $\hat{\mathbf{E}}(\mathbf{r}, t)$  are the quantised versions of the corresponding classical quantities from Eq. (4.14). Note that we now define  $\hat{\mathbf{P}}_{\text{NL}} = \varepsilon_0 d_{\text{eff}} \hat{\mathbf{E}} \hat{\mathbf{E}}$ , where  $d_{\text{eff}}$  is the *effective* nonlinearity (for more information see the appendix A.3). Obviously, the expression for the quantised fields is all we need in order to write down the Hamiltonian.

### 5.1.1 Field quantisation in waveguides

The derivation of the quantised electric fields inside weakly guiding waveguides has, to the best of our knowledge, not been considered in detail before. Therefore, we start from very fundamental considerations. Maxwell's equations require that the electric and magnetic field operators can be associated with a vector potential  $\hat{\mathbf{A}}(\mathbf{r}, t)$  via [78]

$$\hat{\mathbf{E}}(\mathbf{r}, t) = -\partial_t \hat{\mathbf{A}}(\mathbf{r}, t), \quad \hat{\mathbf{B}}(\mathbf{r}, t) = \nabla \times \hat{\mathbf{A}}(\mathbf{r}, t). \quad (5.4)$$

In the following, we follow along the lines of [79], but adapt the vector potential presented there (compare Eq. (A.12)) to accurately reflect the properties of our waveguides, in particular the spatial modes they impose on the light field:

$$\hat{\mathbf{A}}^+(\mathbf{r}, t) = \int d\mathbf{k} \left( \frac{\hbar v_g(\omega)}{16\pi^3 \varepsilon_0 c \omega n(\omega)} \right)^{1/2} \hat{a}(\mathbf{k}) \xi(k_x, k_y) e^{-i\omega t + i\mathbf{k}\mathbf{r}}. \quad (5.5)$$

Note that in the remainder of this work integral boundaries are  $-\infty$  and  $\infty$  unless stated otherwise. The quantity  $v_g(\omega)$  is the group velocity of the light inside the waveguide which is given



by  $v_g(\omega) = \frac{\partial \omega}{\partial k}$ . In addition, we have introduced the function  $\xi(k_x, k_y)$ , which is calculated via the asymmetric Fourier transform

$$\xi(k_x, k_y) = \int dx dy \zeta(x, y) e^{-ik_x x - ik_y y}, \quad (5.6)$$

where the spatial field mode

$$\zeta(x, y) = \frac{1}{(2\pi)^2} \int dk_x dk_y \xi(k_x, k_y) e^{ik_x x + ik_y y} \quad (5.7)$$

inside the waveguide is derived from classical optics as sketched in Sec. 4.1.2. Inserting this result into Eq. (5.5), we obtain the formally one-dimensional integral

$$\hat{A}^+(\mathbf{r}, t) = 2\pi \zeta(x, y) \int dk_z \left( \frac{\hbar v_g(\omega)}{4\pi \varepsilon_0 c \omega n(\omega)} \right)^{1/2} \hat{a}(k_z) e^{-i\omega t + ik_z z}. \quad (5.8)$$

We can translate the integration over  $k_z$  into a frequency integral by substituting [79]

$$dk_z \rightarrow \frac{d\omega}{v_g(\omega)}, \quad \hat{a}(k_z) \rightarrow \sqrt{v_g(\omega)} \hat{a}(\omega), \quad (5.9)$$

and end up with

$$A^+(\mathbf{r}, t) = 2\pi \zeta(x, y) \int d\omega \left( \frac{\hbar}{4\pi \varepsilon_0 c \omega n(\omega)} \right)^{1/2} \hat{a}(\omega) e^{-i\omega t + ik_z z}. \quad (5.10)$$

Performing the derivation of this expression with respect to time yields the quantised electric field operator

$$\hat{E}^+(\mathbf{r}, t) = i 2\pi \zeta(x, y) \int d\omega \left( \frac{\hbar \omega}{4\pi \varepsilon_0 c n(\omega)} \right)^{1/2} \hat{a}(\omega) e^{-i\omega t + ik_z z}. \quad (5.11)$$

Since we know that different spatial field modes may be supported by our waveguides, we can further generalise this expression and find

$$\hat{E}^+(\mathbf{r}, t) = i \cdot 2\pi \sum_k \zeta_k(x, y) \int d\omega \sqrt{\frac{\hbar \omega}{4\pi \varepsilon_0 c n_k(\omega)}} \hat{a}_k(\omega) e^{-i\omega t + i\beta_k z} \quad (5.12)$$

which is the final expression for quantised light fields in optical waveguides as published in [61]. Note that we have implicitly included the condition that  $k_z$  can only take the values of the propagation constants  $\beta_k$  of the respective modes to fulfil Helmholtz's equation. In addition,  $n_k(\omega)$  now labels the effective refractive index as discussed in Sec. 4.1.



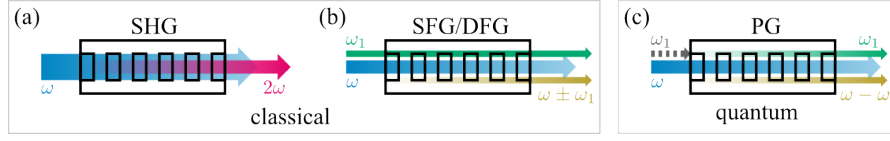


**Figure 5.1** – Illustration of three-wave mixing processes. (a) In a purely classical approach, one single input field at frequency  $\omega$  (blue arrow) can generate only SH radiation at  $2\omega$  (red arrow). (b) For the generation of other frequency components, a second input field at  $\omega_1$  (green arrow) is required to drive an SFG/DFG process (yellow arrow). (c) In the quantum description (or in a semi-classical approach), vacuum fluctuations serve as a second input field, with an infinite frequency spectrum (grey dashed arrow). Hence, the generation of new frequencies (green and yellow arrows) is possible even without a classical second input, a process referred to as parametric generation (PG).

### 5.1.2 Quantum three-wave mixing

With the quantised electric fields at hand, we can now calculate the three-wave mixing Hamiltonian  $\hat{H}_{\text{TWM}}(t)$ . However, before doing so we emphasise an important difference in the origin of the nonlinear polarisation compared to the previous chapter. In our classical treatment we found that, given a monochromatic input field only the SHG process occurred (compare Eq. (4.16)). For an SFG/DFG process to happen, we required an input field to generate additional terms in  $P_{\text{NL}}(t, z)$  (compare Eq. (4.17)).

We have illustrated this in Fig. 5.1. In (a) only one input field is present and consequently only the SH radiation emerges in agreement with Eq. (4.16). In (b), a second bright input field facilitates SFG/DFG processes and thus the generation of new frequency components. The situation is different in (c): the quantum approach takes into account the non-vanishing energy content of the quantum mechanical vacuum which can seed a DFG process under the conditions of energy conservation and phasematching<sup>9</sup>. The generation of light fields from the quantum mechanical vacuum is commonly referred to as *parametric generation* (PG) in a semi-classical theory, or *parametric down-conversion* (PDC) in quantum optics.

Let us now derive the three-wave mixing Hamiltonian  $\hat{H}_{\text{TWM}}(t)$ . We assume the nonlinear polarisation to be excited by quantum fields

$$\hat{E}_1(\mathbf{r}, t) = \hat{E}_1^+(\mathbf{r}, t) + \hat{E}_1^-(\mathbf{r}, t), \quad (5.13)$$

$$\hat{E}_2(\mathbf{r}, t) = \hat{E}_2^+(\mathbf{r}, t) + \hat{E}_2^-(\mathbf{r}, t) \quad (5.14)$$

and mix them with a strong pump field

$$E_p(\mathbf{r}, t) = E_p^+(\mathbf{r}, t) + E_p^-(\mathbf{r}, t), \quad (5.15)$$

<sup>9</sup>This can be incorporated into classical theory as well. Then, all frequencies are populated with half a photon at the input of the waveguide and thus can seed the process. Note that, due to the introduction of photons, this approach is referred to as semi-classical.



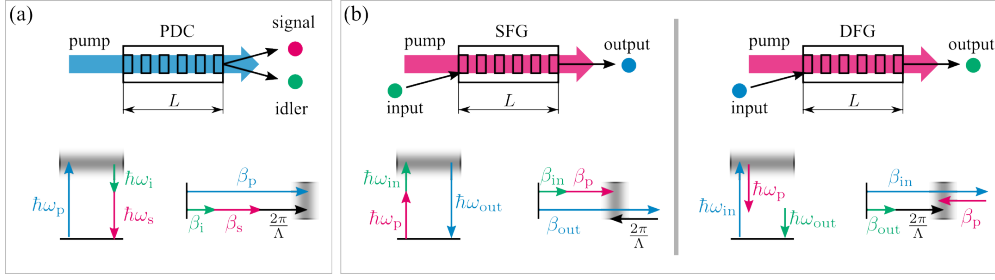


**Figure 5.2** – Visualisation of PDC and frequency conversion (FC) processes. For more information see the text.

which does not get depleted during the process and is thus modelled as a classical field. Consequently, we can calculate the Hamiltonian  $\hat{H}_{\text{TWM}}(t)$  and find (for more information see the appendix A.4)

$$\hat{H}_{\text{TWM}}(t) = \varepsilon_0 \int_V d\mathbf{r} \left[ d_{\text{eff}} E_p^+(\mathbf{r}, t) \left( \hat{E}_1^-(\mathbf{r}, t) \right)^2 + d_{\text{eff}} E_p^+(\mathbf{r}, t) \hat{E}_1^-(\mathbf{r}, t) \hat{E}_2^-(\mathbf{r}, t) \right. \\ \left. + d_{\text{eff}} E_p^+(\mathbf{r}, t) \hat{E}_1^+(\mathbf{r}, t) \hat{E}_2^-(\mathbf{r}, t) + \text{h.c.} \right]. \quad (5.16)$$

Here, we have colour coded the different contributions with respect to the underlying physical processes and the respective effective nonlinearities  $d_{\text{eff}}$  include the degeneracy factors as discussed before.

The **orange** term<sup>10</sup> corresponds to a time-inverted SHG process, during which a pump photon decays into a pair of photons that is emitted into the same quantum field. This process is also referred to as *type I PDC*. Since it plays no role for our work<sup>11</sup>, we will not consider it further. The **red** term, in contrast, describes the process of *type II PDC*, where the generated photons – called *signal* and *idler* are emitted into distinguishable field modes, that is, orthogonal polarisations. The source we present in Chap. 6 is based on this process, which is why we investigate it in more detail. Finally, the **blue** term describes quantum SFG/DFG processes, during which an input photon is annihilated and an output photon is created. These processes are at the heart of our new devices presented in Chap. 7 and are therefore also considered in detail.

A visualisation of the two types of processes is presented in Fig. 5.2. Panel (a) displays a type II PDC process, during which photons from a bright, classical pump (blue arrow) decay into pairs of photons, commonly labelled signal and idler (red and green disc). The strict energy correlations are slightly relaxed due to the finite spectral bandwidth of the pump. This is illustrated by the blurred, grey-shaded region in the energy level diagram in the lower left. The same holds true for the phasematching condition, which relaxes due to the finite waveguide length, as shown on the lower right. In (b), we show SFG (left) and DFG (right), respectively. During these processes, a green (blue) input photon interacts with the strong pump (red arrow) and is converted into a blue (green) output. Note that both energy conservation and phasematching

<sup>10</sup>We implicitly include the associated h.c. terms in this discussion.

<sup>11</sup>There are other applications where type I PDC is indispensable, for instance the generation of squeezed light.



diagrams have to be adapted to reflect the corresponding experimental situation. This means in particular that in (b), the  $-1^{\text{st}}$  and  $+1^{\text{st}}$  QPM orders have to be utilised for SFG and DFG, respectively, as illustrated by the different directions of the grating vectors  $\frac{2\pi}{\Lambda}$ .

Taking into account all additional information, we finally find the most simplistic three-wave mixing Hamiltonian for our work, which reads

$$\hat{H}_{\text{TWM}}(t) = \varepsilon_0 \int_V d\mathbf{r} \left[ d_{\text{eff}} E_{\text{p}}^+(\mathbf{r}, t) \hat{E}_1^-(\mathbf{r}, t) \hat{E}_2^-(\mathbf{r}, t) + \text{h.c.} \right. \\ \left. + d_{\text{eff}} E_{\text{p}}^+(\mathbf{r}, t) \hat{E}_1^+(\mathbf{r}, t) \hat{E}_2^-(\mathbf{r}, t) + \text{h.c.} \right] \quad (5.17)$$

### 5.1.3 Time-frequency representation

#### 5.1.3.1 Joint spectral amplitude functions

Let us have a closer look at the internal structure of the three-wave mixing Hamiltonian  $\hat{H}_{\text{TWM}}$  from Eq. (5.17). We know already that we can generate a unitary transformation from an input quantum state to an output quantum state with the knowledge of the Hamiltonian using, for instance, Eq. (5.1). To do so, we have to substitute 'realistic' expressions for the fields and consequently utilise the quantised fields from Eq. (5.12). The pump field is an ultrafast laser pulse containing at least  $10^6$  photons in our experiments. As such, we again assume that it is not depleted during the three-wave mixing and write it as a classical field

$$E_{\text{p}}^+(\mathbf{r}, t) = A_{\text{p}} \zeta_{\text{p}}(x, y) \int d\omega_{\text{p}} \alpha(\omega_{\text{p}}) e^{-i\omega_{\text{p}}t + i\beta_{\text{p}}z}, \quad (5.18)$$

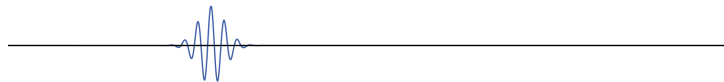
where the constant  $A_{\text{p}}$  is the maximum amplitude of the pump and the function  $\alpha(\omega_{\text{p}})$  – referred to as *pump envelope function* – describes its complex spectrum. Naturally, we require that the area integral over the pump intensity  $I_{\text{p}} = \frac{1}{2} c n_{\text{p}}(\omega_{\text{p}}) \varepsilon_0 |E_{\text{p}}|^2$  is a power with units of [W]. Hence, we can relate the pump amplitude  $A_{\text{p}}$  to the pump power averaged over the duration of the pulse  $P_{\text{p}}$  by<sup>12</sup>

$$A_{\text{p}} = \sqrt{\frac{2P_{\text{p}}}{c \varepsilon_0 n_{\text{p}}(\omega_{\text{p}}) \int d\omega_{\text{p}} |\alpha(\omega_{\text{p}})|^2}}. \quad (5.19)$$

This result is convenient, because the pump spectrum and its temporal shape can be measured directly. In addition, the pulse energy can be evaluated, which together with the temporal shape allows for the calculation of  $P_{\text{p}}$ . Thus,  $A_{\text{p}}$  is accessible from experimental quantities.

Putting things together we obtain an expression for the three-wave mixing Hamiltonian. Note

<sup>12</sup>This corresponds to approximating the pulse with a boxcar function.



that again, integral boundaries are taken to be  $-\infty$  and  $\infty$  unless stated otherwise:

$$\begin{aligned} \hat{H}_{\text{TWM}}(t) = & \varepsilon_0(2i\pi)^2 \sum_{k,l,m} \int_V dx dy dz \int d\omega_p d\omega_{s/\text{in}} d\omega_{i/\text{out}} \\ & \times \left[ d_{\text{eff}} \zeta_{p,k}(x,y) \zeta_{s,l}^*(x,y) \zeta_{i,m}^*(x,y) A_{p,k} \sqrt{\frac{\hbar\omega_s}{4\pi c \varepsilon_0 n_{s,l}(\omega_s)}} \sqrt{\frac{\hbar\omega_i}{4\pi c \varepsilon_0 n_{i,m}(\omega_i)}} \right. \\ & \alpha_k(\omega_p) e^{-i(\omega_p - \omega_s - \omega_i)t} e^{i(\beta_{p,k} - \beta_{s,l} - \beta_{i,m} + \beta_{\text{QPM}})z} \hat{a}_l^\dagger(\omega_s) \hat{b}_m^\dagger(\omega_i) \\ & + d_{\text{eff}} \zeta_{p,k}(x,y) \zeta_{\text{in},l}(x,y) \zeta_{\text{out},m}^*(x,y) A_{p,k} \sqrt{\frac{\hbar\omega_{\text{in}}}{4\pi c \varepsilon_0 n_{\text{in},l}(\omega_{\text{in}})}} \sqrt{\frac{\hbar\omega_{\text{out}}}{4\pi c \varepsilon_0 n_{\text{out},m}(\omega_{\text{out}})}} \\ & \left. \alpha_k(\omega_p) e^{-i(\omega_p \pm \omega_{\text{in}} \mp \omega_{\text{out}})t} e^{i(\beta_{p,k} \pm \beta_{\text{in},l} \mp \beta_{\text{out},m} + \beta_{\text{QPM}})z} \hat{a}_l(\omega_{\text{in}}) \hat{c}_m^\dagger(\omega_{\text{out}}) + \text{h.c.} \right]. \end{aligned} \quad (5.20)$$

The indices  $k, l$  and  $m$  describe the spatial modes of the three fields and the operators  $\hat{a}$ ,  $\hat{b}$  and  $\hat{c}$  are standard creation and annihilation operators, which operate on the spatial modes labeled in the corresponding subscripts. We have also introduced our standard labelling for the different processes, marking the PDC photons signal and idler as 's' and 'i', and the input and output fields of the SFG/DFG as 'in' and 'out', respectively. In our notation, we implicitly assume  $\beta = \beta(\omega)$  for all propagation constants. Note that we account for the fact that different spatial pump modes  $k$  might also exhibit different pump spectra  $\alpha_k(\omega_p)$ .

The next few steps will solely be focussed on the simplification of this Hamiltonian. First, we apply the slowly varying envelope approximation (SVEA), which allows us to take the square root factors and pump amplitude, which are assumed as constant in this approximation, out of the integrals. Second, we define effective interaction areas  $\mathcal{A}_{klm}$  as

$$\frac{1}{\mathcal{A}_{klm}} = \begin{cases} \left[ \int dx dy \zeta_{p,k}(x,y) \zeta_{s,l}^*(x,y) \zeta_{i,l}^*(x,y) \right]^2, \\ \left[ \int dx dy \zeta_{p,k}(x,y) \zeta_{\text{in},l}(x,y) \zeta_{\text{out},l}^*(x,y) \right]^2, \end{cases} \quad (5.21)$$

where the upper solution is for PDC, and the lower for SFG/DFG, respectively.

Third, we define a frequency and a phase mismatch

$$\Delta\omega_{\text{PDC}} = \omega_p - \omega_s - \omega_i, \quad (5.22)$$

$$\Delta\beta_{\text{PDC},klm} = \beta_{p,k} - \beta_{s,l} - \beta_{i,m} + \beta_{\text{QPM}}, \quad (5.23)$$

$$\Delta\omega_{\text{FC}} = \omega_p \pm \omega_{\text{in}} \mp \omega_{\text{out}}, \quad (5.24)$$

$$\Delta\beta_{\text{FC},klm} = \beta_{p,k} \pm \beta_{\text{in},l} \mp \beta_{\text{out},m} + \beta_{\text{QPM}}, \quad (5.25)$$

where FC labels a general frequency conversion process (either SFG or DFG) and the signs are valid for SFG, respectively DFG. We recall that  $\beta_{\text{QPM}} = \frac{2\pi}{\Lambda}$  is the quasi-phasesmatching vector which originates in the periodic poling of the waveguide.



Fourth, we perform the  $z$ -integrations over the waveguide length  $L$ , which yields

$$\int_0^L dz e^{i\Delta\beta_{\text{PDC},klm}z} = L \underbrace{\text{sinc}\left(\frac{\Delta\beta_{\text{PDC},klm}L}{2}\right)}_{=:\phi_{\text{PDC},klm}(\omega_p, \omega_s, \omega_i)} e^{i\frac{\Delta\beta_{\text{PDC},klm}L}{2}}, \quad (5.26)$$

$$\int_0^L dz e^{i\Delta\beta_{\text{FC},klm}z} = L \underbrace{\text{sinc}\left(\frac{\Delta\beta_{\text{FC},klm}L}{2}\right)}_{=:\phi_{\text{FC},klm}(\omega_p, \omega_{\text{in}}, \omega_{\text{out}})} e^{i\frac{\Delta\beta_{\text{FC},klm}L}{2}}, \quad (5.27)$$

where we defined the *phasematching functions* as  $\phi_{\text{PDC},klm}(\omega_p, \omega_s, \omega_i)$  and  $\phi_{\text{FC},klm}(\omega_p, \omega_{\text{in}}, \omega_{\text{out}})$ , respectively. With the help of these four steps, we obtain a simplified version of  $\hat{H}_{\text{TWM}}(t)$ :

$$\begin{aligned} \hat{H}_{\text{TWM}}(t) = \varepsilon_0(2i\pi)^2 \sum_{k,l,m} \int d\omega_p d\omega_{s/\text{in}} d\omega_{i/\text{out}} \\ \left[ d_{\text{eff}}\theta_{\text{PDC},klm}\alpha_k(\omega_p)\phi_{\text{PDC},klm}(\omega_p, \omega_s, \omega_i)e^{-i\Delta\omega_{\text{PDC}}t}\hat{a}_l^\dagger(\omega_s)\hat{b}_m^\dagger(\omega_i) \right. \\ \left. + d_{\text{eff}}\theta_{\text{FC},klm}\alpha_k(\omega_p)\phi_{\text{FC},klm}(\omega_p, \omega_{\text{in}}, \omega_{\text{out}})e^{-i\Delta\omega_{\text{FC}}t}\hat{a}_l(\omega_{\text{in}})\hat{c}_m^\dagger(\omega_{\text{out}}) + \text{h.c.} \right], \end{aligned} \quad (5.28)$$

where we defined new constants

$$\theta_{\text{PDC}} = \frac{A_{p,k}L}{\sqrt{\mathcal{A}_{klm}}} \sqrt{\frac{\hbar\omega_s}{4\pi c\varepsilon_0 n_{s,l}(\omega_s)}} \sqrt{\frac{\hbar\omega_i}{4\pi c\varepsilon_0 n_{i,m}(\omega_i)}}, \quad (5.29)$$

$$\theta_{\text{FC}} = \frac{A_{p,k}L}{\sqrt{\mathcal{A}_{klm}}} \sqrt{\frac{\hbar\omega_{\text{in}}}{4\pi c\varepsilon_0 n_{\text{in},l}(\omega_{\text{in}})}} \sqrt{\frac{\hbar\omega_{\text{out}}}{4\pi c\varepsilon_0 n_{\text{out},m}(\omega_{\text{out}})}}. \quad (5.30)$$

This looks better, but we can still improve it. Recapitulating Eq. (5.1), we find that we need the time integrated Hamiltonian to generate our transformation from input to output state:

$$|\psi(T)\rangle = \exp\left[-\frac{i}{\hbar} \int_0^T dt \hat{H}(t)\right] |\psi(0)\rangle, \quad (5.31)$$

where we explicitly neglect the time-ordering operator  $\hat{T}$ . First we reason that we can take the boundaries of this integral to infinity. The input state  $|\psi(0)\rangle$  will, in the absence of losses, not change before the nonlinear interaction. This is also true for the output state  $|\psi(T)\rangle$ , only now we consider the state after the interaction. Hence, we can safely integrate the time from  $-\infty$  to  $+\infty$ , if  $t = 0$  marks the state at the input facet of the waveguide and  $t = T$  the state at the waveguide output facet. The only time-dependent terms in  $\hat{H}_{\text{TWM}}(t)$  are the two exponents



containing the frequency mismatches. These readily evaluate to

$$\int dt e^{-i\Delta\omega_{\text{PDC}}t} = 2\pi\delta(\omega_p - \omega_s - \omega_i), \quad (5.32)$$

$$\int dt e^{-i\Delta\omega_{\text{FC}}t} = 2\pi\delta(\omega_p \pm \omega_{\text{in}} \mp \omega_{\text{out}}). \quad (5.33)$$

Hence we can directly perform the integration over the pump frequency  $\omega_p$  and find  $\omega_p \rightarrow \omega_s + \omega_i$  for PDC and  $\omega_p \rightarrow \pm\omega_{\text{out}} \mp \omega_{\text{in}}$  for SFG/DFG, respectively. In addition we define the joint spectral amplitude (JSA) functions

$$F_{klm}(\omega_s, \omega_i) := \alpha_k(\omega_s + \omega_i)\phi_{\text{PDC},klm}(\omega_s, \omega_i), \quad (5.34)$$

$$G_{klm}(\omega_{\text{in}}, \omega_{\text{out}}) := \alpha_k(\pm\omega_{\text{out}} \mp \omega_{\text{in}})\phi_{\text{FC},klm}(\omega_{\text{in}}, \omega_{\text{out}}), \quad (5.35)$$

which contain complete information over the spectral-temporal properties of the processes. With this we present our final expression for the time-integrated three-wave mixing Hamiltonian:

$$-\frac{i}{\hbar} \int dt \hat{H}_{\text{TWM}}(t) = \sum_{k,l,m} \left[ \mathcal{B}_{klm} \int d\omega_s d\omega_i F_{klm}(\omega_s, \omega_i) \hat{a}_l^\dagger(\omega_s) \hat{b}_m^\dagger(\omega_i) + \text{h.c.} \right. \\ \left. + \mathcal{C}_{klm} \int d\omega_{\text{in}} \omega_{\text{out}} G_{klm}(\omega_{\text{in}}, \omega_{\text{out}}) \hat{a}_l(\omega_{\text{in}}) \hat{c}_m^\dagger(\omega_{\text{out}}) + \text{h.c.} \right] \quad (5.36)$$

We have merged all constants into the two overall coupling constants  $\mathcal{B}_{klm}$  and  $\mathcal{C}_{klm}$  and have separated the PDC and FC parts of the Hamiltonian.

### 5.1.3.2 Schmidt decomposition

The next step is to apply a Schmidt decomposition [80] to the JSA functions. The idea to use this decomposition on bipartite quantum systems was introduced by Everett in 1957 [81] and was later advanced as a means of quantifying correlations in a general bipartite quantum system [82]. Law, Walmsley and Eberly transferred this procedure to the TF degree of freedom of ultrafast PDC [48] and during this thesis we have transferred this approach to FC.

A general Schmidt decomposition of a two-dimensional function  $f(\omega_1, \omega_2)$  yields two sets of basis functions  $\{g_k\}$  and  $\{h_k\}$  with pairwise correlations such that

$$f(\omega_1, \omega_2) = \sum_k \sqrt{\kappa_k} g_k(\omega_1) h_k(\omega_2). \quad (5.37)$$

The expansion coefficients  $\sqrt{\kappa_k}$  fulfil the normalisation condition  $\sum_k \kappa_k = 1$ . Applying this to the JSA function from PDC, one can subsequently define so-called *broadband* or *time-frequency (TF) mode* operators [83]:

$$F_{klm}(\omega_s, \omega_i) = \sum_j \sqrt{\kappa_{j,klm}} g_{j,klm}(\omega_s) h_{j,klm}(\omega_i) \quad (5.38)$$

$$\Rightarrow \hat{A}_{j,klm}^\dagger := \int d\omega_s g_{j,klm}(\omega_s) \hat{a}_l^\dagger(\omega_s), \quad (5.39)$$

$$\Rightarrow \hat{B}_{j,klm}^\dagger := \int d\omega_i h_{j,klm}(\omega_i) \hat{b}_m^\dagger(\omega_i). \quad (5.40)$$



Substituting these TF mode operators into the expression for the time-integrated Hamiltonian for PDC facilitates the reformulation:

$$\int d\omega_s d\omega_i F_{klm}(\omega_s, \omega_i) \hat{a}_l^\dagger(\omega_s) \hat{b}_m^\dagger(\omega_i) = \sum_j \sqrt{\kappa_{j,klm}} \hat{A}_{j,klm}^\dagger \hat{B}_{j,klm}^\dagger, \quad (5.41)$$

where the correlations indicated by the Schmidt coefficients are between the generated signal and idler. Note that the cumbersome notation is mainly due to taking into account the spatial properties inside the waveguide. For most experiments presented later, this will be dropped since the fields propagate in the fundamental waveguide mode.

We have reinterpreted SFG/DFG in light of the Schmidt decomposition [60, 61], and rewrite

$$\int d\omega_{\text{in}} d\omega_{\text{out}} G_{klm}(\omega_{\text{in}}, \omega_{\text{out}}) \hat{a}_l(\omega_{\text{in}}) \hat{c}_m^\dagger(\omega_{\text{out}}) = \sum_j \sqrt{\kappa_{j,klm}} \hat{A}_{j,klm} \hat{C}_{j,klm}^\dagger, \quad (5.42)$$

similar to the case of PDC. We emphasise, however, that the correlations are now evaluated between the input and output modes of a quantum process. This introduces a new notion to the concept of the Schmidt decomposition, which before was used only to decompose quantum systems instead of unitary quantum operations. To conclude this section, we present the unitary transformation from input to output state in the TF mode picture:

$$|\psi(T)\rangle = \prod_{j;k,l,m} \exp \left[ \mathcal{B}_{j,klm} \hat{A}_{j,klm}^\dagger \hat{B}_{j,klm}^\dagger + \mathcal{C}_{j,klm} \hat{A}_{j,klm} \hat{C}_{j,klm}^\dagger + \text{h.c.} \right] |\psi(0)\rangle, \quad (5.43)$$

where the indices  $k, l, m$  label spatial modes, the index  $j$  labels TF modes and we have included the expansion coefficients  $\sqrt{\kappa_{j,klm}}$  into the coupling constants.

## Summary

In this section we have derived the quantum description of three-wave mixing processes in the time-frequency mode framework. We started with the field quantisation inside our nonlinear waveguides. Then, we derived the three-wave mixing Hamiltonian and adapted it to our experimental situations, considering only type II PDC and SFG/DFG processes. Finally, we introduced the joint spectral amplitude functions which contain complete information on the TF structure of the processes and decomposed them by means of Schmidt decompositions into pairwise correlated basis functions.

## 5.2 Understanding quantum

In this section we aim for an intuitive understanding of the time-frequency (TF) mode structure of PDC and FC. We will introduce physical interpretations for the Schmidt modes and explain their connection to the quantum feature of entanglement. To begin with, we concentrate on PDC which is today well understood [48, 49, 84]. Thereafter, we present our own results on FC [60, 61, 85], which help in understanding the similarities and differences between PDC and FC in the framework of TF modes.



### 5.2.1 Parametric down-conversion

The intricate TF mode structure of PDC paves the way towards an intuitive description of this process. Let us clarify this by means of the PDC part of Eq. (5.43):

$$|\psi\rangle_{\text{PDC}} = \prod_{j;k,l,m} \exp \left[ \mathcal{B}_{j,klm} \hat{A}_{j,klm}^\dagger \hat{B}_{j,klm}^\dagger + \text{h.c.} \right] |0\rangle. \quad (5.44)$$

We bear in mind that the indices  $k, l, m$  label spatial modes, whereas the index  $j$  labels the TF modes from the Schmidt decomposition. In addition, PDC operates on the quantum mechanical vacuum as input state.

As long as we assume small coupling constants – this is equivalent to low pump powers – we can expand the exponential function and end up with

$$|\psi\rangle_{\text{PDC}} \approx \sum_{j;k,l,m} \left( 1 + \mathcal{B}_{j,klm} \hat{A}_{j,klm}^\dagger \hat{B}_{j,klm}^\dagger + \text{h.c.} \right) |0\rangle, \quad (5.45)$$

which simplifies to (compare [86])

$$\begin{aligned} |\psi\rangle_{\text{PDC}} &\approx \sum_{j;k,l,m} \mathcal{B}_{j,klm} \hat{A}_{j,klm}^\dagger \hat{B}_{j,klm}^\dagger |0\rangle \\ &\approx \sum_{k,l,m} \mathcal{B}_{klm} \int d\omega_s d\omega_i F_{klm}(\omega_s, \omega_i) \hat{a}_l^\dagger(\omega_s) \hat{b}_m^\dagger(\omega_i) |0\rangle \end{aligned} \quad (5.46)$$

if we only consider the photon-pair contributions and neglect the remaining vacuum. Note that we have reverted the Schmidt decomposition in the second line to obtain the alternative notation of the PDC state. We can interpret this state as such: the TF mode operators create single photons in ultrafast pulse shapes defined by the corresponding Schmidt mode functions. This means that PDC actually generates independent pairs of ultrafast pulses. The probability to find the signal and idler in a certain pair  $j$  of pulses in a single-shot measurement is given by the squared Schmidt coefficients  $\kappa_j$ . Note that this is a discretised way to evaluate the TF correlations between the generated signal and idler, as introduced in [48].

It is also possible to directly evaluate the frequency information contained in the JSA function  $F_{j,klm}(\omega_s, \omega_i)$  in a two-dimensional representation [86]. We recall that the JSA function is the product of the pump envelope function  $\alpha_k(\omega_s + \omega_i)$ , which reflects energy conservation, and the phasematching function  $\phi_{klm}(\omega_s, \omega_i)$ . Both functions can be plotted in the  $(\omega_s, \omega_i)$  frequency plane and correlations between the photons manifest themselves as a tilt in the resulting JSA [49]. Note that any information on the PDC TF structure gained from the evaluation of the Schmidt decomposition is also contained in the two-dimensional frequency representation of the JSA function, and vice versa.

We have gathered our previous findings in Fig. 5.3. In (a), we juxtapose a standard monochromatic creation operator  $\hat{a}^\dagger(\omega_0)$  (blue line), which creates a photon at one single frequency and a TF mode operator  $\hat{A}^\dagger$  (red area), which creates a photon in an ultrafast pulse with spectrum  $f(\omega)$ . The graphical representation of a PDC in (b) emphasises this. The PDC pump (blue arrow) decays inside the waveguide into pairs of ultrafast pulses, illustrated by the red pulses



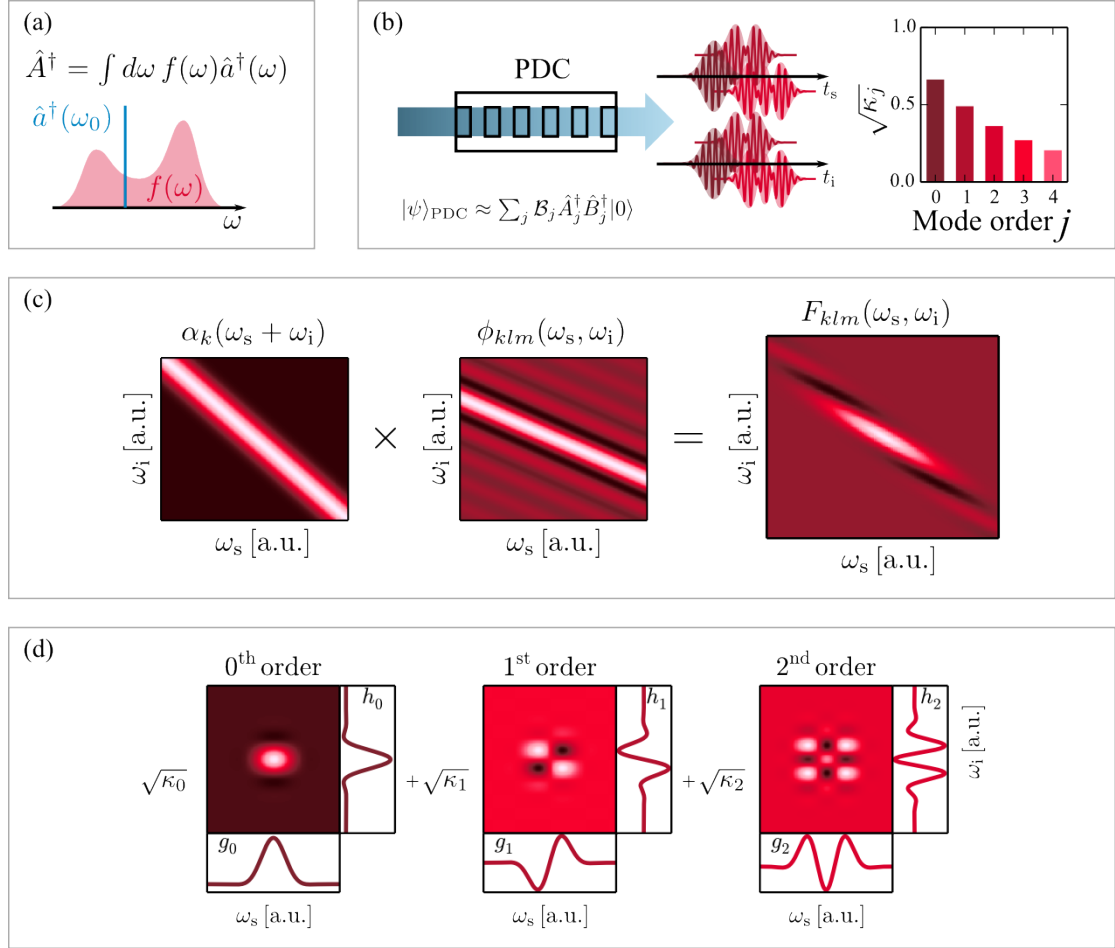


**Figure 5.3** – Roundup of the intuitive PDC interpretation in the TF mode framework. (a) Graphical representation of the TF mode operators. As opposed to a monochromatic operator, a TF mode operator creates a photon in an ultrafast pulse shape. (b) Illustration of the PDC state. During the process independent pairs of ultrafast pulses are generated with relative weights given by the Schmidt coefficients  $\sqrt{\kappa_k}$ . (c) Plot of the pump envelope function, the phasematching function and the JSA of the PDC. (d) Schmidt decomposition of the JSA above. The retrieved signal and idler Schmidt modes are well approximated by Hermite-Gaussian functions. For more details see the text



in the time domain. The relative weights between different orders  $j$  are given by the Schmidt expansion coefficients  $\sqrt{\kappa_j}$ , as plotted on the right.

In (c), we concentrate on the two-dimensional frequency representation of the PDC. We plot from left to right the pump envelope function  $\alpha_k(\omega_s + \omega_i)$ , the phasematching function  $\phi_{klm}(\omega_s, \omega_i)$  and the resulting JSA function  $F_{klm}(\omega_s, \omega_i) = \alpha_k(\omega_s + \omega_i)\phi_{klm}(\omega_s, \omega_i)$ , which contains complete information on the TF structure of the generated PDC state. In the case depicted here, the JSA function is tilted with respect to the axes, which indicates the presence of TF correlations between the generated signal and idler. A Schmidt decomposition of this JSA yields, on the one hand, the Schmidt coefficients from (b) and, on the other hand, the signal and idler TF modes shown in (d). For most PDC sources, these modes can be well-approximated by Hermite-Gaussian functions.

## 5.2.2 Time-frequency correlations

We have hinted already a few times at the possibility of expressing TF correlations (or energy-time entanglement) between PDC pair photons with the help of the Schmidt decomposition. In [48], the authors suggest deploying the Schmidt decomposition of the PDC JSA function  $F_{klm}(\omega_s, \omega_i)$  to calculate the *entropy of entanglement*<sup>13</sup> [87]

$$S = - \sum_{j=1}^N \kappa_j \log_2 \kappa_j \quad (5.47)$$

which measures the strength of the TF correlations between the generated photons. Here,  $N$  denotes the dimensionality of the system and the  $\kappa_j$  are the squared Schmidt coefficients. Note that for a purely two-dimensional encoding, that is  $N = 2$ , the entropy of entanglement has a maximum value of one, which is reached for instance by the well-known Bell states. In our example from Fig. 5.3, we find an entropy of entanglement of  $S \approx 2.4$ , hinting already at a dimensionality of the TF correlations of greater than two as illustrated by the three pairs of pulses in Fig. 5.3 (b).

### 5.2.2.1 The Schmidt number $K$

Another appealing entanglement measure is the so-called *cooperativity* or *Schmidt number*  $K$  which is defined as [88, 89]

$$K = \frac{1}{\sum_k \kappa_k^2}. \quad (5.48)$$

The physical meaning of this number is particularly handy: it counts the effective number of entangled modes present in the PDC state.

Let us explain this: given a separable (not-entangled) PDC state, the Schmidt decomposition would only yield a single non-zero coefficient, which consequently would equal one. Formally this corresponds to

$$F_{\text{sep}}(\omega_s, \omega_i) = g(\omega_s)h(\omega_i), \quad \Rightarrow K = 1. \quad (5.49)$$

<sup>13</sup>In classical information theory this quantity is better known as the *Shannon entropy*.



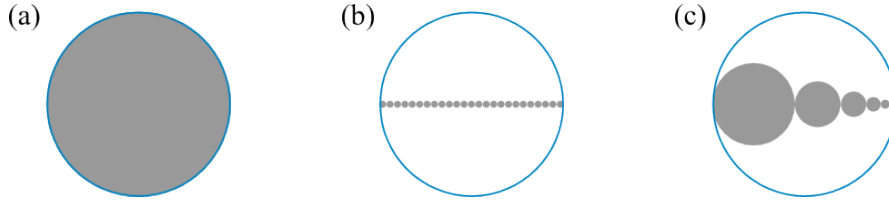


**Figure 5.4** – Graphic illustrating the contribution of different Schmidt modes to the state in an intuitive manner. For more information see the text.

In contrast, a perfectly correlated PDC state (maximally TF entangled) would comprise an infinite number of Schmidt modes with equal coefficients just above zero, meaning

$$F_{\max}(\omega_s, \omega_i) = \sum_{i=0}^{\infty} \sqrt{\kappa_k} g_k(\omega_s) h_k(\omega_i), \quad \Rightarrow K = \frac{1}{\sum_{i=0}^{\infty} \kappa_k^2} \xrightarrow{\sqrt{\kappa_k} \rightarrow 0} \infty. \quad (5.50)$$

Hence, the Schmidt number takes on a minimum value of one for separable states and increases towards  $\infty$  for perfect correlations. Note that the PDC state from Fig. 5.3 has a Schmidt number of  $K \approx 3.6$ , telling us that it is only weakly correlated. We can illustrate this graphically in a very nice way suggested in [90]. Assuming a circle with a radius of one as basis, we can compare the area of this circle to the area of a row of circles with radii given by the respective  $\kappa_k^2$ . This is shown in Fig. 5.4. The case of a separable state is depicted in (a). Since the only Schmidt coefficient equals one, its circle (grey area) perfectly overlaps with the reference (blue line). In (b), we show the situation for the nearly perfectly correlated state. All coefficients are equal and tend towards zero, hence we find a large number of very small circles. Finally, (c) shows the situation for the aforementioned PDC. The ratio of the area of the grey discs and the area of the blue circle is again the Schmidt number  $K$ .

### 5.2.2.2 Impact of TF correlations

There are applications, for instance linear optical quantum computation [30], which heavily rely on pure, indistinguishable single photons. In today's laboratories, PDC sources are amongst the most widely used sources for heralded single photons, which is the next best thing to deterministic single photon sources. However, TF correlations between the photons diminish the purity of the heralded single photons<sup>14</sup>. This is depicted in Fig. 5.5. Typically, photons are detected with non-frequency resolving detectors, for instance avalanche photo diodes (APDs) or superconducting detectors, which also cannot resolve Schmidt modes. Obviously, detecting a photon in the signal arm collapses the idler photon into a mixture of all possible Schmidt modes (left).

We can also treat this issue in the two-dimensional frequency representation of the PDC state (right). A successful detection event of one PDC photon, for instance the signal, cannot reveal the central frequency of the corresponding idler. Hence, the heralded photon inevitably collapses into a mixture of all possible frequency modes. This effect can be mitigated by applying spectral

<sup>14</sup>This is actually true for any kind of correlations. However, we have already taken care of the spatial degree of freedom by utilising waveguides.



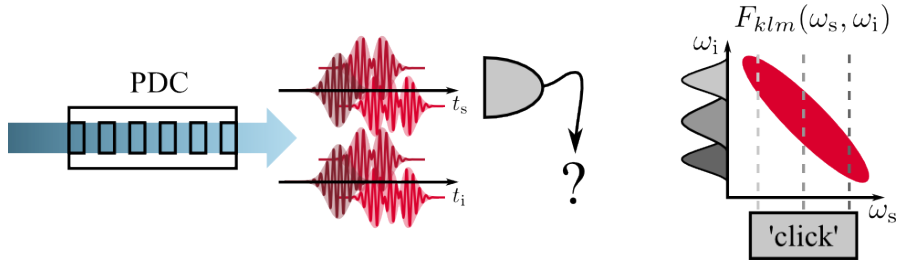


**Figure 5.5** – Schematic illustrating the collapse of an idler photon into a mixed state upon the detection of the signal. For more information see the text.

filtering to the herald, however only in the limit of infinitely narrow filtering will the heralded photon be in a pure state [91]. Moreover, tight spectral filtering also imposes tremendous loss on the PDC state and thus lowers dramatically the photon generation rate.

Note that spectral filtering is also not compatible with the general idea of ultrafast pulses, which are based on broad spectral distributions. This issue can be overcome if photon pairs are generated in separable states exhibiting no TF correlations ( $K = 1$ ). Then, even a non-frequency, non-mode resolved detection of one PDC photon heralds a genuine quantum pulse in the other output arm of the PDC.

In contrast, high-dimensional systems with a large number of entangled modes are appealing candidates for high-dimensional quantum information coding. Not only can the information capacity of a single photon be increased when utilising high-dimensional or *qudit* coding, but also the security of quantum cryptography protocols provably increases in that case [92–94]. TF modes of PDC states are notable candidates for the realisation of qudit coding schemes, because their intrinsic pulse characteristics lend themselves to applications where synchronisation is necessary. In addition they are intrinsically compatible with existing single-mode fiber communication networks, because the information is encoded in the TF degree of freedom.

In conclusion, detailed knowledge over the TF entanglement of a PDC state is a prerequisite for the exploitation of the full potential of TF modes. We have introduced measures for these correlations, in particular the Schmidt number  $K$  and briefly discussed potential applications for high- and low-dimensional PDC states.

### 5.2.3 Frequency conversion

FC is different in comparison with PDC, as we have learned during this thesis. The FC conversion part of Eq. (5.43) reads [60, 61]

$$|\psi\rangle_{\text{out}} = \bigotimes_{j;k,l,m} \exp \left[ \mathcal{C}_{j,klm} \hat{A}_{j,klm} \hat{C}_{j,klm}^\dagger + \text{h.c.} \right] |\psi\rangle_{\text{in}}, \quad (5.51)$$

where we recall that the TF mode operators  $\hat{A}_{j,klm}$  and  $\hat{C}_{j,klm}^\dagger$  are obtained from the Schmidt decomposition of the JSA function  $G_{klm}(\omega_{\text{in}}, \omega_{\text{out}}) = \sum_j \sqrt{\kappa_j} g_k(\omega_{\text{in}}) h_j(\omega_{\text{out}})$  and that the

coupling constant  $\mathcal{C}_{j,klm}$  is a function of the pump power. Looking closely at Eq. (5.51), we observe a surprising similarity with a standard quantum optical beamsplitter, the Hamiltonian of which is given by

$$\hat{H}_{\text{BS}} = \theta \hat{a} \hat{c}^\dagger + \theta^* \hat{a}^\dagger \hat{c}. \quad (5.52)$$

Here,  $\theta$  denotes the so-called beamsplitter angle, which defines the transmission and reflection ratios by means of the well-known beamsplitter input/output relations [95]

$$\hat{a} \rightarrow \cos(\theta) \hat{a} - \imath \sin(\theta) \hat{c}, \quad (5.53)$$

$$\hat{c} \rightarrow -\imath \sin(\theta) \hat{a} + \cos(\theta) \hat{c}. \quad (5.54)$$

We can see from those that  $T = \cos^2(\theta)$  is the transmission and  $R = \sin^2(\theta)$  is the reflection, respectively. Hence we conclude that FC can be understood as a very peculiar kind of beamsplitter, which connects pairs of ultrafast TF modes centred around different frequencies via the relations

$$\hat{A}_{j,klm} \rightarrow \cos(\mathcal{C}_{j,klm}) \hat{A}_{j,klm} - \imath \sin(\mathcal{C}_{j,klm}) \hat{C}_{j,klm}, \quad (5.55)$$

$$\hat{C}_{j,klm} \rightarrow -\imath \sin(\mathcal{C}_{j,klm}) \hat{A}_{j,klm} + \cos(\mathcal{C}_{j,klm}) \hat{C}_{j,klm}. \quad (5.56)$$

Note that the similarity between a beamsplitter and a FC has been first noted by Raymer et al in [62], however without the connection to TF modes.

As with PDC, we have summarised our findings in Fig. 5.6. Panel (a) schematically depicts the complete FC process, during which an input state  $|\psi\rangle_{\text{in}}$  is transformed into an output state  $|\psi\rangle_{\text{out}}$ . From left to right we depict the input state, which is expressed in terms of FC input TF modes  $g_j(\omega_{\text{in}})$ , here depicted in the temporal domain. The FC conversion process itself is described as a series of  $j$  special beamsplitters (magnified view), which operate on the FC TF input modes. Each mode is converted into an output mode  $h_j(\omega_{\text{out}})$  (blue pulses) with an efficiency  $\sin^2(\mathcal{C}_j)$  and the remaining part of the mode (red pulses) is transmitted. At the output, we find light at two frequencies, illustrated in red and blue, respectively. A recombination of the modes yields the FC output state  $|\psi\rangle_{\text{out}}$ , which can be split over two frequencies, illustrated by the upper and lower arrow. In the lower right we plot the beamsplitter reflectivity or *conversion efficiency* for the first three FC TF modes  $j = 0, 1, 2$  from dark blue to light blue.

In (b), we plot again the pump envelope function  $\alpha_k(\omega_{\text{out}} - \omega_{\text{in}})$ , the phasematching function  $\phi_{klm}(\omega_{\text{in}}, \omega_{\text{out}})$  and the resulting JSA function  $G_{klm}(\omega_{\text{in}}, \omega_{\text{out}})$ . Note that, in contrast to PDC, the pump envelope function is oriented along  $+45^\circ$  in the frequency plane.

In (c), we performed a Schmidt decomposition of the JSA function from (b). The resulting TF modes  $g_j(\omega_{\text{in}})$  and  $h_j(\omega_{\text{out}})$  for input and output are again well-approximated by Hermite-Gaussian functions. The Schmidt coefficients  $\sqrt{\kappa_j}$  are shown on the lower right. As for PDC we can calculate the Schmidt number  $K$ , which now denotes the effective number of beamsplitters that the FC process comprises.

We want to emphasise an important result: Looking at the efficiency curves in (a) at the bottom right, we find that there is no coupling constant for which every TF mode is converted with 100% efficiency. If the input state  $|\psi\rangle_{\text{in}}$  is composed of several FC TF modes – in the illustration it is three modes – it cannot be completely converted, because if any mode experiences 100% conversion efficiency, the other modes are partly transmitted. There is a notable exception to this



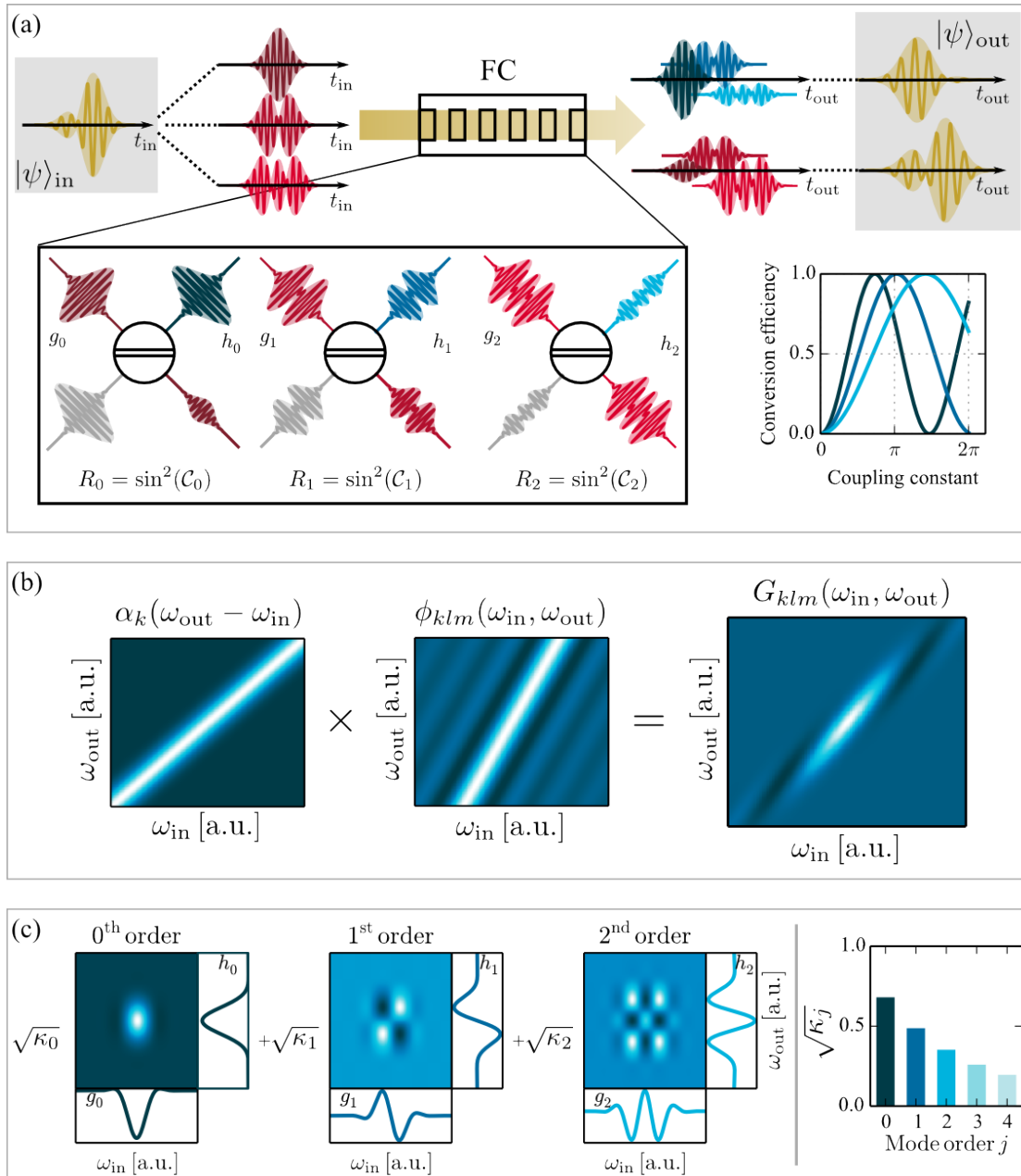


**Figure 5.6** – Collected results on FC. (a) Schematic representation of the FC process with different conversion efficiencies defined by the coupling constants  $\mathcal{C}_j$ . (b) Pump, phasematching and JSA functions. (c) Schmidt modes and Schmidt coefficients. For more information see the text.

statement: If the FC is driven by a very narrow (quasi-cw) pump laser, then we are in the highly multimode regime again, where every TF mode has the same very small Schmidt coefficient. Then, complete conversion is possible (see for instance [96]), however at the cost of an increase in required pump power compared to a mode-matched case. We will discuss the latter in detail in Chap. 7, when we introduce the quantum pulse gate (QPG) and quantum pulse shaper (QPS).

### Summary

We have presented an intuitive interpretation of the TF structure of PDC and FC. In a PDC process, the photon pairs are generated in a plethora of pairs of so-called TF modes. These are actually ultrafast pulses. The number of TF mode-pairs is directly correlated with the amount of TF entanglement between the generated photons via the Schmidt number  $K$ : the higher the entanglement, the more TF modes are present in the PDC state. In contrast, FC can be understood as a series of special quantum mechanical beamsplitters which connect pairs of TF modes centred at different frequencies. For both processes, control over the TF structure is beneficial to realise energy-efficient high-dimensional quantum applications.

## 5.3 Engineering quantum

We have illustrated the intricate TF structure of PDC and FC in Figs 5.3 and 5.6, respectively. However, we have already pointed out potential applications that require very specific TF properties. The heralded generation of pure single photons strongly benefits from a TF decorrelated PDC featuring a Schmidt number of  $K = 1$ , whereas high-dimensional quantum information applications based on TF modes require the controlled generation of a specific number of modes. In addition, a mode-selective manipulation with FC becomes possible only when the TF structure of the underlying process can be actively controlled.

In this section we introduce different techniques to achieve this aim with high precision, thus allowing for a change from multimode to single-mode behaviour and vice versa. In the first part we focus on the phasematching function  $\phi_{klm}(\omega_1, \omega_2)$ . Although it is mainly defined by material parameters, a clever choice of wavelengths in conjunction with advanced fabrication techniques grants access to a surprising degree of control. In contrast, the second part is dedicated to engineering the pump envelope function  $\alpha_k(\omega_1, \omega_2)$ . This can be conveniently accomplished with well-established methods from the research field of coherent control [75]. We will discuss how the shape of the pump pulses influences the TF structure of PDC and FC for selected phasematching conditions.

### 5.3.1 Phasematching

The phasematching functions of PDC or FC are given by (compare Eqs. (5.26) and (5.27))

$$\phi(\omega_1, \omega_2) = \text{sinc} \left( \Delta\beta(\omega_1, \omega_2) \frac{L}{2} \right) e^{i\Delta\beta(\omega_1, \omega_2) \frac{L}{2}}, \quad (5.57)$$



where  $\Delta\beta(\omega_1, \omega_2)$  labels the respective phase mismatch for PDC or FC and  $L$  is again the waveguide length. Note that we have dropped the spatial mode indices to allow for a concise notation. To simplify our notation, we perform a Taylor expansion of the phase mismatch  $\Delta\beta(\omega_1, \omega_2)$  up to first order and obtain [97]

$$\Delta\beta(\omega_1, \omega_2) = \begin{cases} (\beta_p^{(1)} - \beta_s^{(1)})\nu_s + (\beta_p^{(1)} - \beta_i^{(1)})\nu_i, \\ \pm (\beta_p^{(1)} - \beta_{in}^{(1)})\nu_{in} \mp (\beta_p^{(1)} - \beta_{out}^{(1)})\nu_{out}, \end{cases} \quad (5.58)$$

for PDC and FC, respectively. The  $\beta_j^{(1)}$  are the inverse group velocities of the respective fields, evaluated at their perfectly phasematched central frequencies  $\Omega_j$  such that

$$\beta_j^{(1)} \equiv \left. \frac{\partial\beta_j}{\partial\omega} \right|_{\Omega_j} = \frac{1}{v_g^{(j)}(\Omega_j)} \quad (5.59)$$

and the  $\nu_j$  are frequency offsets defined as  $\nu_j = \Omega_j - \omega_j$ .

In this approximation, the phasematching function is a linear function with a *group-velocity angle*  $\alpha_{PM}$  with respect to the  $\omega_1$ -axis that is given by

$$\alpha_{PM} = \begin{cases} -\arctan\left(\frac{\beta_p^{(1)} - \beta_s^{(1)}}{\beta_p^{(1)} - \beta_i^{(1)}}\right), \\ +\arctan\left(\frac{\beta_p^{(1)} - \beta_{in}^{(1)}}{\beta_p^{(1)} - \beta_{out}^{(1)}}\right), \end{cases} \quad (5.60)$$

again for PDC and FC, respectively. Note that the expansion up to first order is only valid for cases where  $v_g(\Omega_1) \neq v_g(\Omega_2)$ , which is the case for our work. For a more complete investigation of the phasematching including an expansion up to second order, we refer to [49].

We have illustrated the above formulas in Fig. 5.7 for PDC, using the more intuitive temporal domain. In all three panels, the pump pulse (blue pulse) is our moving reference and as such defines the zero-point in time. In (a), we illustrate the case for a typical non-engineered PDC. Due to the material dispersion, both signal and idler (red pulses) travel faster than the pump and exhibit different group velocities. The photon pair generation is a coherent process over the whole waveguide length, depicted by the grey-shaded region. At the output of the waveguide, signal and idler have relative timings of  $\tau_s$  and  $\tau_i$ , which are defined by the waveguide length as well as the difference in group velocities between the photons and the pump. If we draw a two-dimensional  $\tau_s - \tau_i$ -diagram, we find a curve with an increasing slope. This is reasonable, since a later arrival of the signal photon implies a later arrival of the idler, as well. From this diagram, we retrieve the frequency representation via a two-dimensional Fourier transform, which conveniently boils down to a  $90^\circ$  rotation and a relabelling of the axes. Note that we have indicated the group-velocity angle  $\alpha_{PM}$ , which in this case is negative.

Panel (b) shows the interesting case of so-called *asymmetric group-velocity matching* (AGVM), where one photon (the signal) travels at the speed of the pump. Since this photon will always arrive at the same time as the pump irrespective of the waveguide length, the function in the  $\tau_s - \tau_i$ -diagram is aligned with one axis. Consequently the frequency representation is, too. Please note that the alignment in the frequency representation is parallel to the frequency axis that represents the group-velocity matched photon, in our example the signal.



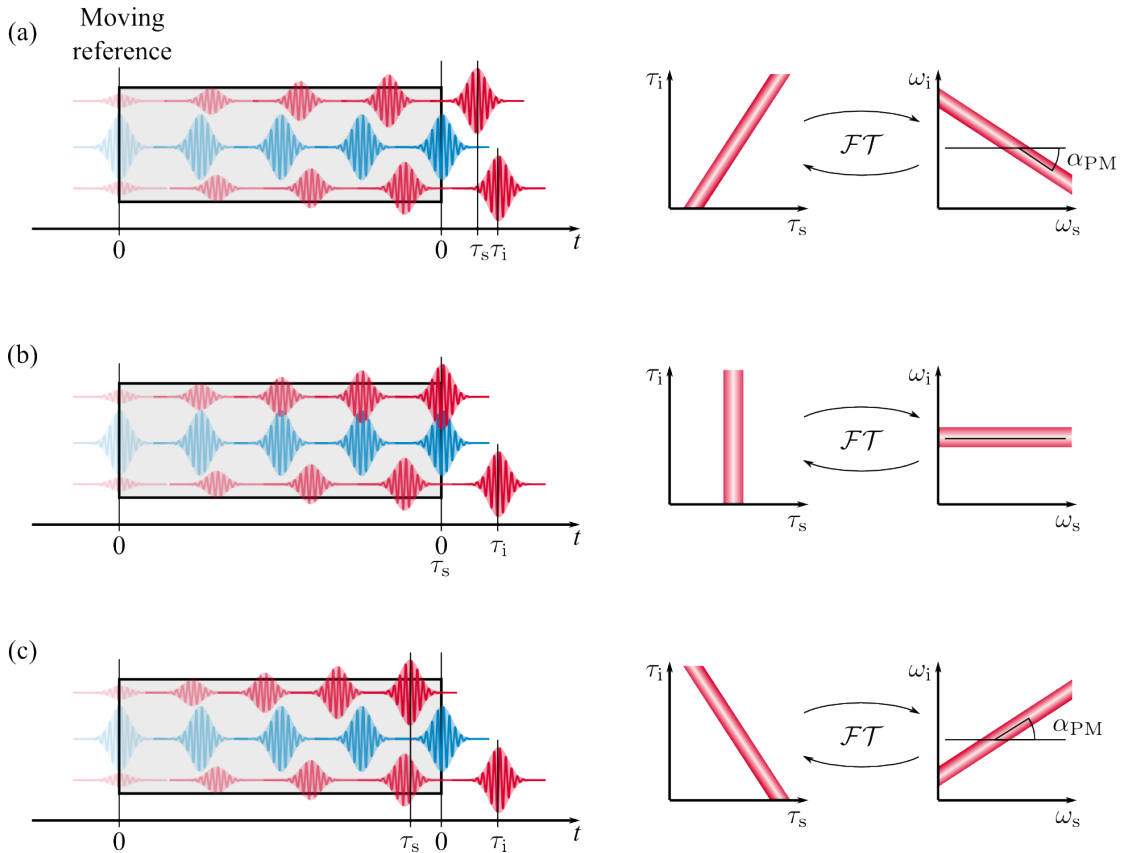


**Figure 5.7** – Illustration of the relation between group velocities and group-velocity angle  $\alpha_{PM}$  in PDC. In (a), the generated signal and idler, shown as red pulses, propagate faster through the waveguide (grey-shaded region) than the blue pump pulse. Analysing signal and idler arrival times with respect to the pump results in a function with positive slope (left plot). In the frequency domain, this corresponds to a negative group-velocity angle  $\alpha_{PM}$  with respect to the  $\omega_s$ -axis, due to the Fourier relationship between time and frequency (right plot). In (b), we illustrate asymmetric group-velocity matching, where one photon travels at the speed of the pump. In this case, the arrival time and phasematching curves are aligned with the respective axes. Finally, in (c), we consider symmetric group-velocity matching, where the velocity of the pump lies in between the signal and idler velocities. In agreement with the negative slope in the arrival time histogram, we recover a positive group-velocity angle in the frequency domain.



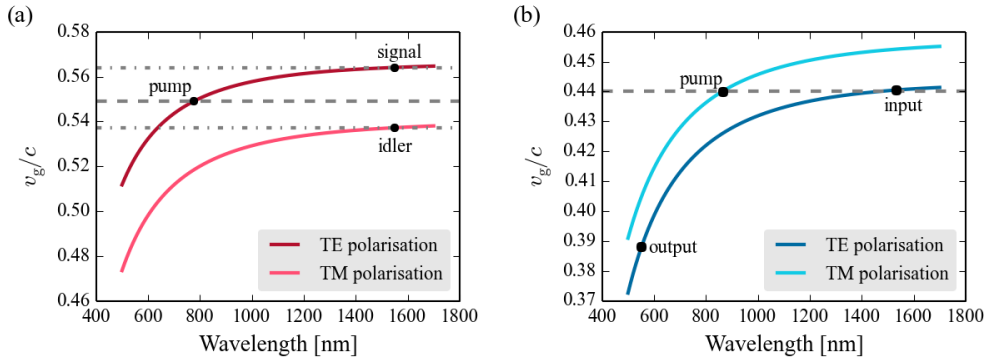


**Figure 5.8** – Group-velocity matching exploiting material birefringence. (a) Symmetric group-velocity matching in KTP. (b) Asymmetric group-velocity matching in LN. For more details see the text.

Finally, panel (c) depicts the case of *symmetric group-velocity matching* (SGVM), where one photon travels faster than the pump, whereas its sibling is slower. We will meet this configuration again in the next chapter, when we discuss our PDC source. With the same reasoning as before, we find a negative slope in the arrival time diagram, which enforces a positive slope in the frequency representation.

One might wonder why this is possible at all, since material dispersion enforces that longer wavelengths travel at a faster group velocity than shorter wavelengths for the materials and wavelength regimes considered in this work. However, many nonlinear materials exhibit birefringence. If we succeed in exciting a PDC process where pump, signal and idler are not co-polarised, then group-velocity matching becomes possible.

In Fig. 5.8 (a) we have plotted the group velocities for our PDC source from Chap. 6. In this process, a TE-polarised pump photon at a wavelength of 775 nm decays into two orthogonally polarised photons at 1550 nm inside a KTP waveguide. The group velocity of the pump (dashed line) lies between the group velocities of the photons (dash-dotted lines) thanks to the material birefringence. In contrast, panel (b) shows the case of AGVM in a LN waveguide. Here, the TM-polarised pump light at 865 nm shares the group-velocity of the TE-polarised input light at 1535 nm, whereas the group velocity of the converted output light at 553 nm differs. We exploit this process for the realisation of our new FC devices in Chap. 7.

Let us now briefly turn our attention towards the question of the shape of the phasematching function. We have seen in Eqs. (5.26) and (5.27) that the phasematching function has a sinc-shape, which originates from the Fourier transformation of the phase mismatch. This shape is not beneficial, because, on the one hand, it prevents an efficiency analytical TF description of parametric processes, and, on the other hand, it limits the purity of heralded single photons to around 83% (see for instance [98]). Therefore, different approaches have been realised to modify the shape of the phasematching function with the aim of producing a Gaussian phase-matching.

We have illustrated the non-engineered case in Fig. 5.9 (a), where the dashed grey lines il-

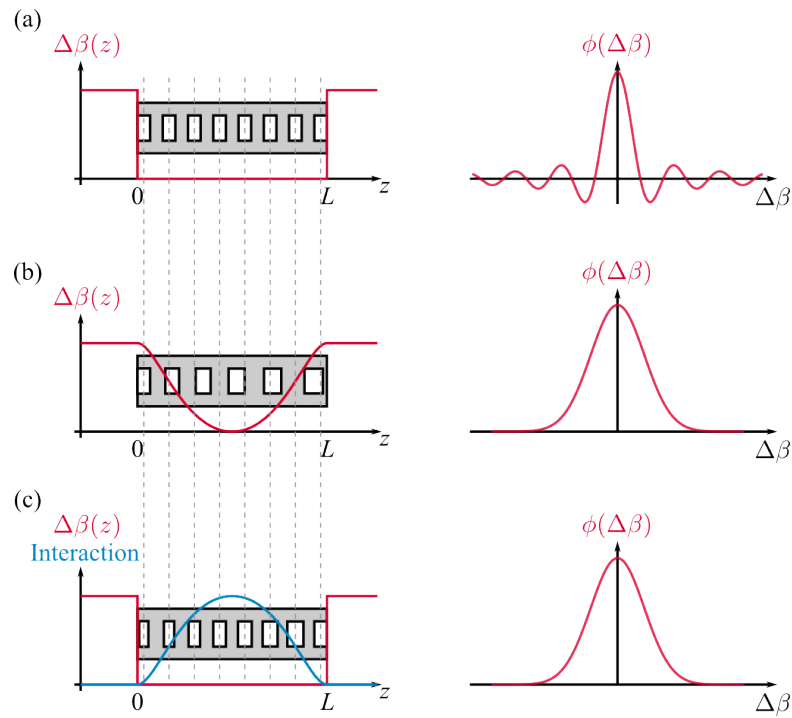


**Figure 5.9** – Manipulation of the shape of the phasematching function. In (a), we plot a uniform periodic poling, the period of which is illustrated by the dashed grey lines, and recover the well-known sinc shape. In (b), the poling period and hence the phase mismatch  $\Delta\beta$  changes over the crystal length, giving rise to a smooth phasematching function. In contrast to that, the poling period stays constant in (c), whereas the ratio of poled (white rectangles) and unpoled (grey) regions changes gradually. This mimics the gradual onset and decay of the nonlinear interaction, which again yields a smooth phasematching function.

illustrate the period of the periodic poling. As soon as light enters the waveguide (grey area), the interaction is immediately 'on' and the phase mismatch vanishes (left). This situation does not change until the light leaves the waveguide again. Hence, the phase mismatch as a function of propagation distance  $z$  is a rectangular function. Consequently, the integration over the waveguide length  $L$  yields the sinc-shaped phasematching function on the right.

There are two possible avenues to approach this issue. One method is to deploy a position-dependent grating period [99]. This is shown in (b). When the light enters the crystal, the phasematching condition is not fulfilled at first. This gradually changes until perfect phase-matching is realised, which again degrades afterwards (left). If the modulation of the phase mismatch follows a Gaussian shape, the resulting phasematching function is Gaussian as well (right).

The second approach is based on a position-dependent duty cycle [98], as illustrated in (c).



Here, the poling period stays constant, but the ratio between poled (white) and unpoled (grey) regions is gradually changed from zero to one (left). Although phasematching is in principle guaranteed over the whole crystal, the interaction strength is gradually turned 'on' and 'off' again, which facilitates the realisation of a Gaussian phasematching curve, too (right).

These results are very convenient, because they allow us in principle to approximate the phasematching function with a Gaussian:

$$\phi(\omega_1, \omega_2) \approx e^{-\gamma(\Delta\beta(\omega_1, \omega_2) \frac{L}{2})^2} e^{i\Delta\beta(\omega_1, \omega_2) \frac{L}{2}}. \quad (5.61)$$

Here, the additional factor  $\gamma$  is needed to adjust the widths of the functions. Using for instance  $\gamma = 0.193$  matches the FWHMs of the main peak of the sinc and the Gaussian. This result allows us to write the JSA function as a two-dimensional Gaussian function, since both constituents (pump and phasematching) are Gaussian. This simplifies calculations such that many considerations can be performed analytically. We have, for instance, made use of this for the four-dimensional time-frequency modelling of PDC in Chap. 6 and even Schmidt decompositions can be carried out analytically within a purely Gaussian framework [100].

### 5.3.2 Pump

We have learned how to manipulate the shape and the orientation of the phasematching function  $\phi(\omega_1, \omega_2)$  in the frequency plane. Yet, the JSA functions describing the nonlinear processes comprise a second function: the pump envelope function  $\alpha(\omega_1, \omega_2)$ .

In this section we concentrate on the influence of different pump pulse shapes on the JSA functions and their correlations for two chosen cases of phasematching configurations, namely the cases from Fig. 5.8, which correspond to the devices presented in Chaps. 6 and 7.

As usual, we start with PDC: pump photons at 775 nm decay inside a nonlinear PPKTP waveguide into signal and idler centred around 1550 nm. Due to the birefringence in the waveguide, the group velocity of the pump is in between the velocities of signal and idler (compare Fig. 5.8), which in our case leads to a group-velocity angle  $\alpha_{PM}$  of  $+63^\circ$ . According to [49], a positive group-velocity angle is a prerequisite for TF decorrelation, which is tantamount to a Schmidt number of  $K = 1$  and in turn facilitates the heralding of pure single photon pulses.

We numerically model the behaviour of this process when changing the spectral bandwidth of the pump pulses, which can easily be accomplished with standard pulse shaping techniques, in Fig. 5.10. In panel (a), we assumed a pump with a FWHM of 0.5 nm. In the upper plot we see that the product of the pump envelope function (solid lines) and the phasematching function (dashed lines) results in a frequency anti-correlated JSA function, which is governed by the negative pump slope. Note that the plots are against wavelengths because we find this to be more intuitive. However, the small red tick labels are the respective frequencies in PHz. In the lower plot we show the Schmidt expansion coefficients  $\sqrt{\kappa_j}$  obtained via a Schmidt decomposition of the JSA. Several coefficients are greater than zero, which is also reflected by the Schmidt number  $K \approx 1.6$ .

In (b), the pump bandwidth of 1.5 nm is ideally adapted to the phasematching function and we obtain a leading Schmidt coefficient of  $\sqrt{\kappa_0} \approx 0.9999$ , which is very close to the optimum of  $\sqrt{\kappa_j} = 1$  and most probably deviates due to numerical errors. This is formally supported by



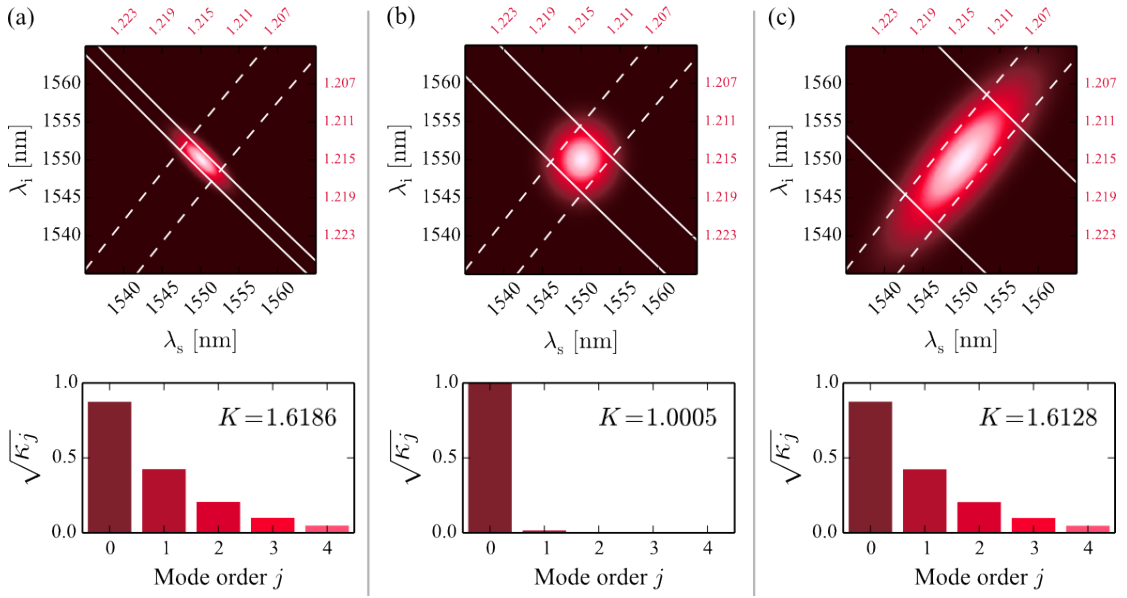


**Figure 5.10** – JSA functions of our PDC. (a) We assume a narrow pump (solid lines), which in conjunction with the positive phasematching (dashed lines) function generates a frequency anti-correlated JSA exhibiting a Schmidt number of  $K \approx 1.6$ . (b) In this case, the pump bandwidth is ideally adapted to TF single-mode operation, which is confirmed by the Schmidt number of  $K \approx 1.0$ . (c) Too broad a pump leads to positive frequency correlations between the generated signal and idler, which is reflected by the Schmidt number of  $K \approx 1.6$  again. The lower row shows the Schmidt coefficients, whereas the red tick labels in the upper row are the respective signal and idler frequencies in PHz.

the Schmidt number of  $K \approx 1.0$ , which means that signal and idler are generated in one TF mode each. Intuitively this result can be seen by the shape of the JSA. If the JSA is aligned with the frequency axes, there are no correlations between signal and idler and we are in the single mode operation regime. Note that with this configuration, the heralding of pure single photons becomes possible [49].

Finally, we model a pump with a FWHM of 4.2 nm in (c). Clearly this pump is too broad in comparison to the phasematching function, which in turn leads to a frequency correlated JSA function. Note that the slope of the JSA is now governed by the positive slope of the phasematching function. Interestingly, we again find a Schmidt number of  $K \approx 1.6$  as in the first example, which tells us that we cannot directly see the type of TF correlations from the Schmidt number  $K$ .

These investigations show that a positive phasematching slope not only facilitates the generation of photon pairs without any TF correlations, but also allows for a smooth tuning of the frequency correlations from anti-correlated to correlated. We have exploited this for our PDC



source, as we will discuss in the next chapter.

Let us now investigate the impact of different TF shapes of the pump pulses on the PDC TF structure. To this end we concentrate on case (b) from Fig. 5.10, which yields the cleanest results with only one single TF mode. We plotted this once more in Fig. 5.11 (a).

In (a.1), we show a sketch of the pump pulse TF shape in the temporal domain, which translates directly into the spectrum. In (a.2), we show again the JSA function, which is the product of the pump (solid lines) and the phasematching (dashed lines) functions. Again, a Schmidt decomposition of the JSA yields the Schmidt coefficients in (a.3). Note that here, we have included the more intuitive disc-diagram from Fig. 5.4, where we recall that the blue circle describes an ideal TF single-mode state and the grey discs are the mode contributions for the state under consideration. The almost single-mode state with  $K \approx 1.0$  fills the blue circle as we would have expected. Finally, in (a.4) we plot the modulus of the signal and idler TF modes  $|g(\lambda_s)|$  and  $|h(\lambda_i)|$ , respectively.

In (b), we considered a pump with a first-order Hermite-Gaussian shape. We find that the JSA function in (b.2) now comprises two peaks, corresponding to the modified pump function. From the Schmidt decomposition we obtain two Schmidt coefficients that differ from zero, as shown in (b.3). Note that they have similar magnitudes, which is also reflected in the disc diagram where the two grey circles have almost the same size, and in the Schmidt number of  $K \approx 2.0$ . In (b.4), we have plotted the signal and idler TF modes corresponding to the two non-zero coefficients. Interestingly we find that a Gaussian signal TF mode implies a first-order Hermite-Gaussian idler mode, and vice versa. The generated state is a close to perfect TF Bell state, that is a maximally entangled state. Note that a group-velocity angle of  $+45^\circ$  facilitates the generation of genuine TF Bell states in this configuration with a Schmidt number of  $K = 2.0$ . However, we rather decided to model the characteristics of the PDC source utilised in this thesis.

In (c), we increased the pump mode order one step further to a second-order Hermite-Gaussian. As expected, the JSA function in (c.2) now exhibits three peaks and the Schmidt decomposition yields three non-zero Schmidt coefficients, depicted in (c.3). However, in this case the magnitude of the coefficients differs notably, which reduces the Schmidt number to  $K \approx 2.6$ . This fact can be seen from the disc diagram, as well, where the three grey discs now have observably different sizes. In (c.4), we plot the corresponding signal and idler TF modes. Again, we find a one-to-one correspondence of a certain signal to a certain idler mode. Hence, the generated state exhibits higher-dimensional entanglement, but further work is needed for the generation of a generalised three-dimensional Bell state<sup>15</sup>. For a more detailed and complete study along these lines we refer to [101], where the authors investigated an optical parametric oscillator based on degenerate type I PDC.

We conclude this section with a brief consideration of our FC from Fig. 5.8 (a). We already stated that in this situation we find AGVM between the photons at 1530 nm and the pump at 860 nm. Consequently, we expect that the phasematching function is aligned with the 1530 nm axis. Actually this is confirmed by Fig. 5.12.

In (a), we consider a Gaussian TF shape of the pump pulses, as sketched in (a.1). In (a.2) we see that the pump envelope function (solid lines) now has a positive slope. Note that the deviation from an ideal  $+45^\circ$  slope is due to the different scaling of the axes in the frequency

<sup>15</sup>This could also not be achieved with a  $+45^\circ$  group-velocity angle, which only facilitates the generation of a state with  $K = 2.6$ .



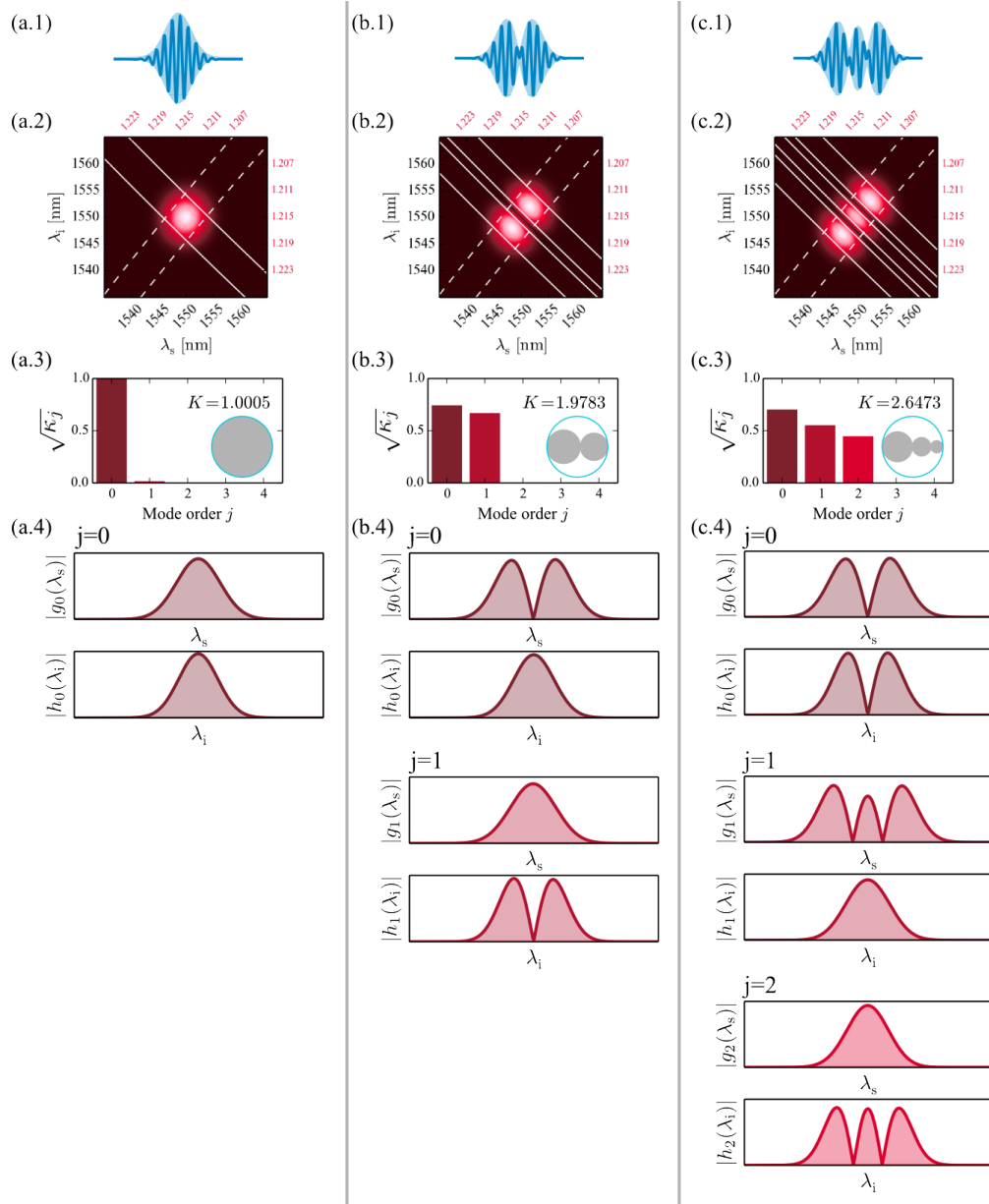


**Figure 5.11** – Impact of difference TF shapes of the pump on the TF structure of our PDC source. For more information see the text.



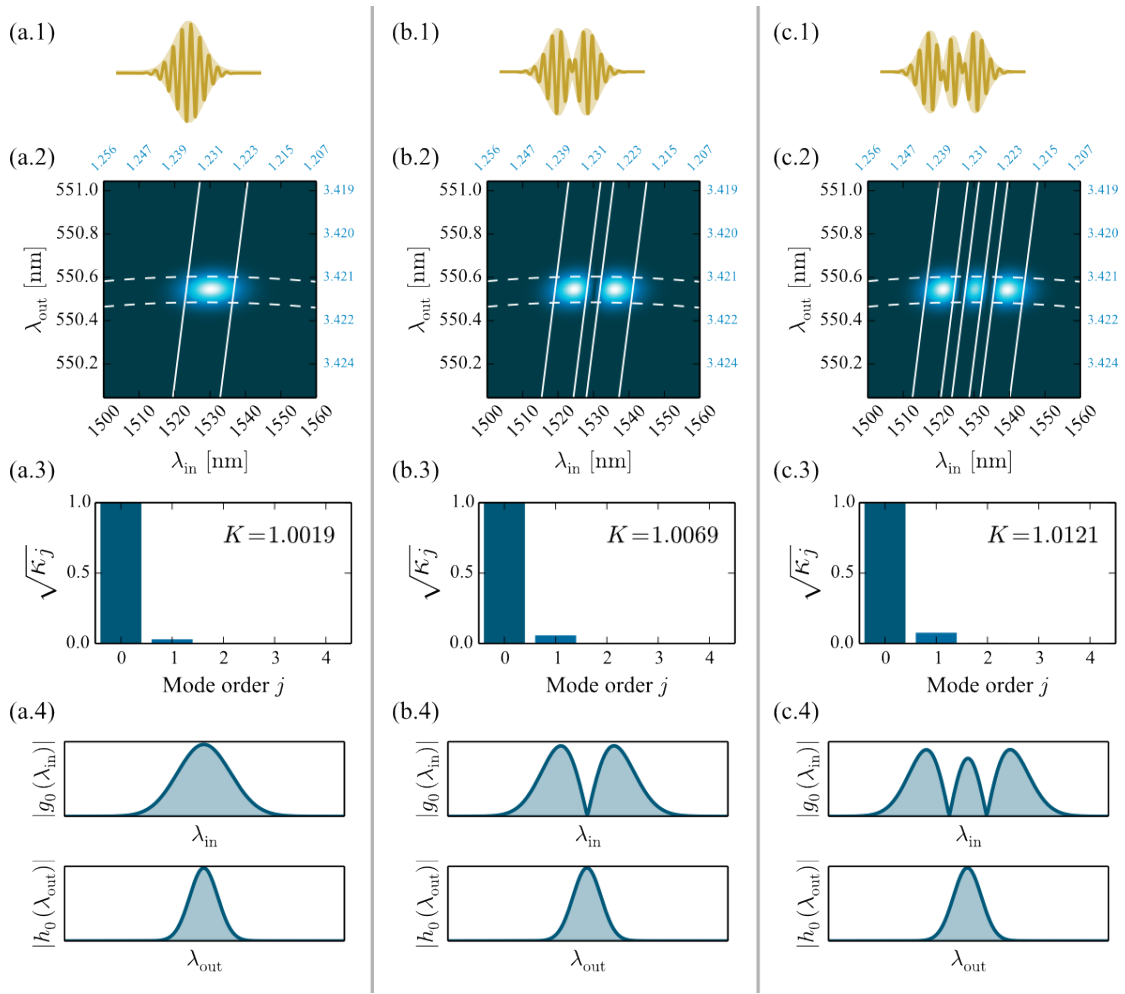


**Figure 5.12** – Impact of different TF shapes of the pump on the TF structure of our FC device. For more information see the text.

domain (see small blue ticks). The phasematching function (dashed lines) is now parallel to the input axis, as we would have expected from the AGVM condition.

The width of the JSA along the input axis is roughly 10 THz, whereas the extent in the output is only around 0.5 THz, corresponding to a bandwidth compression of a factor of 20 between input and output. Larger values have already been reported in the literature [102], but they were achieved with considerable experimental effort including the opposite chirping of a single photon and an ultrafast pump pulse. In our device, we get the compression *for free* as a result of the careful dispersion engineering.

From the Schmidt decomposition in (a.3) we deduce a Schmidt number of  $K \approx 1.0$ , which verifies the single TF mode configuration of the device. The Schmidt modes of input and output  $|g_0(\lambda_{in})|$  and  $|h_0(\lambda_{out})|$  are shown in (a.4)

In (b), we changed the pump to a first-order Hermite-Gaussian. The JSA function in (b.2)



again comprises two peaks, as was the case for the PDC in Fig. 5.11. However, we note that the JSA is still oriented along the axes of the diagram. It is thus not surprising that the Schmidt decomposition again yields  $K \approx 1.0$ , as shown in (b.3). If we look at the Schmidt modes in (b.4), we now find that the input mode has changed its shape, whereas the output mode is still the same as in (a.4). From this we conclude that the TF shape of the pump defines the input TF mode  $g_0(\lambda_{\text{in}})$ . Consequently, the output TF mode  $h_0(\lambda_{\text{out}})$  must be defined solely by the phasematching function.

We cross-check this behaviour in (c), where we assume a second order Hermite-Gaussian pump shape. As before, we obtain a JSA function exhibiting three distinct peaks in (c.2). Again, the Schmidt decomposition yields  $K \approx 1.0$ , illustrated in (c.3). The Schmidt modes in (c.4) support our conclusion, because the input mode is now a third-order Hermite-Gaussian as the pump. The output mode, in contrast, is still a fundamental Gaussian as in cases (a) and (b). We have discussed this behaviour in great detail in [60] and [61], and will again do so in Chap. 7 when presenting the quantum pulse gate and quantum pulse shaper.

As a final remark, we emphasise that this behaviour breaks down as soon as the pump becomes spectrally narrow. Then, the slope of the pump envelope function introduces again TF correlations between input and output and single-mode operation is not given anymore. We also find a limitation in the maximum pump bandwidth due to the curvature of the phasematching function. We have used the complete model for  $\Delta\beta(\omega_1, \omega_2)$  for the calculation of these plots and find that increasing the pump bandwidth to large values, the JSA adopts the curvature of the phasematching, leading to a Schmidt number which is larger than one. Again, this will be discussed in Chap. 7.

## Summary

We have investigated ways to engineer the TF structure of PDC and FC processes. In the first part, we focussed on the phasematching function and discussed how the orientation in the frequency plane depends on the group velocities of the involved fields. We have identified two scenarios – symmetric and asymmetric group-velocity matching – which facilitate processes comprising only one single TF mode. Furthermore, we have mentioned experimental approaches towards engineering the actual shape of the phasematching function to replace the sinc with a more preferable Gaussian. In the second part, we have considered a TF shaping of the pump pulses. We have seen that for our PDC source, we can smoothly tune the shape and strength of the frequency correlations between the generated signal and idler and have motivated ways to generate quantum states exhibiting a well-defined number of TF modes. We concluded this section with a brief review of the functionality of our FC devices. Here, the TF shape of the pump pulse defines the TF mode of the group-velocity matched field, whereas the phasematching defines the other TF mode. Changing the pump shape does not affect the number of modes in the process, but rather the shape of the one TF mode supported by the FC.

## 5.4 Time-ordering: a genuine quantum effect

So far we have neglected a small but unfriendly subtlety when considering the temporal evolution of a quantum state: time-ordering. The electric field operators involved in the TWM



processes and hence the Hamiltonians at different instants in time do not necessarily commute. We recall Eq. (5.1), where we found the time-ordering operator  $\hat{\mathcal{T}}$ , which we neglected before:

$$|\psi(T)\rangle = \hat{\mathcal{T}} \exp \left[ -\frac{i}{\hbar} \int_0^T dt \hat{H}(t) \right] |\psi(0)\rangle. \quad (5.62)$$

Note that, by considering the complete time-ordered solution of this equation, we advance from the photon-pair picture of PDC to an analysis of the complete state, including higher-order photon numbers which become important at elevated PDC pump powers.

Unfortunately, this expression cannot be solved analytically anymore for pulsed pump light and a numerical approach has to be considered. Note that for a cw pump, the problem has been solved analytically in [103]. However, since our Hamiltonian is bilinear (see Eq. (5.36)), we can also deploy the Heisenberg picture (compare Eq. (5.2)), where the solution of this problem is a linear unitary Bogolyubov transformation given by [104–106]

$$\hat{a}^{(\text{out})}(\omega) = \int d\omega' U_a(\omega, \omega') \hat{a}^{(\text{in})}(\omega') + \int d\omega' V_a(\omega, \omega') \hat{b}^{(\text{in})\dagger}(\omega'), \quad (5.63)$$

$$\hat{b}^{(\text{out})}(\omega) = \int d\omega' U_c(\omega, \omega') \hat{b}^{(\text{in})}(\omega') + \int d\omega' V_c(\omega, \omega') \hat{a}^{(\text{in})\dagger}(\omega'), \quad (5.64)$$

for PDC and

$$\hat{a}^{(\text{out})}(\omega) = \int d\omega' U_a(\omega, \omega') \hat{a}^{(\text{in})}(\omega') + \int d\omega' V_a(\omega, \omega') \hat{c}^{(\text{in})}(\omega'), \quad (5.65)$$

$$\hat{c}^{(\text{out})}(\omega) = \int d\omega' U_c(\omega, \omega') \hat{c}^{(\text{in})}(\omega') - \int d\omega' V_c(\omega, \omega') \hat{a}^{(\text{in})}(\omega'), \quad (5.66)$$

for FC, where the superscripts (in) and (out) label the operators before and after the unitary transformation. Under the constraint that our particular transformations are canonical operator transformations, we can reformulate them in our TF mode framework and find

$$\hat{A}_j^{(\text{out})} = \cosh(\mathcal{B}_j) \hat{A}_j^{(\text{in})} + \sinh(\mathcal{B}_j) \hat{B}_j^{(\text{in})\dagger}, \quad (5.67)$$

$$\hat{B}_j^{(\text{out})} = \sinh(\mathcal{B}_j) \hat{A}_j^{(\text{in})\dagger} + \cosh(\mathcal{B}_j) \hat{B}_j^{(\text{in})}, \quad (5.68)$$

and

$$\hat{A}_j^{(\text{out})} = \cos(\mathcal{C}_j) \hat{A}_j^{(\text{in})} + \sin(\mathcal{C}_j) \hat{C}_j^{(\text{in})}, \quad (5.69)$$

$$\hat{C}_j^{(\text{out})} = -\sin(\mathcal{C}_j) \hat{A}_j^{(\text{in})} + \cos(\mathcal{C}_j) \hat{C}_j^{(\text{in})}, \quad (5.70)$$

again for PDC and FC, respectively. Please note that we will not further detail the numerical implementation of the solution of the above transformation equations, but rather refer to [76] for extensive reading. What we will do here, however, is to discuss the impact of time-ordering on PDC and FC. In Fig. 5.13, we compare the analytical solutions of PDC (a) - (c) and FC (d) - (f) developed in earlier sections with the rigorous numerical solution including time-ordering.

Let us discuss PDC first. From panel (a) to (c), the pump power is increasing and we plot the analytical JSA function  $F_{\text{ana}}(\omega_s, \omega_i)$  (top left) as well as the rigorous JSA function  $F_{\text{rig}}(\omega_s, \omega_i)$



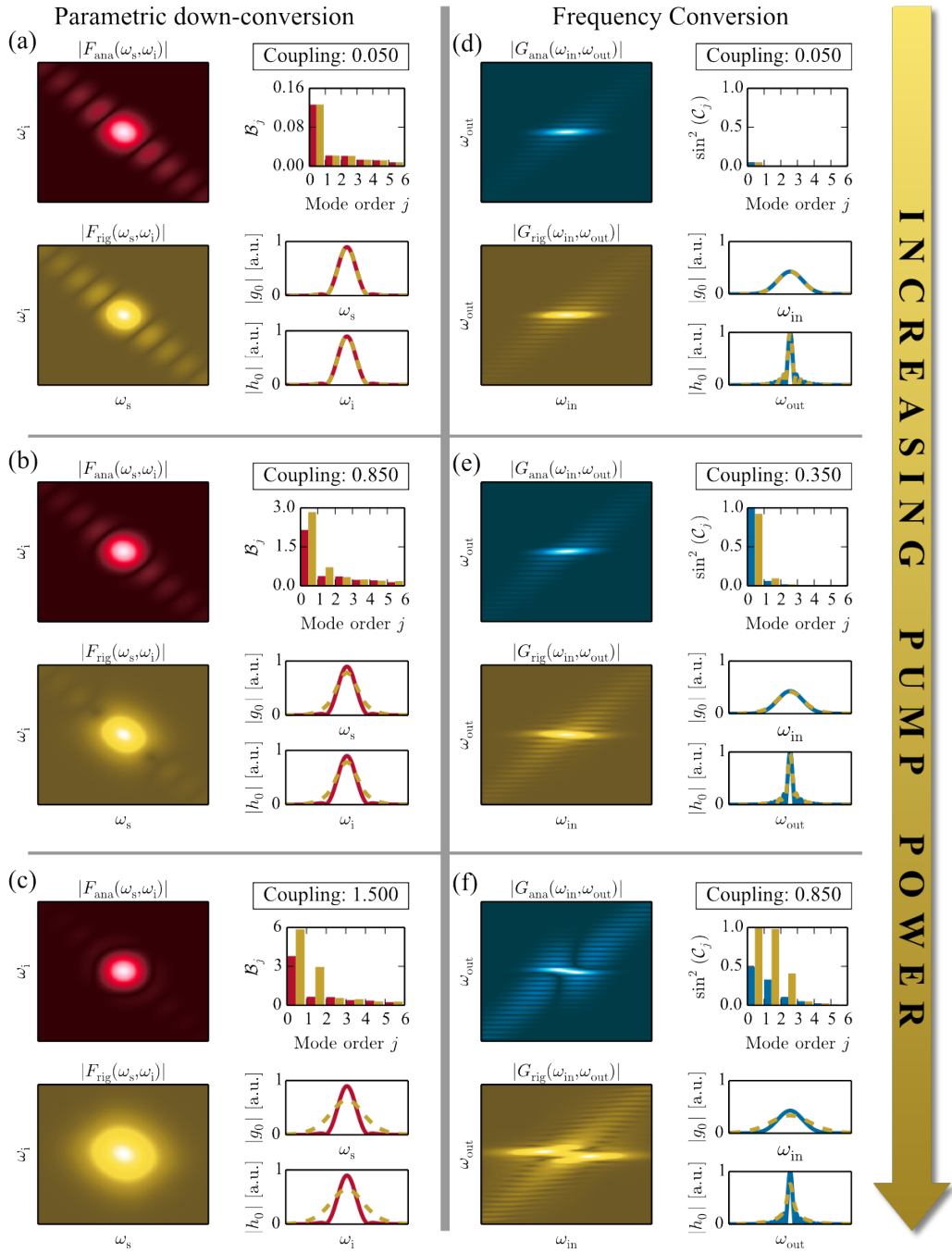


**Figure 5.13** – Impact of time-ordering on PDC (a) - (c) and FC (d) - (f). For more information, see the text.



(bottom left). Note that the analytical JSA function originates from the solution of the state evolution when neglecting time-ordering, and is thus identical to our previously discussed JSA function  $F_{\text{ana}}(\omega_s, \omega_i) \equiv F_{klm}(\omega_s, \omega_i)$ , when incorporating higher-order photon number contributions.

In addition to the respective JSA functions, we show the gain coefficients of the different TF modes  $\mathcal{B}_j$  (top right) and the shape of the first pair of TF modes  $|g_0(\omega_s)|$  and  $|h_0(\omega_i)|$  (bottom right). Red colour coding always refers to the analytical solution, whereas yellow denotes the rigorous numerical approach. We recall that the  $\mathcal{B}_j$  coefficients are connected to the Schmidt coefficients  $\sqrt{\kappa_j}$  but weighted with the overall gain of the PDC. They are a measure for the amount of generated photon pairs in the different modes. Note that the respective values for the utilised pump power in arbitrary units are indicated in the upper right of every plot for comparison between the cases.

We find that with increasing pump power, the shape of the TF modes changes, or more precisely broadens. In addition, the side peaks in the JSA function, which originate from the sinc-shaped phasematching function, become less visible. Consequently, we observe a relative increase in the weight of the first and second  $\mathcal{B}_j$  coefficient, meaning that it is more probable that photon pairs are generated in either the fundamental or first pair of TF modes. Additionally the overall efficiency of the process increases. In essence, the process is driven towards TF single-mode behaviour when incorporating time-ordering into the theory. Note that we have considered the case of our PDC source from Chap. 6 (compare also Fig. 5.11) and that typical experiments use pump power levels comparable to panel (a), where time-ordering effects may be neglected<sup>16</sup>.

We now turn our attention towards FC, where we discuss the case of the group-velocity matched FC introduced earlier (compare Fig. 5.12). Again, the pump power increases from panel (d) to (f). Note that we did not use the same parameters as for the PDC, but rather adapted the pump power to highlight the impact of time-ordering in the best possible way. Again, we plot the JSA functions  $G_{\text{ana}}(\omega_{\text{in}}, \omega_{\text{out}})$  and  $G_{\text{rig}}(\omega_{\text{in}}, \omega_{\text{out}})$  on the left side of the panels. On the right, we now plot the conversion efficiencies for different TF modes  $g_j(\omega_{\text{in}})$  (top), as well as the fundamental TF modes (bottom). Colorwise yellow still marks the rigorous solution, whereas the analytical approach is now represented by the blue shades.

For low conversion efficiencies (d) we find very good overlap between the analytical and rigorous solutions. First slight deviations arise, when the conversion efficiency for the fundamental TF mode approaches unity (e). The rigorous solution shows decreased conversion efficiency for the fundamental mode, but an increased conversion of the first order TF mode. Note that the mode shapes however still agree fairly well for both approaches. The deviations become more pronounced when considering even higher pump powers beyond unity conversion of the fundamental TF mode. In panel (f), for instance, we consider a pump power which leads to several conversion and back-conversion processes during the propagation through the sample.

In this case we get several results: first, the shape of the TF modes changes dramatically, even if this behaviour is more pronounced for the input mode  $g_0(\omega_{\text{in}})$ , which is defined by the shape of the ultrafast pump; second, the shape of the overall JSA function also changes significantly; third, the conversion efficiencies develop a peculiar and, as of yet, not fully un-

<sup>16</sup>We refer to cases where  $\langle n \rangle < 1$  is the mean generated photon number in signal or idler. In this regime PDC sources serve as heralded single photon sources with acceptable performance.



derstood behaviour. As soon as the fundamental TF mode reaches unit conversion efficiency in the rigorous solution, it is not back-converted. Instead, the first higher order TF mode gets converted. After that, the second higher order mode emerges and so on. We find that panel (e), where the conversion efficiency in the fundamental TF mode is around 87% for the rigorous solution is the best possible scenario when including time-ordering. A further increase in pump power introduces new TF modes to the process and destroys the single-mode character. Note that similar results have been obtained by the group of Michael Raymer, who used a different theoretical and numerical approach [64]. In essence, these results threaten an intrinsic limitation to the performance of our device from Chap. 7, which has to be further investigated in future experiments.

### Summary

We have briefly spoken about the issues of time-ordering, which essentially arise from the fact that the electric fields involved in the three-wave mixing processes do not necessarily commute in time. We have presented the essential results of our work published in (76) and found that PDC is driven towards single-mode behaviour when including time-ordering. In contrast, FC becomes multimode when time-ordering effects are taken into account, which might constitute an intrinsic boundary to the performance of our device presented in Chap. 7.



[...] This makes the reality of  $P$  and  $Q$  depend upon the process of measurement carried out on the first system, which does not disturb the second system in any way. No reasonable definition of reality could be expected to permit this.

*A. Einstein, B. Podolsky and N. Rosen*



---

# Ultrafast parametric down-conversion

---

## Contents

6.1 Continuous variable description . . . . .	60
6.2 Chronocyclic representation of PDC states . . . . .	63
6.3 On the correlation time of ultrafast biphotons . . . . .	70
6.4 Theory put to test. . . . .	75

In the last two chapters, we have introduced the theoretical framework which forms the basis for the understanding of the devices we present in this thesis. This chapter now focusses on the process of *ultrafast parametric down-conversion*<sup>17</sup> (PDC). PDC has been first experimentally demonstrated in 1970 [23], and has since become the established agent of choice for the generation of a multiplicity of quantum

optical states of light. These include heralded pure single photons [51, 53], entangled [44, 107–109] and hyper-entangled states [110–112], high-dimensional states [59, 113–117] and cluster states [118–122]. Naturally, a versatile theoretical framework has been developed to accurately describe the spatial [123–125], spectral-temporal [48, 49, 86] and photon-number [126, 127] characteristics of PDC.

In agreement with the focus of our work, we have particularly highlighted the intricate time-frequency (TF) structure of PDC states in the last chapter. We have shown how, by controlling the TF shape of the ultrafast pump and the waveguide dispersion, this structure can be actively controlled as first proposed in [49]. Mosley et al first succeeded in realising this theory by engineering an ultrafast bulk crystal PDC such that the generated signal and idler were TF decorrelated [51]. As stated in the last chapter, this particular configuration is essential for the efficient generation of pure heralded single photons for networking applications.

In our group, we have taken this method and combined it with waveguided PDC. This promised three main advantages: first, waveguided PDC has been shown to be several orders of magnitude more efficient than bulk PDC [47] due to the potentially long interaction lengths and

---

<sup>17</sup>For our work this means that we focus on waveguided type II PDC processes that are pumped by ultrafast pump pulses. There are of course other experimental settings, however they are of no immediate interest for this thesis and are thus largely omitted.

the discretisation of the spatial degree of freedom into distinct waveguide modes; second, the waveguiding structure decouples the spectral and spatial degrees of freedom, which in a bulk crystal source can only be achieved in conjunction with considerable alignment effort; third, waveguided sources commend themselves for an efficient integration into networking applications based on single-mode fiber. As a result, our group succeeded in implementing the first dispersion-engineered waveguided PDC source, where the TF decorrelated signal and idler were conveniently located in the telecom wavelength regime [53]. In parallel to this thesis, our source was further optimised and now generates signal and idler which are not only TF decorrelated, but also indistinguishable in all degrees of freedom except their polarisation [54].

Further work in our group has focussed on a more thorough understanding of the PDC process. A novel type of single photon spectrometer was developed which allowed for a high-resolution characterisation of the joint spectral intensity distribution of photon pairs at telecom wavelengths [128]. In addition, our group has implemented a novel technique for a complete TF quantum process tomography of PDC, which facilitates direct, phase-sensitive access to the joint spectral amplitude (JSA) function [129]. For a better understanding of the impact of different spatial waveguide modes on the generated PDC state, we have conducted experimental and theoretical studies [124, 130] that suggest that superfluous spatial modes can be easily suppressed by appropriate broadband spectral filtering. In this way it becomes possible to select specific spatial modes without influencing the spectral characteristics of the PDC state living in the desired mode.

Note that we also focussed on elaborating on the theory for the generation of pure of single photons heralded from TF correlated PDC states [91, 131–133]. Spectrally pure single photon can only be heralded in the case of infinitesimally narrow spectral filtering in the presence of TF correlations between signal and idler. This result is detrimental for any system design, where a high photon flux has to be achieved with minimum pump power, since narrow spectral filtering is tantamount to a large number of lost photons. Note that our work on the quantum pulse gate, presented in Chap. 7, can serve as a solution to this problem, since the QPG facilitates quantum coherent broadband spectral filtering.

Finally, the work of our group also covered the continuous variable (CV) description of PDC [134–137]. We have so far not considered this picture in our general treatment of three-wave mixing processes, since the CV description focusses on photon-number correlations and largely neglects spectral-temporal properties. We will however briefly introduce the CV notion of PDC states in the next section, before we turn our attention towards results achieved during this thesis, where we merged the intuitive pictures from the CV description of PDC with our TF representation. Thereafter we discuss the important *correlation time* of a PDC photon pair, a quantity that determines the simultaneity of the two photons. We develop a theory that explains the impact of different experimental parameters on this correlation time and conclude this chapter with the experimental verification of our theory.

## 6.1 Continuous variable description

Compared to our previous theoretical considerations, we change gears in this section and consider the continuous variable (CV) description of PDC. But first things first: In CV quantum



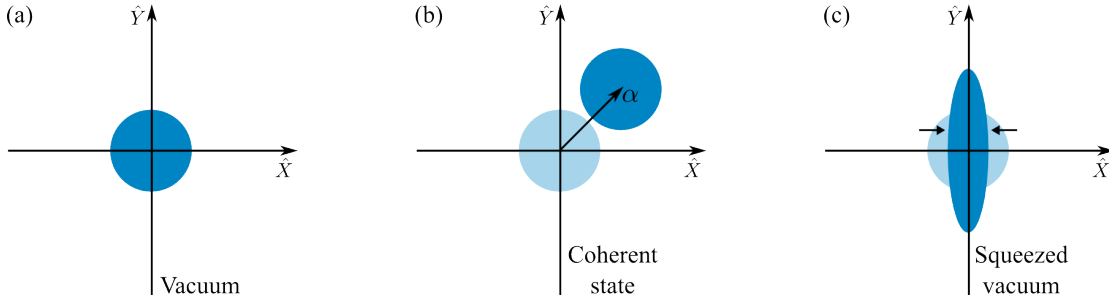


**Figure 6.1** – Phase space representation of several common quantum optical states. For more information see the text.

optics, states are commonly described by their Wigner function  $\mathcal{W}(\hat{X}, \hat{Y})$ , where  $\hat{X}$  and  $\hat{Y}$  are so-called *field quadratures* defined as

$$\hat{X} = (\hat{a}^\dagger + \hat{a}), \quad \hat{Y} = i(\hat{a}^\dagger - \hat{a}). \quad (6.1)$$

This representation is also referred to as *phase space* representation. Non-classical features are typically associated with quadrature fluctuations that are below the quantum vacuum noise level or negative values of the Wigner function. Note that Heisenberg's uncertainty relation requires that  $\Delta^2 \hat{X} \Delta^2 \hat{Y} \geq 1$

To provide an intuition on how quantum optical states look in the phase space, we have plotted a selection of several common states in Fig. 6.1. In (a) the quantum mechanical vacuum state is shown, which is centred at  $\langle \hat{X} \rangle = \langle \hat{Y} \rangle = 0$ . It is characterised by symmetric quadrature fluctuations which are given by  $\Delta^2 \hat{X} = \Delta^2 \hat{Y} = 1$ . In (b), we sketch a coherent state. In comparison to the vacuum state (shaded area), the coherent state is displaced from the origin of the phase space. The amount of displacement is characterised by the coherent field amplitude  $\alpha$ , as indicated in the illustration. Nevertheless, it still features the same quadrature fluctuations as the vacuum state<sup>18</sup>.

Panel (c) shows a non-classical state, namely a squeezed vacuum, which exhibits fluctuations in one quadrature that are below the vacuum fluctuations (shaded area). Naturally, this comes at the expense of increased fluctuations in the other quadrature. Note that in this respect, coherent states represent *minimum uncertainty* states, for which the equality in the uncertainty relation is fulfilled.

At this point, we emphasise that the CV framework focusses on the photon-number statistics of the quantum states under investigation and neglects the temporal-spectral degree of freedom. In this context, PDC states can be understood as special bi-partite systems with strict photon-number correlations. They are typically described with a four dimensional Wigner function  $\mathcal{W}(\hat{X}_s, \hat{Y}_s, \hat{X}_i, \hat{Y}_i)$ . To date it is well-known that PDC generates optical EPR states [138], which exhibit correlations in the  $\hat{X}$ -quadrature and anti-correlations in the  $\hat{Y}$ -quadrature. This means that a certain measurement result  $X_0$  in the signal implies the same in the idler, whereas measuring  $Y_0$  in the signal enforces a measurement of  $-Y_0$  in the idler.

<sup>18</sup>Notably, the vacuum state itself is also a coherent state with zero amplitude.



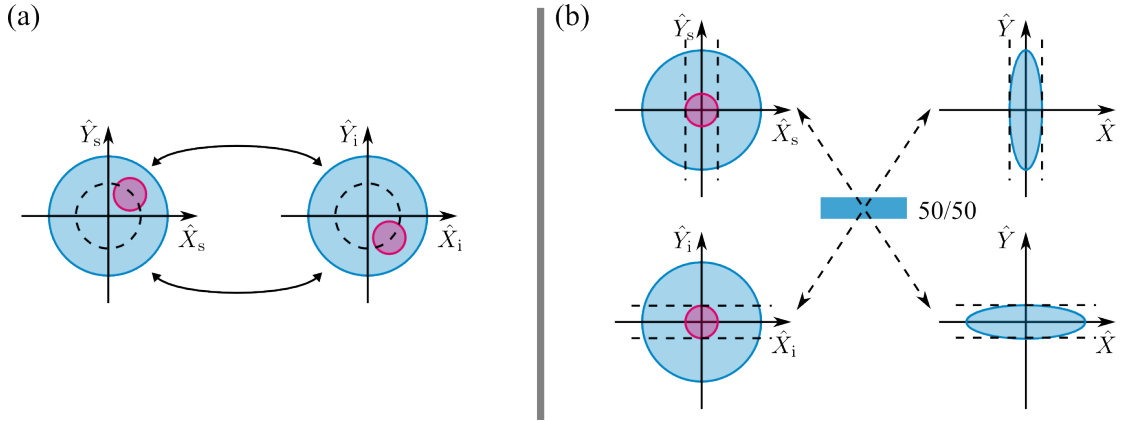


**Figure 6.2** – Schematic illustration of EPR correlations in the phase space of signal and idler. For more information see the text.

This is illustrated in Fig. 6.2 (a). Measuring the quadrature fluctuations of only signal or idler results in the blue shaded areas, which are larger than vacuum fluctuations (dashed black circle). However, when conditioning the measurement of the uncertainty along  $\hat{X}_i$  on a certain measurement result in  $\hat{X}_s$  and doing the same for the  $\hat{Y}$  quadratures, we obtain the purple regions, which can become smaller than the vacuum fluctuations [139]. Formally, this is expressed by

$$\langle (\hat{X}_s - \hat{X}_i)^2 \rangle \langle (\hat{Y}_s + \hat{Y}_i)^2 \rangle \leq 1, \quad (6.2)$$

where the plus and minus signs reflect the quadrature correlations and anti-correlations, respectively. Note that a joint squeezing of both  $\hat{X}$  and  $\hat{Y}$  quadratures can be observed when performing joint measurements on the signal and idler modes. Therefore, PDC states are also called *two-mode squeezed* states.

A remarkable attribute of these states is that, when interfering the two modes on a 50/50 beamsplitter, we find two squeezed vacuum states in the beamsplitter output ports which are squeezed in conjugate quadratures. This behaviour is sketched in Fig. 6.2 (b). The squeezing at the output of the beamsplitter is given by the strength of the initial EPR correlations (dashed lines) and a perfect EPR state with ideal point-to-point correlations would imply infinite squeezing<sup>19</sup>. As a side-remark we want to add that this process is reversible. Hence, interfering two squeezed beams with correct phases on a balanced beamsplitter leads to an EPR state at the output ports. This is a common tool in CV quantum optics experiments for the generation of optical EPR states [140] and is remarkable, because only linear optical elements are required.

<sup>19</sup>Such a state is non-physical, since infinite squeezing is tantamount to an infinite energy content of the state.



## Summary

We have briefly introduced the continuous variable description of parametric down-conversion states, which focusses on the photon-number correlations between the generated signal and idler and neglects the spectral-temporal degree of freedom, and motivated that these states are optical EPR states. Although we did not go into detail, we hope we brought across that the continuous variable description is an intuitive way of quantifying the strength of correlations, which can be graphically compared to vacuum fluctuations.

## 6.2 Chronocyclic representation of PDC states

During the work leading to this thesis, we have borrowed from the concepts of CV quantum optics introduced in the last section, and combined them with the intuitive chronocyclic representation associated with ultrafast light pulses (compare Chap. 4). It turns out that a behaviour similar to two-mode squeezing can be found in the TF structure of PDC, as we have published in [84]. This is reasonable, since just as amplitude and phase, time and frequency constitute a pair of (Fourier) conjugate variables. However, we emphasise that CV quantum optics and the TF description of PDC are two fundamentally different frameworks: whereas CV quantum optics focusses on the photon-number degree of freedom and largely neglects spectral-temporal properties, the TF description of PDC is often restricted to the photon-pair regime and evaluates time-frequency correlations.

We have seen in the last chapter that PDC can be interpreted such that signal and idler are generated in a plethora of ultrafast pulses. This suggests a TF description of PDC which utilises the framework of chronocyclic Wigner functions. For a PDC state, the chronocyclic Wigner function is a four-dimensional function, which can be calculated from the JSA function  $F(\omega_s, \omega_i)$  via a two-dimensional Wigner transformation such that [84]

$$\begin{aligned} \mathcal{W}(\omega_s, \omega_i, \tau_s, \tau_i) &= \frac{1}{(2\pi)^2} \int d\omega' d\omega'' e^{i\omega'\tau_s + i\omega''\tau_i} \\ &\times \left\langle \omega_s - \frac{\omega'}{2}, \omega_i - \frac{\omega''}{2} \left| \hat{\rho}_{\text{PDC}} \right| \omega_s + \frac{\omega'}{2}, \omega_i + \frac{\omega''}{2} \right\rangle. \end{aligned} \quad (6.3)$$

Here,  $\hat{\rho}_{\text{PDC}} = |\psi\rangle_{\text{PDC}} \langle\psi|_{\text{PDC}}$  is the PDC density operator and  $\tau_s$  and  $\tau_i$  are the signal and idler timings with respect to the moving reference frame of the pump pulses, respectively. We deploy the PDC state from Eq. (5.46) given by

$$|\psi\rangle_{\text{PDC}} = \mathcal{B} \int d\omega_s d\omega_i F(\omega_s, \omega_i) \hat{a}^\dagger(\omega_s) \hat{b}^\dagger(\omega_i) |0\rangle, \quad (6.4)$$

where we neglect the spatial mode indices in order to keep the notation as clean as possible. For these considerations, we assumed a JSA

$$F(\omega_s, \omega_i) = \underbrace{\exp\left[-\frac{\Delta\omega^2}{2\sigma^2} - i a \Delta\omega^2\right]}_{:=\alpha(\omega_s+\omega_i)} \underbrace{\exp\left[-\gamma\left(\frac{L}{2}\Delta\beta\right)\right]}_{:=\phi(\omega_s,\omega_i)} e^{i\frac{L}{2}\Delta\beta}. \quad (6.5)$$



We modelled the pump as an ultrafast pulse with spectral width  $\sigma$  and accounted for a quadratic chirp characterised by the chirp parameter  $a$ . In addition, we abbreviated  $\Delta\omega = \omega_p^{(0)} - (\omega_s + \omega_i)$ , where  $\omega_p^{(0)}$  is the central pump frequency. The phase mismatch given by  $\Delta\beta = \beta_p(\omega_s + \omega_i) - \beta_s(\omega_s) - \beta_i(\omega_i) + \beta_{\text{QPM}}$  is the standard expression from Chap. 5 and we used the Gaussian phasematching approximation. The factor  $\gamma$  is a numerical factor to match the FWHM of the phasematching to the width of the original sinc function. Again, we approximate  $\Delta\beta$  with a first-order Taylor expansion (compare Eq. (5.58)) and rewrite the JSA function in terms of frequency offsets  $\nu_s$  and  $\nu_i$  from the perfectly phasematched frequencies  $\omega_s^{(0)}$  and  $\omega_i^{(0)}$ :

$$F(\nu_s, \nu_i) = \exp \left[ -\frac{(\nu_s + \nu_i)^2}{2\sigma^2} - \frac{\gamma L^2}{4c^2} (n_{\text{ps}}\nu_s + n_{\text{pi}}\nu_i)^2 \right] \times \exp \left[ -ia(\nu_s + \nu_i)^2 + i\frac{L}{2c} (n_{\text{ps}}\nu_s + n_{\text{pi}}\nu_i) \right], \quad (6.6)$$

where we defined  $n_{ij} = n_i^{(g)} - n_j^{(g)}$  for  $i, j = \{\text{p, s, i}\}$  as the difference in *group refractive indices*<sup>20</sup> and explicitly used the dispersion relation  $\beta(\omega) = \frac{n_{\text{eff}}(\omega)\omega}{c}$ , with  $c$  denoting again the speed of light. A straightforward – though admittedly tedious – calculation yields an analytical expression for the four-dimensional chronocyclic Wigner function of a PDC state

$$\begin{aligned} \mathcal{W}(\nu_s, \nu_i, \tau_s, \tau_i) &= \sqrt{\frac{2}{\gamma}} \frac{|\mathcal{B}|^2 c \sigma}{L \pi |n_{\text{si}}|} e^{-1/2\gamma} \\ &\times \exp \left[ -\frac{1}{\sigma^2} (\nu_s + \nu_i)^2 - \frac{\gamma L^2}{2c^2} (n_{\text{ps}}\nu_s + n_{\text{pi}}\nu_i)^2 - 4a^2 \sigma^2 (\nu_s + \nu_i)^2 \right] \\ &\times \exp \left[ -\frac{2c^2}{\gamma L^2 n_{\text{si}}^2} (\tau_s - \tau_i)^2 - \frac{\sigma^2}{n_{\text{si}}^2} (n_{\text{pi}}\tau_s - n_{\text{ps}}\tau_i)^2 + \frac{2c}{\gamma L n_{\text{si}}} (\tau_s - \tau_i) \right] \\ &\times \exp \left[ \frac{4a\sigma^2}{n_{\text{si}}} (\nu_s + \nu_i) (n_{\text{pi}}\tau_s - n_{\text{ps}}\tau_i) \right]. \end{aligned} \quad (6.7)$$

What can we learn from this expression? First of all we note that we can obtain the joint spectral and temporal intensity distributions (JSI / JTI) of the PDC from tracing out the remaining degrees of freedom:

$$|F(\nu_s, \nu_i)|^2 = \int d\tau_s d\tau_i \mathcal{W}(\nu_s, \nu_i, \tau_s, \tau_i), \quad (6.8)$$

$$|\tilde{F}(\tau_s, \tau_i)|^2 = \int d\nu_s d\nu_i \mathcal{W}(\nu_s, \nu_i, \tau_s, \tau_i). \quad (6.9)$$

Second, we have a closer look at the different components of the chronocyclic PDC Wigner function. The first line in Eq. (6.7) contains only constants. Note however that we encounter the limitations of our first-order phasematching approximation here: if the group refractive indices of signal and idler become similar,  $n_{\text{si}}$  tends towards zero. Hence, the Wigner function diverges.

<sup>20</sup>The group refractive index is defined as  $n^{(g)}(\omega) = n(\omega) + \omega \partial_\omega n(\omega)$



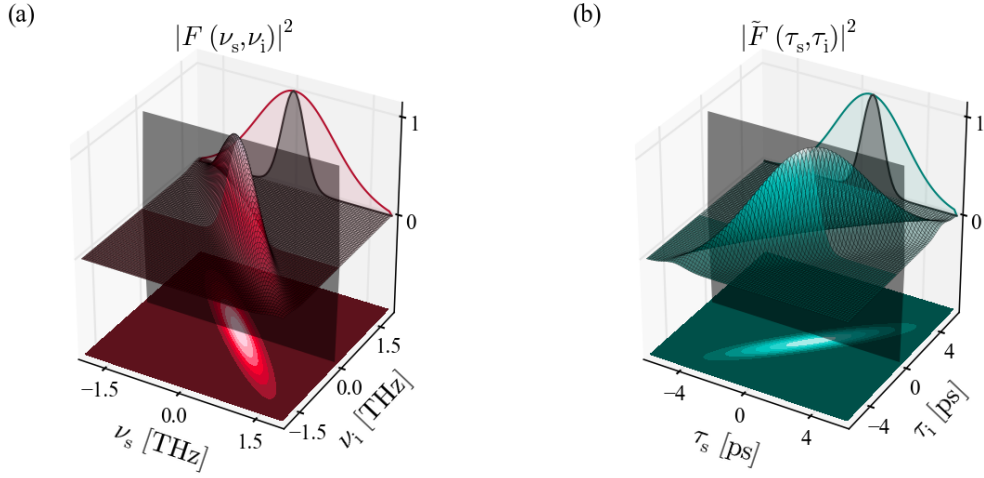


**Figure 6.3** – Joint spectral and temporal intensity distributions of a TF correlated PDC. For more information see the text.

Still, this issue can be overcome by numerical methods, which include the full dispersion relation of the waveguide.

The second line of Eq. (6.7) contains only spectral terms, whereas the third line contains the temporal contributions. The interesting part, however is the exponential term in the last line. Here we see that a non-vanishing pump chirp  $a \neq 0$  inevitably introduces a coupling of spectral and temporal degree of freedom. We will show in the following how this contribution influences the TF correlations between signal and idler.

Before we present the formal derivation of a novel TF entanglement measure inspired by CV quantum optics, we motivate our approach with a qualitative discussion of the spectral-temporal properties of a PDC pair. We consider a case similar to the one in Fig. 5.10 with an anti-correlated spectral distribution function. In Fig. 6.3 (a) we plot the JSI of the PDC, which was obtained from  $\mathcal{W}(\nu_s, \nu_i, \tau_s, \tau_i)$  by tracing out over the temporal degrees of freedom. The plotted spectra are, on the one hand, the projection of the JSI onto the  $\nu_s$ -axis, that is the signal marginal distribution (red area), and on the other hand, it is the cut through the JSI indicated by the black plane (black area). Note that the latter corresponds to a conditioned signal spectrum<sup>21</sup>, when conditioning on a specific idler frequency  $\nu_i^{(0)}$ . Notably, the conditioned signal spectrum is narrower than the width of the marginal distribution.

In panel (b) we plot the JTI of the PDC, retrieved from the chronocyclic Wigner function by tracing out over the frequencies. The projections onto the  $\tau_s$ -axis show the signal arrival time marginal distribution (green area) as well as the conditioned distribution (black area), when conditioning on a certain idler arrival time  $\tau_i^{(0)}$ . Again, the conditioned distribution is significantly narrower than the marginal function.

<sup>21</sup>Experimentally this means that we have to place a narrow spectral filter in the idler arm of the PDC.

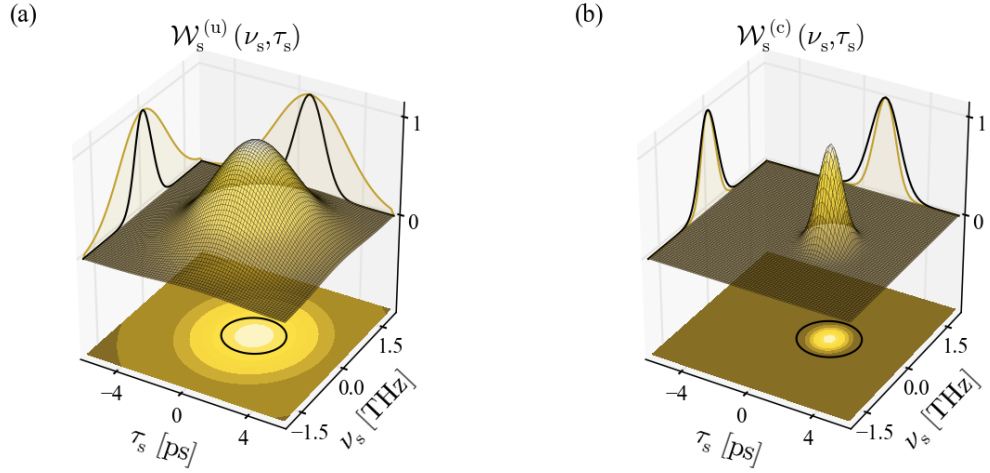


**Figure 6.4** – The unconditioned (a) and conditioned (b) chronocyclic Wigner functions for the PDC from Fig. 6.3. Solid black lines illustrate Fourier-limited pulses.

At this point we find a surprising analog to two-mode squeezing: the intrinsic spectral broadband nature of the ultrafast PDC leads to accordingly broad spectral marginal distributions, whereas the uncertainty in the exact generation position of the photon pair enforces the corresponding broad temporal marginals. However, knowledge of either idler frequency or arrival time immediately reveal the corresponding quantity for signal with very low uncertainty. Hence, TF correlations enforce an effect similar to two-mode squeezing, which we call *time-frequency squeezing*.

For two-mode quadrature squeezing we could see that EPR correlations between signal and idler can lead to joint quadrature fluctuations which overcome an apparent Heisenberg’s uncertainty relation. Remarkably, there is an equivalent quantity for time and frequency: the time-bandwidth product (TPB), which is bound from below such that  $\Delta\nu\Delta\tau \geq 0.441$  for Gaussian shaped pulses. Note that the TPB was introduced as a purely classical limitation. It has, however, been shown that in quantum mechanics an energy-time-uncertainty relation exists [141], similar to the original formulation of Heisenberg’s uncertainty relation in space and momentum.

A rough estimate for the TPB from the plots in Fig. 6.3 yields

$$\Delta\nu\Delta\tau \approx \frac{1}{2\pi} 1 \cdot 10^{12} \text{ Hz} \cdot 1.5 \cdot 10^{-12} \text{ s} \approx 0.239 < 0.441 \quad (6.10)$$

and we actually find a violation of the Fourier limit, which is tantamount to finding TF entanglement. Note that for a perfectly TF decorrelated PDC, the two photons are generated in Fourier-limited pulses and thus the conditioned TPB exactly equals 0.441 [84].

In the following we will put this result onto more formal footing. From the chronocyclic PDC Wigner function, we retrieve the reduced single-photon Wigner functions (SPWFs) of the signal



field

$$\mathcal{W}_s^{(u)}(\nu_s, \tau_s) = \int d\nu_i d\tau_i \mathcal{W}(\nu_s, \nu_i, \tau_s, \tau_i), \quad (6.11)$$

$$\mathcal{W}_s^{(c)}(\nu_s, \tau_s) = \mathcal{W}(\nu_s, \tau_s; \nu_i = \nu_i^{(0)}, \tau_i = \tau_i^{(0)}), \quad (6.12)$$

where the superscripts (u) and (c) label the unconditioned and conditioned case, respectively. Note that the SPWF has been investigated in [142–144], however without the full implications resulting from our analysis of the complete four-dimensional PDC Wigner function. We plot the two SPWFs corresponding to the JSI and JTI from Fig. 6.3 in Fig. 6.4. Panel (a) shows  $\mathcal{W}_s^{(u)}(\nu_s, \tau_s)$ . The solid black lines illustrate the SPWF of a Fourier-limited quantum pulse exhibiting a TBP of  $\Delta\nu\Delta\tau = 0.441$ . As expected, the unconditioned SPWF is broader than the Fourier-limited function in both, frequency and time. For a comparison we plot the conditioned SPWF in panel (b). Notably, this function is narrower than the Fourier-limited pulse in the spectral as well as the temporal degree of freedom, which confirms our rough estimate from above. Note that the position of the maximum of the conditioned SPWF depends on the exact values of the parameters  $\nu_i^{(0)}$  and  $\tau_i^{(0)}$ , the choice of which does not influence the shape of the SPWF as long as they are chosen from inside the respective idler marginal distributions.

Finally, we performed a more thorough study of the TF correlations of a PDC. Again, we deployed our PDC process from Fig. 5.10 but now calculated the *normalised, inverse conditioned-TBP*  $\delta_{\text{TBP}}$ , which is defined as

$$\delta_{\text{TBP}} = \frac{0.441}{\Delta\nu^{(c)}\Delta\tau^{(c)}}. \quad (6.13)$$

Given the analytical expression for  $\mathcal{W}(\nu_s, \nu_i, \tau_s, \tau_i)$  we can calculate  $\delta_{\text{TBP}}$  and obtain

$$\delta_{\text{TBP}} = \sqrt{\frac{n_{\text{pi}}^2 + n_{\text{ps}}^2}{n_{\text{si}}^2} + \frac{\gamma(L\sigma n_{\text{pi}}n_{\text{ps}})^2}{2(cn_{\text{si}})^2} + \frac{2c^2(1 + 4a^2\sigma^2)}{\gamma(L\sigma n_{\text{si}})^2}}. \quad (6.14)$$

With our current knowledge, we expect  $\delta_{\text{TBP}}$  to equal one for a TF decorrelated PDC. As soon as signal and idler become correlated, however, the conditioned TBP decreases and we consequently expect  $\delta_{\text{TBP}}$  to increase. We have studied this behaviour for two different cases: first, we consider the case of unchirped pump pulses with  $a = 0$ ; second, we investigate the case of chirped pump pulses with  $a = 3 \cdot 10^5 \text{ fs}^2$ . Typically, in an experiment the pump pulse passes several optical elements before the PDC, which are dispersive and thus chirp the pulse. Note that our value is comparably high and we have chosen it to emphasise the impact of a pump chirp on the TF correlations. Lower values of pump chirp decrease these effects, but do not completely suppress them.

As we aim for introducing  $\delta_{\text{TBP}}$  as a new TF entanglement measure, we have to compare it against existing quantities and have chosen the Schmidt number  $K$  as such. The latter can either be obtained from the experiment or from numerical calculations. Typically, one measures the JSI  $|F(\omega_s, \omega_i)|^2$  in the experiment [51, 53]. Thus, by analysing measurement results, one neglects any phase information of the original JSA. For assessing the impact of this, we compare both the Schmidt number from the JSI and JSA with  $\delta_{\text{TBP}}$ .

In Fig. 6.5 (a) we consider the case of Fourier-limited pump pulses. On the  $x$ -axis we plot the spectral bandwidth of the pump by which the TF correlations can be tuned. On the left  $y$ -axis



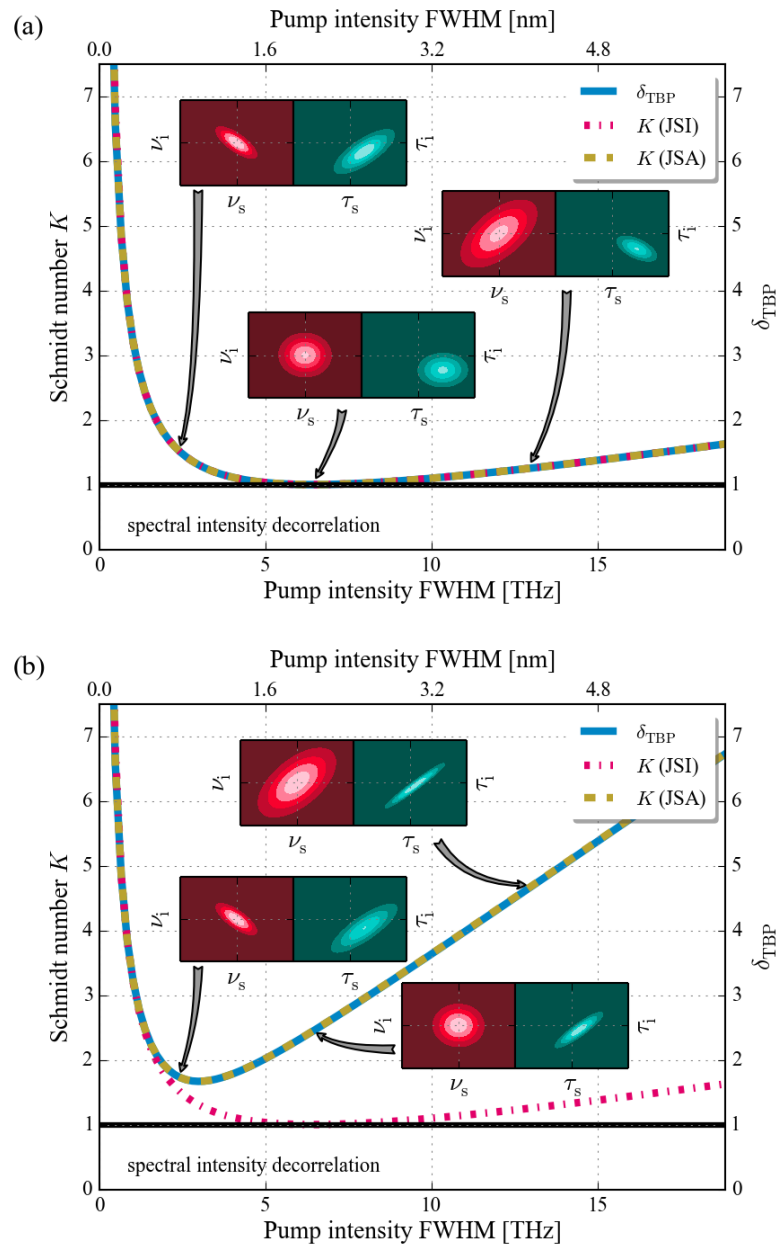


**Figure 6.5** – Comparison between the inverse conditioned TBP  $\delta_{\text{TBP}}$  and the Schmidt number  $K$  introduced in Chap. 5. In (a), the pump pulse is Fourier-limited, whereas in (b) it exhibits a frequency chirp with a chirp parameter of  $a = 3 \cdot 10^5 \text{ fs}^2$ . For more information see the text.



we indicate the Schmidt number  $K$  and on the right  $y$ -axis the value of  $\delta_{\text{TBP}}$ . The insets show the JSI (red) and the JTI (green) for three values of the spectral pump bandwidth that correspond to spectral anti-correlations, decorrelation and correlations. They were calculated from the chronocyclic Wigner function to reflect the information contained in our model (compare Fig. 6.3). The offset of the JTI functions from the centre of the diagram highlights the situation of asymmetric group-velocity matching in our PDC, where one photon travels faster than the pump whereas the other one is slower. The solid black line at  $K = 1$  is the boundary for spectrally decorrelated PDC and poses a lower limit to the Schmidt number.

Remarkably, the Schmidt numbers and  $\delta_{\text{TBP}}$  are exactly the same, even in their numerical values. We observe the expected behaviour of decreasing TF entanglement when approaching TF decorrelation and increasing entanglement beyond. Please note that – for Fourier limited pump pulses – frequency decorrelation is tantamount to temporal decorrelation.

The situation changes as soon as the pump pulses exhibit a non-vanishing chirp, as shown in Fig. 6.5 (b). First of all, the Schmidt number from the JSI does not fit to the other two quantities anymore. This is reasonable: a chirp of the pump pulse manifests itself in the phase of the JSA and thus its impact is lost when considering the JSI. Interestingly, the  $K$  number from the JSA and  $\delta_{\text{TBP}}$  are still equal. This shows that our model of the PDC TF structure which exploits the chronocyclic Wigner function formalism contains the complete information on the PDC. The next thing which becomes obvious is that the minimum value of  $\delta_{\text{TBP}}$  is above one, meaning that perfect TF decorrelation is not possible. Looking at the insets we find that, even for a spectrally decorrelated JSI,  $\tau_s$  and  $\tau_i$  are correlated as an effect of the pump chirp. Note that the minimal TF correlations are also shifted towards smaller pump bandwidths. This comes from the fact that spectral anti-correlations can partially compensate for temporal correlations induced by a chirp, as shown in the leftmost inset.

Why are these results important? When using PDC to generate heralded, pure single photons, perfect TF decorrelation is required. From our analysis we find that an engineered process without a pump chirp exhibits no hidden correlations in either the temporal or spectral degree of freedom. However, in general a characterisation of either the spectral or temporal intensity distribution of a PDC state – as is the common procedure [51, 53, 145] – is insufficient for revealing the TF correlations. Contrariwise, a spectral *and* temporal characterisation or a phase-sensitive analysis of either degree of freedom provide complete knowledge on the TF structure of a PDC. Although we have recently succeeded in implementing a direct, phase-sensitive measurement of the JSA of a PDC [129], a method based only on intensity measurements is still appealing because of its relative simplicity.

We have introduced a simple method to evaluate TF correlations in PDC. Measuring  $\delta_{\text{TBP}}$  allows for a complete reconstruction of the amount of TF entanglement, which makes it superior to the Schmidt number  $K$ , since the latter can be misleading. Hence, the next step along this line is the investigation of novel temporal detection methods which allow for a high temporal resolution in conjunction with single-photon sensitivity.

In addition, our analytical expression for the chronocyclic PDC Wigner function  $\mathcal{W}(\nu_s, \nu_i, \tau_s, \tau_i)$  provides a versatile analysis tool for most PDC processes and allows a quick assessment of the impact of different experimental settings on the generated photon pairs. Furthermore, the inverse TBP  $\delta_{\text{TBP}}$  as a novel TF entanglement measure bridges the gap between the seemingly



disparate TF and CV descriptions of PDC.

### Summary

We have introduced the four-dimensional chronocyclic representation of a PDC state, which unites concepts from continuous variable quantum optics and ultrafast physics. The resulting chronocyclic PDC Wigner function provides a complete description of the TF structure of a photon pair state. In addition, it allows to define a novel measure of TF entanglement - the normalised, inverse conditioned time-bandwidth product  $\delta_{\text{TBP}}$  - that behaves exactly the same as the Schmidt number  $K$  of the JSA, which can only be obtained with considerable experimental effort. This is not the case for our new measure, which accurately reflects the TF correlations between signal and idler even for unfavourable experimental settings but, on the downside, poses stringent requirements on the detector's temporal resolution.

## 6.3 On the correlation time of ultrafast biphotons

Following along our path to explore not only the spectral but also the temporal characteristics of PDC, we came across another important time-constant, the *correlation time*  $T_c$  of the photon pair, which essentially tells us, during which time span an idler will be detected after the detection of an associated signal. Note that the experiments presented here have been carried out by Vahid Ansari, in the course of this Master's thesis. The supervision of this thesis were part of our work.

Typically in the order of a few hundreds of femtoseconds, the correlation time is not only a measure of the simultaneity of the generated photons but also reflects the maximum timing information that can be extracted from a PDC state. It is therefore the benchmarking limitation to the achievable precision of quantum-enhanced applications such as quantum clock synchronisation [146, 147], quantum optical coherence tomography [148] and quantum interferometric optical lithography [149].

Still we find that the underlying physics of the correlation time are not yet fully understood. Naively one would think that  $T_c$  is directly influenced by the coherence properties of the pump light. This seems sensible under the assumption that the photon pair generation is an instantaneous process, hence signal and idler photon have to be generated inside the coherence length of the pump. We will show in the following, however, that the correlation time  $T_c$  is completely independent of the properties of the pump light. Indeed we will even present cases where  $T_c$  is larger than the pump's coherence time, which can be associated with a *loss of timing information* during the PDC process [150].

Unfortunately,  $T_c$  is typically a few hundreds of femtoseconds and thus cannot directly be measured with state-of-the-art detectors, which have timing jitters in the order of a few tens of picoseconds. This problem has first been circumvented by Hong, Ou and Mandel (HOM) in their seminal work in 1987 [29], where they succeeded in measuring sub-picosecond time intervals by exploiting quantum interference of single photons at a beamsplitter. They generated PDC photon pairs and sent the two photons into the two input ports of a balanced beamsplitter. In the following we briefly sketch what happens, if both photons are indistinguishable: the operators  $\hat{c}$



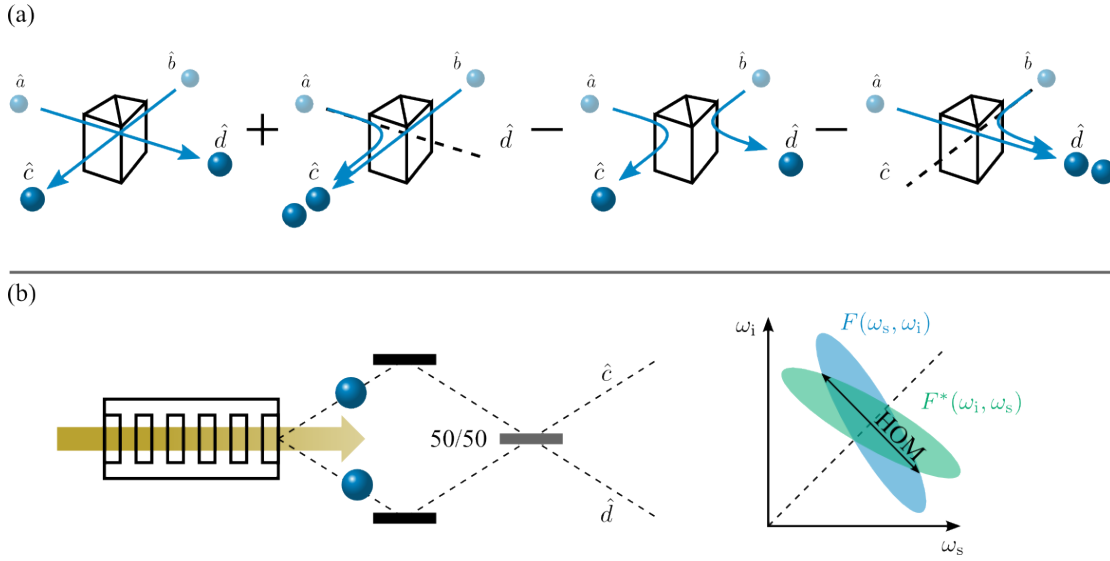


**Figure 6.6** – (a) Schematic of a HOM interference. If the two photons are indistinguishable, the two possible cases where one photon ends up in each output port cancel out and the photons bunch. (b) General setup for measuring HOM interference with a PDC source. Essentially, the interference measures the overlap of the JSA function under exchange of signal and idler, as sketched on the right.

and  $\hat{d}$  associated with the output ports of a balanced beamsplitter can be expressed in terms of the operators  $\hat{a}$  and  $\hat{b}$  at the input (see also Fig. 6.6).

$$\hat{c} = \frac{1}{\sqrt{2}} (\hat{a} + \hat{b}), \quad \hat{d} = \frac{1}{\sqrt{2}} (\hat{a} - \hat{b}). \quad (6.15)$$

Thus, the input state  $|\psi\rangle_{\text{in}} = \hat{a}^\dagger \hat{b}^\dagger |0\rangle$  is transformed into

$$|\psi\rangle_{\text{out}} = \frac{1}{2} (\hat{c}^\dagger + \hat{d}^\dagger) (\hat{c}^\dagger - \hat{d}^\dagger) |0\rangle = \frac{1}{2} ((\hat{c}^\dagger)^2 - (\hat{d}^\dagger)^2 - \hat{c}^\dagger \hat{d}^\dagger + \hat{d}^\dagger \hat{c}^\dagger) |0\rangle. \quad (6.16)$$

If the two photons in input ports  $a$  and  $b$  are indistinguishable in all degrees of freedom (spectral-temporal, spatial, polarisation), the last two terms in the above expression cancel out and we find the state

$$|\psi\rangle_{\text{out}} = \frac{1}{2} ((\hat{c}^\dagger)^2 - (\hat{d}^\dagger)^2) |0\rangle = \frac{1}{\sqrt{2}} (|2\rangle_c |0\rangle_d - |0\rangle_c |2\rangle_d) \quad (6.17)$$

at the output of the beamsplitter. This behaviour is called *bunching* and is a genuinely quantum behaviour since it is founded on the interference of quantum mechanical probability amplitudes [29].

From an experimental point of view this means that, for perfectly indistinguishable photons, we will not measure any coincidence events between the output ports of the beamsplitter. However, when introducing a temporal delay  $\tau$  between the two photons, we can gradually make



them distinguishable. In particular for the case of photons generated from PDC, the expected coincidence rate between the ports  $c$  and  $d$  as a function of time delay is given by [86]

$$R_c(\tau) \propto 1 - \int d\omega_1 d\omega_2 e^{i(\omega_1 - \omega_2)\tau} F(\omega_1, \omega_2) F^*(\omega_2, \omega_1). \quad (6.18)$$

Note that the drop in the expected coincidence rate is proportional to the symmetry of the JSA function under exchange of signal and idler [151], as sketched in Fig. 6.6. In contrast, the width of the interference pattern is given by the correlation time  $T_c$  of the photon pair, which is the average amount of time required to destroy the simultaneous arrival of the photons at the beam-splitter. Hence, the HOM interference provides an established means of probing the correlation time of a photon pair in the laboratory, even with insufficient detector timing resolution.

We have investigated the shape of the HOM interference dip analytically by deploying the JSA function from Eq. (6.6). Note that we have neglected the linear phase terms arising from the phasematching function, since they only impose an overall shift in the absolute timings of signal and idler. Using this, the coincidence rate  $R_c(\tau)$  can be written as

$$R_c(\tau) \propto 1 - \int d\nu_s d\nu_i e^{i(\nu_s - \nu_i)\tau} e^{-(A\nu_s^2 + A\nu_i^2 + B\nu_s\nu_i)}, \quad (6.19)$$

where we have defined the abbreviations

$$A = \frac{1}{\sigma^2} + \frac{\gamma L^2}{4c^2} (n_{ps}^2 + n_{pi}^2), \quad B = \frac{2}{\sigma^2} + \frac{\gamma L^2}{c^2} n_{ps} n_{pi}. \quad (6.20)$$

We recall that  $\sigma$  is the spectral pump bandwidth,  $L$  is the waveguide length and  $n_{ij} = n_i^{(g)} - n_j^{(g)}$  is the difference in group-refractive index. After some straightforward calculations we obtain

$$R_c(\tau) \propto 1 - \mathcal{A}(\sigma, L, n_{ps}, n_{pi}) \exp \left[ -\frac{\tau^2}{2 \cdot \frac{\gamma L^2 n_{si}^2}{4c^2}} \right]. \quad (6.21)$$

Here, the parameter  $\mathcal{A}$  depends on the pump as well as on the waveguide parameters and dictates the drop in coincidence rate, whereas the width of the exponential function given by  $\sigma_{\text{HOM}} = \frac{\sqrt{\gamma} L n_{si}}{2c}$  only depends on the waveguide parameters. In fact, we can reformulate this parameter and find

$$\sigma_{\text{HOM}} = \sqrt{\gamma} \frac{L}{2} \left( \frac{1}{v_s^{(g)}} - \frac{1}{v_i^{(g)}} \right), \quad (6.22)$$

where  $v_j^{(g)}$  labels the group velocities of signal and idler inside the waveguide. Finally, we can define the correlation time  $T_c$  as the FWHM of the HOM interference pattern and obtain

$$T_c = \sqrt{8\gamma \ln(2)} \frac{L}{2} \left( \frac{1}{v_s^{(g)}} - \frac{1}{v_i^{(g)}} \right). \quad (6.23)$$

This result facilitates an elegant and intuitive interpretation of the correlation time. Analysing a large ensemble of PDC processes, we find that the generation of a photon pair occurs most frequently at the centre of the waveguide. Then, the generated signal and idler propagate through



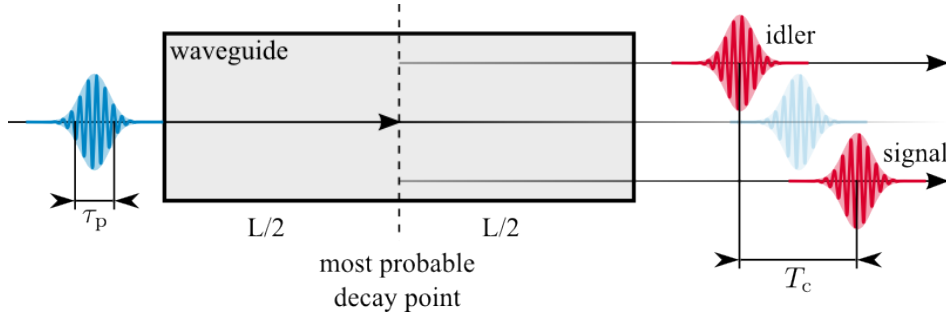


**Figure 6.7** – Illustration of the physics underlying the correlation time of PDC photon pairs. On average, the photons, sketched as red pulses, are generated at the centre of the waveguide and then propagate the remaining distance at their respective group velocities. The time difference they acquire at the output of the waveguide is referred to as *correlation time*  $T_c$ . Note that the coherence time of the pump (blue pulse)  $\tau_p$  does not affect  $T_c$ .

the remaining half of the waveguide at their respective group velocities and acquire an corresponding time difference, as illustrated in Fig. 6.7. In this picture, the decay happens instantaneous. If a pump photon passes the 'decay point' it can generate a photon pair, regardless of the coherence properties of the overall pump field.

However, we emphasise at this point that the PDC process of course happens coherently over the whole waveguide length, and the increased decay probability in the centre of the waveguide is a result of interference between pump, signal and idler. It is possible to calculate back to the 'decay point' from a measurement result, however only because the quantum mechanical measurement collapses the PDC wavefunction into a single result. Hence, it is not possible to predict the exact time and position of the next decay, as might come across from our interpretation.

To support our analytical solution, we have carried out full numerical studies of the HOM interference of photon pairs from generic PDC processes. The results are shown in Fig. 6.8. Note that we utilised a phasematching function with a positive slope, as is the case for our PDC source. However, our statements are general and valid for any PDC process.

In the left column, we plot the pump envelope function  $\alpha(\nu_s + \nu_i)$  (blue shaded region), the phasematching function  $\phi(\nu_s, \nu_i)$  (red shaded region) and the resulting modulus of the JSA function  $|F(\nu_s, \nu_i)|$  (black solid line). We have also indicated the values of the spectral pump width  $\sigma$  and the waveguide length  $L$  for each case. In the right column, you find the coincidence rate  $R_c(\tau)$  at the output of the beamsplitter, plotted against the time delay  $\tau$  between the signal and idler. The yellow shaded regions highlight the FWHMs of the interference dip, which correspond to the photon pair correlation time  $T_c$ .

In (a) to (c), we have kept the waveguide length constant and varied the spectral pump width. This is the typical situation that can easily be achieved in the laboratory. We find that although the shape of the JSA function changes significantly, the correlation time  $T_c$  is completely unaffected. Only the depth of the dip changes in agreement with Eq. (6.21). In contrast we assumed



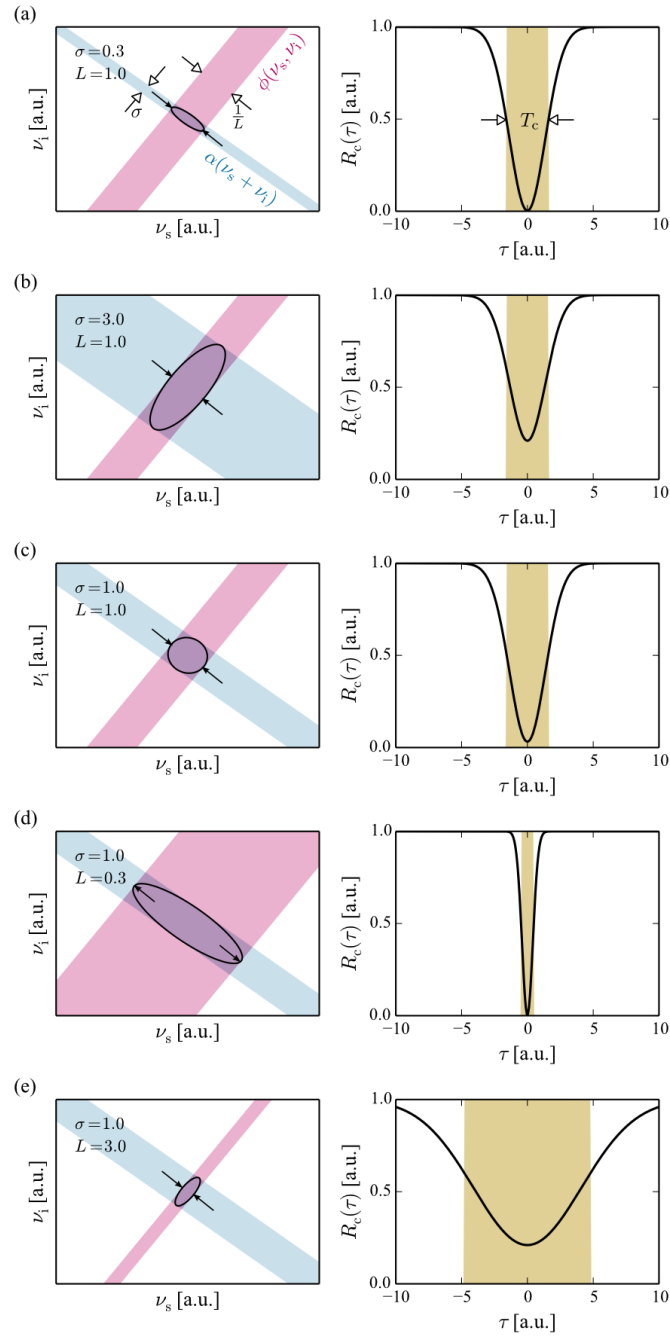


**Figure 6.8** – HOM interference dips for different generic PDC processes. In (a) to (c), the spectral pump width  $\sigma$  changes while the waveguide length  $L$  is kept constant. This does not affect the correlation time  $T_c$ . In (c) to (e) however, we vary  $L$  for a fixed  $\sigma$  and see a notable impact on  $T_c$ . For detailed information see the text.



a fixed pump width in (c) to (e) but simulated different waveguide lengths. This time, the correlation time strongly varies for different waveguide lengths. Again, this is according to our expectations.

We can understand this by noticing that an exchange between signal and idler (compare Eq. (6.18)) corresponds to mirroring the JSA along a  $+45^\circ$  axis, as sketched in Fig. 6.6. Then, the spectral width of the overlapping regions is along the  $-45^\circ$  line that is along the pump envelope function. Essentially, the HOM dip probes the width of the JSA along the axis given by  $\alpha(\nu_s + \nu_i)$ . We find that this width indicated by the black arrows does not change in (a) to (c), since a change in the pump shape only has an influence orthogonal to the  $-45^\circ$  axis. In contrast, in (c) to (e) this width does change due to different phasematching functions and we find a shorter correlation time for broader spectral widths and vice versa, in agreement with the Fourier relationship between time and frequency.

Also note that for the case of a similar amount of spectral correlations with opposing signs as for instance in panels (a) and (e), the timing information gained from the spectrally correlated state is worse than for the anti-correlated state. This has already been investigated theoretically and it has been shown that, while anti-correlated states are optimal for arrival time difference measurements as the HOM interference experiment, correlated states are apt for absolute timing measurements [146]. In addition, correlated states are highly beneficial for long-distance fiber-based quantum communication, because they do not suffer from spectral chirp. For more information on this see [152] and the citations therein.

## Summary

We have introduced the correlation time  $T_c$  of a PDC photon pair. We motivated that this quantity on the one hand measures the degree of simultaneity between the two photons and, on the other hand, is tantamount to the timing information that can be gained from the PDC state. In contrast to the common assumption that  $T_c$  must be related to the coherence properties of the pump, we have shown that in fact only the waveguide parameters define the correlation time. We presented an analytical and numerical study that supports our claim and facilitates a simple and efficient estimation of the temporal information in the PDC state for particular experimental settings.

## 6.4 Theory put to test

In the last section, we have studied the correlation time  $T_c$  of a PDC photon pair and found that it depends only on the parameters of the waveguide source, not on the properties of the PDC pump. In this section we present the experimental verification of our theory. To this end, we deployed the PDC source first published in [53] and later refined in [54].

A schematic of the experimental setup is shown in Fig. 6.9. An ultrafast Ti:Sapph oscillator (Coherent Chameleon Ultra II) generated Fourier-limited laser pulses at a central wavelength of  $\lambda_p = 768$  nm with a bandwidth of  $\Delta\lambda_{\text{Ti:Sapph}} \approx 5$  nm and a repetition rate of 80 MHz. The maximum output power of the laser was 3.5 W cw-equivalent power, which is equivalent to a maximum pulse energy of around 44 nJ. The laser light was attenuated with a combination of a half-wave plate (HWP) and a polarising beamsplitter (PBS), denoted as *power control* in the



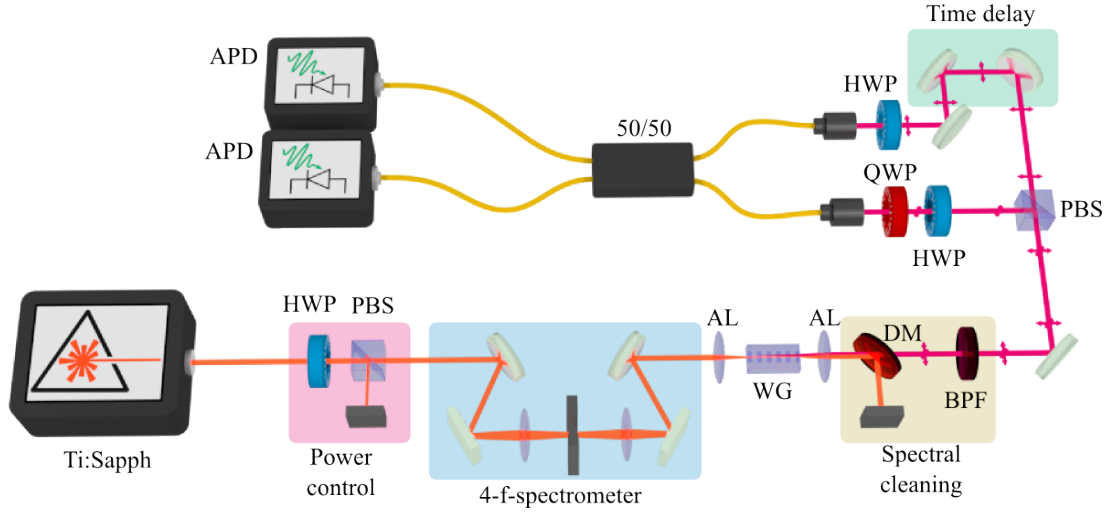


**Figure 6.9** – Experimental setup for the HOM measurements. Abbreviations: HWP - half-wave plate, PBS - polarising beamsplitter, AL - aspheric lens, WG - waveguide sample, DM - dichroic mirror, BPF - bandpass filter, QWP - quarter-wave plate, 50/50 - fiber integrated balanced beamsplitter, APD - avalanche photo diode. For more information see the text.

schematic. Then, the pulses were sent through a 4-f-spectrometer consisting of two gratings, two lenses and an adjustable slit in the centre. In agreement with the peculiar name, all elements are placed at a distance of the focal length  $f = 100$  mm of the lenses from each other. Note that the slit of the grating was rotated around the beam axis, which effectively implements a Gaussian reshaping of the pump spectrum (for more information see the appendix A.5). The maximum resolution of our spectrometer is around 0.5 nm, as measured with an optical spectrum analyser.

After spectral shaping, the pump pulses were coupled to the KTP waveguide (WG) sample (AdvR) with an aspheric lens (AL). The waveguide has a size of  $4 \times 6 \mu\text{m}^2$ , a length of  $L = 8$  mm and a poling period of  $\Lambda = 117 \mu\text{m}$ . Behind the WG, the remaining pump and generated PDC light were collimated with another AL. A dichroic longpass filter (DM, Semrock LP02-808RU-25) and a broad bandpass filter (BPF, Semrock NIR01-1535/3-25) with an effective bandwidth of 8 nm were used to filter the remaining pump light and the broad spectral background [153] from the PDC. The signal and idler photons were spatially separated at another PBS and a temporal delay was realised with a motorised linear translation stage (PI M-112). The generated photons were coupled to single mode fibers after their polarisation was adjusted with two HWPs and a quarter-wave plate (QWP).

Finally, the fibers were connected to a fiber-integrated balanced beamsplitter (50/50) to guarantee a maximum spatial overlap and the output ports of the beamsplitter were fed into two InGaAs avalanche photo diodes (NuCrypt CPDS-1000-4), the signals of which were analysed using a homebuilt field programmable gate array (FPGA). Note that for the measurements of the JSI distribution, we fed the fiber output ports into two fiber spectrometers [128] instead of



the 50/50 splitter and directly measured the coincidence counts.

The measured Klyshko efficiencies [154–156], that is the efficiencies with which a generated photon is also detected, are  $\eta_s = 20.5\%$  for the signal and  $\eta_i = 15.5\%$  for the idler, respectively [54]. They are calculated as the ratio of measured coincidences and single counts in the other arm as

$$\eta_{s/i} = \frac{R_{\text{coinc}}}{R_{i/s}}. \quad (6.24)$$

From these we can calculate back on the heralding efficiencies by factoring out the detector losses. We find heralding efficiencies of 80% (70%) into the single-mode fibers, which is among the highest values reported to date. This result highlights the excellent compatibility of our source with existing single-mode fiber communication networks. A detailed analysis of the performance benchmarks of the PDC source can be found in [54].

For measuring the HOM interference patterns, we concentrated on three scenarios corresponding to the cases (a) to (c) in Fig. 6.8, since we were not able to change the length of our sample. We measured the JSI distribution  $|F(\omega_s, \omega_i)|^2$  for three different types of spectral correlations, as well as the associated HOM interference dips. The measurement results are shown in Fig. 6.10.

The left column shows the measured JSI distributions, whereas the right column shows the associated HOM interference dips. Note that error bars are smaller than the symbol size. The yellow shaded regions reflect again the correlation time  $T_c$  of the generated photon pairs. Note that the JSIs are not background-corrected. In panel (a), we have chosen a spectral pump FWHM of 0.7 nm which yields a spectrally anti-correlated PDC. The correlation time of the photon pair evaluates to 1.10 ps. Note that the Gaussian fit to the measured interference pattern (grey line) does not fit to the data very well. This may have two reasons: first, the sinc-shape of the phasematching function enforces a triangular HOM interference pattern [157]; second, a misalignment of the pump incoupling can excite multiple spatial modes, which result in a distorted shape of the HOM interference [158]. We also fitted a triangular function to the measurement data, which yields a visibility of 92% and the same FWHM of 1.10 ps. This function fits better to the data in the central part of the dip, but has larger deviations in the wings, which leads us to the conclusion that an ideal fit is a mixture of Gaussian and triangular function. This most probably originates from the broadband spectral filter, which cuts away part of the sinc side lobes and thus leads to the peculiar shape of the dip.

In (b), we have adapted the pump bandwidth to the phasematching function to generate TF decorrelated PDC states. From our intensity measurement we obtain a Schmidt number of  $K \approx 1.0$ . Note that the excellent indistinguishability of signal and idler is reflected by the high visibility of the HOM interference of almost 95%. Still, the FWHM of the dip – and thus the correlation time  $T_c$  – is 1.16 ps. Finally, we have chosen the maximum pump bandwidth of 4.5 nm to generate spectrally correlated photon pairs. Note that for this measurement we removed the BPF from the setup as to not cut the signal and idler marginal distributions. This time the correlation time is evaluated to  $T_c = 1.21$  ps.

We have wrapped up the results of these measurements in Tab. 6.3, where we listed the measured correlation times  $T_c$ , the marginal bandwidths and durations of signal and idler  $\Delta\lambda_{s/i}$  and  $\Delta\tau_{s/i}$  as retrieved from the JSI distributions, the bandwidth and duration of the pump pulses



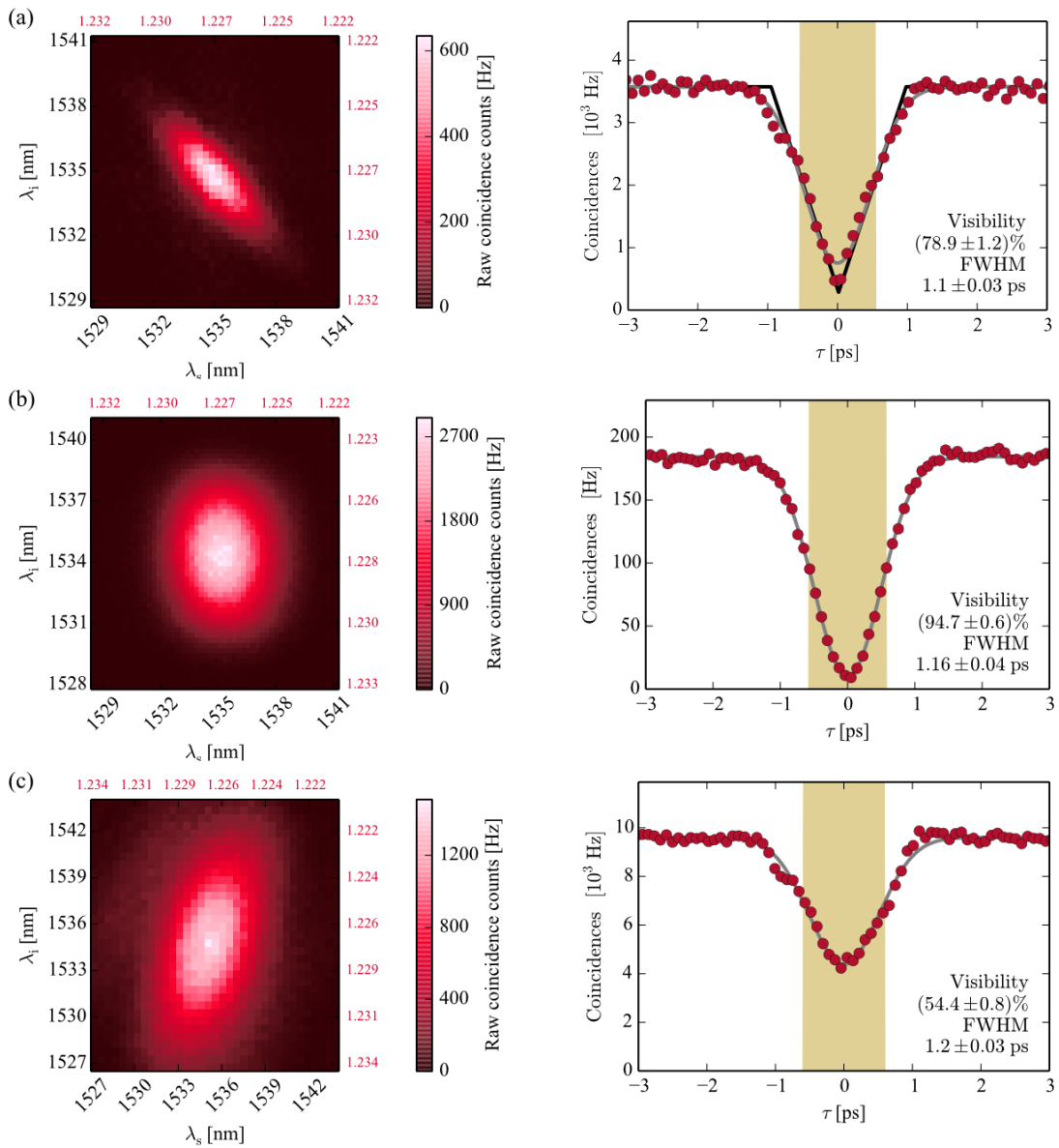


**Figure 6.10** – Measurement results of the HOM dip experiments. The left column shows the raw JSI distributions, the right column the associated HOM interference dips, where error bars are smaller than the symbols. From (a) to (c) we deployed an increasing pump bandwidth to realise the different spectral correlations. For more details see the text.



Correlations	$T_c$ [ps]	$\Delta\lambda_{s/i}$ [nm]	$\Delta\tau_{s/i}$ [ps]	$\Delta\lambda_p$ [nm]	$\Delta\tau_p$ [ps]	$\Delta\tau_{conv}$ [ps]
anti-correlated	$1.10 \pm 0.02$	3.06 / 3.12	1.13 / 1.11	0.7	1.24	1.58
decorrelated	$1.16 \pm 0.01$	4.30 / 5.46	0.80 / 0.63	2.0	0.43	1.02
correlated	$1.21 \pm 0.03$	5.84 / 10.1	0.59 / 0.34	4.5	0.19	0.68

**Table 6.3** – Summary of the measurement results of the HOM dip analysis. Shown are the correlation type, the measured correlation time  $T_c$ , the spectral marginal FWHM of signal and idler  $\Delta\lambda_{s/i}$  and their corresponding marginal durations  $\Delta\tau_{s/i}$ , the spectral bandwidth of the pump  $\Delta\lambda_p$  and its duration  $\Delta\tau_p$  as well as the convoluted duration of signal and idler marginal durations  $\Delta\tau_{conv} = \sqrt{\Delta\tau_s^2 + \Delta\tau_i^2}$ .

$\Delta\lambda_p$  and  $\Delta\tau_p$  and finally a convoluted duration  $\Delta\tau_{conv} = \sqrt{\Delta\tau_s^2 + \Delta\tau_i^2}$ . If we assumed that signal and idler were generated in Fourier-limited pulses – note that this corresponds to signal and idler being in pure states after heralding – the width of the HOM interference would simply correspond to  $\Delta\tau_{conv}$ .

First of all we compare the measured correlation time  $T_c$  to the theoretical value  $T_c^{(th)}$ , which we calculated with the analytical formula derived in the last section. We find  $T_c^{(th)} = 1.22$  ps, which is in excellent agreement with the measurement results given that we do not know the waveguide dispersion perfectly. Then, we want to point out that the pump duration changes about a factor of six without affecting  $T_c$ , as expected from our theory. Also we find a general agreement between  $T_c$  and  $\Delta\tau_{conv}$ . They are similar only for the case of decorrelated PDC, where we can safely assume that signal and idler are generated in Fourier-limited pulses. For the other cases,  $T_c$  and  $\Delta\tau_{conv}$  are clearly different, which can be understood such that the marginal durations are characteristics of traced out subsystems of the photon pair and thus do not contain the complete information.

Finally we want to point out that the correlation time  $T_c$  is larger than the pump pulse duration for the decorrelated and correlated case. We can define a measure for the *gain or loss of temporal information* by relating the correlation time to the pump duration. Obviously, temporal information can only be gained in the case of long pump pulses, corresponding to the situation in the original HOM paper [29]. In other cases, a direct use of the ultrafast pulses for temporal measurements is more beneficial than utilising PDC.



## Summary

We have presented our experimental results which verify our theory on the correlation time of PDC photon pairs. We measured the HOM interference between signal and idler for different coherence times of the pump pulses and found that indeed the pump duration does not influence  $T_c$ , which is in excellent agreement with the theoretically obtained value. In addition, our measurements show that the correlation time cannot simply be reconstructed from measurements on the two subsystems of the PDC state. Instead, a full two-dimensional characterisation is required for retrieving the photon pair characteristics.



It doesn't matter how beautiful your theory is, it doesn't matter how smart you are. If it doesn't agree with experiment, it's wrong.

Richard P. Feynman

# 7

---

## Quantum pulse gate and quantum pulse shaper

---

### Contents

7.1 Quantum pulse gate . . . . .	83
7.2 Quantitative Hamiltonian. . . . .	92
7.3 Experiment. . . . .	94
7.4 Next steps: Quantum pulse shaper. . . . .	107

This chapter is dedicated to the main part of this thesis: The thorough investigation of the two novel devices *quantum pulse gate* (QPG) and the *quantum pulse shaper* (QPS). Both devices are based on dispersion engineered frequency conversion (FC) processes and facilitate a quantum coherent operation on the time-frequency (TF)

modes of ultrafast quantum states. The driving idea behind researching these devices is the vision of future high-dimensional quantum information applications based on TF modes.

This is an interesting topic already from a fundamental point of view. In a large Hilbert space it becomes possible to study, for instance, high-dimensional entanglement [159]. Moreover, there are practical implications. High-dimensional quantum states facilitate a step beyond common two-dimensional encoding of quantum information in qubits. *Qudit* encoding becomes possible, which provably increases the security of quantum communication protocols as well as the amount of information per photon [92, 93]. Seeing things from a slightly different angle, multiple TF modes could also be exploited in conjunction with common qubit encoding to serve as orthogonal channels for information multiplexing. It has been shown that an exponential increase in quantum channel capacity is in reach with this approach [160]. This point is particularly interesting in light of recent research on the information capacity of fiber networks. In [161], the authors have shown that current single-mode communication networks are close to their intrinsic maximum capacity. A possible way out of this dilemma could be energy-efficient channel multiplexing.

Although spatial multiplexing is suggested in [162], TF mode multiplexing could play a central role in future communication scenarios as well, if three prerequisites can be fulfilled: first, TF modes have to be generated in a well-defined way; second, there must be a possibility to coherently manipulate them; third, mode-selective detection schemes must exist. Concerning points one and three, we have shown in Chap. 5 how parametric down-conversion (PDC) can be tailored to generate specific TF modes and first results on a TF mode-selective detection of up

to eight modes have been already reported in literature [59]. The QPG and QPS tackle the remaining obstacle of TF mode manipulation. But before we come to this, we want to give a brief overview over the current state-of-the-art in high-dimensional photonic quantum information and quantum FC.

To date, the majority of experiments on high-dimensional quantum information encode the information in the spatial degree of freedom, most prominently in the orbital angular momentum (OAM) of photons. Impressive results have been achieved in recent years, most notably on the fundamental entanglement of OAM states prepared with PDC [113, 115–117, 163] and on the increased information capacity of high-dimensional communication systems [94, 164, 165]. Naturally, this progress has been accompanied by theoretical work on the generation [123] and experimental manipulation [125, 166] of OAM states. We emphasise that manipulation of OAM states can be conveniently implemented with linear optical elements like spatial light modulators. However, OAM states have a major disadvantage when it comes to real-world applications. They are inherently incompatible with existing and well-developed single-mode fiber communication networks and few-mode or multimode fibers have to be deployed instead.

Turning our attention towards quantum FC, we find that it has been around for almost 25 years. In 1990, Prem Kumar suggested deploying FC to exchange the quantum state of two light beams [45]. Although squeezed states were beneficial for interferometry and precision measurements such as spectroscopy, they could not readily be deployed for all measurements because there were no frequency tuneable sources available. FC provided a solution to this problem, since it allows for a frequency translation of a quantum state without affecting its other characteristics. Thereafter, in 1992, the theoretical proposal was implemented in the laboratory [46]. In their work, the authors monitored the intensity correlations of a pulsed EPR source directly at the source output and after translating one beam to a different frequency and succeeded in monitoring correlations in both cases.

In 2003 it was shown that FC is a so-called *information-preserving* unitary operation which realises a FC of optical quantum superposition states, or qubits [167]. Also during that time, people began to investigate FC in light of implementing efficient single-photon detectors for telecommunication wavelengths. A lot of successful implementations of upconversion detectors which overcome the efficiency limitations of common InGaAs single-photon detectors have been reported since [168–174].

Another aspect of FC was highlighted in [175], where the possibility to bridge the energy gap between flying qubits and stationary quantum memories in a quantum information network was addressed. Again, the successful conversion of a qubit was demonstrated. This time, a fidelity of 98% could be realised. Thinking further along the lines of possible applications in quantum networks, a polarisation independent FC was implemented in [176], conversion efficiencies of 99% for attenuated coherent pulses have been shown [96], FC has been exploited to erase frequency distinguishability of photons [177] and single photons from a quantum dot have successfully been converted [178]. Moreover, even entanglement-conserving FC was demonstrated [179]. At some point, the inverse process of frequency down-conversion of single photons also came to the focus of interest and comparable results to the up-conversion experiments have been published [180–182].

Early in the work on this thesis, our group worked on combining dispersion and state engineering techniques known from ultrafast PDC [48, 49] with FC processes. Until then, FC had



never been studied in conjunction with ultrafast pump pulses or really broad spectra. We have presented the results of these early investigations in Chap. 5. Ultrafast FC can be described as a series of special quantum mechanical beamsplitters that operate on TF modes of quantum states. The group of Michael Raymer was thinking along the same lines and published their results on the '*Interference of two photons of different color*' in [62]. Later that year, they demonstrated the frequency translation of single photons in a FC based on four-wave mixing in photonic crystal fiber [183].

2011 finally was a bright year for engineered, ultrafast quantum FC. In parallel to an in depth theoretical study on four-wave mixing FC which took into account the broadband TF nature of the process [68] and a proposal to deploy FC for pulse shaping of quantum light [184], we brought forward our proposals to implement two novel devices, the QPG and QPS, based on three-wave mixing [60, 61]. In these publications we merged the knowledge on engineering of PDC present in our group with the exciting possibility to actually manipulate the intricate TF mode structure of ultrafast quantum states. Further studies from our side [76] and from Michael Raymer's group [64, 65] have highlighted possible pitfalls for the performance of our devices (compare Sec. 5.4), but have shown that the most promising approach to TF mode-selective operation in a single device is presented by the QPG and QPS instead of other proposed schemes [185]. Note that recent results suggest overcoming time-ordering issues by deploying two successive devices [186], which is an additional experimental difficulty that might be omitted, depending on the exact requirements of the experiment.

In the following, we will introduce the QPG in detail. Thereafter we present a quantitative estimate of the efficiency of our implemented QPG. Then, we focus on the experimental realisation of the QPG and present our measurement results which demonstrate a successful QPG operation. We conclude this chapter by giving an outlook on the QPS, a device which originates from a different treatment of the QPG theory.

## 7.1 Quantum pulse gate

Both of our devices are based on waveguided FC. The QPG, which facilitates the selection of a specific TF mode which can then be singled out from an ensemble is based on sum-frequency generation. Note, however, that only the group-velocity matching inside the deployed waveguide is important. In principle, we could as well implement a QPG based on difference-frequency generation. The QPG allows for the implementation of a drop filter for high-dimensional TF mode networks, as we will show in the following.

### 7.1.1 The QPG unitary operation

Essentially, the QPG implements the process discussed in Fig. 5.12, that is a TF single mode FC process which acts as a special quantum mechanical beamsplitter that operates only on one single TF pulse shape. We deploy asymmetric group-velocity matching, where the input pulse and the bright pump pulse travel at the same velocity. Then, we can switch the selected input mode by shaping the bright pump pulses. This situation is illustrated in Fig. 7.1. One TF mode from a set of input modes  $g_{\text{in}}(\omega_{\text{in}})$  is selected and *converted* into the output mode



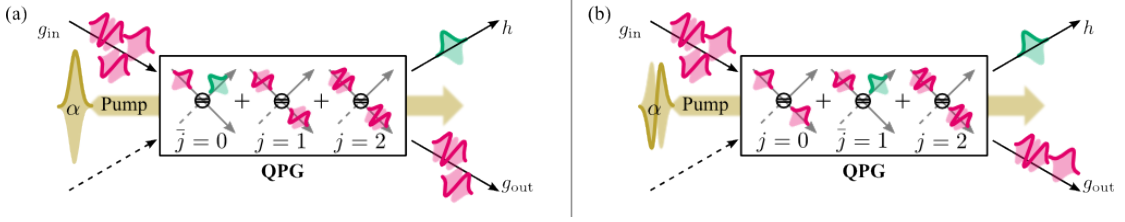


**Figure 7.1** – Illustration of the QPG operation. One mode from the input mode basis  $g_{\text{in}}$  is selected and converted into the output mode  $h$ . All other modes are transmitted and labeled as  $g_{\text{out}}$ . The selected mode is chosen by shaping of the pump envelope function  $\alpha(\omega_p)$ . In essence, the QPG can be regarded as a drop filter.

$h(\omega_{\text{out}})$  with, in principle, unit efficiency. All other modes are simply transmitted and are labeled with  $g_{\text{out}}(\omega_{\text{out}})$ . The inside of the box shows the special beamsplitters corresponding to different mode orders  $j$ . The shape of the selected mode is defined by the TF shape of the pump envelope function  $\alpha(\omega_p)$ , whereas the shape of the converted mode  $h(\omega_{\text{out}})$  is defined by the waveguide dispersion, respectively. In (a), we show the situation for a Gaussian shaped pump pulse, whereas in (b) we consider a first-order Hermite-Gaussian pump. Note that this behaviour corresponds to the action of a drop filter in a TF mode network.

Let us put these statements onto more formal footing. We have seen that we can write the unitary SFG operation in the TF framework as (compare Eq. (5.51))

$$\hat{U}_{\text{SFG}} = \bigotimes_{j;k,l,m} \exp \left[ \mathcal{C}_{j,klm} \hat{A}_{j,klm} \hat{C}_{j,klm}^\dagger + \text{h.c.} \right], \quad (7.1)$$

where the broadband mode operators  $\hat{A}_{j,klm}$  and  $\hat{C}_{j,klm}^\dagger$  describe the annihilation of a photon from input mode  $g_{j,klm}(\omega_{\text{in}})$  and the creation of a photon in output mode  $h_{j,klm}(\omega_{\text{out}})$ , respectively. The efficiency of this operation is given by  $\sin^2(\mathcal{C}_{j,klm})$ . Again, for the sake of simplicity, we assume that all fields propagate in the fundamental spatial mode and omit the spatial mode indices  $k, l$  and  $m$ .

The QPG is defined as a TF single-mode SFG process, for which only one coupling constant  $\mathcal{C}_j$  is unequal to zero. Using this additional information we write the QPG unitary as

$$\hat{U}_{\text{QPG}} = \exp \left[ \mathcal{C}_j \hat{A}_j \hat{C}_j^\dagger + \text{h.c.} \right] \quad (7.2)$$

Here, the index  $j$  highlights that we can still choose between different selected modes, by shaping the bright pump pulses, since the QPG input TF mode  $g_j(\omega_{\text{in}})$  is directly defined by the TF shape of the pump. However, regardless of the choice of  $j$ , the output is always generated in the mode  $h(\omega_{\text{out}})$ , associated with  $\hat{C}_j^\dagger$ .



## 7.1.2 Adding an input state

To this point we have not made any assumptions on the QPG input state  $|\psi\rangle_{\text{in}}$ . The unitary QPG operation is completely defined by the bright pump and the waveguide dispersion. In this section, we assume a TF multimode coherent state at the input of the QPG (compare Fig. 7.1) and derive the output state  $|\psi\rangle_{\text{out}}$ . The choice of the input state is convenient, because coherent states are well understood and can easily be generated in the laboratory.

A broadband coherent state with mean photon number  $\langle \hat{n} \rangle = |\alpha|^2$ , where  $\alpha$  is the coherent state amplitude, is given by

$$|\alpha\rangle_n = \exp \left[ \alpha_n \hat{B}_n^\dagger - \alpha_n^* \hat{B}_n \right] |0\rangle. \quad (7.3)$$

Here,  $\hat{B}_n^\dagger = \int d\omega \mathcal{G}_n(\omega) \hat{b}^\dagger(\omega)$  is a broadband creation operator, which generates one photon in the TF mode  $\mathcal{G}_n(\omega)$ .

In general, the TF mode  $\mathcal{G}_n(\omega)$  can have an arbitrary shape. However, in the scope of this thesis, we restrict ourselves to the Hermite-Gaussian framework<sup>22</sup>, where

$$\mathcal{G}_n(\omega) = \frac{1}{\sqrt{n!} \sqrt{\pi} 2^n \sigma} H_n \left( \frac{\omega - \omega_0}{\sigma} \right) \exp \left[ -\frac{(\omega - \omega_0)^2}{2\sigma^2} \right]. \quad (7.4)$$

In this expression,  $H_n(x)$  is the  $n$ -th order Hermite polynomial,  $\omega_0$  is the central frequency and  $\sigma$  is the spectral width of the TF mode. With this, we define our input state  $|\psi\rangle_{\text{in}}$

$$|\psi\rangle_{\text{in}} = \bigotimes_{n=0}^N \exp \left[ \alpha \hat{B}_n^\dagger - \alpha^* \hat{B}_n \right] |0\rangle, \quad (7.5)$$

where we assume the same central frequency, spectral bandwidth and coherent state amplitude for all  $|\alpha\rangle_n$ .

To assess the action of the QPG on this input state, we expand  $\hat{B}_n^\dagger$  in the QPG input mode basis  $\{\hat{A}_j^\dagger\}$  such that

$$\hat{B}_n^\dagger = \sum_{k=0}^{\infty} \xi_{nk} \hat{A}_k^\dagger. \quad (7.6)$$

Here, the overlap factors

$$\xi_{nk} = \left| \int d\omega \mathcal{G}_n(\omega) g_k^*(\omega) \right| \quad (7.7)$$

describe the overlap between the  $n$ th TF mode of the input and the  $k$ th QPG TF mode. Note that we can directly retrieve these overlap factors from our measurements, as we show in the following.

Now, we apply the QPG beamsplitter transformation which maps input TF modes to output TF modes and find

$$\sum_{k=0}^{\infty} \xi_{nk} \hat{A}_k^\dagger \rightarrow \sum_{k=0}^{\infty} \xi_{nk} \left( \cos(\mathcal{C}_k) \hat{A}_k^\dagger + \sin(\mathcal{C}_k) \hat{C}^\dagger \right). \quad (7.8)$$

<sup>22</sup>Note that the Hermite-Gaussian states form a complete basis. As such, every other state can be expressed using Hermite-Gaussian states.



Using the condition that  $\mathcal{C}_k = 0$  for  $k \neq j$ , we rewrite

$$\hat{B}_n^\dagger \rightarrow \xi_{nj} \left( \cos(\mathcal{C}_j) \hat{A}_j^\dagger + \sin(\mathcal{C}_j) \hat{C}_j^\dagger \right) + \sum_{k \neq j} \xi_{nk} \hat{A}_k^\dagger \quad (7.9)$$

and consequently obtain the QPG output state

$$|\psi\rangle_{\text{out}} = \bigotimes_{n=0}^N \exp \left[ \alpha \xi_{nj} \cos(\mathcal{C}_j) \hat{A}_j^\dagger + \alpha \xi_{nj} \sin(\mathcal{C}_j) \hat{C}_j^\dagger + \sum_{k \neq j} \xi_{nk} \hat{A}_k^\dagger + \text{h.c.} \right] |0\rangle. \quad (7.10)$$

First of all we note that this state is still a tensor product of coherent states, as expected from a *simple* beamsplitter operation. We have coloured the converted part which is centred at  $\omega_{\text{out}}$  in blue. We see that the complete input state can be converted, if  $\xi_{nj} = 1$ , that is if the input mode  $\mathcal{G}_n(\omega)$  overlaps perfectly with the QPG TF mode  $g(\omega)$ . Otherwise, part of the input state is transmitted. This provides us with a handy tool: measuring the converted output intensity for different known input states, we can reconstruct the overlap factor  $\xi_{nj}$ , and thus gain access to the QPG TF mode  $g_j(\omega)$ .

### 7.1.3 Revealing the QPG TF structure

In this section we discuss, how the TF mode structure of the QPG can be uncovered. The idea behind this method has been presented in 2008 in [187]: a phase space tomography of an arbitrary quantum process can be realised when evaluating the action of the process on coherent probe states. Let us be more specific about this. In general, a quantum optical process is described by a unitary matrix. A quantum process tomography facilitates the reconstruction of the magnitude and phase of each matrix entry. To this end, the process is probed with a complete set of basis states and the respective results are evaluated. Notably, these basis states need not be non-classical, but can be coherent states, which are conveniently generated as the output states of lasers. Different basis states are realised by coherent states with different amplitudes and phases.

A similar approach works for the QPG. The process matrix of the QPG is the JSA function  $G_{klm}(\omega_{\text{in}}, \omega_{\text{out}})$ . Again, a process tomography facilitates the reconstruction of both, magnitude and phase, of this matrix. As in the original paper [187], we deploy coherent states as basis states for probing the QPG. Although the theoretical QPG description focusses on single photons, it is in no way limited to low photon numbers. Thus, we have chosen the most simplistic probe states: coherent states.

In contrast to phase space tomography, which focusses on photon number properties, we want to investigate the spectral-temporal structure of the QPG. Hence, the amplitude of the probe states does not matter, but we realise different basis states with different central frequencies. Then, by measuring the *intensity* of the converted light for a fixed pump power and thus a fixed coupling constant  $\mathcal{C}_j$ , we retrieve the TF overlap factor  $\xi_{nj}$ , which allows for a reconstruction of the QPG input TF mode  $g_j(\lambda_{\text{in}})$ . Note that, although we measure an intensity, our method is intrinsically phase-sensitive, as can be seen from the mathematical expression of  $\xi_{nj}$ , which incorporates the complex-valued TF modes.



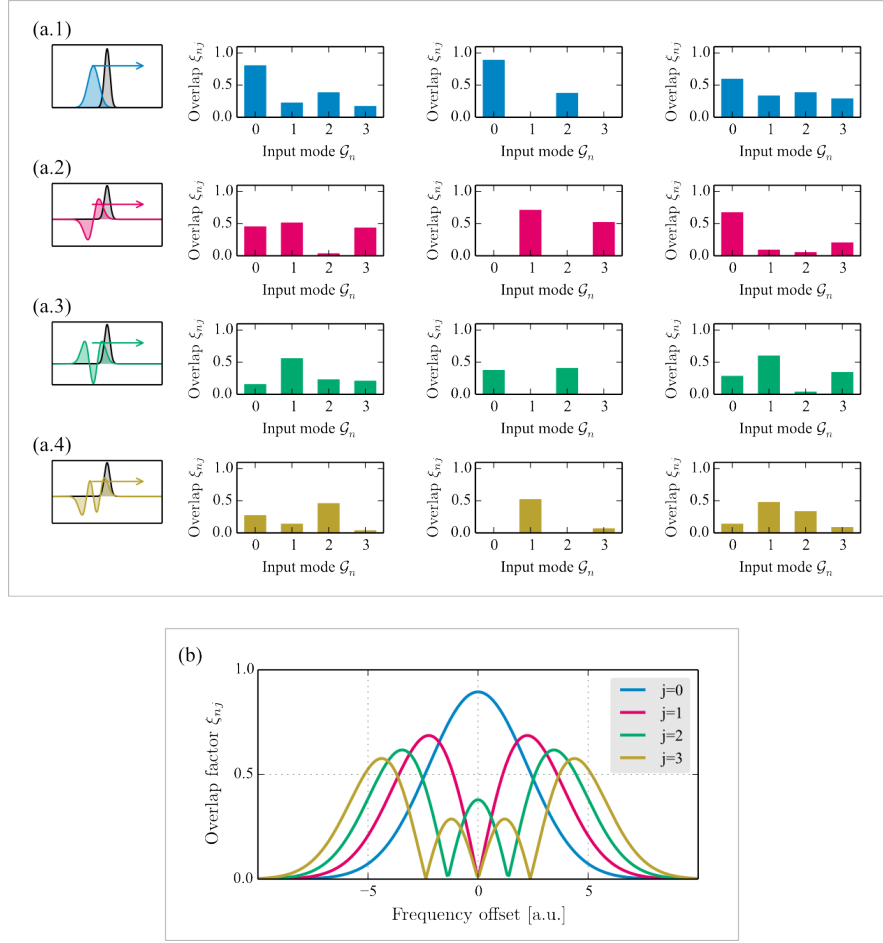


**Figure 7.2** – Overlap factors  $\xi_{nj}$  between the QPG TF mode  $g_j(\omega)$  and probe state TF modes  $\mathcal{G}_n(\omega)$  for  $n = 0 \dots 3$  and different central frequencies. For more information see the text.

We sketch this approach with an example, which reflects the situation we will find again in the measurements presented later in this chapter. We assume that neither the central frequency nor the spectral bandwidth of the QPG TF mode  $g_j(\omega)$  or the input modes  $\mathcal{G}_n(\omega)$  is fully known. This is a reasonable assumption for any experimental implementation of a QPG, and we will show in the following a two-step procedure to reliably adapt the QPG TF structure to the input state. As input state, we assume a tensor product of coherent states in the first four Hermite-Gaussian modes, that is

$$|\psi\rangle_{\text{in}} = \bigotimes_{n=0}^3 \exp \left[ \alpha \hat{B}_n^\dagger - \alpha^* \hat{B} \right] |0\rangle, \quad (7.11)$$

where we assumed the same coherent state amplitude for all four orders  $n = 0 \dots 3$ .

In Fig. 7.2 (a), we evaluate the overlap coefficient  $\xi_{nj}$ , which defines the efficiency of the

QPG. In (a.1), we assume the QPG TF mode  $g_j(\omega)$  to be a fundamental Gaussian, that is  $j = 0$ , with a spectral bandwidth that is double the bandwidth of the input TF modes  $\mathcal{G}_n(\omega)$ . This is sketched in the leftmost plot, where  $g_j(\omega)$ , represented by the blue curve, is scanned over  $\mathcal{G}_n(\omega)$ , shown as the black Gaussian.

The bar plots show the overlap coefficients  $\xi_{nj}$  for the four different input TF modes. From left to right, the QPG TF mode's central frequency is smaller than, equal to and larger than the input mode's, respectively. For the two cases of a non-adapted central frequency (left and right), we see that all four overlap factors are greater than zero. This means that mode-selective operation is not possible in these configurations, and hence they are undesirable for the implementation of a genuine QPG.

In contrast, the centre bar plot shows the situation for an adapted central frequency. We see that the overlap between the QPG TF mode and 1<sup>st</sup> and 3<sup>rd</sup> input TF modes vanishes. This happens due to the characteristics of Hermite-Gaussian modes. If two Hermite-Gaussian modes with different parities have the same central frequency, their overlap vanishes, regardless of their respective spectral bandwidths. Since the QPG TF mode in this case has an order of  $j = 0$ , the overlap to the odd-order input modes is zero. Note that the overlap between the QPG TF mode and the input Gaussian with  $n = 0$  does not equal one, due to their different spectral bandwidths.

In Fig. 7.2 (b), we study the situation for a different QPG with a QPG TF mode  $g_j(\omega)$ , which is given by a first-order Hermite-Gaussian, that is  $j = 1$ . Again, in the leftmost plot, the QPG TF mode is the coloured curve, whereas the input is symbolised by the black Gaussian.

In this case we see that the relative weights of the overlap factors have changed in comparison to case (a). This is reasonable, since we evaluate the overlap between different functions here. However, we find the same qualitative behaviour. Non-adapted central frequencies suppress mode-selective behaviour. For similar central frequencies (central bar plot), we find a vanishing overlap between  $g_j(\omega)$  and the even-order input modes, in agreement to the reasoning before.

For a better agreement with the measurements, we also plotted the case for a QPG with a second-order Hermite-Gaussian mode  $g_j(\omega)$  in (c) and for a QPG with a third-order Hermite-Gaussian mode in (d), respectively. As expected, we retrieve a similar behaviour to the cases (a) and (b). For adapted central frequencies, the overlap to modes with a different parity vanishes.

Note that in Fig. 7.2 (d), the overlap for an adapted central frequency is largest between the QPG TF mode  $g_j(\omega)$  and the input mode  $\mathcal{G}_n(\omega)$  with  $n = 1$ . Ideally, we would expect the largest overlap with the third-order input mode. Due to the non-adapted spectral bandwidths, however, we do not recover this situation here.

In our measurements, we utilised only a single input state with a Gaussian TF mode. This situation corresponds to the leftmost bars in each plot and we study it in more detail in Fig. 7.2 (b). Here, we plot the overlap factor  $\xi_{nj}$  between a Gaussian input  $\mathcal{G}_n(\omega)$  and the QPG TF modes  $g_j(\omega)$  from above for different frequency offsets between the respective modes. The colour-coding is the same as in (a).

Note how the  $\xi_{nj}$  follow the shape of the QPG TF mode for the different mode orders. From this plot we find two criteria for an ideally matched central frequency: first, the overlap between the fundamental QPG mode and the input mode is largest for zero frequency offset; second, the overlap between the QPG TF mode and the input mode vanishes for modes of different parities.

These results are a valuable information for the experiments, because they facilitate an adaptation of the QPG central frequency to an *unknown* input state, given that the input state resides



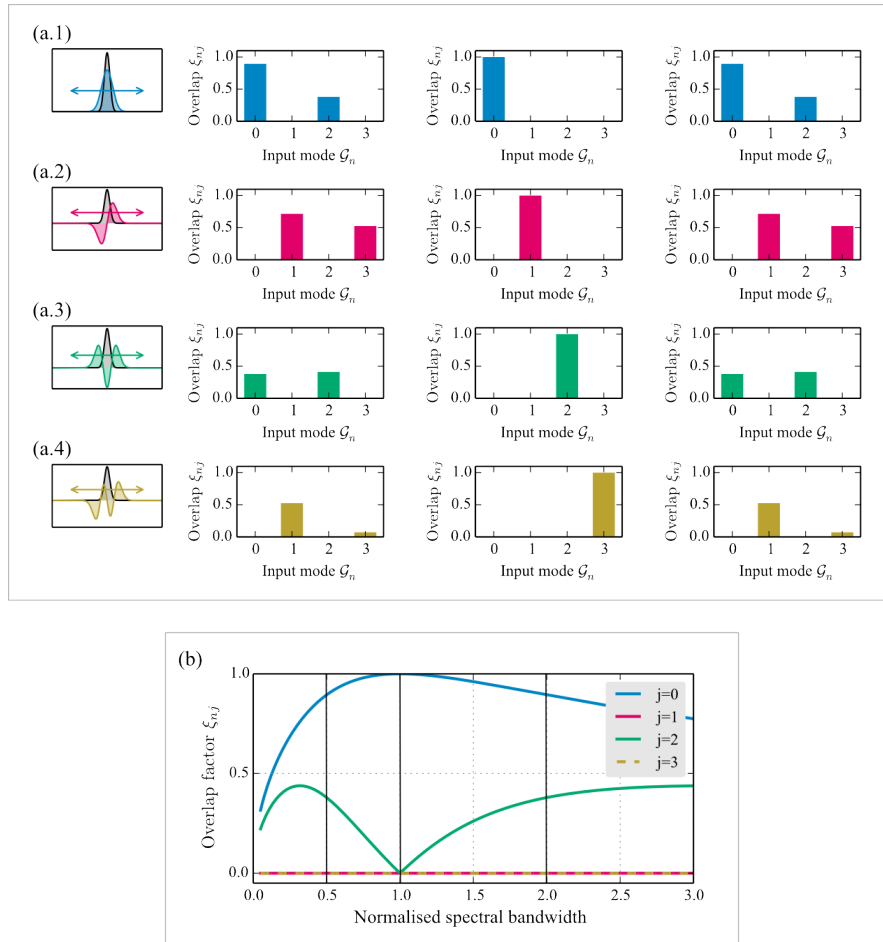


**Figure 7.3** – Overlap factors  $\xi_{nj}$ , evaluated for QPGs with adapted central frequency, but spectral bandwidths that differ from the input state width. For more information see the text.

in the Hermite-Gaussian mode basis. In addition they highlight, that probing the QPG with coherent states suffices to recover the QPG TF modes  $g_j(\omega)$ . Also note that it does not matter whether we use different coherent probe states and only one QPG, or the other way round. For our experiment, we decided to realise many different QPGs and probe them with one state, because of experimental simplicity.

#### 7.1.4 Optimising the QPG TF modes

Having analysed a way to adapt the central frequency of the QPG to an input state, we now turn our attention towards optimising the spectral bandwidth of the QPG TF modes  $g_j(\omega)$ .

In Fig. 7.3, we evaluate the overlap factors for the same input state as before, that is a superposition of coherent states in the first four Hermite-Gaussian modes and QPGs with TF



modes  $g_j(\omega)$  with  $j = 0 \dots 3$ . However, now we assume that the central frequency of the QPG TF mode is already adapted and change the spectral bandwidth of the QPG.

In Fig. 7.3 (a), we assume a Gaussian QPG TF mode  $g_j(\omega)$ , which is represented in the leftmost plot by the blue curve, whereas the black Gaussian symbolises again the input state's TF modes  $\mathcal{G}_n(\omega)$ . The arrow hints at the fact that now we analyse different bandwidths.

In the bar plots, we plot again the overlap factors  $\xi_{nj}$  between the QPG TF mode  $g_j(\omega)$  and the input TF modes  $\mathcal{G}_n(\omega)$ . From left to right we assume a QPG mode spectral bandwidth that is half the input width, the same as the input width and double the input width, respectively. For a non-adapted spectral bandwidth, we find a situation which we have already discussed in detail for Fig. 7.2. The QPG TF mode has a non-vanishing overlap to all input modes with the same parity. However, for an adapted QPG spectral bandwidth (central bar plot), we find mode-selective behaviour. Only a single mode of the input overlaps with the QPG TF mode. This mode is selected and can be converted with unit efficiency.

In Fig. 7.3 (b), we switched the QPG TF mode  $g_j(\omega)$  to a first-order Hermite-Gaussian, as sketched by the red curve in the left plot. From the bar plots we see again, that mode-selective behaviour is achieved for an adapted bandwidth. In this configuration, however, we find that the input mode  $\mathcal{G}_n(\omega)$  with  $n = 1$  overlaps with the QPG TF mode. Hence, a change in the QPG TF mode really selects a different mode from the input state.

As before, we have further considered a second- and third-order Hermite-Gaussian QPG TF mode  $g_j(\omega)$  in (c) and (d), respectively. The qualitative behaviour stays the same. For an adapted bandwidth, the QPG TF mode defines the selected input mode, as can be seen by the respective overlap coefficients  $\xi_{nj}$ , which are one for  $n = j$ .

In (b), we investigate again the situation for our measurements in more detail. The input TF mode is a Gaussian and we evaluate the  $\xi_{nj}$  for the QPG TF modes from (a). On the  $x$ -axis, we plot the spectral bandwidth of the QPG normalised to the bandwidth of the input. The solid black lines at  $x = 0.5$ ,  $x = 1.0$  and  $x = 2.0$ , respectively, correspond to the bar plots in (a) from left to right.

As expected, the overlap between the even input mode with  $n = 0$  and the odd-order QPG TF modes with  $j = 1$  and  $j = 3$  constantly vanishes, regardless of the spectral bandwidth. However, for the second-order mode, the overlap increases first, then decreases to zero and increases again for larger QPG bandwidths. This behaviour is also found in the measurements, as we will show later. It facilitates the optimisation of the QPG spectral bandwidth with respect to an *unknown* input state.

### 7.1.5 Experimental limitations

In the last two sections, we have discussed the expected behaviour of the QPG for the ideal QPG unitary

$$\hat{U}_{\text{QPG}} = \exp \left[ \mathcal{C}_j \hat{A}_j \hat{C}^\dagger + \text{h.c.} \right]. \quad (7.12)$$

In this section we will assess the experimental limitations, which arise from the waveguide dispersion. To this end, we numerically simulate the QPG process we realised in the experiment.

We plot our results in Fig. 7.4. Let us first explain panel (a). The large plot shows the JSA function  $G(\lambda_{\text{in}}, \lambda_{\text{out}})$  of the QPG, which comprises the phasematching function in the Gaussian



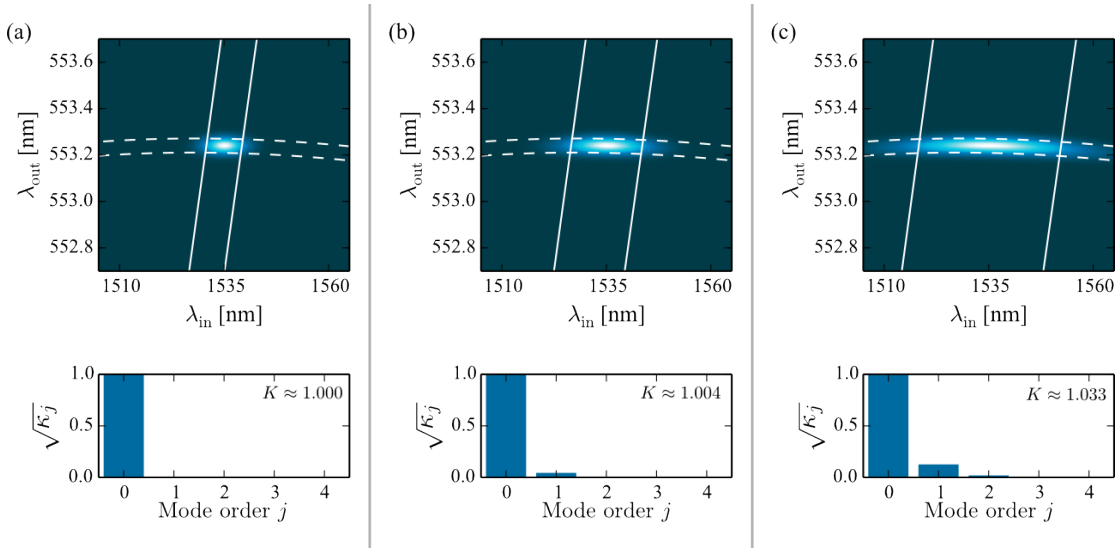


**Figure 7.4** – Estimation of the experimental limitations of our QPG. For more information see the text.

approximation (dashed white lines) and the pump envelope function (solid white lines). The pump envelope function has a positive slope and is assumed to be a Gaussian with a spectral bandwidth of  $\Delta\lambda_p = 1.81$  nm, corresponding to a duration of 576 fs. The phasematching function, in contrast, is oriented along the  $\lambda_{in}$ -axis due to the group-velocity matching between the input light at 1535 nm and the pump at 865 nm. One also sees the curvature of the phasematching, which is a result of the group-velocity dispersion inside the waveguide.

The small plot beneath shows the Schmidt coefficients  $\sqrt{\kappa_j}$ , which we retrieved from the Schmidt decomposition of  $G(\omega_{in}, \omega_{out})$ . We indicated the Schmidt number of  $K \approx 1.000$ , which indicates a close to perfect TF single-mode behaviour, in agreement with our unitary operation.

In (b), we have increased the pump bandwidth to 3.82 nm, corresponding to a duration of 288 fs. The JSA function is still oriented along the input axis, and the Schmidt decomposition yields a Schmidt number of  $K \approx 1.004$ , which is still close to one. However, we can already see an increasing Schmidt coefficient at  $j = 1$ , which indicates the influence of the curved phasematching.

A further increase in pump bandwidth, as shown in (c), finally destroys the TF single-mode behaviour. In this case, the pump bandwidth is  $\Delta\lambda_p = 7.64$  nm, which is the maximum bandwidth of our laser system at this wavelength. This corresponds to a pump pulse duration of 144 fs. Note that a distortion of the JSA function due to the curvature of the phasematching can be seen, which is also reflected by the Schmidt number of  $K \approx 1.033$ , which indicates an increasing multi-mode character of the QPG. In this case, the QPG unitary is only approximately given by the expression in Eq. (7.12). Note that for our measurements, we limited the pump bandwidth to the case investigated in (b), that is  $\Delta\lambda_p = 3.82$  nm, to guarantee genuine

single-mode behaviour of the QPG.

## Summary

In this section, we have introduced the QPG in more detail. We have defined the corresponding TF single-mode unitary operation and discussed, how this unitary transforms an input quantum state. We have then introduced a way to reveal the QPG TF mode structure by probing the device with coherent states, as well as a reliable two-step method to optimise this structure with respect to a given input state. Finally, we have briefly discussed the experimental limitations of the QPG and identified operation parameters for the measurements.

## 7.2 Quantitative Hamiltonian

Before we started to fabricate samples for the QPG in our cleanroom, we first performed extensive theoretical studies to pinpoint the required parameters. In this section we present our initial considerations, which finally led to a quantitative simulation of the device performance.

The material system of our choice is lithium niobate (LN), because of its outstanding dispersion properties, and due to the broad background in our group we settled for titanium-indiffused waveguides which support both polarisations. In addition, we decided on the standard waveguide parameters to ensure a spatially single-mode behaviour at telecommunication wavelengths. We modelled the waveguide dispersion properties with the full numerical FEM model introduced in Chap. 4, to generate effective, temperature-dependent Sellmeier equations for both polarisations. Then, we considered the FC part of the Hamiltonian from Eq. (5.20) to make a quantitative prediction about the performance of our device.

The underlying parts of this Hamiltonian are sketched in Fig. 7.5. In (a), we illustrate the general outline of the device. We utilise a LN waveguide with a length of  $L = 20$  mm at a sample temperature of  $165^\circ\text{C}$ . The simulated waveguide dispersion in (b) tells us that a TE polarised input at  $\lambda_{\text{in}} = 1535$  nm and a TM polarised pump at  $\lambda_{\text{p}} = 865$  nm are group-velocity matched at this temperature. Consequently, the output pulse is centred around  $\lambda_{\text{out}} = 553$  nm and we find a required poling period of  $\Lambda = 4.28$   $\mu\text{m}$  to guarantee quasi-phasematching. Note that poling periods around 4  $\mu\text{m}$  are on the verge of what we could realise in our cleanroom.

To estimate the effective interaction area of the process, we modelled the spatial field distributions of the fundamental modes inside the waveguide and plotted them in (c). Pump and output field exhibit similar spatial distributions, whereas the input mode is considerably larger due to the longer wavelength. The effective mode refractive indices evaluate to  $n_{\text{p}} = 2.184$ ,  $n_{\text{in}} = 2.213$  and  $n_{\text{out}} = 2.320$ . Finally we studied the TF properties of this process. In (d), we plot the JSA function  $G(\lambda_{\text{in}}, \lambda_{\text{out}})$  calculated using the effective Sellmeier equations. We assumed an input pulse bandwidth of  $\Delta\lambda_{\text{in}} = 12$  nm and an adapted pump bandwidth of  $\Delta\lambda_{\text{p}} = 3.82$  nm (compare Fig. 7.4) and found a Schmidt number of  $K = 1.02$  with a leading Schmidt coefficient of  $\sqrt{\kappa_0} = 0.996$ . The expected conversion efficiencies for the first two TF modes are plotted as well. We find that for maximum conversion of the first mode, the second mode is virtually unconverted. Hence, our process is close to TF single mode. A deviation from perfect single-mode behaviour is caused by modelling the phasematching as a sinc-function.



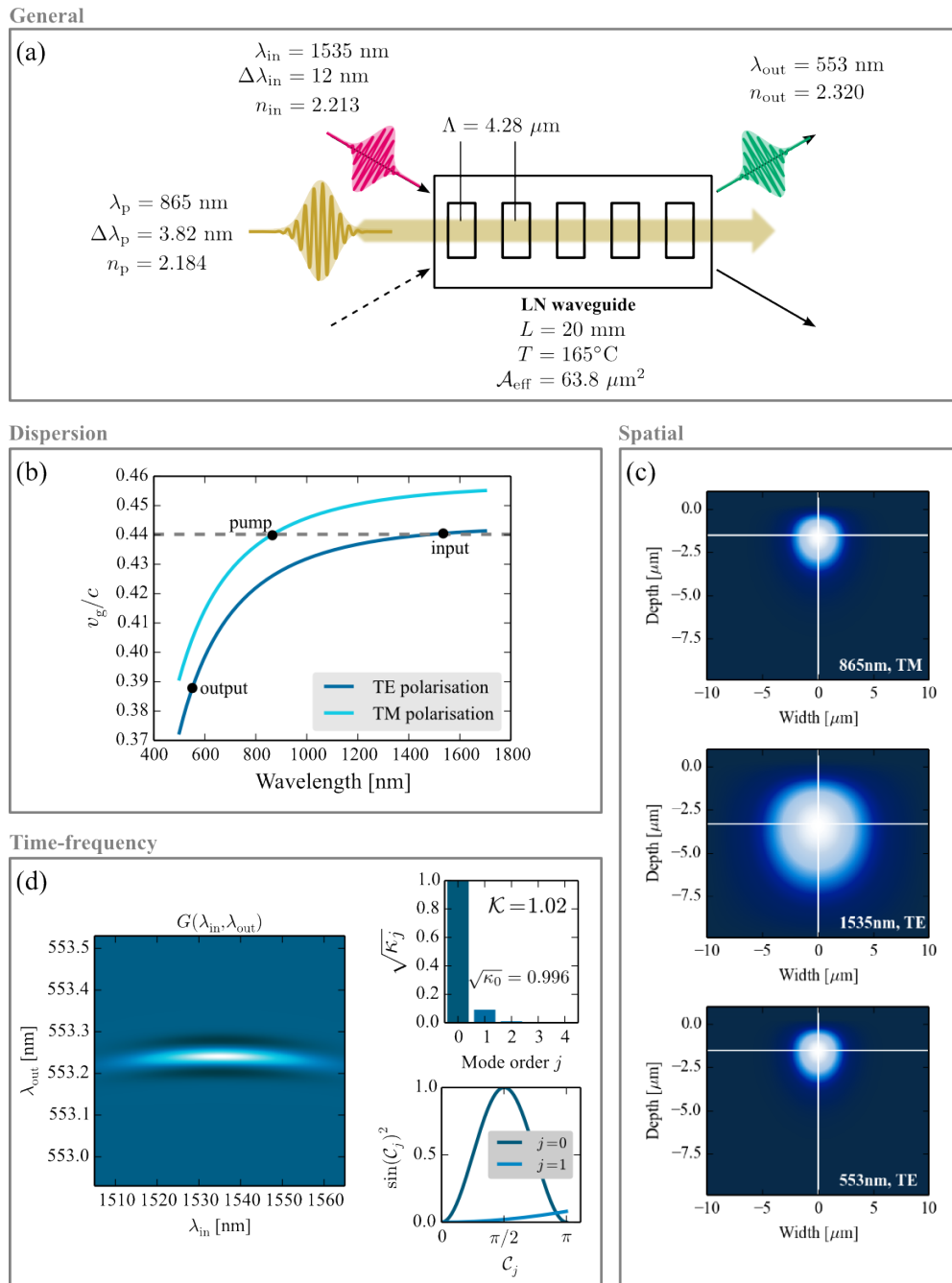


**Figure 7.5** – Considerations for the quantitative prediction of the device performance. For details see the text.

Note that this is a worst-case assumption, since the TF characteristics benefit from a Gaussian phasematching (compare Fig. 7.4).

With these numerical constants, we can write down the coupling constant  $\mathcal{C}_j$  of the process as [61]

$$\mathcal{C}_j = \sqrt{\kappa_j} \cdot \frac{2\pi^2 d_{\text{eff}} L}{c\sqrt{\mathcal{A}_{\text{eff}}}} \sqrt{\frac{2P_p \omega_{\text{in}} \omega_{\text{out}}}{c\epsilon_0 n_p(\omega_p) n_{\text{in}}(\omega_{\text{in}}) n_{\text{out}}(\omega_{\text{out}}) \left| \int d\omega_p \alpha(\omega_p) \right|^2}}, \quad (7.13)$$

where  $d_{\text{eff}}$  is the effective  $\chi^{(2)}$ -nonlinearity of the process,  $P_p$  is the averaged pump pulse power,  $c$  is again the speed of light and  $\epsilon_0$  is the vacuum permittivity.

Since the efficiency of the QPG operation is given by  $\eta_{\text{QPG}} = \sin^2(\mathcal{C})$ , we can calculate the required cycle-averaged pump power  $P_p$ <sup>23</sup> by solving  $\mathcal{C} = \frac{\pi}{2}$  and find for our case

$$P_p = \left( \frac{c \left| \int d\omega_p \alpha(\omega_p) \right|}{4\pi d_{\text{eff}} L} \right)^2 \frac{c\epsilon_0 n_p(\omega_p) n_{\text{in}}(\omega_{\text{in}}) n_{\text{out}}(\omega_{\text{out}}) \mathcal{A}_{\text{eff}}}{2\omega_{\text{in}} \omega_{\text{out}}} \approx 23.29 \text{ W}. \quad (7.14)$$

Hence we expect maximum conversion at an averaged power of around 23 W inside the waveguide. If we assume a boxcar approximation of the pump pulse, which has a width similar to the  $\frac{1}{e^2}$ -width of the actual Gaussian, we retrieve a peak power of the pump pulse of around 37 W. This corresponds to an extraordinarily low pulse energy of  $E_{\text{pulse}} \approx 11.2$  pJ. Our laser system delivers pulses with a repetition rate of 80 MHz. If we assume perfect coupling into the waveguide, we find that for complete conversion we require only 0.9 mW of laser power. This surprising low value is only achieved because of the careful engineering of the QPG process: first, the group-velocity matching lets the input signal experience the high peak power of the pump over the whole interaction length; second, the mode confinement inside a waveguide increases the efficiency compared to bulk crystal experiments; third, the TF single-mode characteristics lead to an optimised efficiency, since no energy is wasted pumping empty TF modes.

## Summary

We have presented a quantitative study of our QPG, taking into account realistic experimental parameters. We find a surprisingly low pump power of 0.9 mW cw-equivalent power in front of the waveguide for achieving unit conversion efficiency. This value has its origin in the careful tailoring of the QPG and commends our device as building block for large scale applications where energy efficiency is a crucial point.

## 7.3 Experiment

In this section we present our experimental setup and, in the end, demonstrate the successful implementation of a QPG. We begin with an explanation of the operating principle of our pulse shaper, followed by a detailed illustration of the experimental setup. We then demonstrate how

<sup>23</sup>We recall that this value corresponds to the approximation of the pump pulse with a boxcar function



the spatial mode properties of the QPG can be controlled during the measurements and conclude with results on the mapping of the QPG TF mode structure and the achieved conversion efficiencies.

### 7.3.1 Pulse shaping with the Dazzler

We deployed an acousto-optical pulse shaper (Fastlite Dazzler) for preparing the ultrafast pump pulses in well-defined TF shapes. The spectral resolution of the Dazzler is limited to roughly 0.5 nm and its working principle is as follows: Light is launched into a birefringent  $\text{TeO}_2$  crystal oriented along the ordinary crystal axis. A traveling acoustic wave propagating through the Dazzler crystal collinearly to the light induces a Bragg grating, which diffracts part of the incoming light to the extra-ordinary crystal axis. Appropriate shaping of the acoustic waves implements a grating that reflects different spectral components of the input light with different efficiencies at different positions of the acoustic waves. In this way, amplitude and phase shaping is accomplished.

We have illustrated this in Fig. 7.6 (a). The pulse train enters the crystal from the left. When a pulse "hits" the acoustic wave, it is diffracted to the other crystal axis, continues propagating under a slightly different angle and can be spatially separated at the output of the crystal. Although the Dazzler facilitates amplitude and phase shaping of the input pulses, it shows some peculiar characteristics that have to be understood in order to interpret measurement results correctly.

This is sketched in (b): In the upper sketch, the red laser pulse enters the crystal and is diffracted to the extra-ordinary axis at position  $x$ . The blue pulse is the succeeding pulse and has not entered the crystal, yet. In the lower sketch, the red pulse has propagated further on the extra-ordinary axis through the crystal, whereas the blue pulse has entered the crystal. During the time  $\Delta\tau$  between the two pulses, the acoustic wave has travelled about a distance  $v_{ac} \Delta\tau$ , where  $v_{ac}$  is the sonic velocity in the crystal, and consequently the blue pulse is diffracted at position  $y$ .

This has an impact on the optical path that each pulse has to travel, since it propagates a longer distance along the ordinary axis compared to its predecessor. In turn, the distance on the extra-ordinary axis is shorter. We show the outcome of this in (c), where we sketched the pulse train at the output of the Dazzler. The vertical black lines are our reference and correspond to the undisturbed pulse spacing. We see that the diffracted pulse train has a different spacing and consequently a different repetition frequency  $f_{rep}$ . Note that for every acoustic wave, this pattern is exactly reproduced when the Dazzler is synchronised to an external clock.

This result is significant for the QPG. The mode-selection only works if pump pulses and input states have a perfect temporal overlap. Hence, only a small part of the diffracted pulse train may be evaluated, which enforces a detection system that is capable of resolving the arrival times of the pulses.

### 7.3.2 Overview over the setup

A detailed sketch of the experimental setup together with a photograph from the laboratory is shown in Fig. 7.7. We use a Ti:Sapph oscillator (Coherent Chameleon Ultra II) and an optical parametric oscillator (OPO, APE Compact OPO) to generate two synchronised trains of



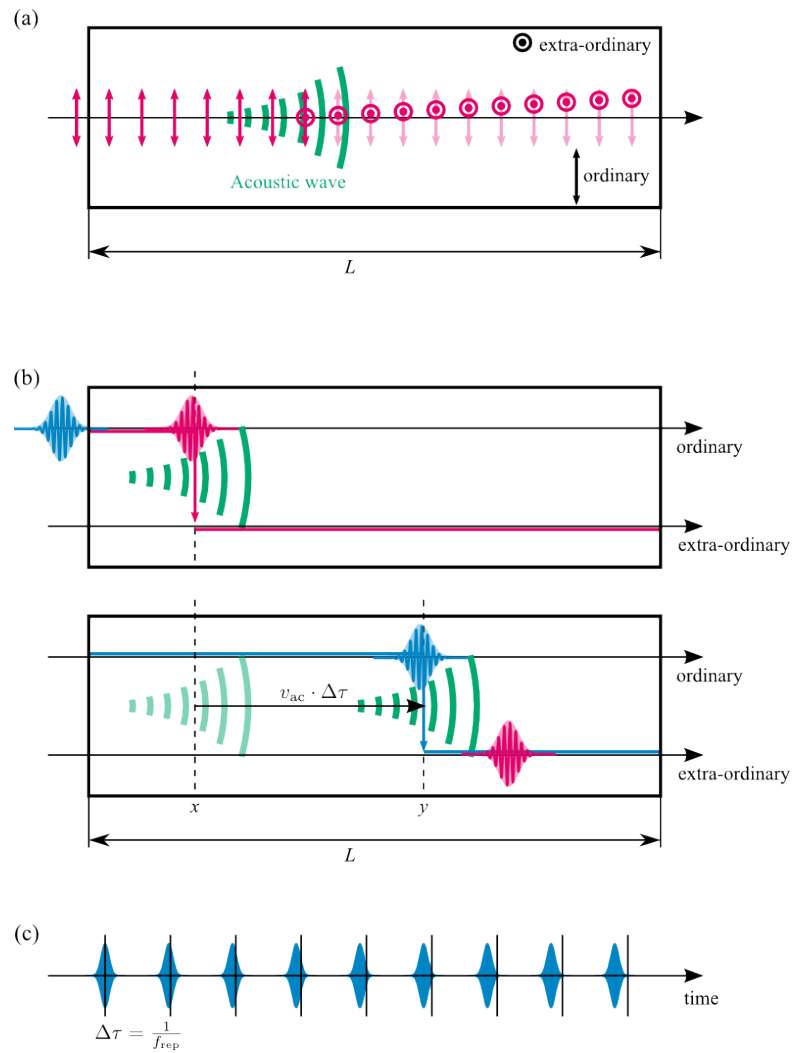


**Figure 7.6** – Schematics illustrating the operation principle of the Dazzler (a) and the associated consequences (b), (c). For more details see the text.

Fourier limited pulses with a repetition frequency of 80 MHz at wavelengths of  $\lambda_p = 865$  nm and  $\lambda_{in} = 1535$  nm, respectively. The pulses have a duration of 140 fs and 200 fs, corresponding to spectral bandwidths of  $\Delta\lambda_p = 7.8$  nm and  $\Delta\lambda_{in} = 17.3$  nm, respectively. In this configuration, the system delivers up to one Watt of cw-equivalent power at the pump wavelength and up to 300mW cw-equivalent power at the input wavelength.

After rotating the polarisation of the 865 nm pump pulses with a half-wave plate (HWP) they were fed into the Dazzler. We divided the master clock of the laser system to trigger the Dazzler with a frequency of 20kHz, while keeping it synchronised to the pulse trains. Each acoustic wave is capable of diffracting approximately 250 laser pulses, leading to bursts of shaped pulses. Behind the Dazzler, the pump pulses were sent through an optical delay line consisting of a



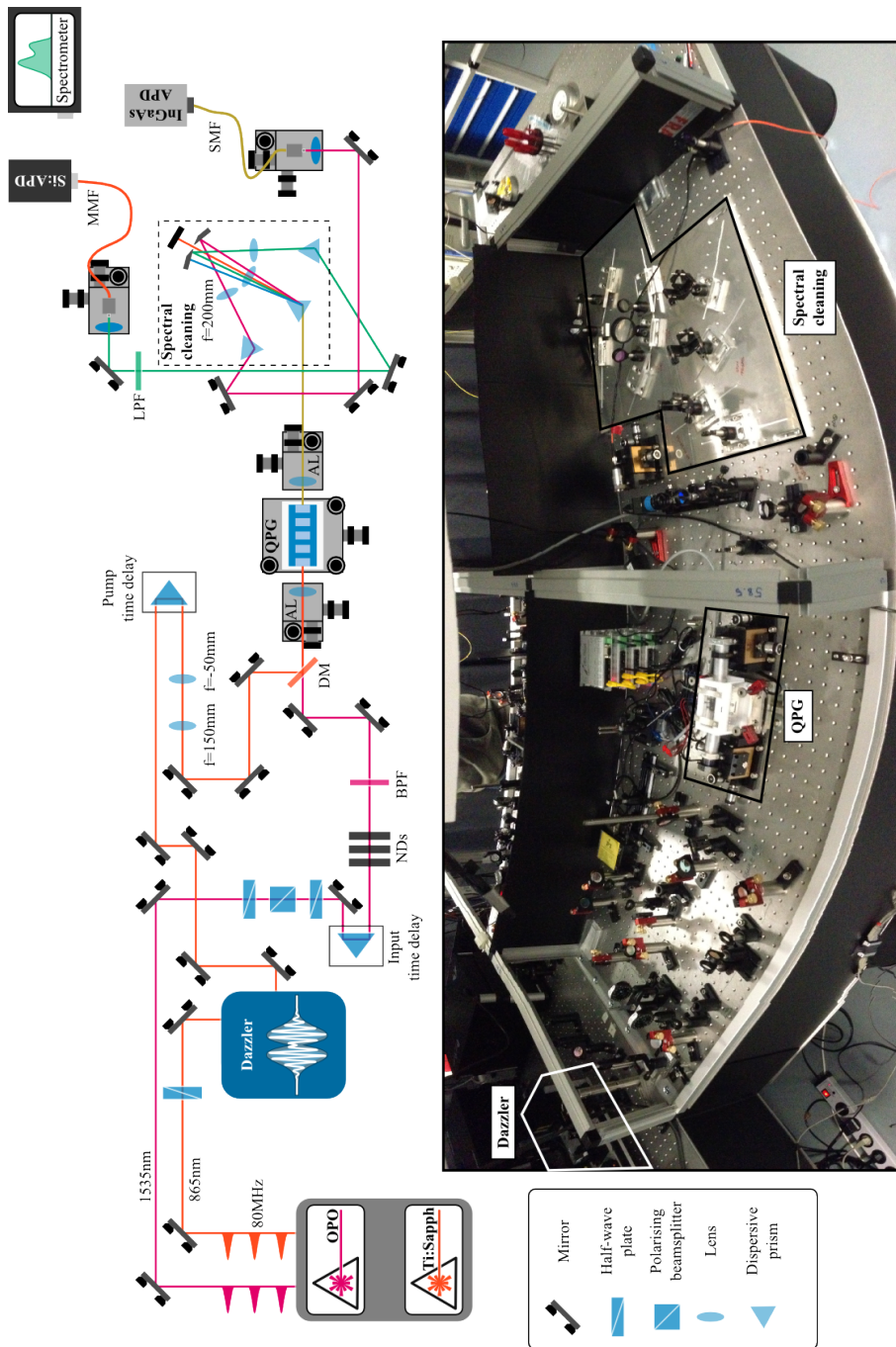


**Figure 7.7** – Detailed sketch and photograph of the experimental QPG setup. Abbreviations: NDs - neutral density filters, BPF - bandpass filter, DM - dichroic mirror, AL - aspheric lens, LPF - longpass filter, MMF - multimode fiber, SMF - single mode fiber, APD - avalanche photo diode.

linear translation state and a rectangular prism and a subsequent telescope made of two AR coated lenses. The focal widths of the lenses ( $f = 150$  mm and  $f = -50$  mm) were chosen to realise a three-times magnification of the beam. Note that the mirrors in the pump beam path were broadband anti-reflection (AR) coated for Ti:Sapph wavelengths (Thorlabs E03).

The 1535 nm input light was sent through a power control consisting of a HWP and a subsequent polarising beamsplitter (PBS). Thereafter the polarisation direction was restored with another HWP and the input was sent through a second optical delay line similar to the one for the pump, which was added for additional flexibility. We attenuated the input light with several neutral density (ND) filters down to the single photon level and applied a 12 nm wide spectral bandpass filter (BPF, Thorlabs FB1540-12), which was slightly tilted to guarantee ideal transmission of the 1535 nm light. After the filtering, the input pulses had a duration of 287 fs. In correspondence to the pump beam path, we deployed broadband AR coated mirrors for telecommunication wavelengths (Thorlabs E04) for the input light.

Pump and input pulses were combined on a dichroic mirror (Thorlabs DMLP1180) which featured a transmission of the input light of more than 95% while at the same time reflecting the pump pulses with more than 97% reflectivity. A coarse temporal overlap between the pulse trains was found by utilising fast InGaAs photo diodes with a bandwidth of 100 MHz, which were able to resolve the pulse train. The signal of the diodes was recorded with a digital oscilloscope (LeCroy Wavepro 7100A) and evaluated in terms of arrival time difference. The analysis of an arrival time histogram allowed for a temporal resolution of around 50 ps. This was precise enough to overlap the pulses within the range of our two temporal delay stages.

Both pulse trains were coupled into the uncoated QPG waveguide sample with an uncoated aspheric lens (AL, Thorlabs A220TM) with an effective focal length of 11 mm and a corresponding working distance of roughly 8 mm. Note that we achieved mutual coupling efficiencies of 50% for the pump light and 45% for the input light, measured in front of and behind the in- and outcoupling lenses, respectively. Taking into account the reflection losses of the lenses (4% per lens) and the losses at the uncoated waveguide facets (14% per facet) but neglecting internal waveguide losses, we would have expected a maximum coupling efficiency of 68% and find that we were satisfyingly close to that value.

The waveguide sample had a length of 22 mm and was mounted in a homebuilt oven, which was kept at a temperature of 190°C to ensure quasi-phasematching and at the same time prevent photorefractive effects. It was temperature stabilised with a cryogenic temperature controller (Oxford Instruments Mercury iTC) and we achieved a long-term stability of  $\pm 75$  mK over a constant on-time of roughly 12 months.

At the output of the waveguide the light was collimated with another AL (Thorlabs A220TM) and sent through a spectral cleaning stage, consisting of a modified 4-f-spectrometer. In our case, we found the peculiar situation that we needed to filter out the remaining pump light at 865 nm, which was in between the input light at 1535 nm and the converted output at  $\lambda_{\text{out}} = 553$  nm. In addition, we had a non-phasematched SHG background at  $\lambda_{\text{SHG}} = 432.5$  nm from the bright pump pulses.

We decided to split up the wavelengths using an equilateral N-SF11 dispersive prism (Thorlabs PS859). For focussing the light we utilised an uncoated lens with a focal width of 200 mm. In the focal plane, we installed two D-shaped mirrors with a gap in between. The short wavelength mirror was AR coated for the visible light (Thorlabs BBD1-E02) and we took care to



ensure that the SH radiation hit the black mirror mount. The remaining pump light passed through the gap into a beam dump. The long wavelength mirror, in turn had the same broadband AR coating as the other input mirrors (Thorlabs BBD1-E04). Then the converted output and remaining input passed two AR coated lenses for the respective wavelengths, again with focal widths of 200 mm, and two dispersive prisms to complete the 4-f-setup.

The unconverted input light was coupled into a standard SMF-28 single-mode fiber (SMF) with a 10x microscope objective and sent to an InGaAs avalanche photo diode (APD, NuCrypt CPDS-4) for photon counting. The converted light passed an additional longpass filter (LPF, Thorlabs FEL500) to get rid of the remaining SH radiation and was coupled into a multimode fiber (MMF), again using a 10x microscope objective. The MMF was fed into either a single-photon sensitive CCD spectrometer (Andor iKon-M 934P-DD / Shamrock SR-303iA) or a silicon APD (Perkin-Elmer SPCM-AQRH-13) for photon counting.

The signals of the APDs were recorded with a time-to-digital converter (ACAM TDC-GPX) with a temporal resolution of 81 ps, which was plenty for resolving the pulse trains. To account for the Dazzler behaviour, we restricted the analysis to the 16 shaped pump pulses that exhibited the largest temporal overlap to the input pulse train. In contrast, this possibility was not given for measurements of the converted spectrum with the CCD, where we had to integrate over the whole signal pulse burst.

### 7.3.3 Spatial mode adaption

For our first measurements, we deployed the CCD spectrometer and comparably high input powers of around  $15 \mu\text{W}$  cw-equivalent power at 1535 nm. We monitored the converted output while adjusting the temporal delay stages. Once we had found a signal, we changed the shape of the pump from a fundamental Gaussian to a first-order Hermite-Gaussian. Theory tells us that, since our input TF mode is a Gaussian, the conversion efficiency should drop in this case. What we measured however can be seen in Fig. 7.8 (a).

In contrast to our theory, the conversion efficiency increases when switching to the higher order pump mode. Note that we took care to keep the pump pulse energies constant for different TF modes, so power fluctuations can be discarded as reason for this behaviour. To explain these results, we have to go back to Chapter 2, where we discussed the influence of different spatial waveguide modes. We had seen (compare Tab. 4.1) that different spatial modes exhibit different effective refractive indices in the waveguide, which leads to shifted phasematching conditions. We investigated this in Fig. 7.9, where we deployed the metallic waveguide model to obtain quick qualitative results.

What do we see from these plots? In the upper left corner of Fig. 7.9, we plotted the JSA function  $|G(\omega_{\text{in}}, \omega_{\text{out}})|$  for a Gaussian TF shape of the pump (solid white lines). The different ellipses correspond to different spatial mode combinations. We knew that our waveguides were single-mode for the input light. However, we considered the fundamental and first higher-order spatial modes for the pump and the converted output, respectively. This gives a total of four possible combinations. In addition, we assumed our input signal with a spectral bandwidth of 12 nm (dashed white lines). Only the part of the input signal that overlaps with the respective JSA function is converted. Exactly these overlaps are plotted in the lower plot (blue lines). We labeled the spatial modes combinations as  $xx,yy$ , where  $xx$  is the pump mode and  $yy$  the



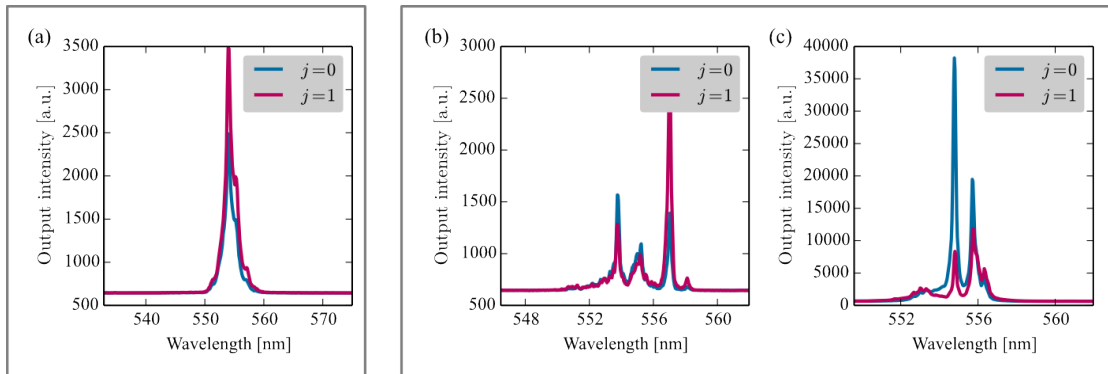


**Figure 7.8** – First measurement result (a). The blue line shows the QPG output light when the pump is in a fundamental Gaussian TF mode, whereas the red line was recorded with a first-order Hermite-Gaussian pump. Contrary to our theory, the conversion efficiency increases when switching to the higher order pump mode. In (b) and (c), we repeated the measurement with higher spectral resolution and resolved a multi-peak structure. The different peaks correspond to different spatial mode combinations and when the incouplings are better aligned (c), the expected behaviour occurs.

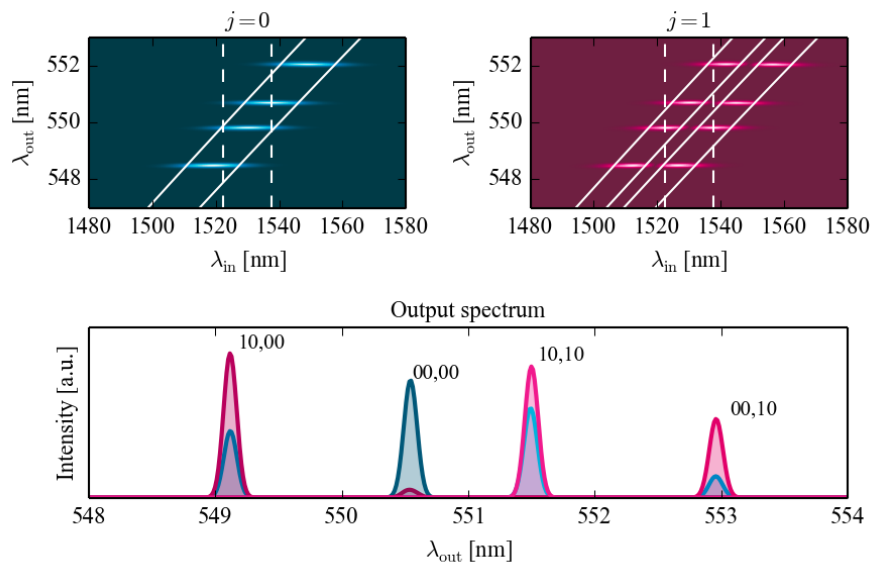


**Figure 7.9** – Theoretical investigation of the impact of different spatial modes in the waveguide on the converted output light. For more details see the text.



output mode, respectively. A value of 00 marks the fundamental spatial mode, whereas 10 is the first-order mode in depth direction.

This becomes interesting when comparing it to the case of a first-order Hermite-Gaussian TF shape of the pump. In the upper right we plotted again the JSA functions. Note how the input signal (dotted white lines) visibly overlaps only with one lobe of the JSA function in three cases. This is reflected in the bottom plot (red lines). We meet the special QPG conditions only if all fields propagate in the fundamental spatial mode, which corresponds to the second peak. Then, switching the pump TF order from  $j = 0$  to  $j = 1$  yields the expected drop in conversion efficiency. For all other cases, we find an increase in conversion efficiency, corresponding to our measurement results.

We crosschecked our theory by repeating the measurement with higher spectral resolution in Fig. 7.8 (b). In fact we find distinct peaks which show opposite behaviour upon a change of the pump TF mode order. The leftmost peak shows the expected decrease in conversion efficiency upon a change of pump mode order from  $j = 0$  to  $j = 1$ . In contrast the rightmost peak shows the opposite behaviour. After optimising the incoupling to obtain the highest coupling to the leftmost peak, we finally measure the expected QPG behaviour in (c), where the dominating peak gets suppressed by around 80% when switching from a Gaussian pump to a Hermite-Gaussian. Note that the remaining second peak is still an unfavourable spatial mode combination, which can be eliminated through further optimisation of the incoupling.

As a result of these measurements, we defined the incoupling working point as the alignment which yielded exactly one peak in the converted output spectrum, which showed a drop in conversion efficiency when switching to higher order pump modes.

### 7.3.4 Mapping of the QPG time-frequency modes

Having found the spatial working point of our device, we moved on to characterising the QPG operation. To do so, we deployed the approach from Sec. 7.1.2. However, for the experiment we deployed a TF single-mode probe state, which was realised with the attenuated 1535 nm pulses from the OPO. We recall that their spectral bandwidth is  $\Delta\lambda_{\text{probe}} = 12$  nm, corresponding to a duration of 287 fs and that they reside in a Gaussian TF mode  $\mathcal{G}_n(\omega)$  with  $n = 0$ .

Our first goal was to experimentally deduce the TF structure of the QPG unitary for different operation conditions, that is, different TF shapes of the pump envelope function  $\alpha(\lambda_p)$ . We fixed the pump spectral width at  $\Delta\lambda_p \approx 5$  nm and scanned the central pump wavelength  $\lambda_p$ . The converted 553 nm output light was recorded with the CCD spectrometer and we repeated the measurements for four different pump TF modes  $g_j(\omega)$ . These were the fundamental Gaussian and the 1<sup>st</sup> to 3<sup>rd</sup> order Hermite-Gaussians.

We illustrate the measurement procedure and the results in Fig. 7.10. In (a), we sketch the situation of a fundamental Gaussian pump (blue), which is scanned over the input Gaussian (red). As the centre of the pump spectrum moves across the input, we record the overlap  $\xi_{nj}$  between both, marked with the striped areas in the illustration. The expected outcome is shown in the diagram on the right, where we have also indicated the overlap values corresponding to the two pump positions on the left (also see Fig. 7.2).

In (b), we consider a first-order Hermite-Gaussian pump (blue). Please note that, although we measure an output intensity, our measurement is intrinsically sensitive to the phase of the



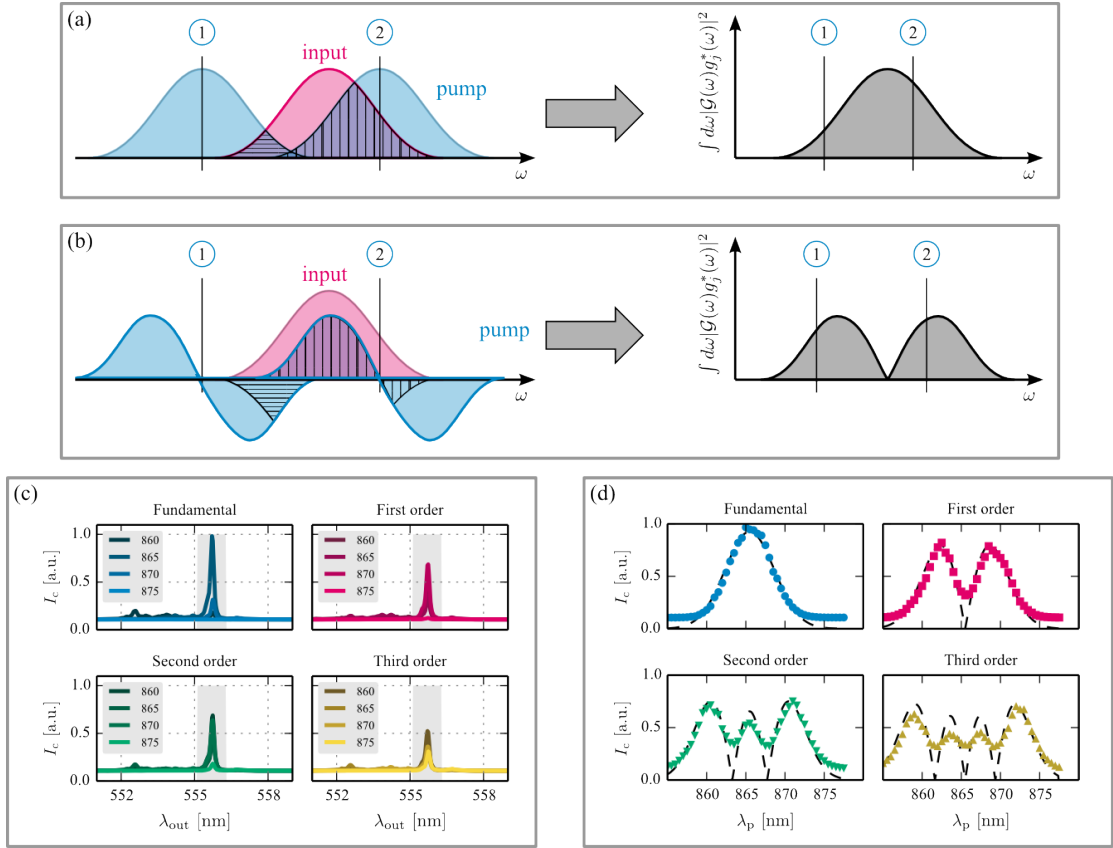


**Figure 7.10** – Measurement of the TF mode structure of the QPG operation. For more information see the text.

pump. If the centres of pump and input (red) are the same, the contributions from the positive and the negative lobe of the pump pulse cancel out, and we measure zero overlap. As before, we indicated the expected measurement result in the right diagram.

In panel (c), we plot the raw output spectra for central pump wavelengths between  $\lambda_p = 860$  nm and  $\lambda_p = 875$  nm. From top left to bottom right, the order of the pump TF mode increases from the fundamental Gaussian to the third order Hermite-Gaussian. Note that the clean spectra are a result of the careful optimisation of the incoupling; no spectral filtering was applied to the output. The offset of the central output wavelength from the expected value of  $\lambda_{out} = 553$  nm is most probably due to an erroneous calibration of the CCD spectrometer, which was not crosschecked prior to the measurements.

We see that, regardless of the central pump wavelength and the pump TF mode order, the output spectrum stays the same. This is in agreement with our theory, which predicts that the output TF mode  $h(\lambda_{out})$  is solely defined by the QPG phasematching function. From the analysis of the spectra, we retrieve an output bandwidth of  $\Delta\lambda_{out} = 0.14$  nm, which corresponds to a duration of  $\Delta\tau_{out} \approx 3.2$  ps. In comparison to the input pulse duration of  $\Delta\tau_{in} = 287$  fs, we find



an increase in the pulse duration about a factor of 11. This factor can become greater for longer waveguides, since the width of the phasematching function is proportional to  $1/L$ . Due to the Fourier relationship between time and frequency, this elongation enforces a compression of the spectral bandwidth of equal size. This exciting feature brings TF modes one step closer to being compatible with narrow band quantum memories, although the bandwidth gap between the QPG output pulses and typical quantum memory linewidths of around 1 GHz (corresponding to roughly 500 ps) is still considerable.

Finally, in panel (d) we plot the output intensities against the central pump wavelength. We obtained the intensities by integrating over the output spectra in the grey-shaded areas in panel (c) and note that it follows the shape of the QPG input TF mode  $g_j(\lambda_{\text{in}})$  as can be seen from Eq. (7.10). The dashed black lines in the plots in (d) are Hermite-Gaussian functions. We fitted a fundamental Gaussian to the blue measurement points and used the obtained width to generate the other three modes. From the fit we obtained an ideal central wavelength of  $\lambda_p = 865.6$  nm with a corresponding of  $\Delta\lambda_p \approx 5.2$  nm. The measured intensities nicely follow these lines and only deviate in the regions of sharp features, which can be attributed to the limited Dazzler resolution of  $\Delta\lambda_{\text{Dazzler}} \approx 0.5$  nm.

In conclusion we succeeded in mapping both, the input and output TF mode of our QPG by utilising a coherent probe state and only monitoring the spectrum and intensity of the converted output light. We find that the QPG input TF modes  $g_j(\lambda_{\text{in}})$  are indeed defined by the TF shape of the pump envelope function, whereas the output mode  $h(\lambda_{\text{out}})$  is given by the phasematching function and does not change for different pump parameters. The ideal pump wavelength for our probe states evaluates to  $\lambda_p = 865.6$  nm.

### 7.3.5 Adapting the QPG TF modes to an unknown input

In a realistic scenario the general shape of the QPG input states might be known – for instance Hermite-Gaussian modes – but the exact central wavelength and width is uncertain. We have just demonstrated that the central wavelength can be determined by scanning the pump wavelength and monitoring the converted output spectrum. Here we adapt the pump width to an *unknown* input. As before, the input state is centred at  $\lambda_{\text{in}} = 1535$  nm and has a spectral width of  $\Delta\lambda_{\text{in}} = 12$  nm.

We have already discussed this in Fig. 7.3. However, we sketch the procedure again in Fig. 7.11 (a.1) and (a.2). We assume a Gaussian input (red pulse), which is overlapped with a Gaussian pump (a.1) or a first-order Hermite-Gaussian pump (a.2), respectively. From left to right, the spectral pump width increases. This consequently leads to a drop in the height of the pump peak, since the pump spectrum is normalised to guarantee a constant pump pulse energy. We find that the overlap for the Gaussian pump is always positive, whereas the overlap for the Hermite-Gaussian has a positive and negative contribution, which always exactly cancel out if the modes have the same centre.

This is schematically drawn in (b), where we plot the overlap integral as a function of the pump width for different pump mode shapes. The overlap for the Gaussian pump increases until it reaches the maximum value of one. For a further increase in pump bandwidth, the overlap decreases again. In addition, the overlap between the probe spectrum and the Hermite-Gaussian pump is constantly zero. However, we find a peculiar situation for the second order



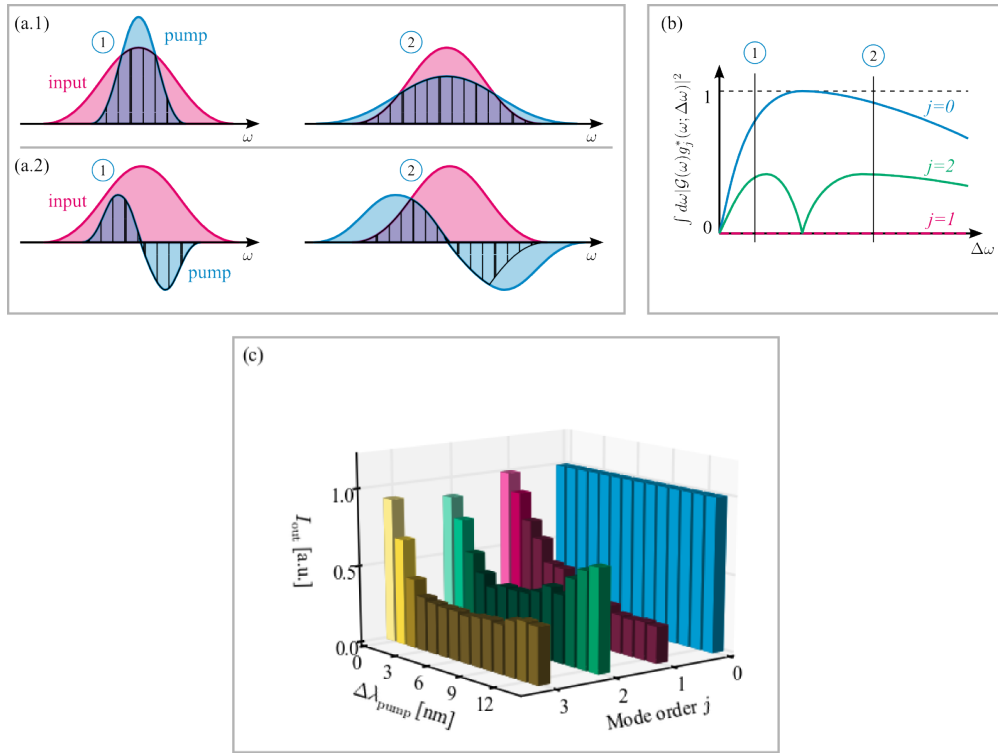


**Figure 7.11** – Measurement results for adapting the pump width to an unknown input state. For more details see the text.

pump mode  $j = 2$ . First, the overlap increases. Then, it starts to decrease and completely vanishes for an adapted pump bandwidth, due to the orthogonality of the Hermite-Gaussian modes. A further increase of the pump bandwidth leads again to a positive overlap. Hence, we can use the minimum overlap between the probe and the second-order Hermite-Gaussian pump as an optimisation criterion for the pump bandwidth (compare Fig. 7.3).

Due to the characteristics of the pulse shaper, which led to a different effective number of shaped pulses per burst for different spectral widths, we could not directly evaluate the raw data, but we evaluated the ratios of converted output intensity for  $j = 0$  and  $j = 1, 2, 3$ . Note that although the shape of the expected curves changes with respect to (b), the essential characteristics stay the same.

The results of this measurement are plotted in panel (c), where we show the normalised output intensities as obtained from the measured spectra. In our plot, the mode order  $j$  refers to the pump TF shape and the pump width  $\Delta\lambda_p$  is now given in units of nanometres. For very narrow pump bandwidths close to the Dazzler resolution limit, all conversion efficiencies are equal, since no shaping takes place. However, when overcoming this limitation, the relative intensities for the odd pump modes  $j = 1$  and  $j = 3$  drops to a low value and does not increase anymore. In contrast, the converted intensity for the even order Hermite-Gaussian pump  $j = 2$  exhibits a



minimum and increases again afterwards. In correspondence to panels (a) and (b), we identify the minimum with the ideal pump bandwidth, which evaluates to  $\Delta\lambda_p \approx 4$  nm. The associated pump pulse duration of  $\Delta\tau_p \approx 275$  fs compares outstandingly well to the known input pulse duration of  $\Delta\tau_{in} = 287$  fs.

In addition, we retrieve from the suppression of the conversion in the higher order pump modes a raw mode-selectivity of 70%, which we calculate from the ratio of converted intensity in  $j = 0$  and the respective intensities in  $j = 1 \dots 3$ . Note that this value is neither corrected for the limited resolution of the Dazzler, nor for the flat spectral background that can be seen in Fig. 7.10 (c), and thus constitutes a lower limit to the QPG performance.

Concluding, we have shown how to adapt the QPG TF mode structure to an unknown input state. First, the central pump wavelength must be determined. Thereafter, the ideal pump bandwidth can be retrieved from measuring the converted intensity for different pump TF shapes and spectral widths. The demonstrated capability to adapt the QPG online to an unknown input state is a large benefit for real world applications, where the initially generated TF shapes might be distorted during long distance transmission or due to the dispersion of optical elements in a networking architecture.

### 7.3.6 Performance benchmarks

In the last experimental section, we analyse the performance benchmarks of the QPF, that is the internal conversion efficiency of the QPG when operated with light at the single photon level and its mode selectivity in detail. For obtaining the conversion efficiency, we attenuated the coherent input pulses to a mean photon number of  $\langle n \rangle \approx 0.15$  per pulse and recorded the converted output counts with the silicon APD which was fed into the TDC. The analysis of these measurements is complicated by the peculiar behaviour of the pulse shaper, in particular the change of the repetition frequency of the shaped pulse train as illustrated in Fig. 7.6 (c).

We have plotted the measurement results in Fig. 7.12. In (a), we show the converted output counts as a function of the pump pulse energy  $E_{pump}$ . We find a maximum conversion efficiency at an energy of  $E_{pump} \approx 16$  pJ in front of the incoupling lens. In the following, we want to detail the origin of these numbers. The open circles are the measured raw counts when both, pump and input signal, are fed into the QPG. For each value, we have additionally measured the APD counts when blocking the input signal and attributed the remaining counts to pump induced background. We subtracted these numbers from the raw counts and plotted the corrected counts with green squares. The theoretical fit is given by the well-known relation for SFG efficiency, given by

$$\eta_{SFG} = \sin^2(\mathcal{C}_j), \quad (7.15)$$

where  $\mathcal{C}_j = \mathcal{C}_j(\sqrt{P_p})$  is a function of the pump pulse peak power and was defined in Eq. (7.13).

For measuring the counts, we have set a 200 ns wide time gate on the TDC, corresponding to 16 shaped pump pulses for which we assume close to ideal temporal overlap with the input signal. The Dazzler is triggered at a repetition frequency of  $f_{Dazzler} = 20$  kHz and the integration time of the photon counting was set to one second. We obtain a total up-time of our system of  $T = 200 \text{ ns} \cdot 20 \cdot 10^3 = 4$  ms, which is also the time constant shown in the plot. With the mean photon number of  $\langle n \rangle \approx 0.15$  of the input pulses, we find a total input photon number of



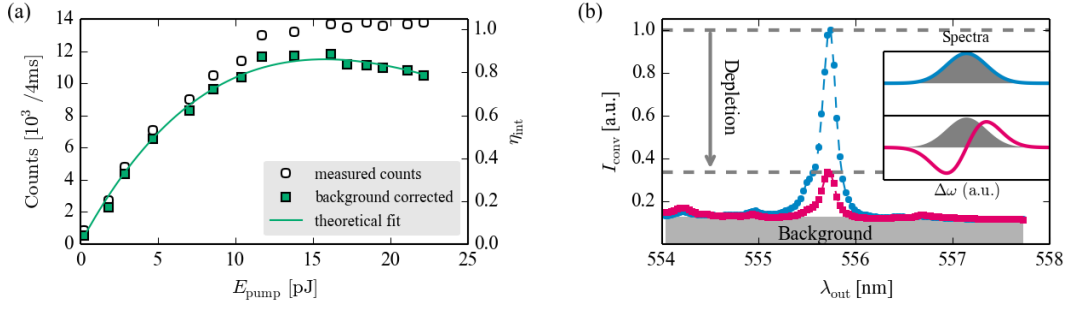


**Figure 7.12** – Measured performance benchmarks of the QPG. In (a), we plot the converted output counts as a function of the pump pulse energy. We find a maximum conversion at an energy of roughly  $E_{\text{pump}} \approx 16$  pJ and the counts follow nicely the theoretical sine-square fit. We obtain a maximum efficiency of 87%. In (b), we analyse the mode-selectivity of the QPG, which evaluates to 80%. Note that this number is mainly limited by the finite resolution of the pulse shaper.

$N_{\text{in}} = 48 \cdot 10^3$  during the up-time of our device, corresponding to  $16 \cdot 20 \cdot 10^3 = 3.2 \cdot 10^5$  input pulses.

From this number we can retrieve the internal conversion efficiency  $\eta_{\text{int}}$  of our device by evaluating the measured counts, since

$$N_{\text{meas}} = N_{\text{in}} \cdot \eta_{\text{tot}} = N_{\text{in}} \cdot \eta_{\text{face1}} \eta_{\text{int}} \eta_{\text{face2}} \eta_{\text{arm}} \eta_{\text{MMF}} \eta_{\text{det}}. \quad (7.16)$$

Here  $\eta_{\text{tot}}$  is the total conversion efficiency of our setup, which evaluates to roughly  $\eta_{\text{tot}} \approx 24\%$ . We can decompose this by evaluating the known losses in our setup. From Fresnel's equations, we find an input waveguide facet transmissivity for the input photons of  $\eta_{\text{face1}} = 0.86$  and an output transmissivity for the converted photons of  $\eta_{\text{face2}} = 0.84$ . The transmission through our setup after the waveguide, including all spectral filtering, was measured to be  $\eta_{\text{arm}} = 0.90$ , the incoupling efficiency into the multimode fiber was  $\eta_{\text{MMF}} = 0.70$  and finally, the detector efficiency as specified from the vendor is  $\eta_{\text{det}} = 0.60$ . Together with the maximum number of detected output counts of  $N_{\text{meas}} \approx 11500$ , we obtain an internal conversion efficiency of

$$\eta_{\text{int}} = \frac{N_{\text{meas}}}{N_{\text{in}} \cdot 0.273} \approx 0.877. \quad (7.17)$$

This is an excellent value, in particular when considering that it is only a lower bound, because we did not account for the propagation losses during the waveguide, which could not be reliably measured at the output wavelength  $\lambda_{\text{out}} = 553$  nm. We emphasise that this maximum efficiency is reached at very low pump pulse energies of  $E_{\text{pump}} = 15.77$  pJ in front of the waveguide, corresponding to a cw-equivalent power at 80 MHz repetition rate of only 1.26 mW. If we take into account our coupling efficiencies, we calculate an pulse energy of roughly 12.35 pJ inside



the waveguide. This is possible only because of the careful device engineering, which leads to the fact that the input light experiences the pump peak power level of around 42.2 W over the whole interaction length, due to their similar group velocities. If we compare this value to our theoretical considerations from Eq. (7.14), where we calculated a pump peak power of around 37 W, we find an excellent agreement to the measurement. The deviations originate from the finite propagation losses in the waveguide and from a non-perfect periodic poling. These two factors essentially lower the effective nonlinearity  $d_{\text{eff}}$ , leading to a power which is slightly higher than expected.

Fig. 7.12 (b) shows once more the depletion of the converted output spectrum when changing the TF shape of the pump. The big plot shows the output spectrum as measured with the CCD spectrometer, where we emphasise that, due to careful incoupling, only a single peak is excited in the output, and we applied no additional spectral filtering. The blue curve corresponds to a Gaussian pump, as shown in the upper inset, where the grey shaded area illustrates the Gaussian input signal. Switching the pump shape to a first-order Hermite-Gaussian, represented by the red curve in the lower inset, we record a depletion in the converted output. Note that in the spectral plots, error bars are smaller than the symbols and the dashed lines are a guide to the eye. We find a depletion of around 80%, when subtracting the flat background, represented by the grey-shaded region in the main plot, and integrating over the dominating peak. We identify this value with the mode-selectivity of our device, which is still a lower bound due to the finite resolution of the Dazzler. Although this value is already very good, we expect to improve it in future experiments by deploying a better pulse shaper.

## Summary

In this section we have demonstrated the experimental implementation and successful characterisation of a QPG. We have shown how the QPG TF mode structure can be revealed by probing the process with coherent basis states and demonstrated an adaption of the QPG input TF mode  $g_j(\lambda_{\text{in}})$  to an ‘unknown’ input state TF mode  $g(\lambda_{\text{in}})$ . Our measurements revealed a TF mode-selectivity of 80%, which is limited by the finite resolution of our pulse shaper. In addition, we measured an internal conversion efficiency of 87.8% for attenuated coherent input pulses with a mean photon number of  $\langle n \rangle = 0.15$ . The overall conversion efficiency evaluated to 24% including detector losses, which is a remarkable value, considering that our QPG converts complete ultrafast pulses. Again, this efficiency is a lower bound since our analysis neglected any losses inside our QPG sample. Our experiments are a proof-of-principle that our device facilitates operation on TF modes of quantum states and is thus a valuable building block for future high-dimensional TF quantum networks.

## 7.4 Next steps: Quantum pulse shaper

Let us now turn our attention towards the second device we studied theoretically during this work, the QPS. In this device, input light in the green wavelength regime is frequency down-converted to an output at 1535 nm, by mixing it with shaped pump pulses at 865 nm. Obviously, this process is simply the inverse of the QPG and consequently we find that pump and output travel at the same group velocity. This implies a phasematching function that is parallel to the



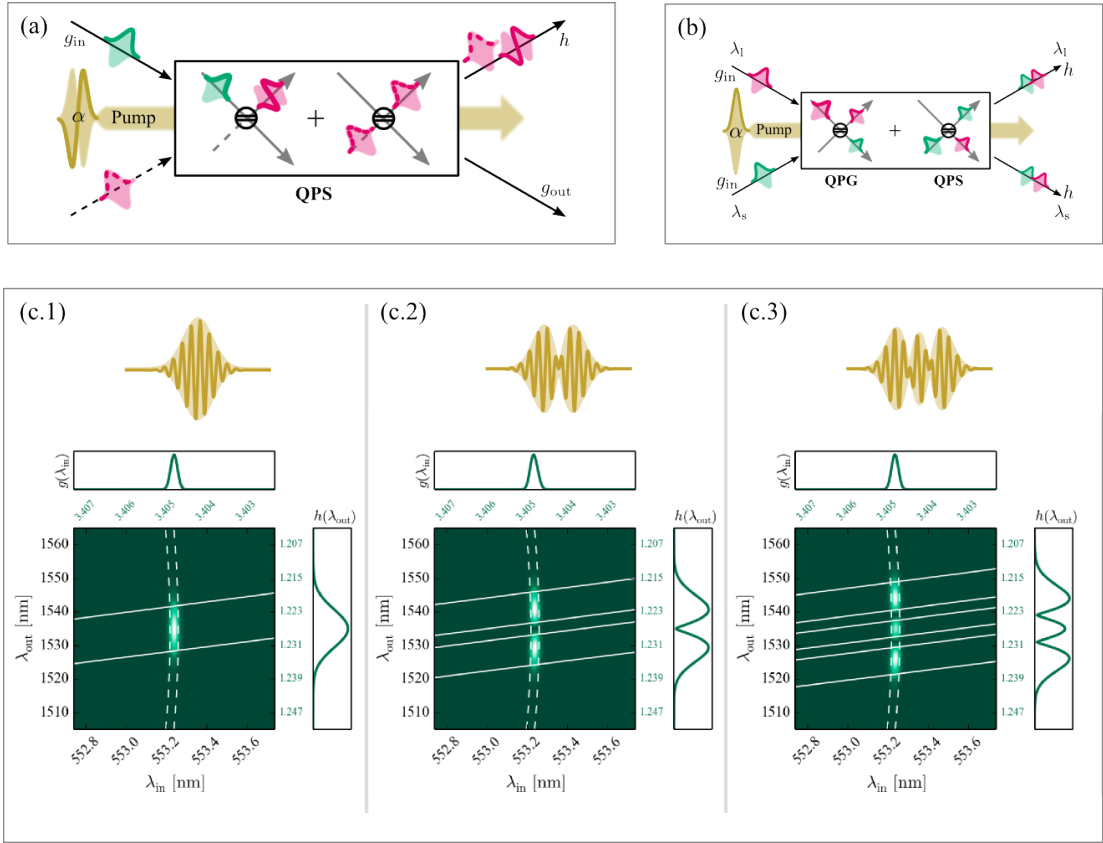


**Figure 7.13** – Schematic illustrating the operation principle of a QPS. Panel (a) depicts how a green input pulse is shaped into the TF mode defined by the pump. If an additional signal that is in an orthogonal TF mode compared to the pump is fed into the device (berry), the QPS acts as an add filter. In (b) we sketch how the combination of QPS and QPG operation can be exploited to implement a tuneable TF mode beamsplitter. Finally, in (c.1) to (c.3) we plot the JSA function  $G(\lambda_{\text{in}}, \lambda_{\text{out}})$  for three different shapes of pump pulses. Note that the input mode  $g(\lambda_{\text{in}})$  does not change, while the output mode  $h(\lambda_{\text{out}})$  mimics the pump shape.

$\omega_{\text{out}}$ -axis. Formally, we find that the QPS operation is given by

$$\hat{U}_{\text{QPS}} = \exp \left[ c_j^* \hat{C} \hat{A}_j^\dagger + \text{h.c.} \right], \quad (7.18)$$

which in correspondence to our explanation is the inverse of the QPG operation  $\hat{U}_{\text{QPG}}$ . Note that we also find that the input mode associated with  $\hat{C}$  is fixed, whereas the output mode  $\hat{A}_j^\dagger$  can be tuned.



We sketch this situation in Fig. 7.13. Panel (a) illustrates the QPS operation in a slightly more general way than discussed before. The green pulse labeled  $g_{\text{in}}$  is the input to the QPS at wavelength  $\lambda_{\text{in}}$ , which is reshaped by interacting with the yellow pump. Again, the inside of the box illustrates the special beamsplitters operating on the input TF modes. At the output, we find a pulse  $h$  with wavelength  $\lambda_{\text{out}}$  which mimics the shape of the pump, whereas nothing is transmitted. In addition, we can feed another pulse with wavelength  $\lambda_{\text{out}}$  into the QPS, which is indicated by the dotted arrow. If we assume that this pulse is orthogonal to the pump TF mode, it is simply transmitted. Hence, the QPS can serve as an add filter in TF mode networking applications.

In (b) we illustrate, how a combination of QPG and QPS operation can be exploited to implement a special, tuneable TF mode beamsplitter. Feeding two adapted pulses with wavelengths  $\lambda_l$  and  $\lambda_s$  (for long and short) into our device, both single mode SFG and DFG can occur simultaneously, if the input pulses overlap with the respective QPG / QPS input modes. By tuning the pump power such that only 50% conversion efficiency is achieved, the QPG converts half of the input pulse at  $\lambda_l$  to  $\lambda_s$ . In parallel, the QPS converts half of the pulse at  $\lambda_s$  to  $\lambda_l$ . Since QPG and QPS are inverse operations, the input modes of the QPG correspond to the output modes of the QPS and vice versa. Consequently, we find a perfect 50/50 TF mode beamsplitter and succeed in realising a mode-selective interference of quantum pulses at different frequencies, as suggested in [62].

For more details we analyse the JSA function  $G(\lambda_{\text{in}}, \lambda_{\text{out}})$  of the QPS in (c.1) to (c.3). The dashed white lines are the phasematching function, which in agreement to our theory is vertical. The solid white lines are the pump envelope function for different TF shapes of the pump (yellow pulses). The plots along the axes show the shape of the input and output modes  $g(\lambda_{\text{in}})$  and  $h(\lambda_{\text{out}})$ , respectively. In contrast to the QPG, where the output modes were fixed and the selected input modes corresponded to the pump (see Fig. 5.12), the QPS has fixed input modes which are defined by the phasematching. The output modes, however are defined by the shape of the pump and we note that input and output can have very different spectral bandwidths, as was the case for the QPG.

For a better comparison with the previous investigations, we have restricted this analysis to TF mode shapes from the Hermite-Gaussian framework. Note however that the QPS is in no way restricted to this. It is also possible to shape an input Gaussian into an output exponential function, which might become beneficial in the future for the coupling of light to quantum memories.

As a final remark we want to emphasise that, although QPG and QPS are described in a purely quantum optical framework, both processes also work for bright light. Hence it is not unlikely that they impact the field of ultrafast physics. A possible application would be the generation of tuneable, ultrafast optical pulses at telecommunication wavelengths from a cw input field in the visible, or vice versa when adapting the dispersion properties accordingly.



## Summary

We have discussed a second device, the quantum pulse shaper, which is the natural opposite of the quantum pulse gate. Whereas the quantum pulse gate facilitates the selection of one mode from a multimode input, the quantum pulse shaper allows for the almost arbitrary reshaping of an input TF mode. In addition, it can be utilised to add new TF modes to an already existing state. In conjunction, quantum pulse gate and quantum pulse shaper provide complete add/drop functionality for high-dimensional TF mode quantum networks.



Es ist eine rätselhafte Sache um die menschlichen Leidenschaften und Kindern geht es damit nicht anders als Erwachsenen. Diejenigen, die davon befallen werden, können sie nicht erklären und diejenigen, die nichts dergleichen je erlebt haben, können sie nicht begreifen.

*Michael Ende - Die unendliche Geschichte*

# 8

---

## Conclusion and outlook

---

### 8.1 Conclusion

This thesis gave us the possibility to study the exciting fields of ultrafast quantum optics and to contribute to its current progress. In this comparably young research area, the properties of ultrafast pulses are combined with the intriguing possibilities of quantum optics to pave the way towards novel quantum applications. Of these, high-dimensional quantum information networks based on time-frequency (TF) modes of ultrafast quantum states of light were one of the main driving forces behind our research.

We have investigated the intricate TF structure of quantum optical states generated in the process of ultrafast parametric down-conversion (PDC). Before this thesis, our group developed a dispersion engineered PDC source which exhibited exceptional properties [53] like a continuously tuneable number of TF modes. This source was further optimised in parallel to our work [54] and we deployed it to study the effect of different pumping conditions on the generated photon pair. We demonstrated that, surprisingly, the temporal coherence properties of the pump do not influence the correlation time of the photon pair, a quantity which measures the simultaneity of the photons and is tantamount to the maximum timing information that can be extracted from the state. In contrast, our studies revealed that the correlation time is solely defined by material parameters of the source, a fact which we could also verify experimentally. This result allowed us to identify operating conditions that either facilitate a gain in timing information or enforce a loss of it. We derived an easy analytical expression directly applicable to many current PDC sources, which will allow other groups to critically crosscheck their experimental settings in light of these results.

In addition, we studied the TF correlations of PDC states from a more fundamental point of view. Entanglement, one of the most fascinating features of quantum mechanics, manifests itself in nonlocal correlations between two parties. It has been shown that parametric down-conversion can generate optical EPR states, where the generated signal and idler have nonclassical correlations between their conjugate field quadratures. We transferred this picture to the spectral-temporal domain, by investigating TF correlations in a PDC photon pair. Interestingly,

an apparent Fourier limit of the spectral and temporal widths can be overcome when TF correlations are present in the state. We formulated a complete four-dimensional chronocyclic Wigner theory of the spectral-temporal properties of PDC states and introduced a novel TF entanglement measure, namely the inverse conditioned-time bandwidth product, which quantifies these correlations in a way known from the treatment of optical EPR correlations [84]. With this work, we managed to build a bridge between two seemingly disparate descriptions of PDC: the discrete variable description on the one hand and the continuous variable description on the other.

Moreover, we conducted a theoretical study to investigate the effects of time-ordering on ultrafast parametric processes [76]. As opposed to the common theoretical treatment, the Hamiltonians of parametric processes do not commute between two instants of time. We carried out numerical studies and found that time-ordering drives parametric down-conversion towards a single TF mode operation regime. On the downside, it suggests an upper limit to the operation fidelity of our frequency conversion devices. This is a result which has to be investigated in more detail in the future.

Finally, the main part of our work was concerned with research on ultrafast frequency translation of photons. We introduced two novel devices, the quantum pulse gate (QPG) and the quantum pulse shaper (QPS), which facilitate a TF mode-selective operation on quantum pulses [60, 61]. Both devices are based on group-velocity matched conversion processes in lithium niobate waveguides. In the case of the QPG, the ultrafast pump pulses and the quantum input pulses travel at the same velocity, whereas in the case of the QPS, it is pump and output that share one velocity.

A detailed theoretical study of the QPS suggests that it can be used to reshape single photon pulses in a quantum coherent way without introducing losses. In addition, since the QPS operation can be modelled with a special quantum mechanical beamsplitter, the QPS preserves the quantum characteristics of the input photon. In contrast, we have seen that the QPG can be deployed to select one specific TF mode from a multimode input state. The selected mode is converted to another frequency, while the remaining modes are transmitted. Classical pulse shaping of the ultrafast pump pulses defines the shape of the selected mode. Since every mode is converted into the same output, interference between formerly orthogonal modes becomes possible after the QPG operation.

During this thesis we succeeded in implementing a working QPG. We characterised our device and found a TF mode-selectivity of at least 80% together with an internal conversion efficiency of 87.7%. These outstanding values were achieved with very low pump pulse energies of only 12.4 pJ inside the waveguide, which is only possible thanks to the careful dispersion engineering of our device. Note that these benchmarks are already satisfying for a proof-of-principle demonstration, but we expect to improve them in future experiments by deploying better equipment, particularly for the shaping of the ultrafast pump pulses.

## 8.2 Outlook

Let us now put the results of this work into a broader context and highlight possible continuations of this thesis. We have discussed the QPG in light of an operation on single photons. Yet,



our theoretical framework is also valid in the CV regime, where higher order photon numbers are crucial. In particular, the QPG, when operated at low conversion efficiencies, can be deployed to implement a mode-selective photon subtraction. This operation is a prerequisite for CV entanglement distillation [188] as well as the generation of exotic quantum states of light light Schrödinger cat and kitten states [189, 190].

As a result of this thesis, we are currently collaborating with the group of Nicholas Treps in Paris to realise a CV QPG for a mode-selective operation on multimode quantum frequency combs [59]. This is also interesting in light of measurement based quantum computation schemes, where different nodes of a large graph state – realised for instance by a multimode quantum frequency comb – must be connected in a distinct order. Here, the QPG can play the role of *linker* to establish the connections between the different nodes.

Another natural application of the QPG technology becomes apparent, when considering the capability of the QPG to convert any frequency inside its acceptance bandwidth to the same output spectrum. This, in combination with a high-density quantum dot sample can be an appealing approach to a deterministic single-photon source. Typically, quantum dots in an ensemble have slightly different emission frequencies, due to their mutual interaction with the sample. This prevents a direct use of several quantum dot sources in a quantum network, where indistinguishable photons are indispensable. Ways to tune single dots, for instance by a field-induced Stark shift, have been demonstrated, but they require a fine control over many parameters for a large number of devices. In contrast, collecting and converting the photons generated by the quantum dots with a QPG automatically translates them to the same frequency, without the need for controlling many parameters. Further research along these lines with a special focus on achievable efficiencies and photon generation rates may provide interesting new technologies and another link between the fields of semiconductor quantum optics and nonlinear quantum optics.

A further branch of future research is the combination of a PDC source and one or more QPGs. First, a QPG can be used to select a specific TF mode from a PDC state. Heralding on the output of the QPG prepares a pure single-photon pulse in the chosen TF shape in the other arm of the PDC. In this way, the generation of specific TF modes for networking applications is feasible. The question is, how the heralded state preparation can be verified. There are two obvious ways: first, one can simply measure the spectrum of the prepared single photons; second, the temporal shape of the prepared photons can be analysed;

Measuring the temporal shape of the heralded photon directly is challenging due to its ultra-short duration. Still, a possible way to achieve this is to deploy single photon sensitive streak cameras with picosecond resolution. We are planning on doing this in the framework of a research grant in collaboration with the group of Manfred Bayer from the University of Dortmund.

Another possibility is the evaluation of the photon number statistics, on the one hand directly at the output of the PDC, and on the other hand behind the QPG. It is well-known that for a single-mode PDC state, signal and idler exhibit thermal photon number statistics, which yield a second-order correlation function of  $g^{(2)} = 2$ , whereas for a multimode PDC, we obtain  $g^{(2)} = 1$ . Since the QPG can be described as a beamsplitter, it can only alter the photon number statistics of light when it operates on the TF modes. Hence, measuring  $g^{(2)} = 2$  at the output of the QPG, while measuring a lower  $g^{(2)}$  directly behind the PDC proves the selection of a single mode. These are immediate steps we are currently undertaking in our labs.



Further steps will include the more thorough investigation of quantum states exhibiting a well-defined number of TF modes generated with our PDC source. We have shown theoretically, that shaping the bright PDC pump pulses directly affects the TF structure of the generated PDC states. We plan to exploit this feature to create higher-dimensional entanglement in a very controlled way suited to experimental work. As a first experiment, we envision our PDC source with two successive QPGs, one in each arm of the PDC, to verify the higher-dimensional entanglement. For this task it is beneficial that the QPG, although performing a TF single-mode operation, not necessarily operates on only one TF mode of the input state. A clever shaping of the pump pulses facilitates an operation on multiple input TF modes, connecting them in arbitrary ways. Thus, we are able to measure the TF correlations in the original as well as in a conjugate basis with our QPGs. We recall that higher-dimensional entanglement is interesting not only for investigating fundamental questions on non-locality [159], but also for quantum information applications, where it for instance promises an increased security in quantum cryptography [93].

Our second device, the QPS has been theoretically shown to facilitate a quantum coherent reshaping of single-photon pulses. However, as for the QPG, the theoretical framework is not limited to single photons. An interesting research task will be to study the QPS as an alternative pulse shaper for classical pulses. At the moment, pulse shaping capabilities are best developed for Ti:Sapph wavelengths between 700 nm and 950 nm. The QPS as discussed in this thesis facilitates the generation of shaped pulses at telecommunication wavelengths from cw input light in the green. This could be an appealing alternative to common Ti:Sapph / OPO systems, if the conversion efficiencies and resulting pulse energies are large enough. Given a positive outcome of this research, we foresee a potential for the foundation of a spin-off company here.

Coming back to quantum optics, we have already shown theoretically, that the QPS can be operated as an add-device for TF multimode quantum networks. Together with the QPG, complete add/drop functionality can be implemented, paving the way towards a TF multiplexing in quantum communication. This prospect is beneficial, since TF modes are compatible with existing single-mode fiber networks, and, due to their careful engineering, QPS and QPG are highly energy efficient devices. In light of telecommunication applications, these features promises a huge amount of savings compared to other approaches based on spatial multiplexing, which require a replacement of most fibers.

The last aspect we want to highlight here is the interfacing between stationary and flying qubits. We have demonstrated that the QPG implements a bandwidth compression from input light to output light of more than an order of magnitude. This value can be increased by deploying longer waveguides. In contrast, the QPS facilitates a coherent reshaping of quantum pulses, allowing for the generation of exponential pulses. It will be highly interesting to assess the limitations of both devices and find ways to exploit them to couple photons from TF quantum networks to narrow bandwidth quantum memories.

In conclusion, the answers we found during this thesis gave rise to even more questions. Our results have laid a solid basis for the advancement of research on ultrafast TF modes of quantum states of light in the single-photon as well as in the CV regime. We have identified possible further research lines and highlighted collaborations that have emerged as a result of this thesis.



---

# Acknowledgements

---

I've had the wonderful opportunity to spend several years researching a truly fascinating topic and contributing to a young and emerging research field. Before this time I could not possibly have imagined the thrill of doing something which has never been done before. Now, after finishing this thesis, I find that this work would not have come to life without the help of many outstanding and extra-ordinary people whom I want to thank.

The foremost thanks goes to my supervisor and guide Professor Christine Silberhorn. Her guidance over the long years since I joined her group as a student helper has been, and will be, invaluable. I very much appreciate her support during the time of our transition to Paderborn, when she made it possible for me to spend much time with my wife on the weekends. Also I want to thank her for the trust she put in me, both in research and administration and for never making me regret to have chosen this path. I really enjoyed these years and am looking forward into the future.

Sincerest thanks then goes to my wife, who never stopped supporting me. I know that I often had science on my mind when reality would have been more appropriate, and I apologise for that. I'm grateful to you for putting up with my work and I'm looking forward to our time together abroad.

Onto all the great colleagues I had the pleasure working with. You guys rock! Special thanks to Hendrik Coldenstrod-Ronge for introducing me to the group in the first place, and to Christoph Söller for supervising my Diploma thesis. I learned a lot from both of them. Further thanks to Malte Avenhaus, for unveiling the mysteries of Apple and Python in a fully non-religious sense. Thanks to Thomas Nitsche and Vahid Ansari, who both survived my supervision and are still carrying on with physics. Thanks heaps, Michael Stefszky, for proofreading my thesis and for introducing me to continuous variable quantum optics. A big "Thank you!" to Fabian Katzschmann and Stephan Krapick, simply for friendship. Many thanks Andreas Christ, for never tiring to try to explain to me this shady thing called *theory* and for being around for so long. Big thanks to Sonja Barkhofen, Matthias Bechert, Agata Brańczyk, Patrick Bronner, Katiúscia Casemiro, Thomas Dirmeier, Olga Driesner, Andreas Eckstein, Christof Eigner, Georg Harder, Harald Herrmann, Felix Just, Regina Kruse, Kaisa Laiho, Thomas Lauckner, Sarah Leineweber, Kai-Hong Luo, Wolfgang Mauerer, Peter Mosley, Viktor Quiring, Raimund Ricken, Peter Rohde, Helge Rütz, Linda Sansoni, Andreas Schreiber and Hubertus Suche, for making my work enjoyable and fun throughout the years, and for actively increasing my knowledge with countless discussions, both scientific and real-world related.

To our secretaries, Rita Prevor and Irmgard Zimmermann, thank you. Without your constant

help the administration would have been too much. Also thanks for always being willing to chat when I was not feeling like physics at all. I always enjoy being around.

Then there is my best friend, Christian, who, to me, is like a brother. Thank you for the fun hours, the nice evenings and long nights. Thank you for all these good years. I always appreciated you keeping me real.

Last but not least I want to thank all members of my family. Thank you for giving me the opportunity to study physics, thank you for your long lasting support and thank you for being there. Special thanks to my mother for taking in Olga in times of need and for genuine honesty when giving advice.

# A

---

## Appendix

---

### A.1 Derivation of the vectorial wave equations in waveguides

In section 4.1 we present the vectorial wave equations of an electromagnetic wave inside a waveguide. Here we illustrate how they are derived from Maxwell's equations.

Maxwell's equations for a lossless, dielectric medium with spatially varying permittivity  $\varepsilon(\mathbf{r})$  are given by

$$\nabla \mathbf{D} = 0, \quad (\text{A.1})$$

$$\nabla \mathbf{B} = 0, \quad (\text{A.2})$$

$$\nabla \times \mathbf{E} = -\omega \mathbf{B}, \quad (\text{A.3})$$

$$\nabla \times \mathbf{B} = \omega \mu_0 \mathbf{D}, \quad (\text{A.4})$$

with  $\frac{1}{\sqrt{\varepsilon_0 \mu_0}} = c$ , where we have used the harmonic ansatz  $\mathbf{E}, \mathbf{B} \propto \exp(-i\omega t)$ . Applying an additional curl operator to Eq. (A.3) yields

$$\nabla \times (\nabla \times \mathbf{E}) = -i\omega (\nabla \times \mathbf{B}) \stackrel{(\text{A.4})}{=} \omega^2 \mu_0 \mathbf{D}. \quad (\text{A.5})$$

By substituting  $\mathbf{D} := \varepsilon_0 \varepsilon(\mathbf{r}) \mathbf{E}$ , we find

$$\nabla \times (\nabla \times \mathbf{E}) = \frac{\omega^2}{c^2} \varepsilon(\mathbf{r}) \mathbf{E}. \quad (\text{A.6})$$

We replace the lefthand side of Eq. (A.6) with the identity

$$\nabla \times (\nabla \times \mathbf{E}) = \nabla(\nabla \mathbf{E}) - \Delta \mathbf{E} \quad (\text{A.7})$$

and rewrite with Eq. (A.1)

$$\begin{aligned} \nabla \mathbf{D} = 0 &= \nabla(\varepsilon_0 \varepsilon(\mathbf{r}) \mathbf{E}) = \varepsilon_0 [(\nabla \varepsilon(\mathbf{r})) \mathbf{E} + \varepsilon(\mathbf{r}) \nabla \mathbf{E}], \\ \Rightarrow \nabla \mathbf{E} &= - \left( \frac{\nabla \varepsilon(\mathbf{r})}{\varepsilon(\mathbf{r})} \right) \mathbf{E}. \end{aligned} \quad (\text{A.8})$$

Putting things together, we retrieve the wave equation from Eq. (A.6):

$$\Delta \mathbf{E} + \frac{\omega^2}{c^2} \varepsilon(\mathbf{r}) \mathbf{E} + \nabla \left[ \left( \frac{\nabla \varepsilon(\mathbf{r})}{\varepsilon(\mathbf{r})} \right) \cdot \mathbf{E} \right] = 0. \quad (\text{A.9})$$

For the second wave equation, we apply a second curl operator to Eq. (A.4):

$$\nabla \times (\nabla \times \mathbf{B}) = i \frac{\omega}{c^2} \nabla \times (\varepsilon(\mathbf{r}) \mathbf{E}). \quad (\text{A.10})$$

For the lefthand side, we deploy the same identity as before. Additionally, we reuse

$$\nabla \times (\varepsilon(\mathbf{r}) \mathbf{E}) = \varepsilon(\mathbf{r}) (\nabla \times \mathbf{E}) + (\nabla \varepsilon(\mathbf{r})) \times \mathbf{E}, \quad (\text{A.11})$$

which leaves us with

$$-\Delta \mathbf{B} = \frac{\omega^2}{c^2} \varepsilon(\mathbf{r}) \mathbf{B} + i \frac{\omega}{c^2} (\nabla \varepsilon(\mathbf{r})) \times \mathbf{E}. \quad (\text{A.12})$$

Now, we identify

$$i \frac{\omega}{c^2} \mathbf{E} \stackrel{(\text{A.4})}{=} \frac{1}{\varepsilon(\mathbf{r})} \nabla \times \mathbf{B} \quad (\text{A.13})$$

and finally end up with

$$\Delta \mathbf{B} + \frac{\omega^2}{c^2} \varepsilon(\mathbf{r}) \mathbf{B} + \left[ \frac{\nabla \varepsilon(\mathbf{r})}{\varepsilon(\mathbf{r})} \times (\nabla \times \mathbf{B}) \right] = 0, \quad (\text{A.14})$$

which is the second vectorial wave equation.

## A.2 Calculation of the electric field strength

In equation (4.14), we truncated the Taylor expansion of the nonlinear polarisation after the second order term. We reasoned that the third order term was several orders of magnitude smaller, because of the given electric field strength. For the convenience of the reader, we briefly detail how the field strength is actually calculated. Note that these calculations assume a continuous wave laser and are only approximately correct in our case of ultrafast laser pulses.

The peak intensity of a spatially Gaussian laser beam with an  $\frac{1}{e}$ -width of  $d$  and an optical power  $P$  is given by [191]

$$I = \frac{P}{\pi d^2/2}. \quad (\text{A.15})$$

Furthermore, the intensity is related to the electric field amplitude  $|E|$  by

$$I = \frac{1}{2} c \varepsilon_0 n |E|^2, \quad (\text{A.16})$$

where  $c$  is the speed of light,  $\varepsilon_0$  is the vacuum permittivity and  $n$  is the refractive index of the medium. Typical parameters for our experiments are a cw-equivalent power of less than 10 mW, a refractive index of  $n \approx 2$  and a beam width inside the waveguide of  $d \approx 6 \mu\text{m}$ . Putting things together we obtain

$$|E| = \sqrt{\frac{4P}{\pi d^2 c \varepsilon_0 n}} \approx 2.58 \cdot 10^5 \frac{\text{V}}{\text{m}}, \quad (\text{A.17})$$

which is the value we used in the main text.

## A.3 The dielectric tensor

### A.3.1 Kleinman symmetry

The  $\chi^{(2)}$ -nonlinearity is generally a tensor of rank three. Since it reflects the response of the medium to the incoming light wave, it is essentially frequency independent as long as the light frequency  $\omega$  is much smaller than any resonance frequency  $\omega_r$  of the material. This assumption is true for the transparency window of the nonlinear materials. In this case, we can also assume a lossless medium, for which a complete permutation symmetry must be valid [50]:

$$\begin{aligned}\chi_{ijk}^{(2)}(\omega_3 = \omega_1 + \omega_2) &= \chi_{jki}^{(2)}(\omega_1 = -\omega_2 + \omega_3) = \chi_{kij}^{(2)}(\omega_2 = \omega_3 - \omega_1) = \\ &= \chi_{ikj}^{(2)}(\omega_3 = \omega_2 + \omega_1) = \chi_{jik}^{(2)}(\omega_1 = \omega_3 - \omega_2) = \\ &= \chi_{kji}^{(2)}(\omega_2 = -\omega_1 + \omega_3).\end{aligned}\quad (\text{A.18})$$

However, we have just stated that the nonlinearity is frequency independent. Hence, we can permute the frequencies without regarding the order of the indices to end up with

$$\begin{aligned}\chi_{ijk}^{(2)}(\omega_3 = \omega_1 + \omega_2) &= \chi_{jki}^{(2)}(\omega_3 = \omega_1 + \omega_2) = \chi_{kij}^{(2)}(\omega_3 = \omega_1 + \omega_2) = \\ &= \chi_{ikj}^{(2)}(\omega_3 = \omega_1 + \omega_2) = \chi_{jik}^{(2)}(\omega_3 = \omega_1 + \omega_2) = \\ &= \chi_{kji}^{(2)}(\omega_3 = \omega_1 + \omega_2).\end{aligned}\quad (\text{A.19})$$

This outcome is called the *Kleinman symmetry condition*, which we can safely apply for our case of light frequencies far away from any material resonance that is absorption line.

### A.3.2 Nonlinear tensor and contracted notation

Given that the Kleinman symmetry condition holds, we can define a rank three tensor  $\mathbf{d} = \frac{1}{2}\chi^{(2)}$  [50]. With this we can formally rewrite the nonlinear polarisation:

$$P_{\text{NL}}^{(i)}(\omega_n + \omega_m) = \sum_{jk} \sum_{(nm)} 2d_{ijk} E_j(\omega_n) E_k(\omega_m).\quad (\text{A.20})$$

In this cumbersome notation, the indices  $i, j, k$  label the coordinate axes of our reference frame and the frequencies  $\omega_n$  and  $\omega_m$  are chosen such that  $\omega_n + \omega_m = \text{const.}$  We now assume that  $d_{ijk}$  is symmetric in its last two indices, which is valid as long as the Kleinman symmetry holds. This allows us to define a contracted notation according to

$$\begin{array}{l}jk: \quad 11 \quad 22 \quad 33 \quad 23,32 \quad 31,13 \quad 12,21 \\ l: \quad 1 \quad 2 \quad 3 \quad 4 \quad 5 \quad 6\end{array}\quad (\text{A.21})$$

Now, the nonlinear tensor  $\mathbf{d}$  can be represented as a 3x6 matrix

$$d_{il} = \begin{bmatrix} d_{11} & d_{12} & d_{13} & d_{14} & d_{15} & d_{16} \\ d_{21} & d_{22} & d_{23} & d_{24} & d_{25} & d_{26} \\ d_{31} & d_{32} & d_{33} & d_{34} & d_{35} & d_{36} \end{bmatrix}\quad (\text{A.22})$$

Considering closely our symmetry conditions, we find that not all elements of this tensor are linearly independent. For instance, we see that  $d_{12} \equiv d_{122} = d_{212} \equiv d_{26}$  and finally recover only ten independent elements. Thus we can rewrite the nonlinear tensor:

$$d_{il} = \begin{bmatrix} d_{11} & d_{12} & d_{13} & d_{14} & d_{15} & d_{16} \\ d_{16} & d_{22} & d_{23} & d_{24} & d_{14} & d_{12} \\ d_{15} & d_{24} & d_{33} & d_{23} & d_{13} & d_{14} \end{bmatrix} \quad (\text{A.23})$$

Taking care of the degeneracy factor which distinguishes SHG and SFG/DFG, we find the nonlinear polarisation for an SHG process:

$$\begin{bmatrix} P_x(2\omega) \\ P_y(2\omega) \\ P_z(2\omega) \end{bmatrix} = 2 \begin{bmatrix} d_{11} & d_{12} & d_{13} & d_{14} & d_{15} & d_{16} \\ d_{16} & d_{22} & d_{23} & d_{24} & d_{14} & d_{12} \\ d_{15} & d_{24} & d_{33} & d_{23} & d_{13} & d_{14} \end{bmatrix} \begin{bmatrix} E_x(\omega)^2 \\ E_y(\omega)^2 \\ E_z(\omega)^2 \\ 2E_y(\omega)E_z(\omega) \\ 2E_x(\omega)E_z(\omega) \\ 2E_x(\omega)E_y(\omega) \end{bmatrix}. \quad (\text{A.24})$$

In addition, we can write the nonlinear polarisation for an SFG process in which  $\omega_3 = \omega_1 + \omega_2$  as

$$\begin{bmatrix} P_x(\omega_3) \\ P_y(\omega_3) \\ P_z(\omega_3) \end{bmatrix} = 4 \begin{bmatrix} d_{11} & d_{12} & d_{13} & d_{14} & d_{15} & d_{16} \\ d_{16} & d_{22} & d_{23} & d_{24} & d_{14} & d_{12} \\ d_{15} & d_{24} & d_{33} & d_{23} & d_{13} & d_{14} \end{bmatrix} \begin{bmatrix} E_x(\omega_1)E_x(\omega_2) \\ E_y(\omega_1)E_y(\omega_2) \\ E_z(\omega_1)E_z(\omega_2) \\ E_y(\omega_1)E_z(\omega_2) + E_y(\omega_2)E_z(\omega_1) \\ E_x(\omega_1)E_z(\omega_2) + E_x(\omega_2)E_z(\omega_1) \\ E_x(\omega_1)E_y(\omega_2) + E_x(\omega_2)E_y(\omega_1) \end{bmatrix}. \quad (\text{A.25})$$

### A.3.3 Lithium niobate and potassium titanyl phosphate

For the two nonlinear material systems used during this work, the nonlinear optical tensors are considerably simplified. For LN we find [72]

$$\mathbf{d}_{\text{LN}} = \begin{bmatrix} 0 & 0 & 0 & 0 & d_{15} & -d_{22} \\ -d_{22} & d_{22} & 0 & d_{15} & 0 & 0 \\ d_{31} & d_{31} & d_{33} & 0 & 0 & 0 \end{bmatrix}, \quad (\text{A.26})$$

whereas for KTP the nonlinear tensor is given by

$$\mathbf{d}_{\text{KTP}} = \begin{bmatrix} 0 & 0 & 0 & 0 & d_{15} & 0 \\ 0 & 0 & 0 & d_{24} & 0 & 0 \\ d_{31} & d_{32} & d_{33} & 0 & 0 & 0 \end{bmatrix}. \quad (\text{A.27})$$

Let us briefly explain how to understand these tensors. We assume a SFG process in KTP, where the incoming light fields have frequencies of  $\omega_1$  and  $\omega_2$  and are both polarised along the  $x$  direction. The resulting nonlinear polarisation will be only oriented along the  $z$  direction, since only the  $d_{31}$  component couples to the incoming light. Similar conclusions can be drawn for any combination of input fields.

## A.4 Three-wave mixing Hamiltonian

In Sec. 5.1.2, we present the three-wave mixing Hamiltonian  $\hat{H}_{\text{TWM}}$ . Here, we go into the derivation of this Hamiltonian. To this end, we assume three quantum fields  $\hat{E}_1$ ,  $\hat{E}_2$  and  $\hat{E}_3$  and drop the time- and space-dependence in our notation. Using the relation

$$\hat{E} = \hat{E}^+ + \hat{E}^-, \quad (\text{A.28})$$

where  $\hat{E}^+$  comprises the annihilation operator and  $\hat{E}^-$  the creation operator, respectively, we can perform the calculations, which yield

$$\begin{aligned} \hat{H}_{\text{TWM}} &\propto \int_V d\mathbf{r} \underbrace{(\hat{E}_1 + \hat{E}_2)(\hat{E}_1 + \hat{E}_2)}_{\propto \hat{P}_{\text{NL}}} \hat{E}_3 = \\ &= \int_V d\mathbf{r} \left( (\hat{E}_1^+)^2 + (\hat{E}_1^-)^2 + (\hat{E}_2^+)^2 + (\hat{E}_2^-)^2 + 2\hat{E}_1^+ \hat{E}_1^- + 2\hat{E}_2^+ \hat{E}_2^- + \right. \\ &\quad \left. + 2\hat{E}_1^+ \hat{E}_2^+ + 2\hat{E}_1^- \hat{E}_2^- + 2\hat{E}_1^+ \hat{E}_2^- + 2\hat{E}_1^- \hat{E}_2^+ \right) (\hat{E}_3^+ + \hat{E}_3^-) = \\ &= \int_V d\mathbf{r} \left[ \underbrace{(\hat{E}_3^+ \hat{E}_1^- \hat{E}_1^- + \text{h.c.}) + (\hat{E}_3^- \hat{E}_2^- \hat{E}_2^- + \text{h.c.}) + (2\hat{E}_3^+ \hat{E}_1^- \hat{E}_2^- + \text{h.c.})}_{\text{PG}} \right. \\ &\quad \left. + \underbrace{(2\hat{E}_3^+ \hat{E}_1^- \hat{E}_2^+ + \text{h.c.}) + (2\hat{E}_3^- \hat{E}_1^+ \hat{E}_2^- + \text{h.c.})}_{\text{SFG/DFG}} \right. \\ &\quad \left. + \underbrace{(2\hat{E}_3^+ \hat{E}_1^+ \hat{E}_1^- + \text{h.c.}) + (2\hat{E}_3^- \hat{E}_2^+ \hat{E}_2^- + \text{h.c.})}_{\text{optical Rectification}} \right. \\ &\quad \left. + \underbrace{(\hat{E}_3^+ \hat{E}_1^+ \hat{E}_1^+ + \text{h.c.}) + (\hat{E}_3^- \hat{E}_2^+ \hat{E}_2^+ + \text{h.c.}) + (2\hat{E}_3^+ \hat{E}_1^+ \hat{E}_2^+ + \text{h.c.})}_{\text{to be considered}} \right] \quad (\text{A.29}) \end{aligned}$$

As marked, the first line of the final expression marks parametric generation (PG) processes, during which one photon of the field  $\hat{E}_3$  decays into a pair of photons which can be distributed between fields  $\hat{E}_1$  and  $\hat{E}_2$ . Note that these terms also describe SHG, which is not present with only quantum fields at the input. The second line describes SFG/DFG processes in agreement to our classical considerations. The third line consists of the optical rectification terms, which we neglect throughout this thesis and which are included here only for reasons of completeness. This leaves us with the fourth line, which has a highly peculiar structure. It includes only terms corresponding to the simultaneous creation or annihilation of three photons. These have to be considered in light of the Manley-Rowe relations [50].

The Manley-Rowe relations relate the photon decay and creation rates for the different fields in three-wave mixing processes. In short, they define three conserved quantities, which can be written as

$$M_1 = \frac{\langle n_2 \rangle^2}{\omega_2} + \frac{\langle n_3 \rangle^2}{\omega_3}, \quad M_2 = \frac{\langle n_1 \rangle^2}{\omega_1} + \frac{\langle n_3 \rangle^2}{\omega_3}, \quad M_3 = \frac{\langle n_1 \rangle^2}{\omega_1} - \frac{\langle n_2 \rangle^2}{\omega_2}. \quad (\text{A.30})$$

Here,  $\langle n_j \rangle^2 \propto I_j$  denotes the mean photon number in field  $j$  which is a measure for the field intensity. We can learn from these quantities that the rate at which photons in field one are created is equal to the rate at which photons in field two are created and is equal to the rate at which photons in field three are *annihilated*.

Hence, we find that the last line in our Hamiltonian consists of terms which violate the Manley-Rowe relations and thus are not physical and can be dropped. Now we can write down a simplified version of  $\hat{H}_{\text{TWM}}$ , which reads

$$\begin{aligned} \hat{H}_{\text{TWM}} \propto \int_V d\mathbf{r} & \left[ \hat{E}_3^+ (\hat{E}_1^-)^2 + \hat{E}_3^+ (\hat{E}_2^-)^2 + \hat{E}_3^+ \hat{E}_1^- \hat{E}_2^- \right. \\ & \left. + 2\hat{E}_3^+ \hat{E}_1^- \hat{E}_2^+ + 2\hat{E}_3^+ \hat{E}_1^+ \hat{E}_2^- + \text{h.c.} \right]. \end{aligned} \quad (\text{A.31})$$

Taking advantage of our freedom to relabel the quantum fields, we can even contract this Hamiltonian and finally obtain

$$\hat{H}_{\text{TWM}} \propto \int_V d\mathbf{r} \left[ 2\hat{E}_3^+ (\hat{E}_1^-)^2 + \hat{E}_3^+ \hat{E}_1^- \hat{E}_2^- + 4\hat{E}_3^+ \hat{E}_1^+ \hat{E}_2^- + \text{h.c.} \right]. \quad (\text{A.32})$$

## A.5 4-f-spectrometer with tilted slit

In our experimental PDC setup we deploy a 4-f-spectrometer to shape the spectrum of the ultrafast pump pulses. In this setup, we rotated the slit of the spectrometer to realise an effective Gaussian spectral filtering [54]. We briefly sketch this situation in Fig. A.1. The plots always show the light distribution at the slit in the centre of the spectrometer. In a 4-f-spectrometer, a dispersive element (in our scenario a grating) maps the wavelength of the incoming light to the propagation direction of the refracted light. A subsequent lens maps the angle degree of freedom to the spatial domain (in  $x$ -direction), where it can be conveniently processed with spatial filtering. The remaining components perform the retransformation.

In panel (a), we plot the wavelength distribution of a laser pulse at the position of the slit. The filtering function of a common vertical slit is illustrated as light and dark shaded area. Panel (b) shows the filtered distribution right behind the slit and the projection onto the wavelength axis shows the processed spectral distribution with the typical *flattop* profile.

Already a small rotation of the slit smooths out the sharp edges in the spectrum, as shown in (c) and (d). However, there is still a little bit of the flattop left, which completely vanishes for larger tilt rotations (e), (f). Note however that the rotation of the slit also diminishes the spectral resolution of the setup, hence a trade-off between spectral shape and resolution has to be made.

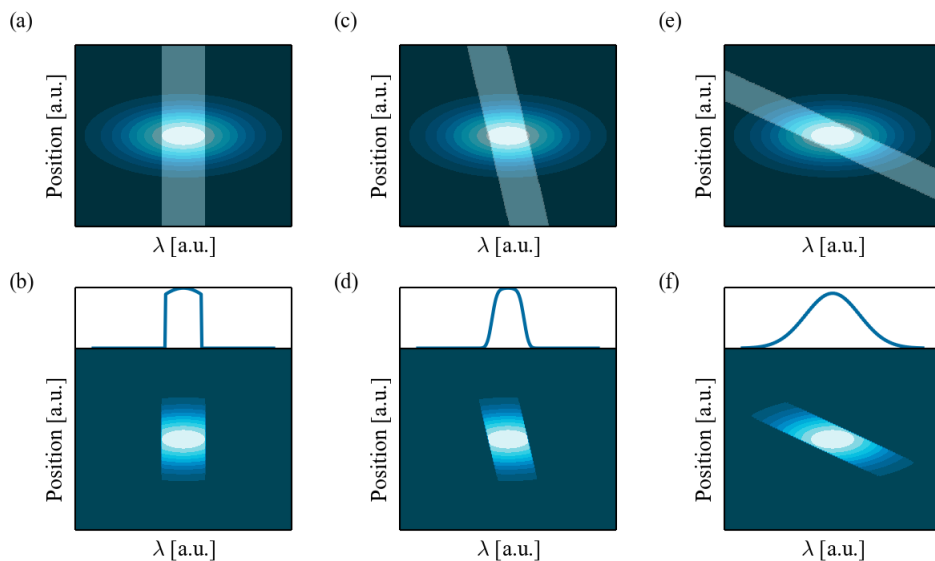


**Figure A.1** – Illustration of the impact of different spatial orientations of the slit in a 4-f-spectrometer on the processed output spectrum. For more information see the text.

---

## References

---

- [1] M. Planck. “Ueber irreversible Strahlungsvorgänge”. *Annalen der Physik* **306**, 69–122 (1900).
- [2] A. Einstein. “Über einen die Erzeugung und Verwandlung des Lichtes betreffenden heuristischen Gesichtspunkt”. *Annalen der Physik* **322**, 132–148 (1905).
- [3] L. d. Broglie. “XXXV. A tentative theory of light quanta”. *Philosophical Magazine Series 6* **47**, 446–458 (1924).
- [4] E. Schrödinger. “An undulatory theory of the mechanics of atoms and molecules”. *Physical Review* ... **28**, 1049–1070 (1926).
- [5] W. Heisenberg. “Über quantentheoretische Umdeutung kinematischer und mechanischer Beziehungen”. *Zeitschrift für Physik* **33**, 879–892 (1925).
- [6] M. Born, W. Heisenberg, and P. Jordan. “Zur Quantenmechanik. II.” *Zeitschrift für Physik* **35**, 557–615 (1926).
- [7] M. Born. “Quantenmechanik der Stoßvorgänge”. *Zeitschrift für Physik* **38**, 803–827 (1926).
- [8] A. Einstein, B. Podolsky, and N. Rosen. “Can quantum-mechanical description of physical reality be considered complete?” *Physical Review* ... **47**, 777–780 (1935).
- [9] W. Heisenberg. “Über den anschaulichen Inhalt der quantentheoretischen Kinematik und Mechanik”. *Zeitschrift für Physik* **33**, 172–198 (1927).
- [10] J. P. Gordon, H. J. Zeiger, and C. H. Townes. “The maser—new type of microwave amplifier, frequency standard, and spectrometer”. *Physical Review* ... **99**, 1264–1274 (1955).
- [11] A. Einstein. “Zur Quantentheorie der Strahlung”. *Physikalische Gesellschaft Zürich* **18**, 47–62 (1916).
- [12] R. Ladenburg. “Untersuchungen über die anomale Dispersion angeregter Gase”. *Zeitschrift für Physik* **48**, 15–25 (1928).
- [13] H. Kopfermann and R. Ladenburg. “Untersuchungen über die anomale Dispersion angeregter Gase”. *Zeitschrift für Physik* **48**, 26–50 (1928).
- [14] A. Carst and R. Ladenburg. “Untersuchungen über die anomale Dispersion angeregter Gase”. *Zeitschrift für Physik* **48**, 192–204 (1928).

- [15] T. H. Maiman. “Stimulated optical radiation in ruby”. **187**, 493–494 (1960).
- [16] W. H. Louisell, A. Yariv, and A. E. Siegman. “Quantum Fluctuations and Noise in Parametric Processes. I.” *Physical Review* ... **124**, 1646–1654 (1961).
- [17] R. J. Glauber. “The quantum theory of optical coherence”. *Physical Review* ... **130**, 2529–2539 (1963).
- [18] J. S. Bell. “On the Einstein Podolsky Rosen paradox”. *Physics* **1**, 195–200 (1964).
- [19] J. F. Clauser, M. A. Horne, and A. Shimony. “Proposed experiment to test local hidden-variable theories”. *Physical Review Letters* **23**, 880 (1969).
- [20] W. E. Lamb Jr. “Theory of an optical maser”. *Physical Review* ... **134**, A1429–A1450 (1964).
- [21] P. F. Moulton. “Spectroscopic and laser characteristics of Ti: A1203”. *J. Opt. Soc. Am. B* **3**, 125 (1986).
- [22] B. Y. Zel’Dovich and D. N. Klyshko. “Field statistics in parametric luminescence”. *ZhETF Pis ma Redaktsiiu* **2**, 69–72 (1969).
- [23] D. C. Burnham and D. L. Weinberg. “Observation of simultaneity in parametric production of optical photon pairs”. *Physical Review Letters* **25**, 84 (1970).
- [24] S. J. Freedman and J. F. Clauser. “Experimental test of local hidden-variable theories”. *Physical Review Letters* **28**, 938 (1972).
- [25] A. Aspect, P. Grangier, and G. Roger. “Experimental tests of realistic local theories via Bell’s theorem”. *Physical Review Letters* **47**, 460 (1981).
- [26] H. J. Kimble and M. Dagenais. “Photon antibunching in resonance fluorescence”. *Physical Review Letters* **39**, 691 (1977).
- [27] C. H. Bennett and G. Brassard. “Quantum cryptography: Public key distribution and coin tossing”. In: *Proceedings of IEEE International* ... 1984.
- [28] R. E. Slusher, L. W. Hollberg, B. Yurke, and J. C. Mertz. “Observation of squeezed states generated by four-wave mixing in an optical cavity”. *Physical Review Letters* **55**, 2409 (1985).
- [29] C. K. Hong, O. Z. Y, and L. Mandel. “Measurement of subpicosecond time intervals between two photons by interference”. *Physical Review Letters* **59**, 2044–2046 (1987).
- [30] E. Knill, R. Laflamme, and G. J. Milburn. “A scheme for efficient quantum computation with linear optics”. *Nature* **409**, 46–52 (2001).
- [31] L. E. Hargrove, R. L. Fork, and M. A. Pollack. “Locking of He-Ne laser modes induced by synchronous intracavity modulation”. *Applied Physics Letters* **5**, 4–5 (1964).
- [32] D. E. Spence, P. N. Kean, and W. Sibbett. “60-fsec pulse generation from a self-mode-locked Ti: sapphire laser”. *Optics Letters* **16**, 42–44 (1991).
- [33] J. Paye. “The chronocyclic representation of ultrashort light pulses”. *Quantum Electronics, IEEE Journal of* **28**, 2262–2273 (1992).

- 
- [34] D. N. Fittinghoff, K. W. DeLong, R. Trebino, and C. L. Ladera. “Noise sensitivity in frequency-resolved optical-gating measurements of ultrashort pulses”. *JOSA B* **12**, 1955–1967 (1995).
- [35] C. Iaconis and I. A. Walmsley. “Spectral phase interferometry for direct electric-field reconstruction of ultrashort optical pulses”. *Optics Letters* **23**, 792–794 (1998).
- [36] J. C. Knight, T. A. Birks, P. S. J. Russell, and D. M. Atkin. “All-silica single-mode optical fiber with photonic crystal cladding”. *Optics Letters* **21**, 1547–1549 (1996).
- [37] R. R. Alfano and S. L. Shapiro. “Direct distortion of electronic clouds of rare-gas atoms in intense electric fields”. *Physical Review Letters* **24**, 1217 (1970).
- [38] R. R. Alfano and S. L. Shapiro. “Emission in the region 4000 to 7000 Å via four-photon coupling in glass”. *Physical Review Letters* **24**, 584 (1970).
- [39] R. R. Alfano and S. L. Shapiro. “Observation of self-phase modulation and small-scale filaments in crystals and glasses”. *Physical Review Letters* **24**, 592 (1970).
- [40] J. G. Rarity, P. R. Tapster, and E. Jakeman. “Observation of sub-poissonian light in parametric downconversion”. *Optics Communications* **62**, 201–206 (1987).
- [41] Y. H. Shih and C. O. Alley. “New Type of Einstein-Podolsky-Rosen-Bohm Experiment Using Pairs of Light Quanta Produced by Optical Parametric Down Conversion”. *Physical Review Letters* **61**, 2921–2924 (1988).
- [42] P. Tapster, J. Rarity, and J. Satchell. “Use of parametric down-conversion to generate sub-Poissonian light”. *Physical Review A* **37**, 2963–2967 (1988).
- [43] T. E. Kiess, Y. H. Shih, A. V. Sergienko, and C. O. Alley. “Einstein-Podolsky-Rosen-Bohm experiment using pairs of light quanta produced by type-II parametric down-conversion”. *Physical Review Letters* **71**, 3893–3897 (1993).
- [44] P. Kwiat, K. Mattle, H. Weinfurter, et al. “New High-Intensity Source of Polarization-Entangled Photon Pairs”. *Physical Review Letters* **75**, 4337–4341 (1995).
- [45] P. Kumar. “Quantum frequency conversion”. *Optics Letters* **15**, 1476–1478 (1990).
- [46] J. Huang and P. Kumar. “Observation of quantum frequency conversion”. *Physical Review Letters* **68**, 2153–2156 (1992).
- [47] S. Tanzilli, H. De Riedmatten, H. Zbinden, et al. “Highly efficient photon-pair source using periodically poled lithium niobate waveguide”. *Electronics Letters* **37**, 26–28 (2001).
- [48] C. K. Law, I. A. Walmsley, and J. H. Eberly. “Continuous frequency entanglement: effective finite Hilbert space and entropy control”. *Physical Review Letters* **84**, 5304–5307 (2000).
- [49] A. B. U’Ren, C. Silberhorn, K. Banaszek, et al. “Generation of Pure-State Single-Photon Wavepackets by Conditional Preparation Based on Spontaneous Parametric Downconversion”. *Laser Physics* **15**, 146–161 (2005).
- [50] R. W. Boyd. *Nonlinear optics*. Elsevier, 2003.

- [51] P. J. Mosley, J. S. Lundeen, B. J. Smith, et al. “Heralded Generation of Ultrafast Single Photons in Pure Quantum States”. *Physical Review Letters* **100**, (2008).
- [52] T. Gerrits, M. J. Stevens, B. Baek, et al. “Generation of degenerate, factorizable, pulsed squeezed light at telecom wavelengths”. *Optics Express* **19**, 24434–24447 (2011).
- [53] A. Eckstein, A. Christ, P. J. Mosley, and C. Silberhorn. “Highly efficient single-pass source of pulsed single-mode twin beams of light”. *Physical Review Letters* **106**, 13603 (2011).
- [54] G. Harder, V. Ansari, B. Brecht, et al. “An optimized photon pair source for quantum circuits”. *Optics Express* **21**, 13975 (2013).
- [55] C. Söller, B. Brecht, P. J. Mosley, et al. “Bridging visible and telecom wavelengths with a single-mode broadband photon pair source”. *Physical Review A* **81**, (2010).
- [56] C. Söller, O. Cohen, B. Smith, I. Walmsley, and C. Silberhorn. “High-performance single-photon generation with commercial-grade optical fiber”. *Physical Review A* **83**, (2011).
- [57] G. J. de Valcárcel, G. Patera, N. Treps, and C. Fabre. “Multimode squeezing of frequency combs”. *Physical Review A* **74**, 061801 (2006).
- [58] O. Pinel, P. Jian, R. de Araújo, et al. “Generation and Characterization of Multimode Quantum Frequency Combs”. *Physical Review Letters* **108**, 083601 (2012).
- [59] J. Roslund, R. M. de Araújo, S. Jiang, C. Fabre, and N. Treps. “Wavelength-multiplexed quantum networks with ultrafast frequency combs”. *Nature Photonics* **AOP**, (2013).
- [60] A. Eckstein, B. Brecht, and C. Silberhorn. “A quantum pulse gate based on spectrally engineered sum frequency generation”. *Optics Express* **19**, 13370 (2011).
- [61] B. Brecht, A. Eckstein, A. Christ, H. Suche, and C. Silberhorn. “From quantum pulse gate to quantum pulse shaper—engineered frequency conversion in nonlinear optical waveguides”. *New Journal of Physics* **13**, 065029 (2011).
- [62] M. G. Raymer, S. J. van Enk, C. J. McKinstrie, and H. J. McGuinness. “Interference of two photons of different color”. *Optics Communications* **283**, 747–752 (2010).
- [63] M. G. Raymer and K. Srinivasan. “Manipulating the color and shape of single photons”. *Physics Today* **65**, 32 (2012).
- [64] D. V. Reddy, M. G. Raymer, C. J. McKinstrie, L. Mejling, and K. Rottwitt. “Temporal mode selectivity by frequency conversion in second-order nonlinear optical waveguides”. *arXiv.org*, (2013).
- [65] L. Mejling, C. J. McKinstrie, M. G. Raymer, and K. Rottwitt. “Quantum frequency translation by four-wave mixing in a fiber: low-conversion regime”. *Optics Express* **20**, 8367 (2012).
- [66] C. J. McKinstrie, L. Mejling, M. G. Raymer, and K. Rottwitt. “Quantum-state-preserving optical frequency conversion and pulse reshaping by four-wave mixing”. *Physical Review A* **85**, 053829 (2012).

- 
- [67] H. J. McGuinness. “The Creation and Frequency Translation of Single-Photon States of Light in Optical Fiber”. PhD thesis. 2011.
- [68] H. McGuinness, M. Raymer, and C. McKinstrie. “Theory of quantum frequency translation of light in optical fiber: application to interference of two photons of different color”. *Optics Express* **19**, 17876–17907 (2011).
- [69] H. J. McGuinness, M. G. Raymer, C. J. McKinstrie, and S. Radic. “Wavelength Translation Across 210 nm in the Visible Using Vector Bragg Scattering in a Birefringent Photonic Crystal Fiber”. *IEEE Photonics Technology Letters* **23**, 109–111 (2011).
- [70] E. Marcatili. “Dielectric rectangular waveguide and directional coupler for integrated optics”. *Bell Syst Tech J* **48**, 2071–2102 (1969).
- [71] E. Strake, G. Bava, and I. Montrosset. “Guided modes of Ti:LiNbO<sub>3</sub> channel waveguides: a novel quasi-analytical technique in comparison with the scalar finite-element method”. *Lightwave Technology, Journal of* **6**, 1126–1135 (1988).
- [72] T. Suhara and M. Fujimura. *Waveguide Nonlinear-Optic Devices*. Vol. 11. Springer Series in Photonics. Berlin, Heidelberg: Springer Berlin Heidelberg, 2003.
- [73] Z. H. Wang, X. Z. Zhang, J. J. Xu, and Q. Wu. “Time-resolved femtosecond degenerate four-wave mixing in LiNbO<sub>3</sub>: Fe, Mg crystal”. *Chinese Physics ...* **22**, 2831–2833 (2005).
- [74] M. Yamada, N. Nada, M. Saitoh, and K. Watanabe. “First-order quasi-phase matched LiNbO<sub>3</sub> waveguide periodically poled by applying an external field for efficient blue second-harmonic generation”. *Applied Physics Letters* **62**, 435–436 (1993).
- [75] A. Monmayrant, S. Weber, and B. Chatel. “A newcomer’s guide to ultrashort pulse shaping and characterization”. *Journal of Physics B: Atomic, Molecular and Optical Physics* **43**, 103001 (2010).
- [76] A. Christ, B. Brecht, W. Mauerer, and C. Silberhorn. “Theory of quantum frequency conversion and type-II parametric down-conversion in the high-gain regime”. *New Journal of Physics* **15**, 053038 (2013).
- [77] F. Dell’Anno, S. De Siena, and F. Illuminati. “Multiphoton quantum optics and quantum state engineering”. *Physics reports* **428**, 53–168 (2006).
- [78] U. Leonhardt. *Essential Quantum Optics. From Quantum Measurements to Black Holes*. Cambridge: Cambridge University Press, 2009.
- [79] K. J. Blow, R. Loudon, and S. J. D. Phoenix. “Continuum fields in quantum optics”. *Physical Review A* **42**, 4102–4114 (1990).
- [80] E. Schmidt. “Zur Theorie der linearen und nichtlinearen Integralgleichungen”. *Math. Ann.* **63**, 433–476 (1907).
- [81] H. Everett III. ““Relative state” formulation of quantum mechanics”. *Reviews of Modern Physics* **29**, 454–462 (1957).
- [82] A. Ekert and P. L. Knight. “Entangled quantum systems and the Schmidt decomposition”. *American Journal of Physics* **63**, 415 (1995).

- [83] P. P. Rohde, W. Mauerer, and C. Silberhorn. “Spectral structure and decompositions of optical states, and their applications”. *New Journal of Physics* **9**, 91–91 (2007).
- [84] B. Brecht and C. Silberhorn. “Characterizing entanglement in pulsed parametric down-conversion using chronocyclic Wigner functions”. *Physical Review A* **87**, 053810 (2013).
- [85] B. Brecht, A. Eckstein, and C. Silberhorn. “Controlling the correlations in frequency upconversion in PPLN and PPKTP waveguides”. *physica status solidi (c)* **8**, 1235–1238 (2011).
- [86] W. P. Grice and I. A. Walmsley. “Spectral information and distinguishability in type-II down-conversion with a broadband pump”. *Physical Review A* **56**, 1627 (1997).
- [87] A. Wehrl. “General properties of entropy”. *Reviews of Modern Physics* **50**, 221–260 (1978).
- [88] R. Grobe, K. Rzazewski, and J. H. Eberly. “Measure of electron-electron correlation in atomic physics”. *Journal of Physics B: Atomic* **27**, 503–508 (1994).
- [89] J. H. Eberly. “Schmidt analysis of pure-state entanglement”. *Laser Physics* **16**, 921–926 (2006).
- [90] M. C. Tichy, P. A. Bouvrie, and K. Mølmer. “Bosonic behavior of entangled fermions”. *Physical Review A* **86**, 042317 (2012).
- [91] A. M. Brańczyk, T. C. Ralph, W. Helwig, and C. Silberhorn. “Optimized generation of heralded Fock states using parametric down-conversion”. *New Journal of Physics* **12**, 063001 (2010).
- [92] H. Bechmann-Pasquinucci and A. Peres. “Quantum Cryptography with 3-State Systems”. *Physical Review Letters* **85**, 3313–3316 (2000).
- [93] H. Bechmann-Pasquinucci and W. Tittel. “Phys. Rev. A 61, 062308 (2000): Quantum cryptography using larger alphabets”. *Physical Review A* **61**, (2000).
- [94] J. Leach, E. Bolduc, D. J. Gauthier, and R. Boyd. “Secure information capacity of photons entangled in many dimensions”. *Physical Review A* **85**, 060304 (2012).
- [95] R. A. Campos, B. Saleh, and M. C. Teich. “Quantum-mechanical lossless beam splitter: SU (2) symmetry and photon statistics”. *Physical Review A* **40**, 1371–1384 (1989).
- [96] A. P. VanDevender and P. G. Kwiat. “Quantum transduction via frequency upconversion (invited)”. *J. Opt. Soc. Am. B* **24**, 295–299 (2007).
- [97] W. P. Grice, A. B. U’Ren, and I. A. Walmsley. “Eliminating frequency and space-time correlations in multiphoton states”. *Physical Review A* **64**, 063815 (2001).
- [98] P. Ben Dixon, J. H. Shapiro, and F. Wong. “Spectral engineering by Gaussian phase-matching for quantum photonics”. *Optics Express* **21**, 5879–5890 (2013).
- [99] A. M. Brańczyk, A. Fedrizzi, T. M. Stace, T. C. Ralph, and A. G. White. “Engineered optical nonlinearity for a quantum light source”. *Optics Express* **19**, (2011).
- [100] W. Mauerer. “On Colours, Keys, and Correlations: Multimode Parametric Downconversion in the Photon Number Basis”. PhD thesis. University of Erlangen, 2009.

- 
- [101] G. Patera, C. Navarrete-Benlloch, G. J. de Valcárcel, and C. Fabre. “Quantum coherent control of highly multipartite continuous-variable entangled states by tailoring parametric interactions”. *The European Physical Journal D* **66**, 1–14 (2012).
- [102] J. Lavoie, J. M. Donohue, L. G. Wright, A. Fedrizzi, and K. J. Resch. “Spectral compression of single photons”. *Nature Photonics* **7**, 363–366 (2013).
- [103] M. Kolobov. “The spatial behavior of nonclassical light”. *Reviews of Modern Physics* **71**, 1539–1589 (1999).
- [104] A. K. Ekert and P. L. Knight. “Relationship between semiclassical and quantum-mechanical input-output theories of optical response”. *Physical Review A* **43**, 3934–3938 (1991).
- [105] S. Braunstein. “Squeezing as an irreducible resource”. *Physical Review A* **71**, 055801 (2005).
- [106] S. L. Braunstein. “Quantum information with continuous variables”. *Reviews of Modern Physics* **77**, 513–577 (2005).
- [107] W. Wieczorek, R. Krischek, N. Kiesel, et al. “Experimental Entanglement of a Six-Photon Symmetric Dicke State”. *Physical Review Letters* **103**, 020504 (2009).
- [108] A. Martin, A. Issautier, H. Herrmann, and W. Sohler. “A polarization entangled photon-pair source based on a type-II PPLN waveguide emitting at a telecom wavelength”. *New Journal of Physics* **12**, (2010).
- [109] H. Herrmann, X. Yang, A. Thomas, and A. Poppe. “Post-selection free, integrated optical source of non-degenerate, polarization entangled photon pairs”. *Optics Express* **21**, 27981 (2013).
- [110] J. Barreiro, N. Langford, N. Peters, and P. Kwiat. “Generation of Hyperentangled Photon Pairs”. *Physical Review Letters* **95**, 260501 (2005).
- [111] P. G. Kwiat. “Hyper-entangled states”. *Journal of Modern Optics* **44**, 2173–2184 (2009).
- [112] W. B. Gao, C. Y. Lu, X. C. Yao, et al. “Experimental demonstration of a hyper-entangled ten-qubit Schrödinger cat state”. *Nature Physics* **6**, 331–335 (2010).
- [113] A. Mair, A. Vaziri, G. Weihs, and A. Zeilinger. “Entanglement of the orbital angular momentum states of photons”. *Nature* **412**, 313–316 (2001).
- [114] G. Molina-Terriza, J. P. Torres, and L. Torner. “Twisted photons”. *Nature Physics* **3**, 305–310 (2007).
- [115] J. Leach, B. Jack, J. Romero, A. K. Jha, and A. M. Yao. “Quantum Correlations in Optical Angle–Orbital Angular Momentum Variables”. *Science* **329**, 662 (2010).
- [116] A. C. Dada, J. Leach, G. S. Buller, M. J. Padgett, and E. Andersson. “Experimental high-dimensional two-photon entanglement and violations of generalized Bell inequalities”. *Nature Physics* **7**, 677–680 (2011).
- [117] R. Fickler, R. Lapkiewicz, W. N. Plick, et al. “Quantum Entanglement of High Angular Momenta”. *Science* **338**, 640–643 (2012).
- [118] N. Kiesel, C. Schmid, U. Weber, et al. “Experimental Analysis of a Four-Qubit Photon Cluster State”. *Physical Review Letters* **95**, 210502 (2005).

- [119] P. Walther, K. J. Resch, T. Rudolph, and E. Schenck. “Experimental one-way quantum computing”. *Nature* **434**, 169–176 (2005).
- [120] R. Prevedel, P. Walther, F. Tiefenbacher, et al. “High-speed linear optics quantum computing using active feed-forward”. *Nature* **445**, 65–69 (2007).
- [121] C.-Y. Lu, X.-Q. Zhou, O. Gühne, et al. “Experimental entanglement of six photons in graph states”. *Nature Physics* **3**, 91–95 (2007).
- [122] K. Chen, C.-M. Li, Q. Zhang, et al. “Experimental Realization of One-Way Quantum Computing with Two-Photon Four-Qubit Cluster States”. *Physical Review Letters* **99**, 120503 (2007).
- [123] G. Molina-Terriza, J. Torres, and L. Torner. “Management of the Angular Momentum of Light: Preparation of Photons in Multidimensional Vector States of Angular Momentum”. *Physical Review Letters* **88**, 013601 (2001).
- [124] P. Mosley, A. Christ, A. Eckstein, and C. Silberhorn. “Direct Measurement of the Spatial-Spectral Structure of Waveguided Parametric Down-Conversion”. *Physical Review Letters* **103**, (2009).
- [125] G. C. G. Berkhout, M. P. J. Lavery, J. Courtial, M. W. Beijersbergen, and M. J. Padgett. “Efficient Sorting of Orbital Angular Momentum States of Light”. *Physical Review Letters* **105**, 153601 (2010).
- [126] M. Avenhaus, H. B. Coldenstrodt-Ronge, K. Laiho, et al. “Photon number statistics of multimode parametric down-conversion”. *Physical Review Letters* **101**, 53601 (2008).
- [127] W. Mauerer, M. Avenhaus, W. Helwig, and C. Silberhorn. “How colors influence numbers: Photon statistics of parametric down-conversion”. *Physical Review A* **80**, (2009).
- [128] M. Avenhaus, A. Eckstein, P. J. Mosley, and C. Silberhorn. “Fiber-assisted single-photon spectrograph”. *Optics Letters* **34**, 2873–2875 (2009).
- [129] M. Avenhaus, B. Brecht, K. Laiho, and C. Silberhorn. “In preparation”.
- [130] A. Christ, K. Laiho, A. Eckstein, et al. “Spatial modes in waveguided parametric down-conversion”. *Physical Review A* **80**, 033829 (2009).
- [131] A. B. U’Ren, K. Banaszek, and I. A. Walmsley. “Photon engineering for quantum information processing”. *Quantum Information and Communication* **3**, 480–502 (2003).
- [132] K. Laiho, K. N. Cassemiro, and C. Silberhorn. “Producing high fidelity single photons with optimal brightness via waveguided parametric down-conversion”. *Optics Express* **17**, 22823–22837 (2009).
- [133] K. N. Cassemiro, K. Laiho, and C. Silberhorn. “Accessing the purity of a single photon by the width of the Hong–Ou–Mandel interference”. *New Journal of Physics* **12**, 113052 (2010).
- [134] K. Laiho, M. Avenhaus, K. N. Cassemiro, and C. Silberhorn. “Direct probing of the Wigner function by time-multiplexed detection of photon statistics”. *New Journal of Physics* **11**, 043012 (2009).

- 
- [135] K. Laiho, K. N. Cassemiro, D. Gross, and C. Silberhorn. “Probing the Negative Wigner Function of a Pulsed Single Photon Point by Point”. *Physical Review Letters* **105**, (2010).
- [136] K. Laiho, A. Christ, K. N. Cassemiro, and C. Silberhorn. “Testing spectral filters as Gaussian quantum optical channels”. *Optics Letters* **36**, 1476–1478 (2011).
- [137] A. Christ, K. Laiho, A. Eckstein, K. N. Cassemiro, and C. Silberhorn. “Probing multi-mode squeezing with correlation functions”. *New Journal of Physics* **13**, 033027 (2011).
- [138] R. Loudon and M. O. Scully. “The Quantum Theory of Light”. *Physics Today* **27**, 48 (1974).
- [139] M. Reid and P. Drummond. “Quantum Correlations of Phase in Nondegenerate Parametric Oscillation”. *Physical Review Letters* **60**, 2731–2733 (1988).
- [140] A. Furusawa, J. L. Sørensen, S. L. Braunstein, et al. “Unconditional Quantum Teleportation”. *Science* **282**, 706 (1998).
- [141] Y. Aharonov and D. Bohm. “Time in the Quantum Theory and the Uncertainty Relation for Time and Energy”. *Physical Review* ... **122**, 1649–1658 (1961).
- [142] A. U’ren, Y. Jeronimo-Moreno, and H. Garcia-Gracia. “Generation of Fourier-transform-limited heralded single photons”. *Physical Review A* **75**, (2007).
- [143] Y. Jeronimo-Moreno and A. U’ren. “Control, measurement, and propagation of entanglement in photon pairs generated through type-II parametric down-conversion”. *Physical Review A* **79**, (2009).
- [144] X. Sanchez-Lozano, A. B. U’ren, and J. L. Lucio. “On the relationship between pump chirp and single-photon chirp in spontaneous parametric downconversion”. *Journal of Optics A* **14**, (2011).
- [145] O. Kuzucu, F. Wong, S. Kurimura, and S. Tovstonog. “Joint Temporal Density Measurements for Two-Photon State Characterization”. *Physical Review Letters* **101**, 153602 (2008).
- [146] V. Giovannetti, S. Lloyd, and L. Maccone. “Quantum-enhanced positioning and clock synchronization”. *Nature* **412**, 417–419 (2001).
- [147] V. Giovannetti, S. Lloyd, L. Maccone, and F. Wong. “Clock Synchronization with Dispersion Cancellation”. *Physical Review Letters* **87**, 117902 (2001).
- [148] A. Abouraddy, M. Nasr, B. Saleh, A. Sergienko, and M. Teich. “Quantum-optical coherence tomography with dispersion cancellation”. *Physical Review A* **65**, 053817 (2002).
- [149] A. Boto, P. Kok, D. Abrams, et al. “Quantum Interferometric Optical Lithography: Exploiting Entanglement to Beat the Diffraction Limit”. *Physical Review Letters* **85**, 2733–2736 (2000).
- [150] V. Ansari, B. Brecht, G. Harder, et al. “In preparation”.
- [151] M. Avenhaus, M. V. Chekhova, L. A. Krivitsky, G. Leuchs, and C. Silberhorn. “Experimental verification of high spectral entanglement for pulsed waveguided spontaneous parametric down-conversion”. *Physical Review A* **79**, 043836 (2009).

- [152] T. Lutz, P. Kolenderski, and T. Jennewein. “Demonstration of spectral correlation control in a source of polarization entangled photon pairs at telecom wavelength”. *arXiv.org*, (2013).
- [153] A. Eckstein, A. Christ, P. J. Mosley, and C. Silberhorn. “Realistic  $g(2)$  measurement of a PDC source with single photon detectors in the presence of background”. *physica status solidi (c)* **8**, 1216–1219 (2011).
- [154] D. N. Klyshko. “Utilization of vacuum fluctuations as an optical brightness standard”. *Quantum Electronics* **7**, 591–595 (1977).
- [155] J. G. Rarity, K. D. Ridley, and P. R. Tapster. “Absolute measurement of detector quantum efficiency using parametric downconversion”. *Applied optics* **26**, 4616–4619 (1987).
- [156] D. Achilles, C. Silberhorn, and I. Walmsley. “Direct, Loss-Tolerant Characterization of Nonclassical Photon Statistics”. *Physical Review Letters* **97**, 043602 (2006).
- [157] M. H. Rubin, D. N. Klyshko, Y. H. Shih, and A. V. Sergienko. “Theory of two-photon entanglement in type-II optical parametric down-conversion”. *Physical Review A* **50**, 5122–5133 (1994).
- [158] A. Eckstein and C. Silberhorn. “Broadband frequency mode entanglement in waveguided parametric downconversion”. *Optics Letters* **33**, 1825–1827 (2008).
- [159] D. Collins, N. Gisin, N. Linden, S. Massar, and S. Popescu. “Bell Inequalities for Arbitrarily High-Dimensional Systems”. *Physical Review Letters* **88**, (2002).
- [160] A. Christ, C. Lupo, and C. Silberhorn. “Exponentially enhanced quantum communication rate by multiplexing continuous-variable teleportation”. *New Journal of Physics* **14**, 083007 (2012).
- [161] R. Essiambre, G. Kramer, P. J. Winzer, G. J. Foschini, and B. Goebel. “Capacity Limits of Optical Fiber Networks”. *Journal of Lightwave Technology* **28**, 662–701 (2010).
- [162] P. J. Winzer. “Energy-Efficient Optical Transport Capacity Scaling Through Spatial Multiplexing”. *Photonics Technology Letters, IEEE* **23**, 851–853 (2011).
- [163] S. Straupe, D. Ivanov, A. Kalinkin, I. B. Bobrov, and S. Kulik. “Angular Schmidt modes in spontaneous parametric down-conversion”. *Physical Review A* **83**, 060302 (2011).
- [164] J. T. Barreiro, T.-C. Wei, and P. G. Kwiat. “Beating the channel capacity limit for linear photonic superdense coding”. *Nature Physics* **4**, 282–286 (2008).
- [165] J. Wang, J.-Y. Yang, I. M. Fazal, et al. “Terabit free-space data transmission employing orbital angular momentum multiplexing”. *Nature Photonics* **6**, 488–496 (2012).
- [166] E. Nagali, F. Sciarrino, F. De Martini, et al. “Quantum Information Transfer from Spin to Orbital Angular Momentum of Photons”. *Physical Review Letters* **103**, 013601 (2009).
- [167] G. Giorgi, P. Mataloni, and F. De Martini. “Frequency Hopping in Quantum Interferometry: Efficient Up-Down Conversion for Qubits and Ebits”. *Physical Review Letters* **90**, 027902 (2003).
- [168] V. Rostislav, C. Langrock, J. R. Kurz, and M. M. Fejer. “Periodically poled lithium niobate waveguide sum-frequency generator for efficient single-photon detection at communication wavelengths”. *Optics Letters* **29**, 1518 (2004).

- 
- [169] M. A. Albota and F. N. C. Wong. “Efficient single-photon counting at 1.55  $\mu\text{m}$  by means of frequency upconversion”. *Optics Letters* **29**, 1449–1451 (2004).
- [170] A. Vandevender and P. Kwiat. “High efficiency single photon detection via frequency up-conversion”. *Journal of Modern Optics* **51**, 1433–1445 (2004).
- [171] C. Langrock, E. Diamanti, R. Roussev, et al. “Highly efficient single-photon detection at communication wavelengths by use of upconversion in reverse-proton-exchanged periodically poled LiNbO<sub>3</sub> waveguides”. *Optics Letters* **30**, 1725–1727 (2005).
- [172] R. T. Thew, T. S. L. Krainer, et al. “Low jitter up-conversion detectors for telecom wavelength GHz QKD”. *New Journal of Physics* **8**, 32 (2006).
- [173] H. Kamada, M. Asobe, T. Honjo, et al. “Efficient and low-noise single-photon detection in 1550nm communication band by frequency upconversion in periodically poled LiNbO<sub>3</sub> waveguides”. *Optics Letters* **33**, 639–641 (2008).
- [174] M. A. Albota and B. S. Robinson. “Photon-counting 1.55  $\mu\text{m}$  optical communications with pulse-position modulation and a multimode upconversion single-photon receiver”. *Optics Letters* **35**, 2627–2629 (2010).
- [175] S. Tanzilli, W. Tittel, M. Halder, et al. “A photonic quantum information interface”. *Nature* **437**, 116 (2005).
- [176] M. A. Albota, F. N. C. Wong, and J. H. Shapiro. “Polarization-independent frequency conversion for quantum optical communication”. *JOSA B* **23**, 918–924 (2006).
- [177] H. Takesue. “Erasing Distinguishability Using Quantum Frequency Up-Conversion”. *Physical Review Letters* **101**, 173901 (2008).
- [178] M. T. Rakher, L. Ma, O. Slattery, X. Tang, and K. Srinivasan. “Quantum transduction of telecommunications-band single photons from a quantum dot by frequency upconversion”. *Nature Photonics* **4**, 786–791 (2010).
- [179] S. Ramelow, A. Fedrizzi, A. Poppe, N. Langford, and A. Zeilinger. “Polarization-entanglement-conserving frequency conversion of photons”. *Physical Review A* **85**, (2012).
- [180] K. Koshino. “Down-conversion of a single photon with unit efficiency”. *PHYSICAL REVIEW A Phys Rev A* **79**, 5 (2009).
- [181] H. Takesue. “Single-photon frequency down-conversion experiment”. *Physical Review A* **82**, 013833 (2010).
- [182] Y. Ding and Z. Y. Ou. “Frequency downconversion for a quantum network”. *Optics Letters* **35**, 2591–2593 (2010).
- [183] H. McGuinness, M. Raymer, C. McKinstrie, and S. Radic. “Quantum Frequency Translation of Single-Photon States in a Photonic Crystal Fiber”. *Physical Review Letters* **105**, (2010).
- [184] D. Kielpinski, J. F. Corney, and H. Wiseman. “Quantum Optical Waveform Conversion”. *Physical Review Letters* **106**, 130501 (2011).
- [185] Y.-P. Huang and P. Kumar. “Mode-resolved photon counting via cascaded quantum frequency conversion”. *Optics Letters* **38**, 468–470 (2013).

- [186] D. V. Reddy, M. G. Raymer, and C. J. McKinstrie. “Efficient sorting of quantum-optical wave packets by temporal-mode interferometry”. *arXiv.org*, (2014).
- [187] M. Lobino, D. Korystov, C. Kupchak, et al. “Complete Characterization of Quantum-Optical Processes”. *Science* **322**, 563–566 (2008).
- [188] H. Takahashi, J. S. Neergaard-Nielsen, M. Takeuchi, et al. “Entanglement distillation from Gaussian input states”. *Nature Photonics* **4**, 178–181 (2010).
- [189] A. Ourjoumtsev, H. Jeong, R. Tualle-Brouri, and P. Grangier. “Generation of optical ‘Schrödinger cats’ from photon number states”. *Nature* **448**, 784–786 (2007).
- [190] A. Ourjoumtsev, R. Tualle-Brouri, J. Laurat, and P. Grangier. “Generating Optical Schrödinger Kittens for Quantum Information Processing”. *Science* **312**, 83–86 (2006).
- [191] R. Paschotta. *RP Photonics Encyclopedia*.